

Copyright
by
Aysen Ozkan
2010

**The Dissertation Committee for Aysen Ozkan Certifies that this is the approved
version of the following dissertation:**

**STRUCTURAL DIAGENETIC ATTRIBUTES OF THE LATE
CRETACEOUS WILLIAMS FORK SANDSTONES WITH
IMPLICATIONS FOR PETROPHYSICAL INTERPRETATION AND
FRACTURE PREDICTION, PICEANCE BASIN, COLORADO**

Committee:

Kitty Milliken, Supervisor

Stephen E. Laubach, Co-Supervisor

Brian Horton

Ron Steel

Scott Tinker

Linda Bonnell

**STRUCTURAL DIAGENETIC ATTRIBUTES OF THE LATE
CRETACEOUS WILLIAMS FORK SANDSTONES WITH
IMPLICATIONS FOR PETROPHYSICAL INTERPRETATION AND
FRACTURE PREDICTION, PICEANCE BASIN, COLORADO**

by

Aysen Ozkan, B.S., M.S.

Dissertation

Presented to the Faculty of the Graduate School of

The University of Texas at Austin

in Partial Fulfillment

of the Requirements

for the Degree of

Doctor of Philosophy

The University of Texas at Austin

May, 2010

Dedication

To my parents:

Yuksel and Suleyman Ozkan

Acknowledgements

I want to express my appreciation to my supervisors Dr. Kitty L. Milliken and Dr. Stephen Laubach for their consistent guidance and encouragement throughout my graduate study. It would have been impossible to complete this work without their helpful guidance. I would like to extend my sincere appreciation to my committee members, Dr. Linda Bonnell, Dr. Brian Horton, Dr. Ron Steel, and Dr. Scott Tinker for their valuable comments and discussions.

I cannot thank Steve P. Cumella enough. He has been tremendous help in providing data and samples. Discussions with him have greatly expanded my knowledge of the Piceance Basin. I would like to extend my sincere gratitude to Dr. Jon Holder and Dr. Jon Olson for their help in understanding the subcritical crack testing and conducting the measurements.

Rob Lander and Linda Bonnell provided me a depth of knowledge on the application of diagenetic models. I always had fruitful discussions with them which gave me plenty of ideas to pursue in my research.

During my internships I learned a great deal about the application of diagenetic modeling in the oil industry from Andy Thomas, Rick Tobin, Chris Lerch, David Henry, Christine Skirius, and Ann Marchand. I gained a better understanding of tight gas reservoirs from Tony McClain, Laura Banfield, Lee McRae, Chris Yokoyama, Robert Lieber, and Keith Shanley.

I am sincerely grateful for help and advice from Dr. McBride, Dr. Folk, Astrid Makowitz, Jon Hooker, Carlotta Chernoff, Juli Hennings, Julia Gale, Mike Dempsey,

Peter Eichhubl, Andras Fall, Shirley Dutton, Jay Scheevel, and Randy Marrett. Thanks to Roger Gary for field assistance. Appreciation is extended to my friends Ercin Maslen, Alper Atilla, Muzaffer Bayazitoglu, Fatma Toksoy, Umut Yunusoglu, Fatma Geneli, Engin Alkan, Rob Reed, Jason Gumble, and Hyein Ahn for their friendship and help. Thanks to all my Corelab friends particularly Don Harville, Jerry and Cyndy Kier, Joan Spaw, Nancy Houghton, Brian Nicoud, Martin Quest, Drew Dickert, Marzena Jaminski, Yong Wu, and Debra Alvarez for support. Ozlem Okur, Semra Alici and Eloise Doherty are dear friends who passed away during my Ph.D. years. I will always remember them with a smile.

Finally, I want to thank my family Yuksel, Suleyman, Altan, Ertan, Nursen, Makbule, Alper Tuna, Basak, Baris, Roger, and Halide for their endless support.

Funding for this dissertation was available from the GDL Foundation structural diagenesis fellowship, Jackson School Geology Foundation, AAPG Foundation William Dow Ham Memorial Grant, ConocoPhillips SPIRIT Scholarship, industrial associates of the Fracture Research and Application Consortium (FRAC), and Chemical Sciences, Geosciences and Biosciences Division, Office of Basic Energy Sciences, Office of Science, U.S. Department of Energy Grant No. DE-FG02-03ER15430. I am grateful to Bill Barrett Corporation and Encana Corporation for access to data and thin sections. I appreciate Zhiyong He for providing access and guidance to 1D basin modeling program (*GenesisTM*) and Rob Lander and Linda Bonnell for access to diagenetic modeling program (*TouchstoneTM*). Thanks to Greg Thompson for preparing thin sections, Tye Lehman for help with computers, and Dennis Trombatore for library search help.

**STRUCTURAL DIAGENETIC ATTRIBUTES OF THE LATE
CRETACEOUS WILLIAMS FORK SANDSTONES WITH
IMPLICATIONS FOR PETROPHYSICAL INTERPRETATION AND
FRACTURE PREDICTION, PICEANCE BASIN, COLORADO**

Publication No. _____

Aysen Ozkan, Ph.D.

The University of Texas at Austin, 2010

Supervisors: Kitty L. Milliken and Stephen E. Laubach

Diagenetic and structural aspects of tight gas sandstones must be addressed concurrently in order to fully understand low-permeability sandstones and to better predict their reservoir quality attributes that arise from a combination of pore-scale and fracture distribution characteristics. This dissertation focuses on aspects of rock evolution that are germane to concurrent structural and diagenetic evolution, such as loading and thermal history, rock mechanical property evolution, and fracture timing. I tested the hypothesis that the cement precipitation step, governed by thermal exposure and grain surface attributes, governs how sandstone attributes evolve using observations from the Late Cretaceous Williams Fork sandstones from the Piceance Basin, Colorado.

My research shows that essential information for predicting and understanding fracture patterns in sandstone can be obtained by unraveling cement precipitation (diagenetic) history. Fractures depend on the mechanical properties existing during fracture growth. I show that key rock mechanical properties (subcritical crack index, Young's modulus and Poisson's ratio), petrophysical behavior, and reservoir quality depend in a systematic way on time-temperature history and the intrinsic grain surface attributes of these sandstones.

I classified the Williams Fork lithofacies petrographically and correlated those with log responses to create a model that can be used to predict reservoir quality and diagenesis directly from well logs. I determined rock mechanical characteristics by measuring the subcritical crack index (SCI), a mechanical property that influences fracture distribution characteristics, and by examining log-derived bulk mechanical properties. To quantify the influence of quartz cementation on the SCI and to determine the range of SCI values for sandstone of given framework composition at different diagenetic stages, I measured SCI on Williams Fork core samples and their outcrop equivalents. Diagenetic modeling is applied to determine the sandstone characteristics during fracturing.

Table of Contents

List of Tables	xiii
List of Figures	xvi
CHAPTER 1: INTRODUCTION	1
CHAPTER 2: BASIN HISTORY ASSESSMENT WITH DIAGENETIC MODELING	11
2.1. Structural Setting and Stratigraphy of the Williams Fork Formation, Piceance Basin	13
2.2. Petrography of the Williams Fork Formation	17
2.3. Modeling Approach	22
2.3.1. Basin Modeling Approach	22
2.3.1.1. Burial History Input	23
2.3.1.2. Thermal History Input	23
2.3.1.3. Results of Basin Modeling	28
2.3.2. Results of Quartz Cement Simulations	39
2.4. Discussion: Controls on Quartz Cementation	48
2.5. Discussion: Estimation of Removed Overburden	51
2.5.1. Estimation of Sediment Removal with Stratigraphic Inference	53
2.5.2. Estimation of Sediment Removal from Vitrinite Reflectance Evidence	54
2.5.3. Estimation of Sediment Removal with Diagenetic Models: Subsurface	55
2.5.4. Estimation of Sediment Removal with Diagenetic Models: Outcrop	57
2.6. Conclusions: Basin History Assessment with Diagenetic Modeling	61
CHAPTER 3: PREDICTION OF LITHOFACIES AND RESERVOIR QUALITY USING WELL LOGS, WILLIAMS FORK FORMATION, MAMM CREEK FIELD, PICEANCE BASIN	64
3.1. Introduction: Lithofacies Classification	64
3.2. Background Information on Facies Classification	65

3.3. Depositional History of the Williams Fork Formation	69
3.4. Methods for Lithofacies Classification	70
3.5. Framework Composition and Texture of the Williams Fork Sandstones...	73
3.6. Diagenesis of the Williams Fork Sandstones.....	77
3.6.1. Compaction	77
3.6.2. Authigenic Minerals in Pores and Fractures	81
3.6.3. Controls on Diagenesis: Provenance	83
3.6.4. Controls on Diagenesis: Depositional Environment.....	85
3.7. Pore Types and Distributions.....	85
3.8. Reservoir Quality	88
3.8.1. Diagenetic Controls on Reservoir Quality	89
3.8.2. Textural Controls on the Reservoir Quality	89
3.9. Lithofacies Identified in the Williams Fork Sandstones.....	92
3.10. Log Analyses	96
3.10.1. Lithology Identification	96
3.10.2. Assessing Reservoir Quality from Well Logs	105
3.10.2.1. Controls on Grain Density	105
3.10.2.2. Reservoir Quality Prediction.....	106
3.11. Conclusions: Lithofacies Classification Approach.....	112
CHAPTER 4: INFLUENCE OF DIAGENESIS ON ROCK MECHANICAL PROPERTIES	115
4.1 Introduction: Rock Mechanical Properties and Fracturing.....	115
4.1.1. Subcritical Crack Growth	118
4.1.2. Subcritical Crack Index Testing.....	122
4.2. Microscale Textural Controls on Subcritical Crack Index	124
4.2.1. Methods for Determining Microscale Textural Controls on SCI	126
4.2.2. Controls on the Subcritical Crack Index.....	127
4.2.2.1. Effects of Sandstone Texture on Fracture Propagation	127
4.2.2.2. Effects of Chemical Environment on SCI: Water Saturation.....	128

4.2.3. Results of Subcritical Crack Index Measurements	129
4.2.4. Discussion: Diagenetic Controls on SCI	138
4.2.5. Discussion: Microscale Mineralogical and Textural Controls on SCI: Fracture Path Analyses in Quartz- and Calcite-cemented Sandstones.....	141
4.2.6. Conclusions: Crack-Path Mapping	147
4.3. Quantification of Effects of Cementation on SCI by Comparison of Outcrop and Subsurface Samples of Williams Fork Formation	148
4.3.1. Study Area, Piceance Basin, Colorado	149
4.3.2. Depositional History	150
4.3.3. Methods for Outcrop/Subsurface Comparison	150
4.3.4. Petrographical Comparison of Rocks	153
4.3.5. Results of Subcritical Crack Index Measurements for Outcrop/Core Pairs.....	156
4.3.6. Rock Mechanical Comparison of Subsurface Samples and Their Outcrop Equivalents.....	162
4.3.7. Discussion: Is it Possible to Use Rock Mechanical Properties of Outcrop Samples as Analogs of Subsurface Equivalents?	167
4.3.8. Conclusions: Outcrop to Core Comparison	171
4.4. Case Study: Influence of Rock Mechanical Properties on Fracture Distribution in Core	173
4.4.1. Natural Fractures in the Williams Fork Formation.....	174
4.4.2. Causes of Fracturing	176
4.4.3. Rock Mechanical Properties of the Williams Fork Lithofacies	182
4.4.3.1. Lithological Controls on Subcritical Crack Index	185
4.4.3.2. Discussion: Use of Anisotropy for Fracture Density Distribution	186
4.4.3.3. Lithological Controls on Bulk Mechanical Properties: Young`s Modulus and Poisson`s Ratio	188
4.4.3.3.1. Definition of Young`s Modulus and Poisson`s Ratio	188
4.4.3.3.2. Dynamic versus Static Rock Mechanic Parameters.....	190
4.4.3.3.3. Lithological Controls on Bulk Mechanical Properties: Young`s Modulus and Poisson`s Ratio	191
4.4.3.4. Discussion: Lithological Controls on Subcritical Crack Index versus Bulk Mechanical Properties.....	195

4.4.3.5. Discussion: Predictability of Rock Mechanical Properties and Degree of Fracturing	197
4.4.4. Diagenetic State and Permeability of Tight Gas Sandstones at the Time of Gas Generation and Fracturing	202
4.4.4.1. Timing of Gas Generation and Fracturing in the Piceance Basin	202
4.4.4.2. Diagenetic Modeling.....	208
4.4.4.3. Discussion: Diagenetic Evolution during Gas Generation and Fracturing.....	209
4.4.4.4. Conclusions: Influence of Rock Mechanical Properties on Fracture Distribution.....	218
CHAPTER 5: CONCLUSION	220
APPENDIX A: INPUT FOR DIAGENETIC MODELING.....	223
MODAL ANALYSES (POINT COUNT AND TEXTURAL DATA).....	223
APPENDIX B: INPUT AND OUTPUT DATA FOR BASIN MODELS	230
B1: Stratigraphy input.....	231
B2: Vitrinite reflectance and temperature input.....	236
B3: Time versus temperature, depth, excess pressure, and effective pressure ...	241
APPENDIX C: SUBCRITICAL CRACK INDEX MEASUREMENTS FOR THE FLATHEAD, FRONTIER AND WILLIAMS FORK SAMPLES.....	248
APPENDIX D: SAMPLE COLLECTION LOCATIONS	252
APPENDIX E1: REVIEW OF PREVIOUS WORK ON QUARTZ CEMENTATION	259
APPENDIX E2: DIAGENETIC MODELING: HOW DOES IT WORK?.....	264
APPENDIX E3: VITRINITE REFLECTANCE	269
APPENDIX F: TYPE LOG FOR LAST DANCE WELL.....	273
REFERENCES	282
VITA.....	304

List of Tables

Table 2.1. Comparison of heat flow data from the literature and this study.....	28
Table 2.2. Temperature constraints for the paragenetic sequence used in modeling.	40
Table 2.2. (ctd)	41
Table 2.3. Amount of Tertiary section removed at the study wells and outcrop location.....	53
Table 3.1. Summary of petrographic, petrophysical and log characteristics of the Williams Fork sandstones.	93
Table 3.1. (ctd).....	94
Table 3.1. (ctd).....	95
Table 3.2. Comparison of actual lithofacies and predicted lithofacies in the study well.....	100
Table 3.2. (ctd).....	101
Table 3.2. (ctd).....	102
Table 3.3. Evaluation of the performance of the Williams Fork lithofacies classification tool in the study well (success: when the tool successfully predicted the lithofacies at a given depth; overlap: the tool predicted more than one lithofacies at a given depth).	103
Table 3.4. List of core-measured density and matrix density that is used to improve density porosity calculation.	112
Table 4.1. Summary of subcritical crack index results for the Flathead, Frontier and Williams Fork samples (* Measurements from Rijken, 2005). SCI (n): Subcritical Crack Index; KIC: fracture toughness.	130

Table 4.1. (ctd).....	131
Table 4.1. (ctd).....	132
Table 4.2. Results of fracture path analyses for quartz-cemented Flathead and calcite-cemented Williams Fork sample.....	145
Table 4.2. (ctd).....	146
Table 4.3. Results of subcritical crack index testing (SCI) and calculated fracture toughness (K _{Ic}) for the Mesaverde sandstones. The sample type, formation name, localities and number of measurements per sample are also listed.	158
Table 4.4. Point count data and SCI values for the selected sample pairs.....	165
Table 4.5. Rock mechanical properties of the Williams Fork Lithofacies. SCI (n): subcritical crack index measured in this study.	183
Table 4.6. The effects of calcite cement on core measured grain density, dynamic Young`s modulus and Poisson`s ratio of lithofacies C1, C2 and B. C1: quartz-cemented sandstones with medium thick detrital clay coats (Ohio Creek), C2: quartz-cemented sandstones with thin detrital clay coats (Ohio Creek), B: illite/smectite coated sandstones, and G: tightly calcite-cemented sandstones. The unit of Young` modulus is GPa.....	194
Table 4.7. Porosity and permeability of selected Williams Fork samples in the geologic past.	216
Table 4.7. (ctd) Porosity and permeability of selected Williams Fork samples in the geologic past.	217
Table E2.1. Quartz cement volume, precipitation rate, and available surface area estimation equations used by diagenetic modeling programs.....	268

Table E3.1. Three general types of kerogen, their occurrences and the thermal maturity required to generate hydrocarbons (summarized from Nuccio and Roberts, 2003).....	272
--	-----

List of Figures

Figure 2.1. Piceance Basin location map showing sampling locations (yellow stars).	15
Figure 2.2. Stratigraphic nomenclature used in the Piceance Basin (from Pranter et al., 2007).	16
Figure 2.3. Ternary diagram illustrating the differences in detrital composition of outcrop and subsurface sandstones based on ratios of detrital quartz, feldspar, and lithic fragments (Q:F:L) with respect to stratigraphic intervals.....	19
Figure 2.4. Ternary diagram illustrating the differences in rock fragment constituents of the outcrop and subsurface sandstones with respect to stratigraphic intervals.....	20
Figure 2.5. Distribution of (A) quartz cement and (B) primary pores between outcrop (Rifle Gap) and subsurface (MWX-1, GV2, MF31-19G, Last Dance) samples.....	21
Figure 2.6. Available vitrinite reflectance and bottom-hole temperature data were matched to the predictions of the <i>GenesisTM</i> (ARCO and Lawrence and Livermore models).....	31
Figure 2.6. (ctd).....	32
Figure 2.6. (ctd).....	33
Figure 2.6. (ctd).....	34
Figure 2.6. (ctd).....	35
Figure 2.6. (ctd).....	36
Figure 2.6. (ctd).....	37

Figure 2.6 (ctd).....	38
Figure 2.7. Diagenetic model calibration results for quartz cementation. (A) IGV match option was selected so that the errors in the compaction models would not be carried into the quartz cement calibrations. (B) Quartz cement calibration indicating most of the quartz cement predictions are within a $\pm 2\%$ accuracy limit. (C) IGV match option was toggled off and compaction was simulated. (D) Measured versus predicted quartz cement abundances modeling both compaction and quartz cementation.	42
Figure 2.8. (A) Representative burial history models generated with <i>GenesisTM</i> with overlay of predicted temperature history for MWX well.	43
Figure 2.8. (A) (ctd) MF31-19G / T52-19G wells.....	44
Figure 2.8. (A) (ctd) for Last Dance / O`Connell 31x wells.....	45
Figure 2.8. (A) (ctd) Rifle Gap outcrop.	46
Figure 2.8. (B) Representative thermal and burial depth history curves for top and base of Mesaverde interval.	47
Figure 2.9. Comparison of quartz cementation evolution in geologic past for a sample from the outcrop (WF-6) and subsurface (LD 4016 ft). (A) Quartz cementation and burial depth with time. (B) Quartz cementation and temperature with time.	50
Figure 2.10. (A) Quartz cement calibrations for different burial history inputs at the Rifle Gap locality. Alternative burial and thermal history scenarios used for the calibrations are shown for the Cameo coal zone in Figure 2.10B.	59

Figure 2.10. (B) Alternative burial and thermal history scenarios used for the calibrations are shown for the Cameo coal zone.	60
Figure 3.1. Map showing important gas fields in Piceance Basin. The study well (shown with a star) is located in the Mamm Creek field, Garfield County, Colorado (modified from Johnson and Roberts, 2003).....	68
Figure 3.2. Stratigraphic column showing the distribution of Mesaverde depositional environments in the southern Piceance Basin (modified from Cumella and Scheevel, 2008).....	71
Figure 3.3. Distribution of Williams Fork lithofacies and their core-measured densities at different intervals of the study well	72
Figure 3.4. Ternary diagram illustrating detrital composition of sandstones based on ratios of detrital quartz, feldspar, and lithic fragments (Q:F:L). Sandstone clans are designated according to the classification of Folk (1980).....	76
Figure 3.5. Distribution of rock fragments in the Ohio Creek, Lower Williams Fork and Upper Williams Fork intervals: (A) Crystalline fragments. (B) Sedimentary fragments. (C) Rock fragments according to their rigidity.	76
Figure 3.6. (A) Most of the intergranular volume (IGV) is contributed by authigenic minerals, contribution from primary pores and matrix is minor. Evidence of control on compaction by the content of ductile detrital components: intergranular volume (IGV) is lower where ductile grain content is highest (B) and compaction index (Icomp) is greatest for the ductile grain-rich samples (C). (ARF: Argillaceous Rock Fragments).	78

Figure 3.7. Thin section and SEM images characterizing the Williams Fork lithofacies.....	80
Figure 3.8. Distribution of authigenic minerals at different Williams Fork Intervals (authigenic mineral components are normalized to 100%).	84
Figure 3.9. Abundance of Fe-dolomite cement and Dolostone Rock Fragments (DRFs) correlates positively.	86
Figure 3.10. Distribution of pore types between (A) Ohio Creek, Upper Williams Fork and Lower Williams Fork intervals and (B) Williams Fork lithofacies. Micropores = core-measured porosity – total visible point-count porosity.....	87
Figure 3.11. (A) Comparison of point-count porosity with core-measured porosity. (B) Plot showing the relationship between point-count porosity and permeability. The low permeability values are due to abundance of micropores.....	87
Figure 3.12. Core-measured porosity versus klinkenberg gas permeability crossplot for routine core analysis data measured at 800 psi net effective stress. The samples marked with black circle have microfractures. Clay-coated sandstones have the best reservoir quality.	90
Figure 3.13. Effects of grain size on (A) core porosity and (B) permeability. Outlier samples (marked with circles) have grain-coating clays.	91
Figure 3.14. Photomicrographs illustrating characteristics of various lithofacies. Bright blue indicates epoxy filling pore spaces, calcite is stained pink and Fe-dolomite is stained turquoise blue. The images are taken at the same magnification.	92

Figure 3.15. Plots of bulk density versus (A) gamma ray and (B) deep resistivity. Resistivity responds more to fluids than matrix; therefore, bulk density versus resistivity crossplot could be misleading in identifying the lithofacies. Legend is shown in figure 3.12.	99
Figure 3.16 Distribution bar graph showing the performance of the Williams Fork lithofacies classification tool in the study well (success: when the tool successfully predicted the lithofacies at a given depth; overlap: the tool predicted more than one lithofacies at a given depth.)	104
Figure 3.17. Comparison of density derived from bulk-density logs and core measurements. The sandstones with the lowest bulk-density values are clay-coated intervals with best reservoir qualities.	106
Figure 3.18. Prediction of core porosity and permeability with sonic porosity (A, E), neutron porosity (B, F), density porosity (C, G), and average neutron density porosity (D, H). Avg: average.	109
Figure 3.18. (ctd).....	110
Figure 3.19. Comparison of density porosity calculated by using matrix density of 2.68 g/cc for all interval (A and B) and variable matrix densities close to the core-measured densities (data is available in Table 3.2).	111
Figure 4.1. Three regions of crack propagation (Figure after Atkinson and Meredith, 1981).	119
Figure 4.2. The distribution of subcritical crack index values and calculated fracture toughness for sandstones of different formations. The values plotted are the averages for each sample.	134
Figure 4.2. (ctd).....	135

Figure 4.3. Plot of subcritical crack index versus fracture toughness. The toughness values are the predictions from the spreadsheet that is used to calculate the SCI. (UWF: Upper Williams Fork, LWF: Lower Williams Fork, Last Dance and MF31-19G (subsurface), Rifle (Rifle Gap outcrop)). ...136

Figure 4.4. (A) Load decay curves measured for two samples. (B) Log-log plot of velocity (vertical axes), numerically computed from equation 4.3, against load (horizontal axes)137

Figure 4.5. Plot of subcritical crack index versus petrographic parameters.140

Figure 4.6. CL (Cathodoluminescence) and SEI (Secondary Electron Image) image pairsshowing the fracture propagation paths for the (A) tightly quartz-cemented Flathead sandstone (Canyon Ferry locality, Montana) and (B) tightly calcite-cemented Upper Williams Fork sandstone (Mamm Creek field, Piceance Basin).....144

Figure 4.7. Map of Piceance Basin showing the location of well sites for the subsurface samples and outcrop sample location at Rifle Gap area.152

Figure 4.8. Gamma-ray curves for the study well (Last Dance) and well nearby the Rifle Gap outcrop were correlated in order to match the sandstone intervals. Subcritical crack index values are shown in yellow boxes.153

Figure 4.9. (A) Ternary diagram illustrating the differences in detrital composition of outcrop and subsurface sandstones based on ratios of detrital quartz, feldspar, and lithic fragments (Q:F:L). Sandstone clans are designated according to the classification of Folk (1980).154

Figure 4.9. (B) Ternary diagram that illustrates the distribution of lithic grains (VRF: Volcanic Rock Fragments; MRF: Metamorphic Rock Fragments; SRF: Sedimentary Rock Fragments).....155

Figure 4.10. (A) Bar graph showing the distribution of measured-SCI values for the Mesaverde Group sandstones.	159
Figure 4.10. (B) Bar graph showing the distribution of calculated-fracture toughness values for the Mesaverde Group sandstones.....	160
Figure 4.11. Cross plots of subcritical crack index versus petrographical parameters obtained from point count data. The terms COPL: Compactional porosity loss, CEPL: cementational porosity loss, and I_{Comp} : compaction index were described in section 3.6.1 of the previous chapter.	161
Figure 4.12. Thin section photomicrographs showing the contrasting porosity and quartz cement distribution of outcrop (left image) and subsurface (right image) pairs. Bright blue color represents pore spaces filled with blue-dyed epoxy.	164
Figure 4.13. Subcritical crack index value versus petrographical parameters for the outcrop and subsurface samples.....	166
Figure 4.14. 1D Basin Modeling results (Genesis TM) indicate contrasting burial and thermal histories for the outcrop (top) and subsurface (bottom) location.	169
Figure 4.15. Distributions of quartz cement and total porosity at the subsurface (graph on the left) and outcrop (graph on the right).	
Figure 4.16. Graph showing variation in reservoir pressure with depth. Mud weight data is from the study well and log data is from a nearby well (1 mile distant).....	181

Figure 4.17. (A) Fracture density variation with depth for the study well (Cumella and Scheevel, 2008). (B) Subcritical crack index values are higher in the sandstones above top gas. (C) Photomicrographs that represent the petrographic characteristics of the lithofacies and associated subcritical crack index values.....	184
Figure 4.18. Distribution of (A) shear-wave velocity anisotropy, and (B) apparent fracture density from image logs	187
Figure 4.19. Figure showing a metal bar in tension, illustrating the basis of Young`s modulus (from Encyclopedia Britannica Inc., 1996).	188
Figure 4.20. Depth distributions of (A) Young`s modulus (GPa) and (B) Poisson`s ratio calculated from acoustic logs.	193
Figure 4.21. Young`s modulus and Poisson`s ratio plotted against core-measured porosity, log derived bulk density and core-measured grain densities..	196
Figure 4.22. SCI versus (A) Young`s modulus (GPa) and (B) Poisson`s ratio.....	197
Figure 4.23. Young`s modulus versus Poisson`s ratio (A) calculated from logs for the study well and (B) measured on core samples from the MWX well (Cumella and Scheevel, 2008).	201
Figure 4.24. Thermal and pressure history curves for the top of Williams Fork and bottom of Iles Formation at MWX well.	207
Figure 4.25. IGV, quartz cement, porosity and permeability calibrations for the diagenetic modeling of the Williams Fork Sandstones.....	212

Figure 4.26. Evolution of variables that control the reservoir quality over geologic time in selected samples from the Williams Fork: (A) quartz cementation, (B) intergranular pores, (C) core porosity, and (D) permeability.215

CHAPTER 1: INTRODUCTION

Historically, diagenetic and reservoir quality studies of tight gas sandstone have largely ignored fractures (i.e., Dutton, 1991), whereas, conventional fracture research typically takes no notice of diagenesis (e.g., Pollard and Aydin, 1988). Beginning in the late 1980's, however, (e.g., Laubach, 1988; Laubach et al., 1995; Milliken, 1994). it has been appreciated increasingly that diagenesis encompasses both mechanical and chemical processes that interact with primary depositional variations in environment and texture to exert a strong control on pore networks, rock mechanical properties, and natural fractures. Examination of authigenic minerals in fractures shows that fracturing and chemical diagenesis occur concurrently, and that fracture growth and mineral precipitation interact (Laubach, 1988; Laubach et al., 2004b). Studies of these interactions show that diagenesis modifies mechanical stratigraphy (Marin et al., 1993; Laubach et al., 2009), fracture mechanics attributes (Rijken et al., 2002), fracture porosity and fracture porosity history (Laubach and Diaz-Tushman, 2009), the location and heterogeneity of patterns of open and sealed fractures (Laubach, 2003; Laubach and Ward, 2005), fracture system connectivity and permeability (Philip et al., 2005; Olson et al., 2009), fracture stiffness and propensity of fractures to close (Laubach et al., 2004a), and fracture seismic response (Marrett et al., 2007; Sayers et al., 2009). Diagenetic modeling provides quantitative insight into how host rock and fracture porosity evolve (Lander et al., 2008; R. Lander modeling in Laubach et al., 2006) and analysis of fluid inclusions in fracture cement deposits provides evidence of fracture timing (Becker et al., 2009b). It has also been

suggested that quartz cementation concurrent with fracturing may influence fracture size distribution (Hooker et al., 2009).

Because this area of diagenetic/fracturing research concerns the nature of rock properties in the subsurface, most particularly pore system evolution, there are significant practical applications for this work. Growing energy needs and increased interest in cleaner energy resources put tight gas sandstone resources in the spotlight (Tinker and Kim, 2002; Shanley et al., 2008). Tight gas sandstone reservoirs have low porosity and the rock mass generally has permeability of less than 1 mD (Meckel and Thomasson, 2008). Consequently production success depends on hydraulically introduced fractures to connect the low permeability reservoir and wellbore (Holditch et al., 1993). Since the late 1980's, there has been increasing appreciation that natural fractures can augment producibility; such fractures are responsible for production responses that indicate permeability higher than would be expected from the rock mass properties alone (Lorenz et al., 1989; Laubach, 1989; Laubach, 1991; Cumella and Scheevel, 2008). Systematic study of a wide range of tight gas sandstones in the 1980's and 1990's showed that the reason for low porosity and low rock mass permeability in tight gas sandstones is chemical alteration of the sandstone by cement precipitation; the primary cause of reduced porosity (and reservoir quality) being diagenetic alteration by quartz precipitation (Dutton et al., 1993; Pitman et al, 1986).

Understanding the controls and distribution of reservoir quality is an essential part of a comprehensive geologic and engineering analysis that can contribute to the economic success of tight-gas reservoir development (Dutton and Laubach, 1993). Previous observational studies suggested that the high cement contents responsible for low

porosity in tight gas sandstones are correlated with deep or prolonged burial; recent advances in understanding diagenetic processes show that high quartz cement content is the result of the thermal exposure sandstones have experienced, coupled with the grain size and grain surface attributes of the sands (Lander and Walderhaug, 1999; Lander et al., 2008).

Previous work in the area of fracture diagenesis shows that diagenetic and structural aspects of fractured rocks sandstones must be addressed concurrently in order to fully understand low-permeability sandstones and to better predict their reservoir quality attributes that arise from a combination of pore-scale and fracture distribution characteristics.

Cross- training is rare in the two traditionally separate disciplines of sandstone petrology and structural geology. My dissertation explicitly seeks to help build a bridge, across this divide by bringing the perspective and training from traditional sandstone petrology to bear on the issue of mechanical property evolution. My study is in some respects complementary to that of Rijken (2005), who in part addressed some of these issues but from the perspective and training of fracture mechanics. My research focuses on linking pore-scale observations to the reservoir scale to gain a more predictive understanding of reservoir attributes. This work sheds light on aspects of rock evolution that are germane to deciphering concurrent structural and diagenetic evolution, such as loading and thermal history, rock mechanical property evolution, and fracture timing. I address these issues using observations from the Late Cretaceous Williams Fork sandstones from the Piceance Basin, Colorado, a representative tight gas sandstone of the Rocky Mountain region (Dutton et al., 1993; Cumella and Scheevel, 2008).

In Chapter 2, I concentrate on the use of diagenetic modeling for basin history assessment. Diagenetic modeling programs are widely used as an exploration tool for reservoir quality predictions for potential targets for oil and gas (Lander and Walderhaug, 1999; Lander et al., 2008). These models can be applied in reverse, however. Sandstone diagenetic properties, intergranular volume (IGV) and quartz cement abundance, can provide valuable constraints on thermal and burial histories when combined with other thermal indicators. Although paleothermometers such as vitrinite reflectance are sensitive to maximum paleotemperatures, they are relatively insensitive to the timing of erosion and cannot be used to determine the relative magnitude of erosional events that took place. On the other hand, when used in conjunction with paleotemperature data, quartz cementation, which *is* sensitive to temperatures reached and time spent in those temperature ranges, can be used to constrain uplifts. This information is essential for understanding the loads that may have contributed to fracture growth. In conjunction with observations of cement deposits in fractures, such information can constrain fracture timing (Becker et al., 2009b), traditionally one of the most difficult aspects of fracturing to pin down (Engelder, 1985; Hancock, 1985).

Although studies based on paleothermometry and stratigraphy indicate a large-scale post-Laramide erosional event from 10 Ma to present day in the Piceance basin, there is debate about the magnitude of this uplift at different localities. Previously, stratigraphic, vitrinite reflectance extrapolation, and basin modeling approaches were used to determine the amount of uplift. In Chapter 2, I evaluate the utility of the compaction and quartz cementation algorithms of the *Touchstone*TM diagenetic model for

basin history assessment of the Late Cretaceous Williams Fork sandstones from the Piceance Basin, Colorado where rocks went through varying uplift histories.

To test this approach, first I calibrated the temperature and effective stress histories by using 1D basin modeling software (*GenesisTM*) for the study wells for which thermal constrains were available in the form of vitrinite reflectance for paleotemperatures and bottom hole temperatures for present-day temperatures. I produced a number of basin models that fit the present day thermal and pressure data reasonably well and used these basin models and petrography data as inputs for diagenetic models. I simulated the quartz cement abundance by using identical parameter values for compaction and quartz cementation algorithms for all study locations. I tested the performance of the basin models on how well they can predict the amount of quartz cement in the sandstones and selected the best-performing burial curves as representative burial reconstructions for the study areas. I determined the maximum burial depth and amount of erosion from these representative curves.

After the introduction of diagenetic models, which are widely used pre-drill exploration tools for reservoir quality predictions, I present another reservoir quality prediction tool in Chapter 3. This time, however, it is not a pre-drill but post-drill approach. I introduce the use of well log characteristics of the diagenetic lithofacies for reservoir quality prediction by using Late Cretaceous Williams Fork sandstones of the Piceance basin as a case study (Ozkan et al., accepted manuscript in revision).

Core samples and cuttings are used to determine subsurface lithology. However, in most cases, high cost allows coring within only a limited part of the total drilled interval. It is very likely that a cored interval does not represent all of the lithologies in a

well. Well logs, on the other hand, provide a continuous survey of the well interval. By studying rock types in an extensively cored well and translating these facies to log responses, it is possible to generate a model that can be used to predict the likely lithofacies in nearby wells in a given field. Such an approach is applied to a study well within the Mamm Creek field of the Piceance basin. This well provides an excellent opportunity, because all sandstone intervals are cored and thin sectioned (400.5 ft core with 275 thin sections) with laboratory measurements of petrophysical properties.

The lithofacies are identified from core observations and petrographic observations and correlated with log responses to create a model that can be used to predict reservoir quality directly from well logs. The core analysis data are used to determine reservoir qualities of the lithofacies and an algorithm is designed for field-scale application of lithofacies and reservoir quality prediction models. In addition to field scale applications, prediction of diagenesis can be extremely helpful in preventing production problems caused by damaging interactions between incompatible drilling and/or completion/stimulation fluids and authigenic clay minerals or Fe-rich minerals. In this chapter the possibility of predicting core-derived porosity and permeability from log-derived porosity is also evaluated. A correct approximation of porosity and permeability of the reservoir rock can be an invaluable tool while calculating gas-in-place.

Chapter 4 focuses on the fracture aspects of the reservoir quality issue. I present data that serves to link diagenesis and rock mechanical characteristics. Fracture network prediction is especially important in tight gas sandstones like the Williams Fork Formation where matrix permeabilities are very low and fractures are important contributors of gas production. Because it is difficult to sample vertical fractures with

vertical wells, many of the fracture characteristics remain poorly understood in the deep subsurface (Laubach, 1997). Although outcrops are much easier to access for sampling and observations, the use of outcrop samples and observations as analogs to subsurface rock characterization (petrography and fracture) must be assessed. Combining observations and inferences from Chapters 2 and 4 leads to a quantitative approach that can be used to make such an assessment.

Geostatistical and geomechanical models are used to evaluate and forecast characteristics (aperture size, length, aperture and length distributions, connectivity, clustering) which influence fluid flow in the reservoirs. While geostatistical approaches mostly use the fracture attributes collected from rock samples, geomechanical models use measurable rock parameters such as subcritical crack index, Young's modulus, mechanical layer thickness and tectonic strain as inputs. Subcritical crack index is a mechanical rock property that influences fracture characteristics which in turn, for a given mechanical layer thickness, controls aperture distributions and clustering (Olson et al., 2001) In Chapter 4, I evaluate the effects of diagenesis on rock mechanical properties and fracture density distribution. The diagenetic controls on the fracturing are examined within the context of subcritical crack index (SCI), Young's modulus, and Poisson's ratio.

First, I present fracture path analyses to quantify a fracture's behavior with regard to microscale sandstone components (grains, cements, pores). My aim is to understand how the microscale textural differences in the growth mechanisms of pore-filling cements affect the crack path and the subcritical crack index. For this purpose, tightly quartz-cemented and tightly calcite-cemented sandstones were subjected to subcritical crack

testing and the cracks introduced by the test were imaged with secondary electrons and cathodoluminescence. The fracture path was traced and lengths of the intergranular (grain-grain, grain-cement, cement-cement) and intragranular (intragrain and intracement) paths along the fractures were measured.

The influences of rock type, cement type and volume, porosity, tortuosity of the fracture path, and grain size on subcritical crack index are examined in section 4.3. Previous studies point out the difficulty of isolating the effect of an individual rock property (porosity, grain size, cement type etc.) on subcritical crack behavior due to variation in the framework grains and diagenesis in sandstones (Olson et al., 2001; Rijken et al., 2002; and Rijken, 2005). In order to overcome this heterogeneity problem, I isolate the effects of cementation and porosity by comparing the subsurface and outcrop samples of the same formation with similar framework mineralogies. Williams Fork samples from the subsurface and outcrop are advantageous for this study because the degree of lithification is different for the subsurface and outcrop samples owing to contrasting burial and thermal histories documented in Chapter 2. Subsurface samples were subjected to deeper burial and higher temperatures which led to precipitation of considerably more quartz cement compared to the outcrop sandstones. Therefore, deeply buried subsurface samples represent well-consolidated end-members, and their outcrop equivalents can be used as contrasting, poorly to moderately consolidated end-members for subcritical crack index measurements. Subcritical crack index measurements done on the subsurface samples yield a value for the present day characteristics of the rock, however, these values might have been different at the time of fracturing depending on the diagenetic stage (degree of cementation) of the sandstone. The approach taken here not only helps

us quantify the effects of diagenesis on the mechanical properties of the sandstones, but it also helps us to determine a range subcritical crack index values for sandstones of given framework composition.

In the last section of Chapter 4, an example of a diagenetic modeling approach to determine the rock characteristics at the time of fracturing is given in a case study applied to subsurface Williams Fork sandstones from the Mamm Creek field, Piceance Basin. The degree of lithification, which changes during burial through compaction and cementation, affects the rock's response to loading. The diagenetic models (built in Chapter 2) are revisited for the purpose of modeling the diagenetic evolution in the geologic past and determining the quartz cement abundance, porosity and permeability at the time frame of fracturing. In this section, I also examine the rock mechanical characteristics of the lithofacies described in Chapter 3 with the help of measured subcritical crack index values and properties obtained from sonic logs (Young's modulus and Poisson's ratio) and evaluate the lithological controls on fracture distribution in the study well. Results are compared to evidence of fracture timing from fluid inclusions in fracture cements.

In this dissertation each chapter includes introductory material to help readers better understand the topics discussed. The results are followed with discussions and concluding remarks that place the contribution into the broader context of current understanding of the subjects. Data used for this dissertation are available in the appendix section. Appendix A has the input for diagenetic modeling (well information, and textural and modal analyses data). Appendix B has the input and output data for basin modeling (measured and inferred values): (B1) stratigraphy input, (B2) vitrinite reflectance,

temperature and pressure input, and (B3) time versus temperature, depth, excess pressure, and effective pressure. Appendix C has the results of subcritical crack index measurements. Appendix D has the sample collection locations. Appendix E has a summary of previous work on quartz cementation (E1), diagenetic modeling (E2), and vitrinite reflectance (E3). Appendix F has the type well-log for the Last Dance well.

CHAPTER 2: BASIN HISTORY ASSESSMENT WITH DIAGENETIC MODELING

Sandstone diagenesis models such as *Exemplar*TM (Lander and Walderhaug, 1999) or *Touchstone*TM (Lander et al., 2008) are typically used as an exploration tool for predicting the reservoir quality (porosity and permeability) of the potential targets (Bonnell et al., 1998; Lander and Walderhaug, 1999; de Souza and McBride, 2000; Walderhaug, 2000; Bloch et al., 2002; Taylor et al., 2004). Such models are also applied in constraining thermal histories (Awwiller and Summa, 1997, 1998; Lander et al., 1997) and evaluating the potential influence of quartz cementation on grain fracturing (Makowitz et al., 2006). They can also, potentially, be used to help predict how the porosity and permeability of fracture systems may have been modified by cement precipitation (Lander et al., in preparation; Olson et al., 2009).

In this chapter, I evaluated the utility of the compaction and quartz cementation algorithms of the *Touchstone*TM diagenetic model for basin history assessment of the Late Cretaceous Williams Fork sandstones from the Piceance Basin, Colorado where rocks of similar age and depositional history have experienced contrasting uplift histories. Although studies based on paleothermometry and stratigraphy indicate a large-scale post-Laramide erosional event from 10 Ma to present day in the Piceance basin, there is debate about the magnitude of this uplift at different localities. Determining erosion is important for documenting the maximum depth of burial for the Williams Fork sandstones. Loading history controls the thermal exposure and pressure history which in turn influence the timing and amount of gas generation, overpressuring and resulting fracturing, and the

evolution of quartz cementation which controls the rock mechanical properties and therefore fracture distribution.

Sandstone diagenetic properties, intergranular volume (IGV) and quartz cement abundance, can provide valuable constraints on thermal and burial histories when combined with other thermal indicators. Although, organic paleothermometers such as vitrinite reflectance are sensitive to maximum paleotemperature, they are comparatively insensitive to the timing of erosion and cannot be used to determine the relative magnitude of past erosional events that took place. On the other hand, when used in conjunction with paleotemperature data, quartz cementation (which is sensitive to temperatures reached and time spent in those temperature ranges) can be used to constrain the erosional events and amount of uplift.

To test the use of diagenetic modeling to assess Piceance Basin's burial history, first I calibrated the temperature and effective stress histories by using 1D basin modeling software (GenesisTM) for the study wells for which thermal constrains were available in the form of vitrinite reflectance for paleotemperatures and bottom hole temperatures for present-day temperatures. I produced a number of basin models that fit the present day thermal and pressure data reasonably well and used these basin models and petrography data as inputs for diagenetic models. I simulated the quartz cement abundance by using identical parameter values for compaction and quartz cementation algorithms for all study locations. I tested the performance of the basin models on how well they can predict the amount of quartz cement in the sandstones and selected the best-performing burial curves as representative burial reconstructions for the study areas. I determined the maximum burial depth and amount of erosion from these representative curves.

Previously, stratigraphic, vitrinite reflectance extrapolation, and basin modeling approaches were used to determine the amount of erosion at various Piceance basin locations but estimations are highly variable. The estimated amount of eroded section in the literature varies from 3800 ft to 6100 ft for the MWX well, from 3700 ft to 9167 ft for the MF31-19G well and 4400 ft near the Last Dance well location in the literature (Bostick and Freeman, 1984 (Ro); Nuccio and Roberts, 1992 (Vitrinite reflectance (Ro)-depth extrapolation to Ro of 0.2% -0.3%); Wilson et al., 1998 (Apatite Fission Track, Ro, and fluid inclusions); Nuccio and Roberts, 2003 (Basin modeling); and Zhang et al., 2008 (Basin modeling by using Ro data from pyrolysis experiments). Using quartz cement as paleothermometer was helpful in pinning down the amount of erosion. My estimations of the maximum burial depth and removed overburden are respectively: 13,575 ft and 5,147 ft for the MWX, 13,067 ft and 5,068 ft for the Last Dance and 15,163 ft and 3,157 ft for the MF31-19G.

2.1. STRUCTURAL SETTING AND STRATIGRAPHY OF THE WILLIAMS FORK FORMATION, PICEANCE BASIN

During the Late Cretaceous, highlands of moderate relief formed by fold and thrust-style deformation in southeastern California, southern Nevada, and western Utah (the Sevier orogeny). These highlands shed sediment eastward into the Sevier foreland basin which was occupied by the Western Interior Seaway from the Gulf of Mexico to the Arctic (Spieker, 1946; Armstrong, 1968; Fouch et al., 1983; Lawton, 1986; Heller et al., 1986; Decelles, 1996). During the Laramide orogeny basement uplifts partitioned the Sevier foreland basin and created internally drained basins dominated by low-energy fluvial and lacustrine deposition (Chapin and Cather, 1981; Lawton, 1983; Dickinson et

al., 1986). Timing of the Laramide orogeny in the Rocky Mountain region generally spanned latest Cretaceous and Paleogene time, roughly 75–50 Ma (Lawton, 2008).

The Piceance Basin was located along the western margin of the Western Interior Seaway. Sediment that formed the Mesaverde Group was transported by fluvial systems from Utah, Arizona and Wyoming and accumulated as fluvial, near shore, and shallow marine deposits during the Late Cretaceous (~75–65 Ma) (Johnson, 1989; Johnson and Flores, 2003; Cole and Cumella, 2003). The middle to upper Campanian Williams Fork Formation of the Mesaverde Group conformably overlies the Iles Formation and is overlain disconformably by the Paleocene Wasatch Formation (Hettinger and Kirschbaum, 2003) (Figures 2.1 and 2.2). The basin is bounded by the Axial Basin arch to the north, White River uplift to the east, Sawatch uplift to the southeast, Uncompahgre uplift to the southwest, and Douglas Creek arch to the west (Figure 2.1). The Piceance Basin has gently dipping flanks on the west and southwest and a steep flank on the east; the structural axis trends northwest near the eastern margin of the basin (Johnson and Nuccio, 1986).

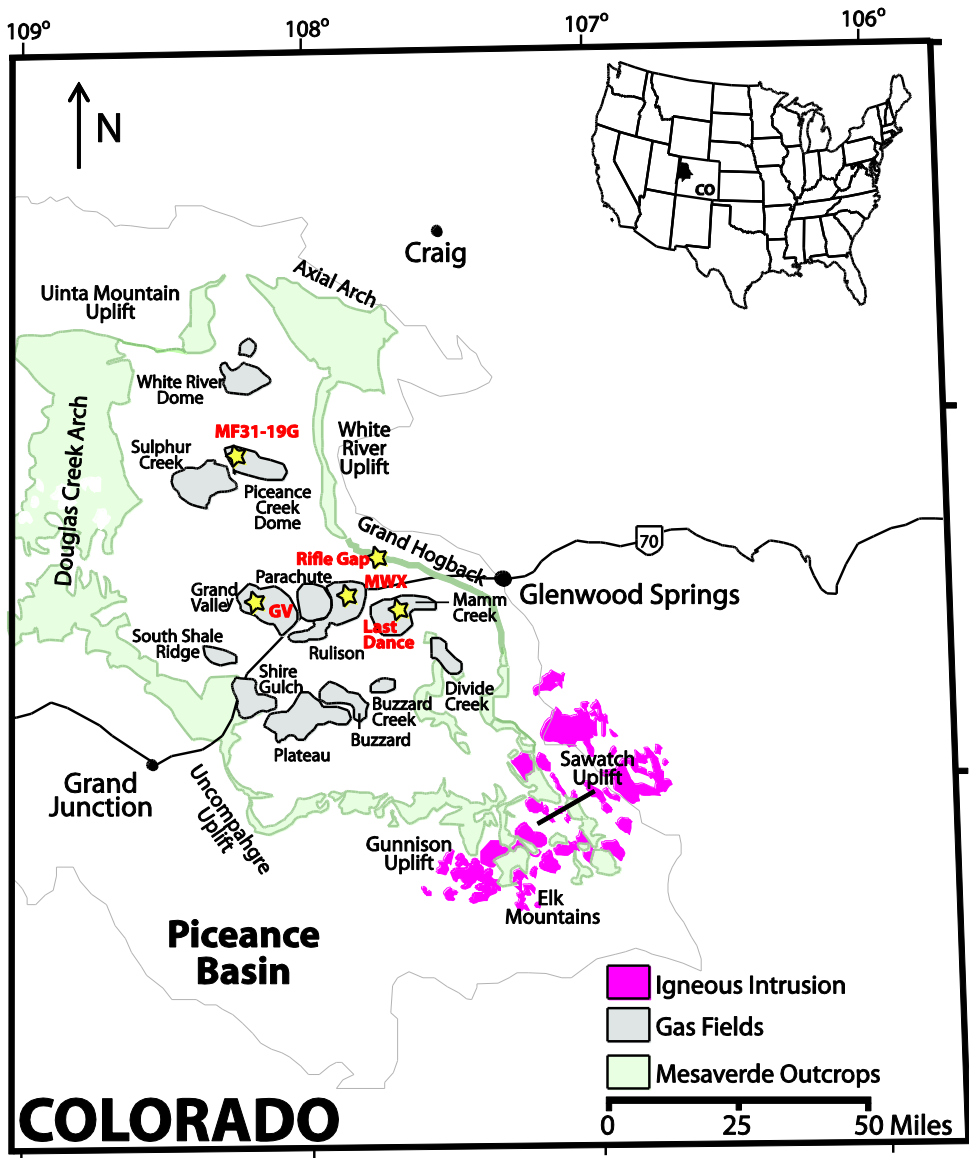


Figure 2.1. Piceance Basin location map showing sampling locations (yellow stars).

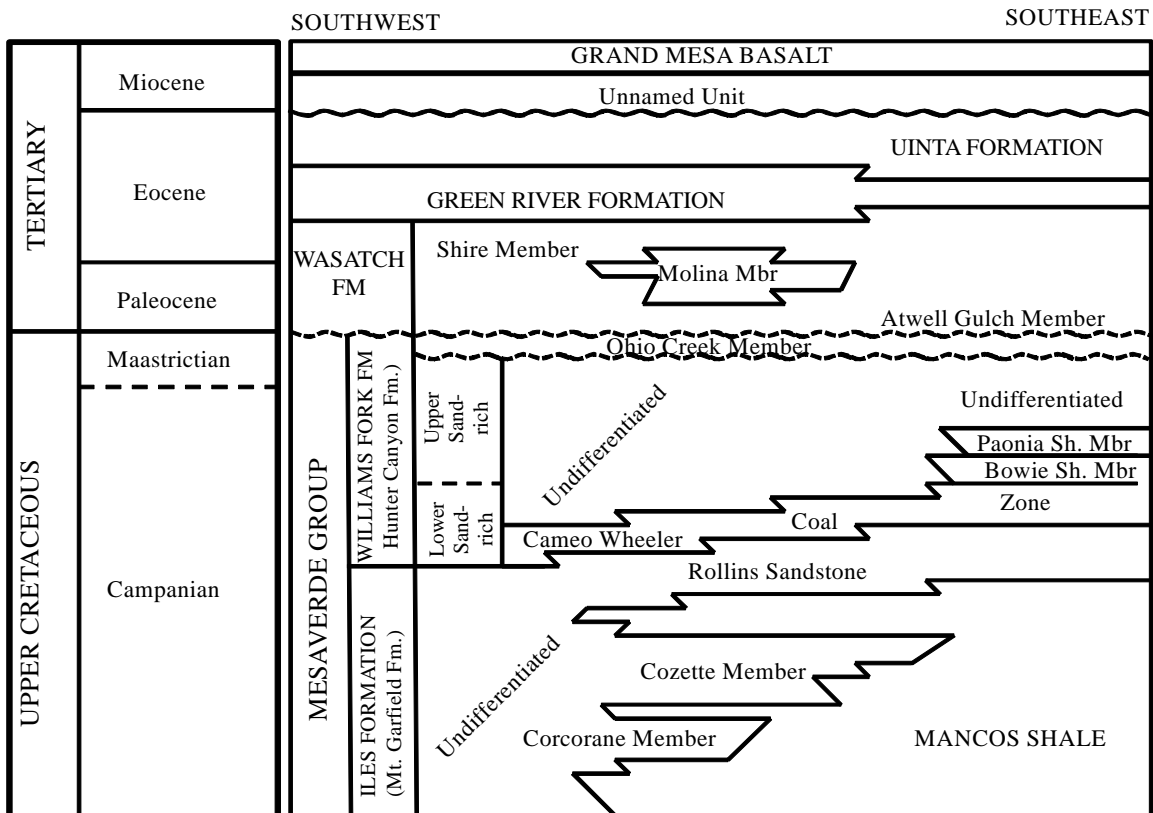


Figure 2.2. Stratigraphic nomenclature used in the Piceance Basin (from Pranter et al., 2007).

When constructing the burial histories for the Mesaverde Group, geologic events outlined for the Piceance region in Johnson and Nuccio (1992) and Zhang et al. (2008) were used:

75 Ma to 65 Ma: Deposition of the Mesaverde Group.

65 Ma: Nondeposition and subsidence. A basinwide unconformity is present at the top of the Williams Fork (Johnson and May, 1978, 1980). The thickness of Cretaceous rocks removed by erosion is unknown. The burial histories available in the literature describe this period as non-deposition instead of erosion which is insignificant for the thermal history of the basin because the source rocks were not buried deep enough to thermally

produce gas at the time (Johnson and Nuccio, 1986; Law et al., 1989). The temperature range would have been less than that is required for copious quartz precipitation as well (~90 °C (194 °F); McBride, 1989; Bjørklykke and Egeberg, 1993), therefore, I followed the same assumption.

~65-61 Ma to 36 Ma: Tertiary sedimentation. Base of the Williams Fork reached its maximum burial during the Laramide orogeny.

36 to 10 Ma: No evidence of deposition.

34 to 29 Ma: Shallow intrusions of intermediate composition were emplaced in the southeastern part of Piceance.

9.7 ± 0.5 Ma: Basaltic extrusions covered much of the central part (dated by Marvin et al., 1966).

10 Ma - Present: From around 10 Ma to the present, the entire region was uplifted and eroded, in part as a result of the development of the Cordilleran extensional province (Zoback et al., 1981; Zoback and Zoback, 1991). The central Piceance Basin underwent a rapid and substantial uplift causing rapid erosion although in the western Piceance Basin erosion is thought to have occurred relatively slowly (Johnson and Nuccio, 1986).

2.2. PETROGRAPHY OF THE WILLIAMS FORK FORMATION

The Williams Fork is composed of very fine- to medium-grained, lithic-rich sandstones, siltstones and mudrocks deposited in fluvial to coastal-plain settings. The composition varies mainly from lithic arkose to litharenite in the subsurface samples and litharenite to feldspathic litharenite in the outcrop samples according to Folk's classification scheme (1980) (Figure 2.3). As illustrated in Figure 2.4, the distribution of

major lithic components is also highly variable. Contrasts in the rigidity/ductility of the lithic components make a big difference in the compaction process (Pittman and Larese, 1991). Therefore, grain deformation characteristics of the lithic grains were carefully assigned while designating the compaction parameters for the diagenetic models.

Although it is more pronounced in the subsurface, in both core and outcrop samples the observed range in reservoir quality reflects the variable diagenetic histories across primary variations in provenance (grain composition), depositional systems, and textures. Comparison of subsurface samples with their outcrop equivalents reveals major differences in the type and amount of cement. In the subsurface Williams Fork is tightly cemented and well-consolidated, whereas, at the outcrop it is characterized by much less cement and poor consolidation. The main difference between the two is the abundance of quartz cement. Quartz cement is more abundant in the deeply buried samples, a result that can be explained as a consequence of protracted exposure to higher temperatures (Lander and Walderhaug, 1999) (Figures 2.5A and 2.5B).

In the subsurface most of the intergranular pore space is lost to cementation by varying amounts of quartz, calcite, Fe-dolomite, mixed-layer illite/smectite, and chlorite, and sparse siderite, pyrite, ferroan calcite, kaolinite, sphene, zeolite, and gypsum. In the outcrop samples, on the other hand, quartz cement is noticeably less, and kaolinite, zeolite and siderite are more commonly observed. Upper Williams Fork is characterized by developments of chlorite and illite/smectite grain-coats in the subsurface samples. At the outcrop level, detrital clay coats with minor recrystallization to authigenic illite are observed.

While porosity consists of micropores with only minor amounts of primary intergranular and secondary intragranular pores in the subsurface samples, sandstones at the outcrop have more common primary pores and minor secondary pores (Figure 2.5B). A thorough description of the diagenesis of subsurface Williams Fork samples can be found in Chapter 3. The petrographic data that was used for diagenetic modeling are included in Appendix A.

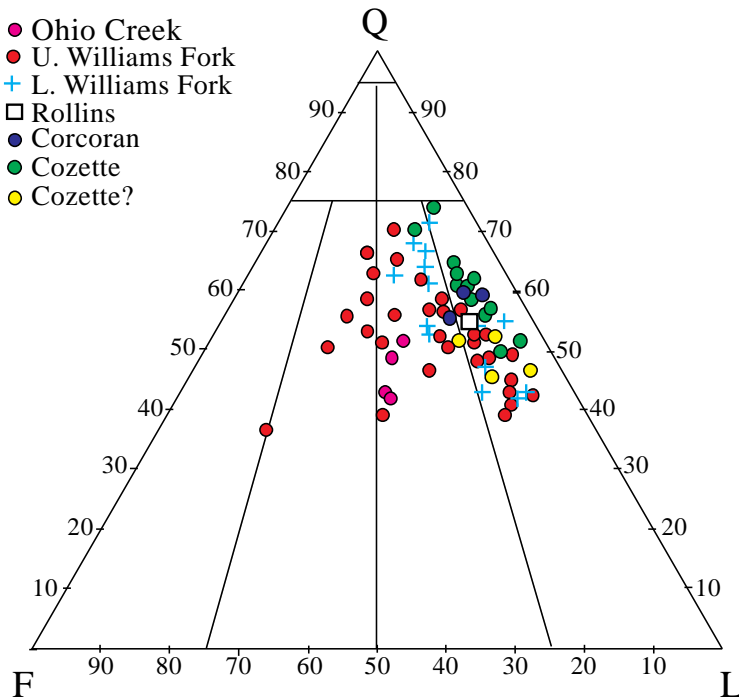


Figure 2.3. Ternary diagram illustrating the differences in detrital composition of outcrop and subsurface sandstones based on ratios of detrital quartz, feldspar, and lithic fragments (Q:F:L) with respect to stratigraphic intervals. Sandstone clans are designated according to the classification of Folk (1980).

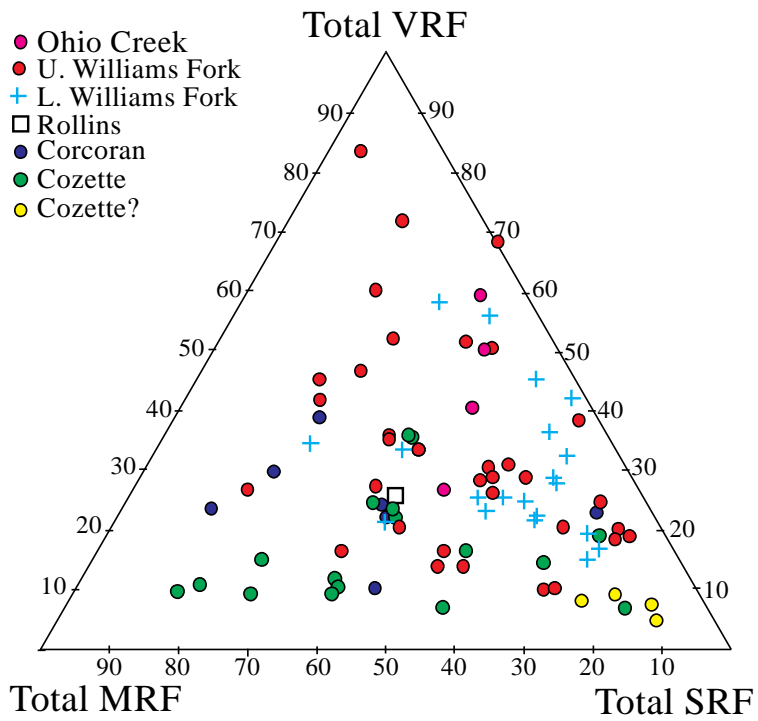


Figure 2.4. Ternary diagram illustrating the differences in rock fragment constituents of the outcrop and subsurface sandstones with respect to stratigraphic intervals. VRF: Volcanic Rock Fragment; MRF: Metamorphic Rock Fragment; SRF: Sedimentary Rock Fragment.

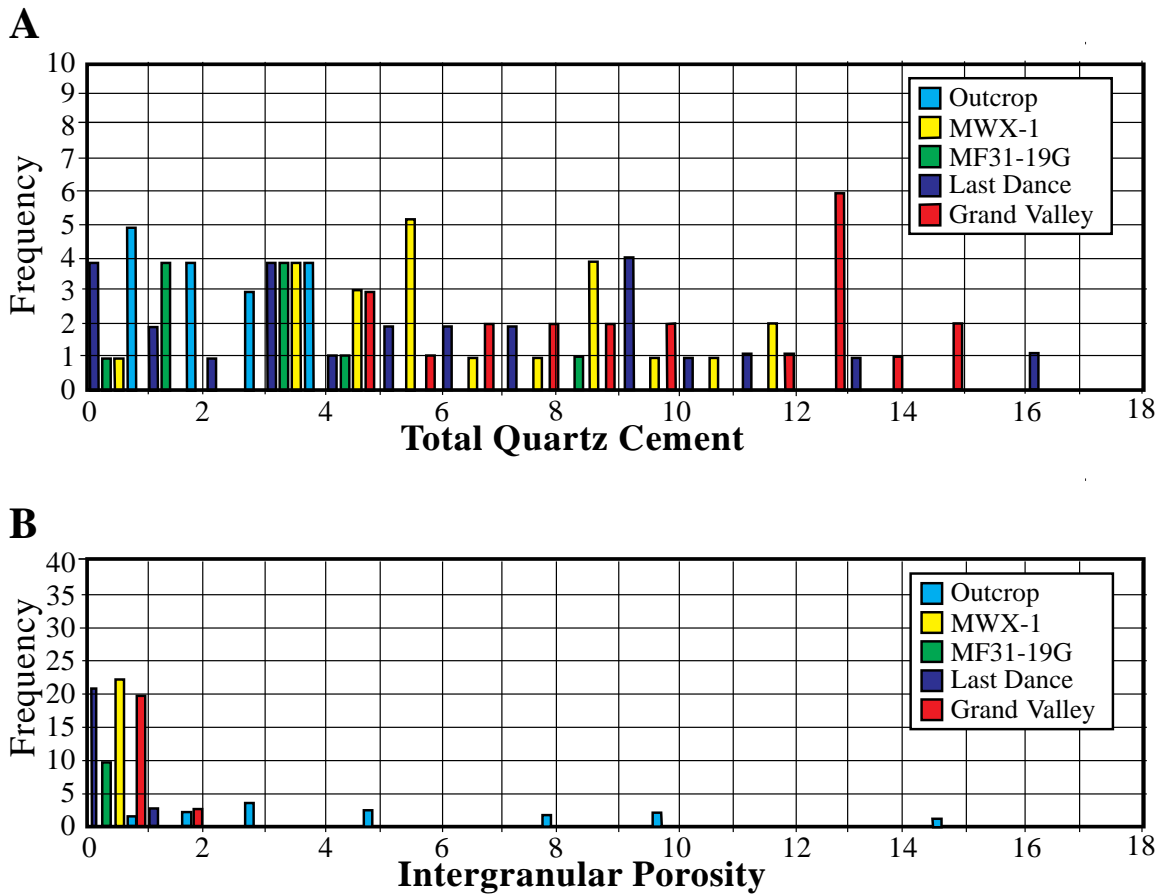


Figure 2.5. Distribution of (A) quartz cement and (B) primary pores between outcrop (Rifle Gap) and subsurface (MWX-1, GV2, MF31-19G, Last Dance) samples. Subsurface samples are dominantly characterized with very low primary porosities and varying amounts quartz cement, whereas, outcrop samples have more primary pore space and relatively low quartz cement.

2.3. MODELING APPROACH

2.3.1. Basin Modeling Approach

The Piceance Basin is the most important gas producing basin in the Rocky Mountains, where most of the gas is sourced from the coastal plain to paludal Cameo coal zone in the Lower Williams Fork interval. Gas was being produced as the coals reached their maximum temperatures in the areas of deepest burial. A thermogenic origin is indicated by gas geochemistry based on carbon isotope compositions (Johnson and Rice, 1990). The presence of energy resources including coal, tight gas sandstones, coalbed gas in the Piceance Basin area have drawn attention to the basin's burial and thermal history (Bostick and Freeman, 1984; Law and others, 1989; Johnson and Nuccio, 1992; Nuccio and Roberts, 2003; Yurewicz et al., 2008; Zhang et al., 2008).

In order to reconstruct the burial, thermal and effective stress histories of the Mesaverde sandstones to use as input for diagenetic models, basin models are built for the study wells and outcrop locations using a one-dimensional (1-D) basin-modeling program (*GenesisTM* developed by *Zetaware*). Basin modeling input data were obtained from log-headers (bottom-hole temperature, circulation time, fluid pressure, mud weights, elevation of Kelly bushing), well-logs (stratigraphy and gross lithology, temperature logs, and pressure logs), and the literature (stratigraphy, vitrinite reflectance, thermal conductivity, heat flow, total organic carbon content of the coals). Where input data were not available, values were estimated by interpolating data from nearby wells. Although there is wealth of paleothermal indicator data for the well locations, only a few vitrinite reflectance values have been measured near the outcrop locality. The steps

followed while setting up basin models are summarized in the following sections and the data used for basin models are listed in Appendix B.

2.3.1.1. Burial History Input

Burial histories are reconstructed for three wells (MWX-1, MF31-19G, Last Dance) and one outcrop location (Rifle Gap) using stratigraphic data (thickness and age of the formations, timing and magnitude of erosional events, and timing of hiatus) provided in a USGS report by Nuccio and Roberts (2003). Gross lithology was determined from the well-logs where available. Stratigraphic data used in burial history reconstruction are shown in Appendix B.

The original thickness of the Tertiary overburden is unknown owing to erosion. Data collected from the literature was used as an initial value for the removed sediments and the estimated thickness of the Tertiary strata was adjusted to get a better fit to the thermal indicator (vitrinite reflectance and down-hole temperature) and pressure (bottom-hole data) profiles. Amounts of erosion were estimated by subtracting the present day depth of the units from their depth at maximum burial.

2.3.1.2. Thermal History Input

The thermal history was calibrated with bottom-hole temperatures and the measured vitrinite reflectance values (R_o) for each well. In most cases, the true temperature is higher than the measured bottom-hole temperature because of the cooling effects of drilling fluid circulation. This discrepancy introduces uncertainty to basin models. For example, bottom-hole temperature derived from the uncorrected geophysical log-header was 200 °F while two temperature logs run 6 months after the drilling gave

temperatures of 244 °F and 266 °F, indicating a large discrepancy between true-formation temperatures and logging temperatures (Johnson and Nuccio, 1986; Spencer 1987). Temperature correction factors were calculated for the MWX well and the same correction factors were applied to the bottom-hole temperatures from the T52-19G well in the Northern Piceance (Johnson and Nuccio, 1986). The temperature-log data for the Last Dance well was obtained 26 days after drilling (oral communication with S. Cumella) which is likely to be representative of the true-formation temperatures.

A wealth of vitrinite reflectance data is available for the Piceance and Uinta Basins in the form of individual data points of vitrinite reflectance, basinwide vitrinite reflectance maps, and cross sections of thermal maturity / vitrinite reflectance with depth (Nuccio and Johnson, 1983; Bostick and Freeman, 1984; Nuccio and Johnson, 1984; Nuccio and Johnson, 1986; Law and others, 1989; Chancellor and Johnson, 1988; Nuccio and Roberts, 2003; Yurewicz et al., 2008, Zhang et al., 2008). Vitrinite reflectance measurements indicate maximum temperatures of 150 - 200°C for the Williams Fork at the MWX well site (Lorenz and Finley, 1991). Published temperature data on fluid inclusions from fracture-filling cements from the MWX site collected on separate studies were also used as supporting evidence of paleotemperatures (Barker, 1990; Lorenz and Finley, 1991, Fall et al., 2009, Becker et al., 2009a). Fluid inclusion measurements of fracture-filling quartz and calcite from the MWX well yield high temperatures varying from 120 to 190°C (Lorenz and Finley, 1991) but this study did not measure fluid inclusion assemblages or relate fluid inclusions to the relative timing of cement deposits. Subsequent studies show that fluid inclusion assemblages in fracture cement deposits are not contemporaneous and many reflect temperatures other than that of maximum burial

(Becker et al., 2009a; Fall et al., 2009). These recent and ongoing fluid inclusion studies are discussed further in section 4.4. Re-equilibration of the fluid inclusions was probably not a problem for Piceance Basin samples since the rocks were uplifted but not deeply reburied after the formation of fluid inclusions.

Thermal conductivity for shales is taken to be 3.87×10^{-3} cal/cm.s.°C (Lerche, 1997), and default values in *GenesisTM* are used for the rest of the lithologies (Appendix B). For coal types and their potential for gas production I used data from Nuccio and Roberts (2003) and Yurewicz et al. (2008).

The thermal history reconstruction is given below with brief explanations of the elements of temperature reconstruction.

2.3.1.2.1. Kinetic Reactions of the Coals in the Piceance Basin

Coals occur throughout the Mesaverde Group, but are best developed in coastal-plain facies that overlie marine shoreline sandstones of the Corcoran, Cozzette, and Rollins members of the Iles Formation (Johnson, 1989; Reinecke et al., 1991). These coals are therefore directly beneath the gas producing Lower Williams Fork interval. Organic-rich continental shales, although thick and present throughout the Mesaverde Group, generally have low hydrogen indices and have generated comparatively small volumes of gas. Marine shales at the base of the Mesaverde section have slightly higher hydrogen indices than continental shales within the Mesaverde Group, but have moderately low total organic carbon and have also generated smaller volumes of gas than the coals. In their study, Yurewicz et al. (2008) demonstrated that the coals within the Iles Formation and the lower part of the Williams Fork Formation have generated the largest

volume of gas. According to their calculations gas generation was highest in or near the deep axis of the basin in the north where thermal maturity of source beds was greatest.

For the basin models, the kerogen types listed by Nuccio and Roberts (2003) were assumed in order to model the kinetic reactions and hydrocarbon generation of the petroleum source rocks in the Piceance-Uinta Basin.

- Green River Formation: Type I,
- Mesaverde Group: Type III,
- Mancos Shale: 50% Type II and 50% Type III, and
- Phosphoria Formation (and other Pennsylvanian-Permian source rocks): Type II.

For the gas generation kinetic reactions, the hydrogen index (HI) and total organic carbon (TOC) values listed in Yurewicz et al. (2008) were used as inputs.

- For marine shales: TOCs (average: 1.25 wt.%) and HIs (average: 160 - 200 mg HC/gC),
- For coals: TOC (average: 65 wt.%) and HI (average: 225 mg HC/gC), and
- For non-marine shales: TOC (average: 2 wt.%; range: 0.5 and 28 wt.); and HIs (average: 58 mg HC/gC; range: 12 to 256 mg HC/gC).

2.3.1.2.2. Regional Heat Flow

The thermal history of a sedimentary basin depends not only on the deposition and erosion history, but also the heat-flow evolution. The present-day geothermal gradients and heat-flow values for each borehole were calculated based on default thermal conductivities for the lithologies (except for shales), down-hole temperature data

(corrected with mud log information if available), and mean annual surface temperature calculated from the paleolatitude.

The dominant heat source responsible for the gas generation was burial, except in the southeastern corner of the basin where magmatic activity had an effect from 35 to 10 Ma and raised the local geothermal gradient (Collins, 1976; Johnson and Nuccio, 1986; Johnson and Nuccio, 2003; Yurewicz et al., 2003, 2008; Zhang et al., 2008). Yurewicz et al. (2003) plotted the down-hole maturation data (vitrinite reflectance) versus present day depth for wells from the northern and southern Piceance Basin and demonstrated that the wells in the southern part of the Piceance Basin have higher levels of maturation at equivalent depths and stratigraphic position compared to the wells in the north. For example, vitrinite reflectance value of 1.5% is reported at a depth of approximately 11,000 feet in the wells from the northern Piceance Basin while this value observed in shallower intervals around 6,500 feet in the southern Piceance Basin wells. In his study of thermal regimes of the southern Rocky Mountains and Wyoming, Decker (1995) found that high heat flows occur near Cenozoic igneous rocks, but drop sharply with increasing distance (High heat flow anomaly in the Leadville-northern Sawatch Range occur within 50-60 km wide zone). Heat flows reported in the literature are presented with the results of this study in Table 2.1.

Table 2.1. Comparison of heat flow data from the literature and this study.

	N-NE Piceance	S-SW Piceance	Piceance and Adjacent Basins	From
Present Day Heat Flow (mW/m²)	50	65		Johnson and Nuccio (1986) Zhang et al. (2008)
			58.5 – 83.6 58.5 – 84	Monroe and Sass (1974) Reiter et al. (1979)
		67 (MWX well)		Law et al. (1989)
	64.85 until 40 Ma and raised to 69 for 10 Ma to present	64.85 until 40 Ma and raised to 79 for 10 Ma to present	.	Yurewicz et al. (2008)
	52- 84		Colorado Front Range: 54 – 58	Decker (1995)
	68.5 (MF31-19G)	78.7 (MWX) 74.7 (Last Dance)		This study

2.3.1.3. Results of Basin Modeling

Most of the modeled temperatures from my basin models match within ± 5 °C of the measured bottom-hole temperatures except for the Last Dance well. Although I was able to get a good match at the Williams Fork interval, the temperatures for the Wasatch and Mancos section are underpredicted. Because the accuracy of the thermal history for the Mesaverde section was important for my diagenetic models, I focused my work on the best match for Williams Fork. As mentioned earlier, the true temperatures are higher than the measured values because of the effects of drilling in most cases.

Modeling results show that the present-day heat flow is around 68.5 mW/m² for the well (MF31-19G) located in northern Piceance Basin and ranges between 74.7 and 78.7 mW/m² in the southern wells (MWX and Last Dance) at the base of Mesaverde. The

heat flow values I obtained for my wells are mostly in agreement with what has been reported in the literature (Table 2.1). Higher heat flows are observed in the southwestern Piceance wells compared to the northern wells due to effects of nearby igneous activity (igneous intrusions are shown in the locality map in Figure 2.1).

*Genesis*TM basin modeling program calculates the heat flow as a function of thermal gradient (calculated from present day temperature measurements) and thermal conductivity. *Genesis*TM assumes three factors as controls of terrestrial heat flow: 1) the thickness of lithosphere (at the base of the lithosphere the temperature is 1330 °C and thinner the lithosphere is the higher the heat flow); 2) radiogenic heat production from the crust (mostly from granites), and 3) radiogenic heat production from the sediments (*Genesis*TM User's Guide). In my research, possible variations of paleoheat flow through time were accounted by using *transient heat flow (steady at the base)* model option embedded in *Genesis*TM basin modeling program. The heat flows at the time of deepest burial were about 10 mW/m² lower than present day heat flows for both northern and southern Piceance wells.

I adjusted the thickness of the eroded Tertiary strata to get a better fit to the present day temperature and pressure profiles. I tested the performance of the resulting basin models as inputs of diagenetic models by comparing the calculated quartz cement abundance with the quartz cement abundance from point-count results. The burial histories that gave the best match between calculated quartz cement and the quartz cement from point-count were selected as representative for the wells. The estimations of the deepest burial and removed overburden are respectively: 13,575 ft and 5,147 ft for the MWX, 13,067 ft and 5,068 ft for the Last Dance and 15,163 ft and 3,157 ft for the MF31-

19G. More discussion on the estimations of removed overburden can be found in section 2.5 and Table 2.3 where I compare my results with the published data.

MWX-1 Well

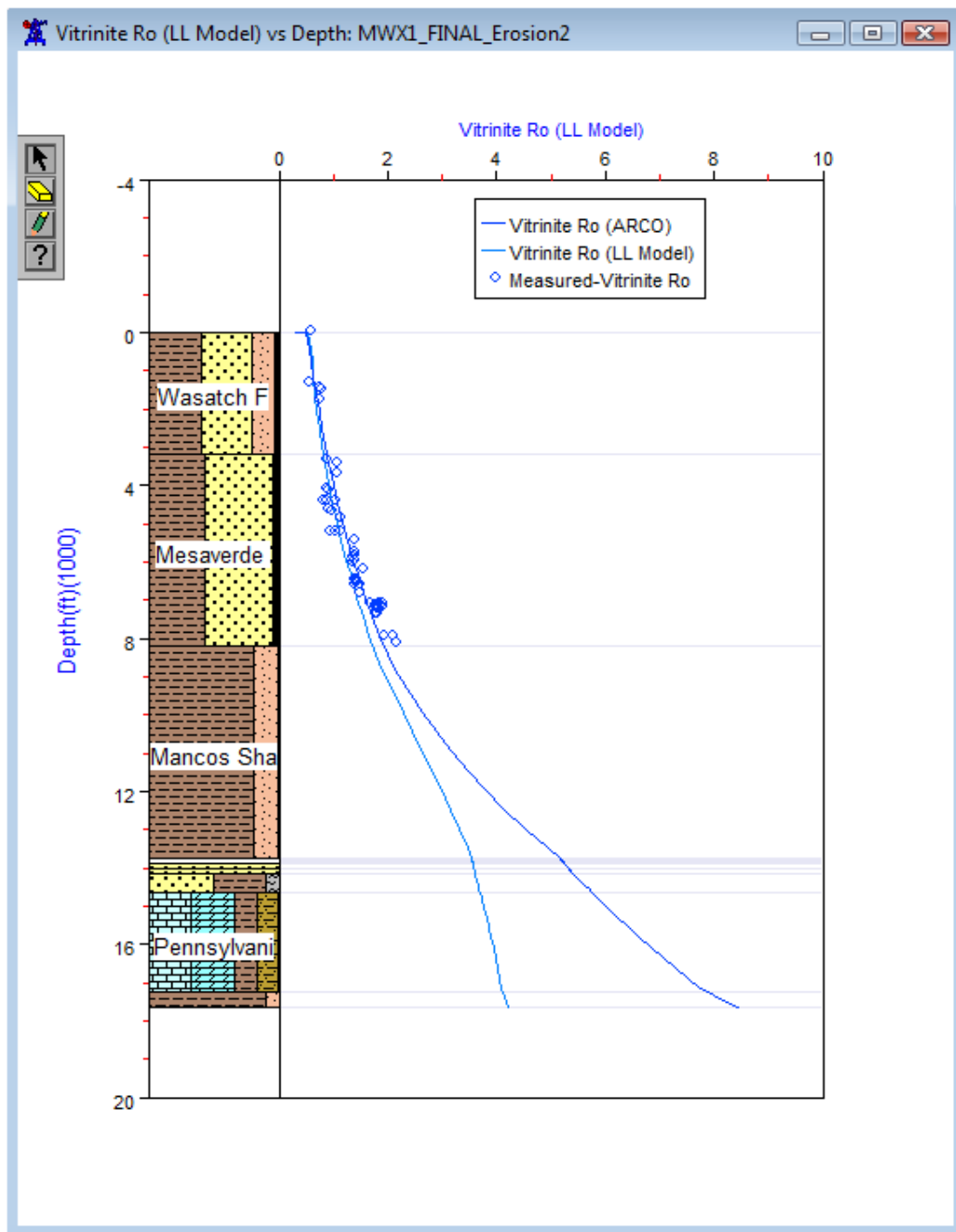


Figure 2.6. Available vitrinite reflectance and bottom-hole temperature data were matched to the predictions of the *Genesis*TM (ARCO and Lawrence and Livermore models).

MWX-1 Well

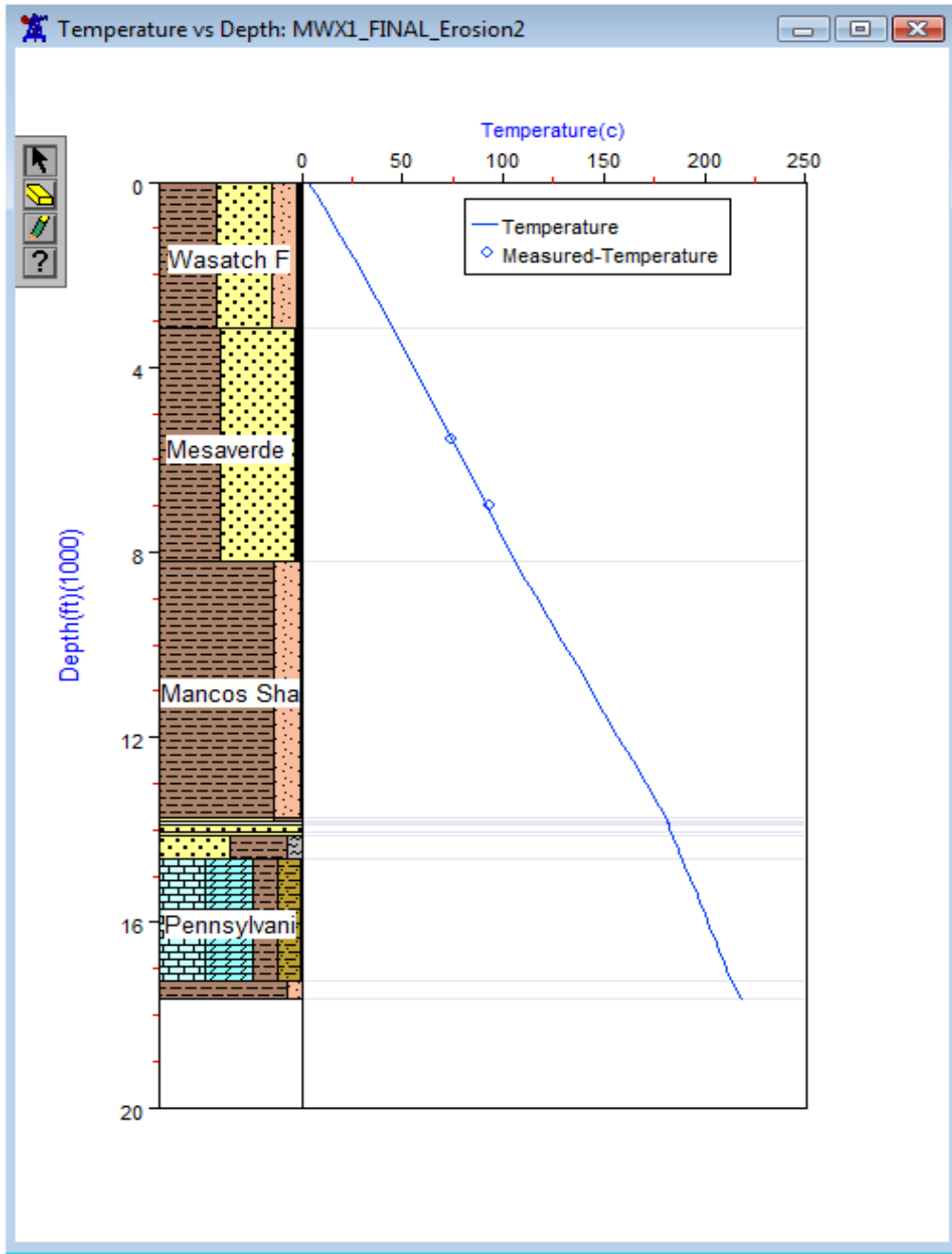


Figure 2.6. (ctd)

MF31-19G Well (represented by T52-19G Well)

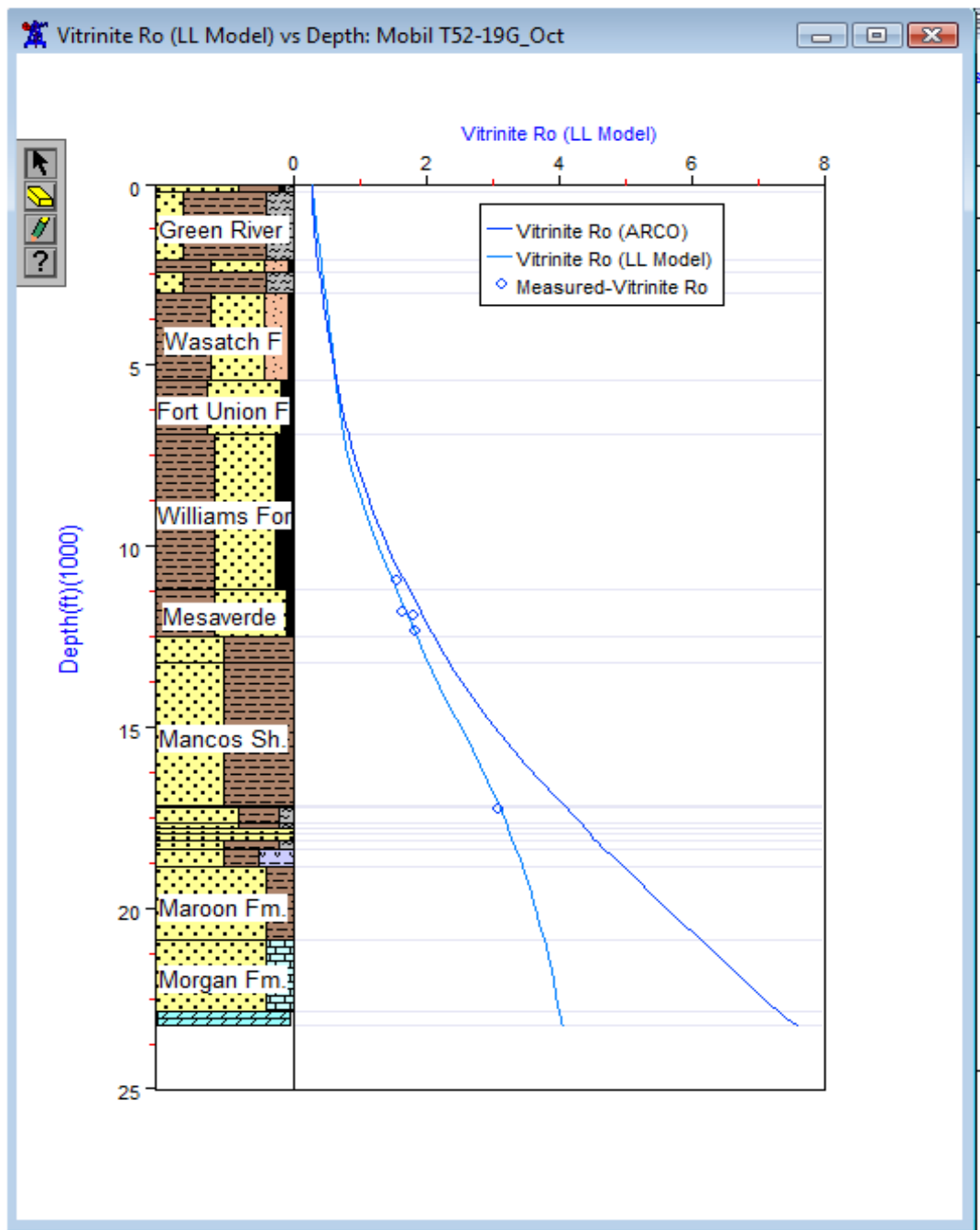


Figure 2.6. (ctd)

MF31-19G Well (represented by T52-19G Well)

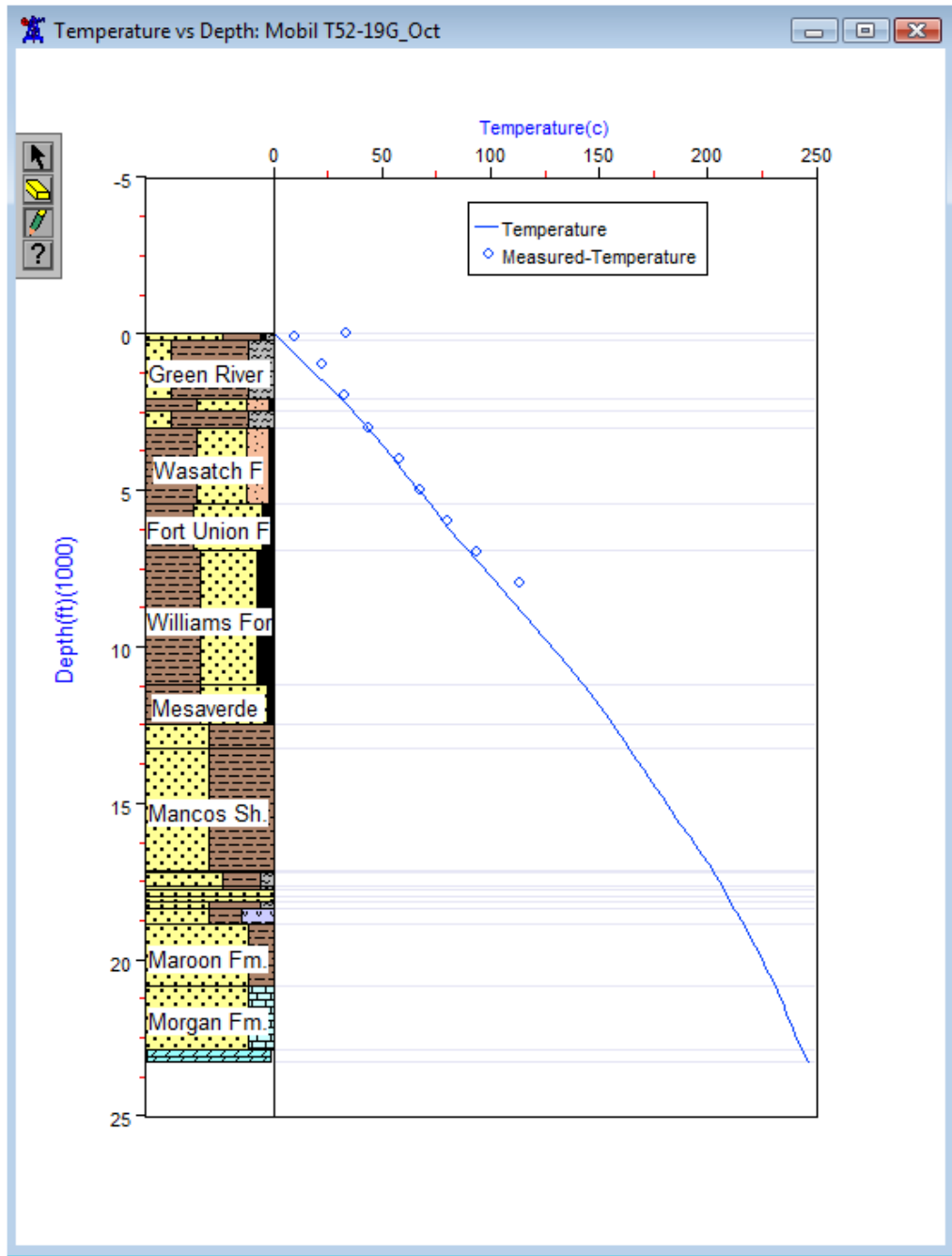


Figure 2.6. (ctd)

Last Dance Well (pressure and vitrinite reflectance data are from O'Connell 31x well)

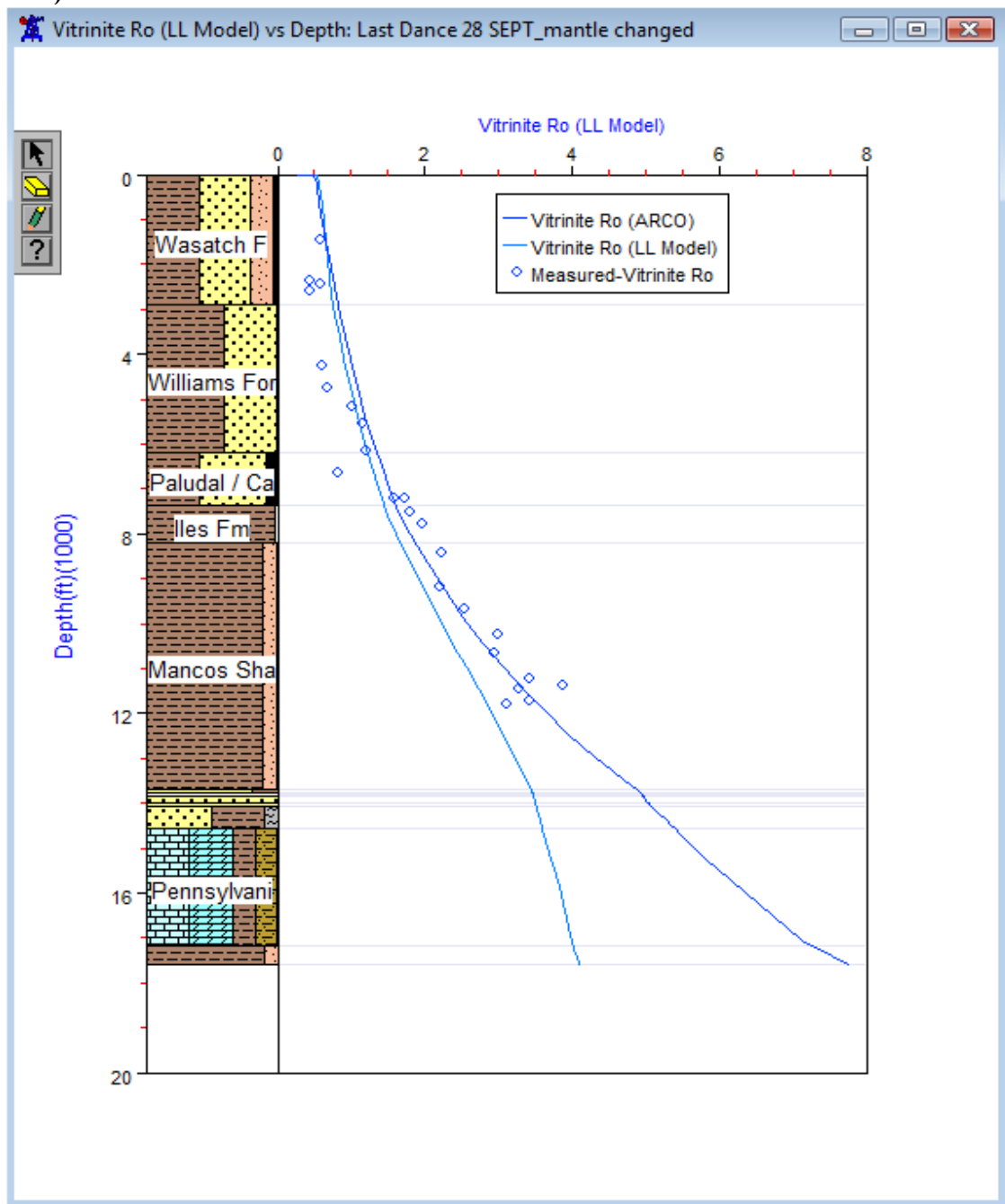


Figure 2.6. (ctd)

Last Dance Well

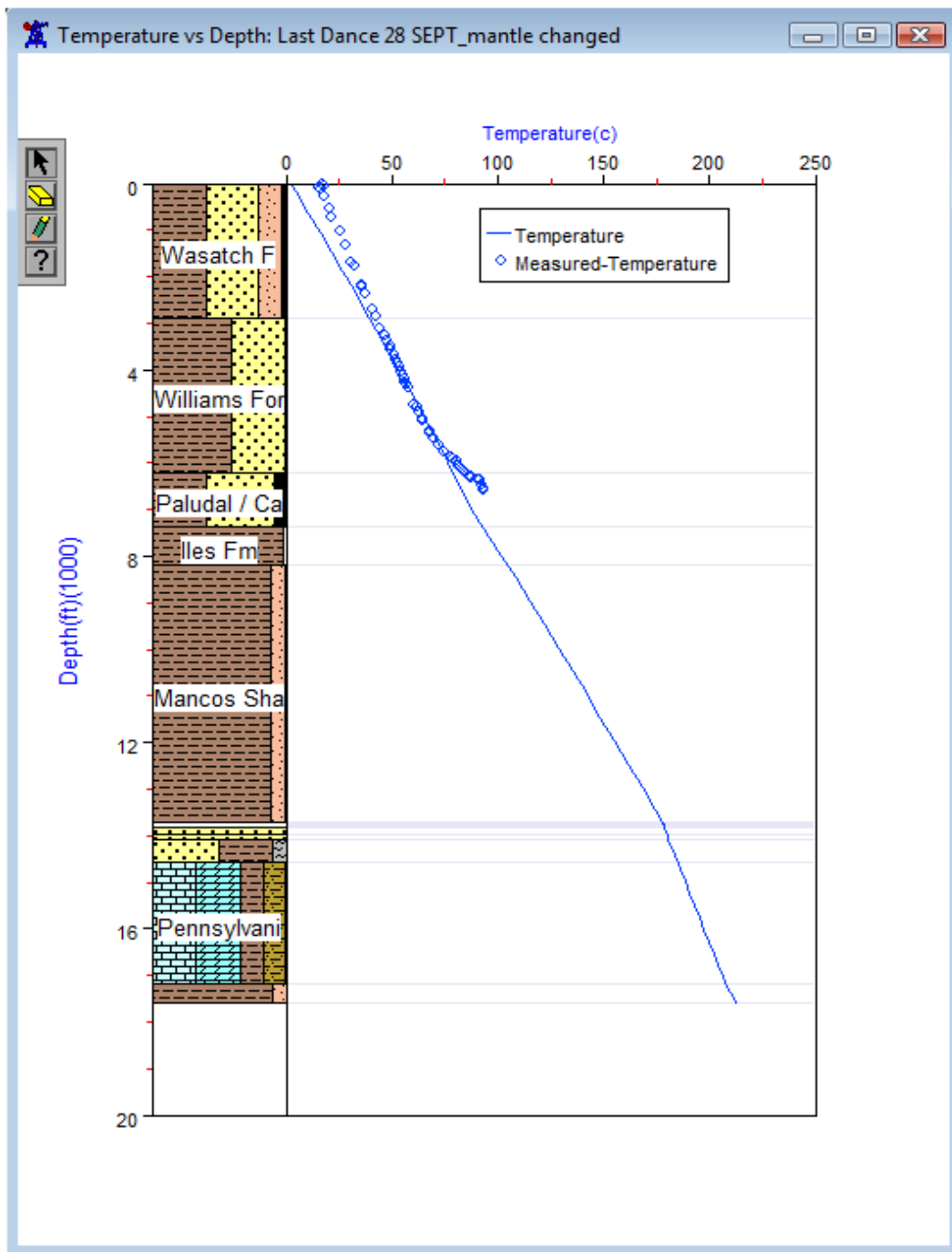


Figure 2.6. (ctd)

Rifle Gap Outcrop

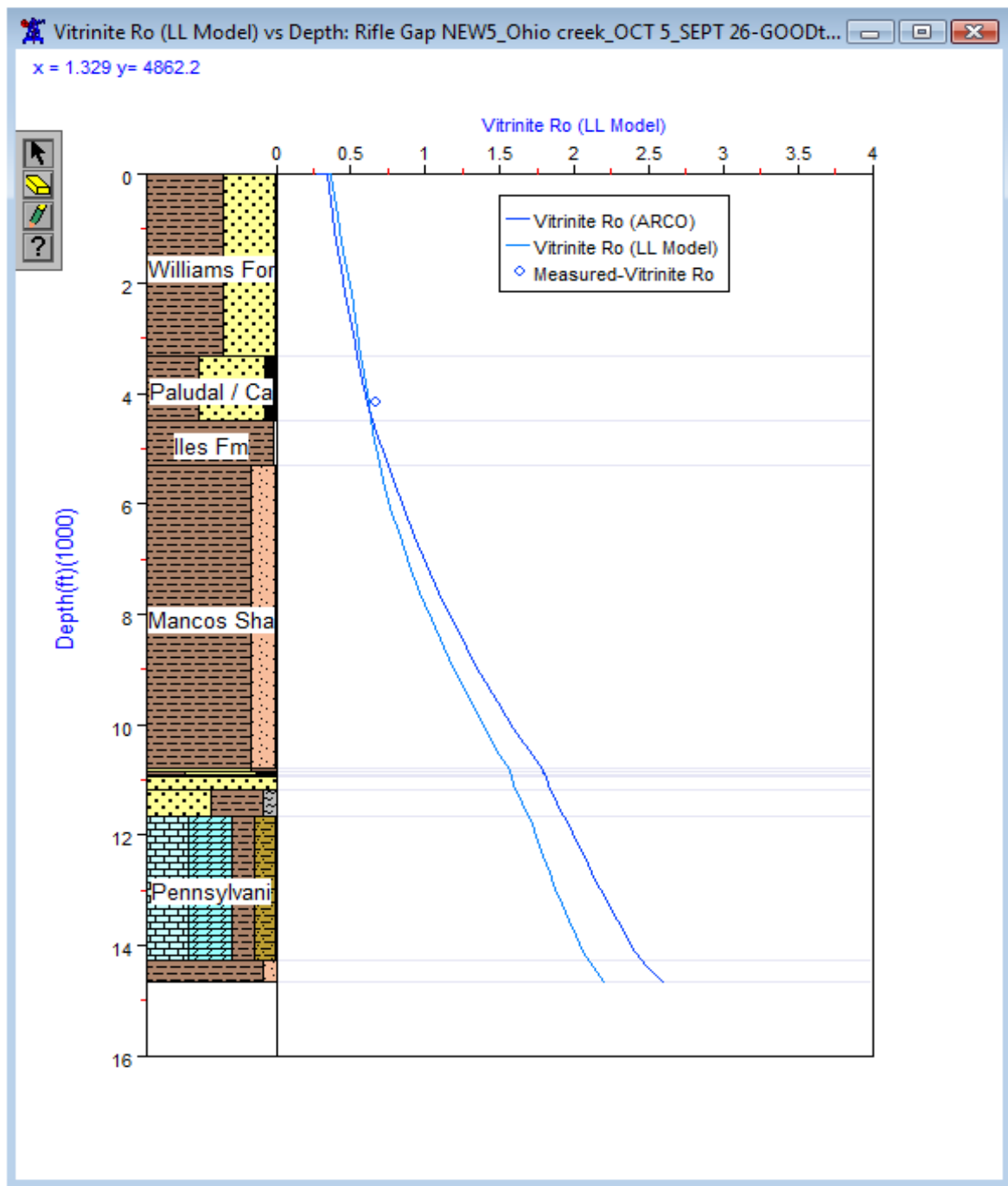


Figure 2.6. (ctd)

Rifle Gap Outcrop

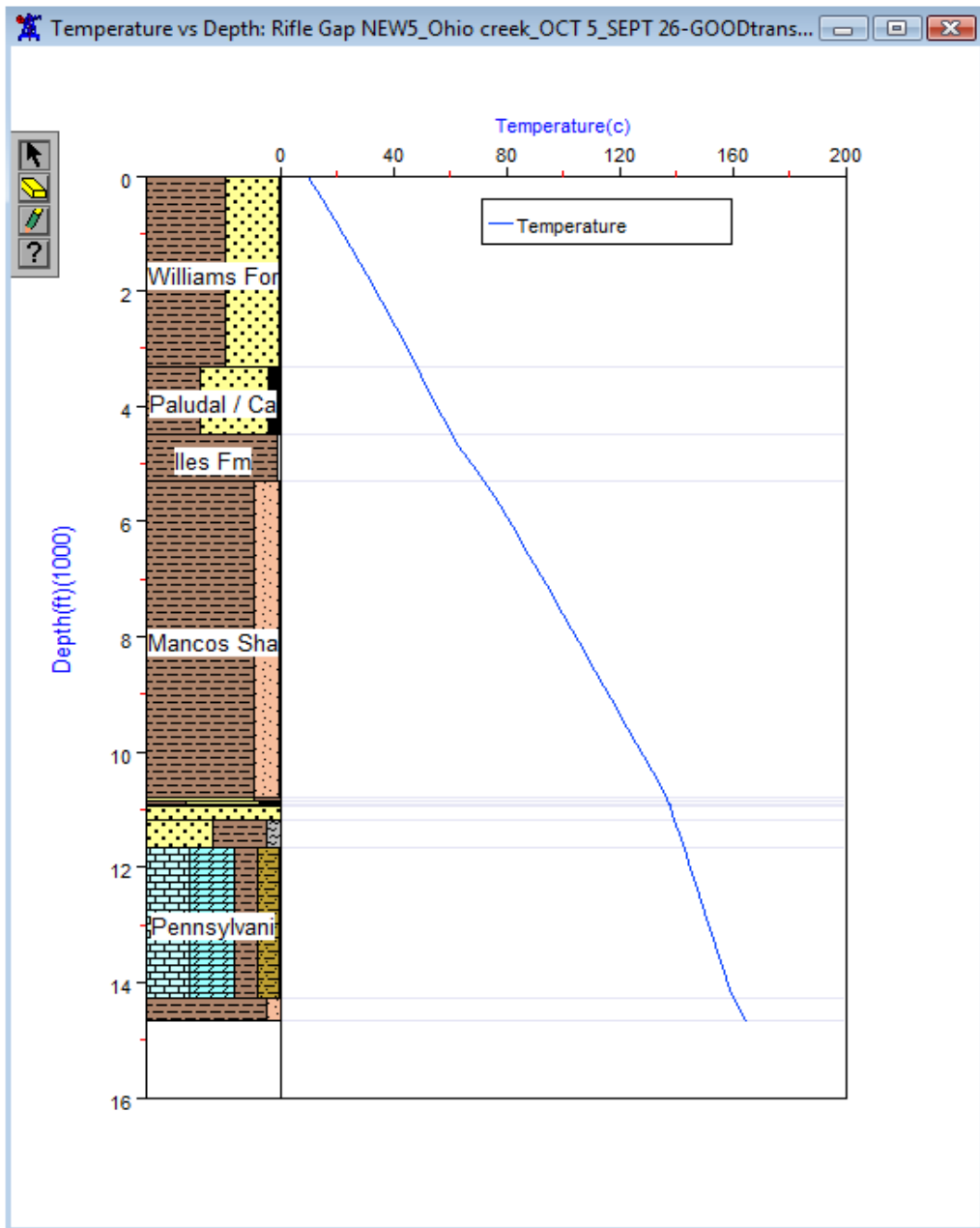


Figure 2.6 (ctd).

2.3.2. Results of Quartz Cement Simulations

Although the *Touchstone*TM diagenetic modeling program is generally used as a tool for predicting porosity and permeability (reservoir quality), for my research I used it for constraining the burial histories. Additionally, I applied it for reconstructing the evolution of cementation, pore space and permeability in the geologic past for one of the study wells (Chapter 4, section 4.4).

*Touchstone*TM is a process-oriented forward model that contains terms optimized empirically using textural, compositional, and burial history data from natural sandstones. By using *Touchstone*TM, temperature, pressure history, timing and depth of quartz cementation can be simulated. Model inputs include (1) textural and compositional characteristics of each analyzed sample; (2) thermal and effective stress histories derived from basin modeling; and (3) other various model parameters discussed in Appendix E2 and presented in Table 2.2.

The program assumes, following Walderhaug (1996), that precipitation is the rate-limiting factor and surface area available is a function of grain size, degree of coating on quartz grains, and the sandstone's porosity

In *Touchstone*TM the errors in the compaction model are carried into the quartz model due to the influence of compaction on the available nucleation surfaces. To minimize this compactional effect, *Touchstone*TM can force the calculated IGVs to match the measured IGV (Figure 2.7A). With this approach I optimized a single set of quartz cement model parameters (activation energy (E_a) and slope) for all samples and kept the same values for the rest of the modeling. For kinetics of quartz cementation I used the RQC grain-size dependent model option which uses normalized rates of quartz

overgrowths with grain size: minimum temperature required for quartz cement to precipitate and the slope that describes the rate of activation energy change with grain size.

Quartz precipitation was simulated by using a single set of temperature-dependent quartz precipitation kinetics for all samples and accuracy was tested by comparing the model results with the present-day cement abundance from the point-count analyses (Figure 2.7B). A thermal history input cooler than the true temperature history of the sandstones results in underprediction of the quartz cement volumes with the diagenetic model and a hotter thermal history input causes overprediction of the quartz cement abundance. Thermal histories were modified by changing the amount of erosion (more sediment eroded meaning the sediment was buried deeper in the geologic past and was exposed to higher temperatures). I tried alternative burial history models until I obtained a quartz cement calibration model replicating the present-day quartz cement abundance within 4% accuracy. The results of quartz simulations are shown in Figure 2.7B and 2.7D and the burial history models that led to the best matches are presented in Figure 2.8A and B.

Table 2.2. Temperature constraints for the paragenetic sequence used in modeling.

Paragenesis Classes	Constraint	Min	Max
Syn depositional	Burial Depth, m	0	250
Low Temperature	Temperature, °C	25	40
Intermediate Temperature	Temperature, °C	40	80
High Temperature	Temperature, °C	80	185
Quartz in Secondary Pores	Temperature, °C	80	185

Table 2.2. (ctd) Temperature constraints for the paragenetic sequence used in modeling.

Category	Paragenesis
Grain Coating	Syn depositional
Secondary Porosity	High Temperature
Quartz Microcrystalline Cement	High Temperature
Calcite cmt	Intermediate Temperature
Fe-calcite cmt	High Temperature
Dolomite cmt	High Temperature
Siderite pore-filling cmt	Intermediate Temperature
Siderite pore-lining cmt	Intermediate Temperature
Carbonate Undiff. Cmt	Intermediate Temperature
Illite pore-filling cmt	High Temperature
Illite pore-lining cmt	High Temperature
Smectite cmt	Syn depositional
Chlorite pore-filling cmt	Syn depositional
Chlorite pore-lining cmt	Syn depositional
Kaolinite cmt	Intermediate Temperature
Sulfate cmt	Intermediate Temperature
Pyrite cmt	High Temperature
K-feldspar cmt	High Temperature
Albite cmt	High Temperature
Zeolite cmt	Intermediate Temperature
HC Pore-filling cmt	High Temperature
HC pore-lining cmt	High Temperature
Ti-oxide cmt	Intermediate Temperature
Cement Undiff.	Intermediate Temperature
Calcite Replacement	Intermediate Temperature
Dolomite Replacement	High Temperature
Siderite Replacement	Intermediate Temperature
Ankerite Replacement	High Temperature
Sericite Replacement	High Temperature
Illite Replacement	High Temperature
Chlorite Replacemene	Intermediate Temperature
Kaolinite Replacement	Intermediate Temperature
Clay Undiff. Replacement	Intermediate Temperature
Pyrite Replacement	High Temperature
K-feldspar Replacement	High Temperature
Albite Replacement	High Temperature
Zeolite Replacement	Intermediate Temperature

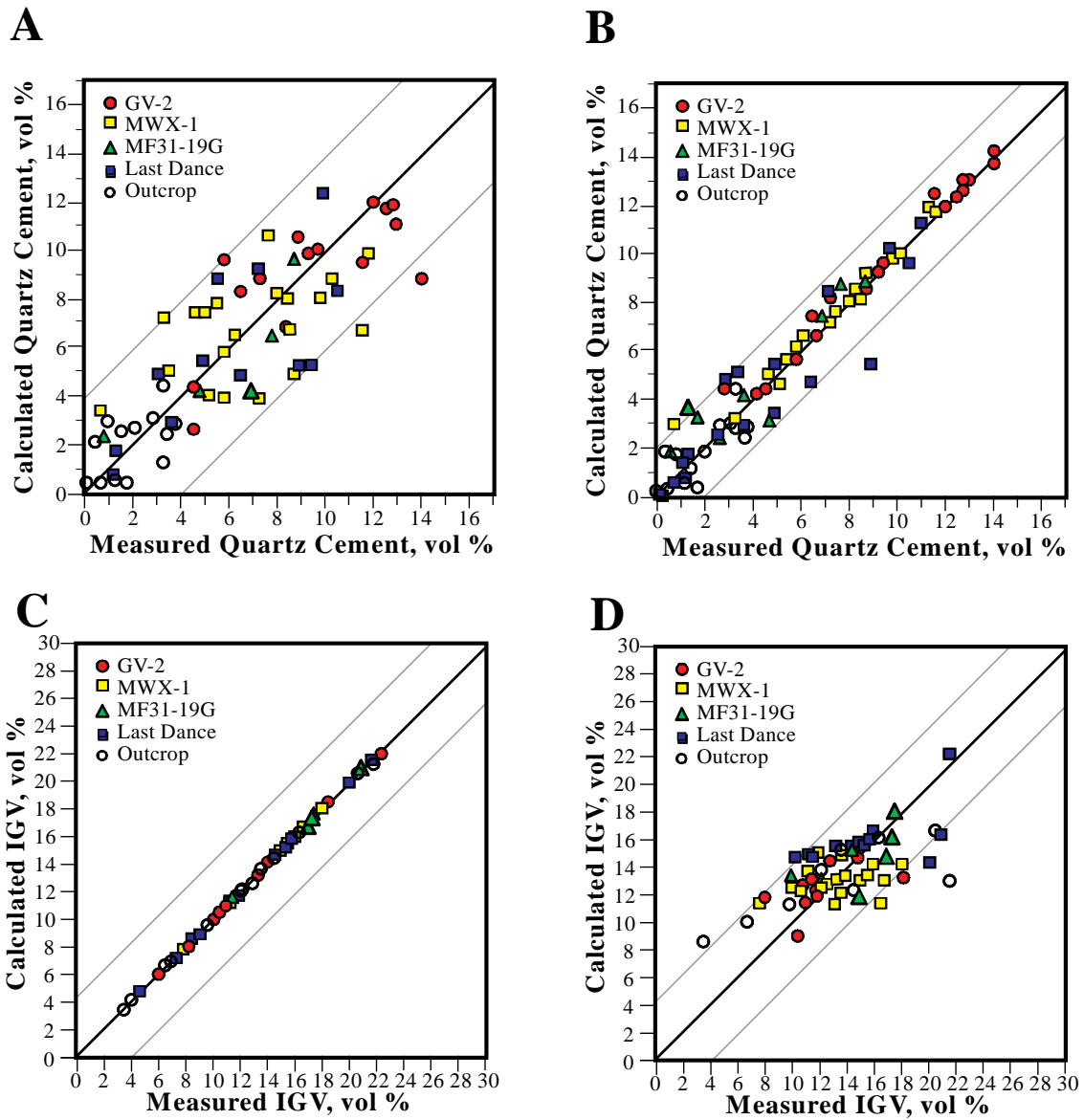


Figure 2.7. Diagenetic model calibration results for quartz cementation. (A) IG V match option was selected so that the errors in the compaction models would not be carried into the quartz cement calibrations. (B) Quartz cement calibration indicating most of the quartz cement predictions are within a $\pm 2\%$ accuracy limit. (C) IG V match option was toggled off and compaction was simulated. (D) Measured versus predicted quartz cement abundances modeling both compaction and quartz cementation. The quartz cement kinetics were the same as those used to generate the results shown in A.

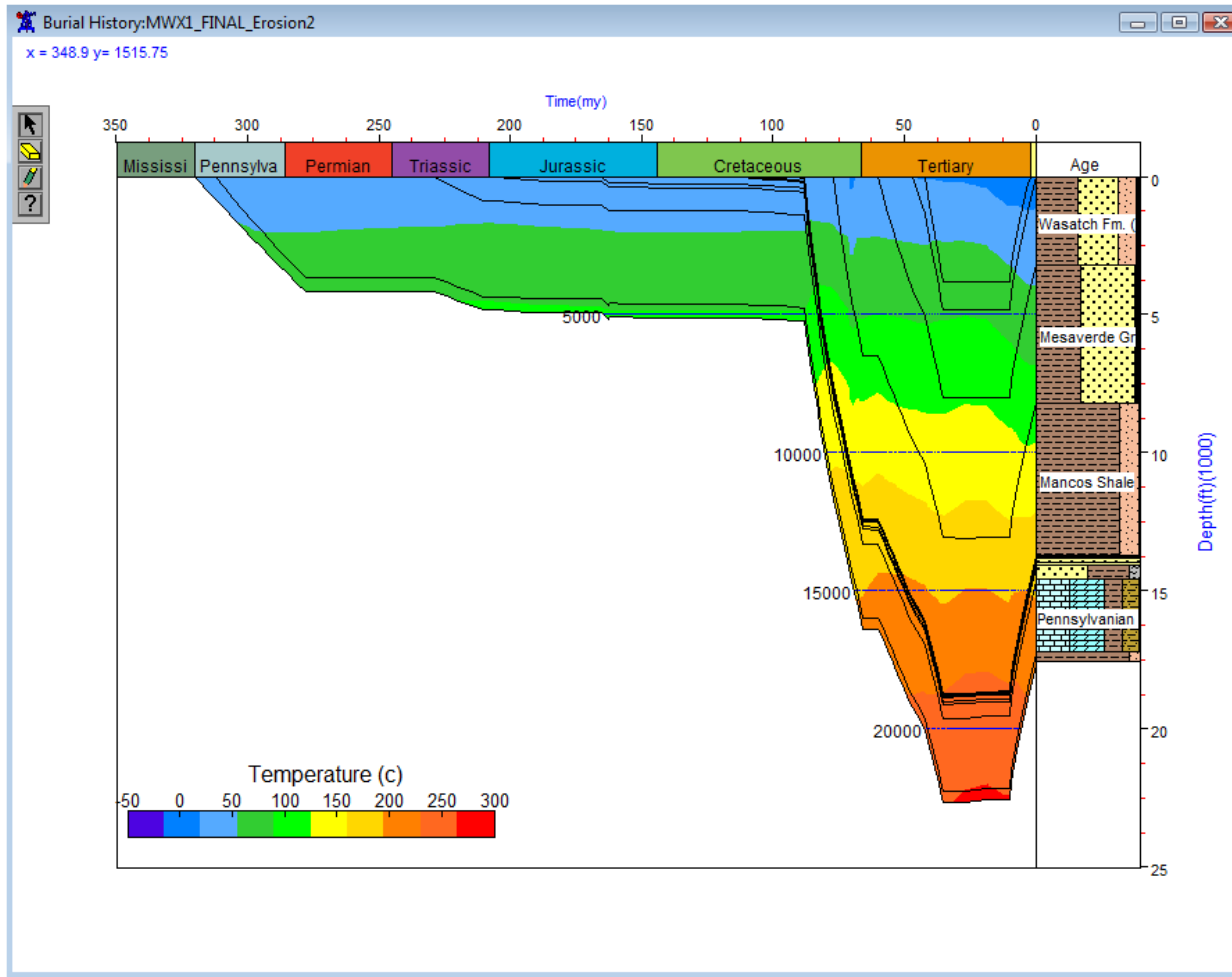


Figure 2.8. (A) Representative burial history models generated with *Genesis*TM with overlay of predicted temperature history for MWX well.

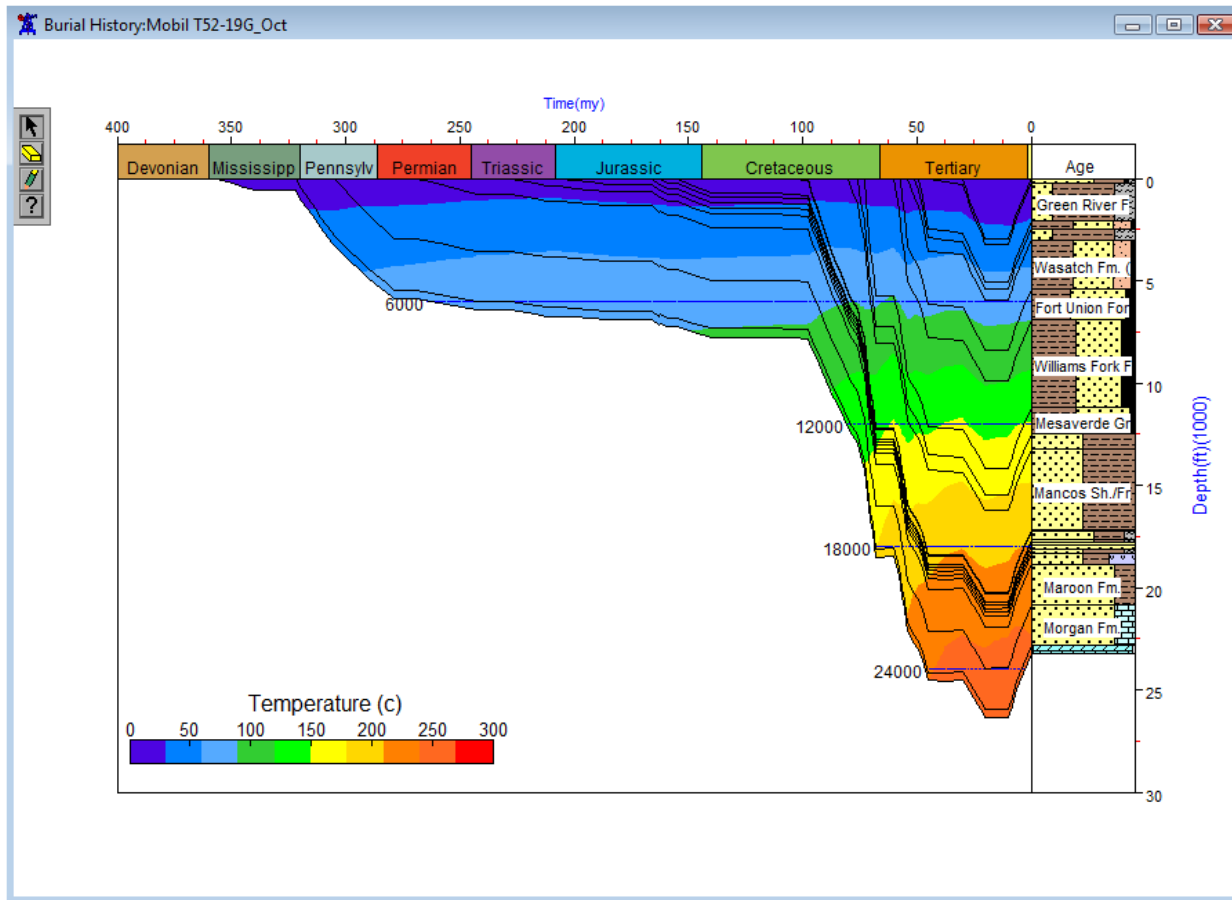


Figure 2.8. (A) (ctd) Representative burial history models generated with *Genesis*TM with overlay of predicted temperature history for MF31-19G / T52-19G wells

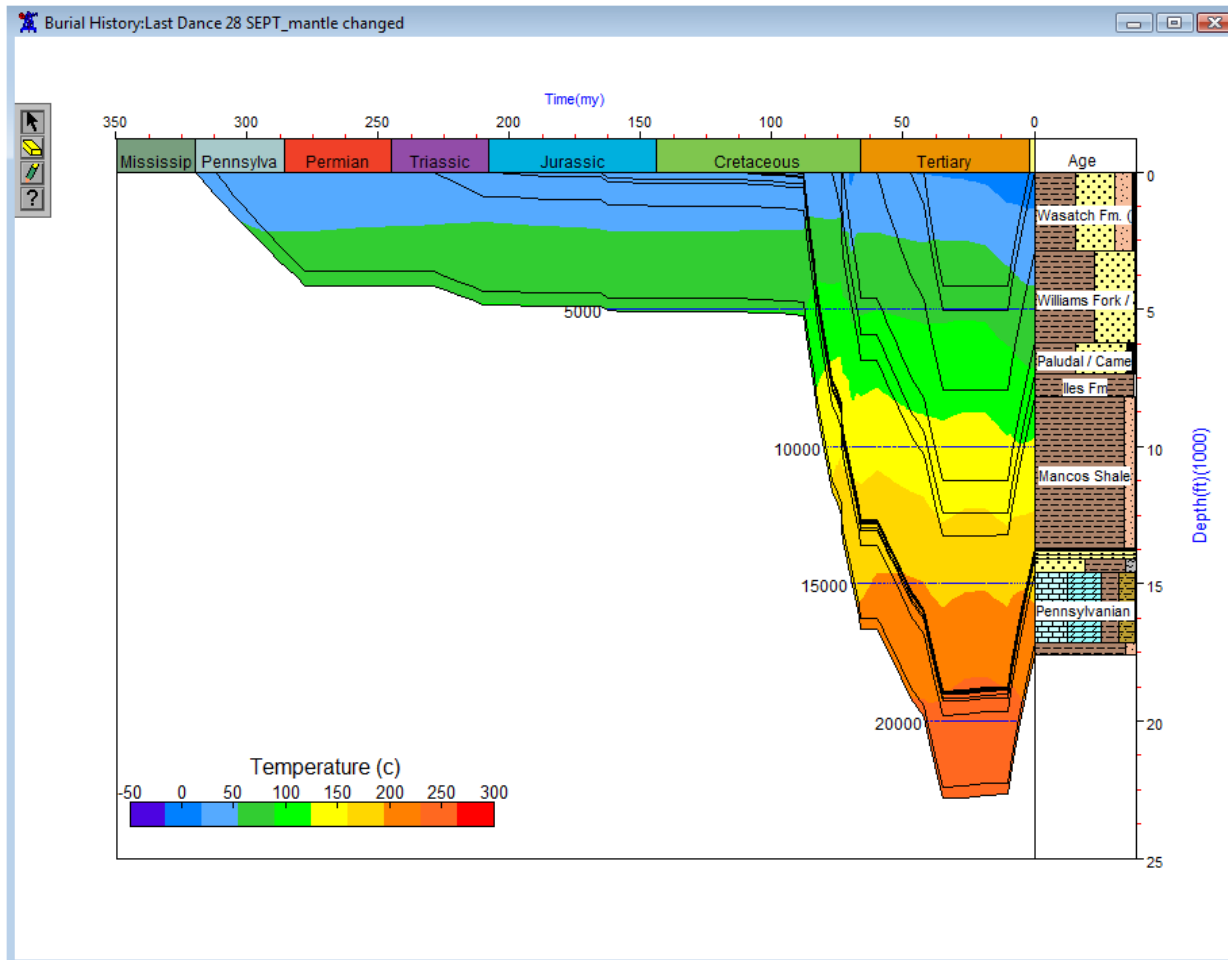


Figure 2.8. (A) (ctd) Representative burial history models generated with *Genesis*TM with overlay of predicted temperature history for Last Dance / O'Connell 31x wells.

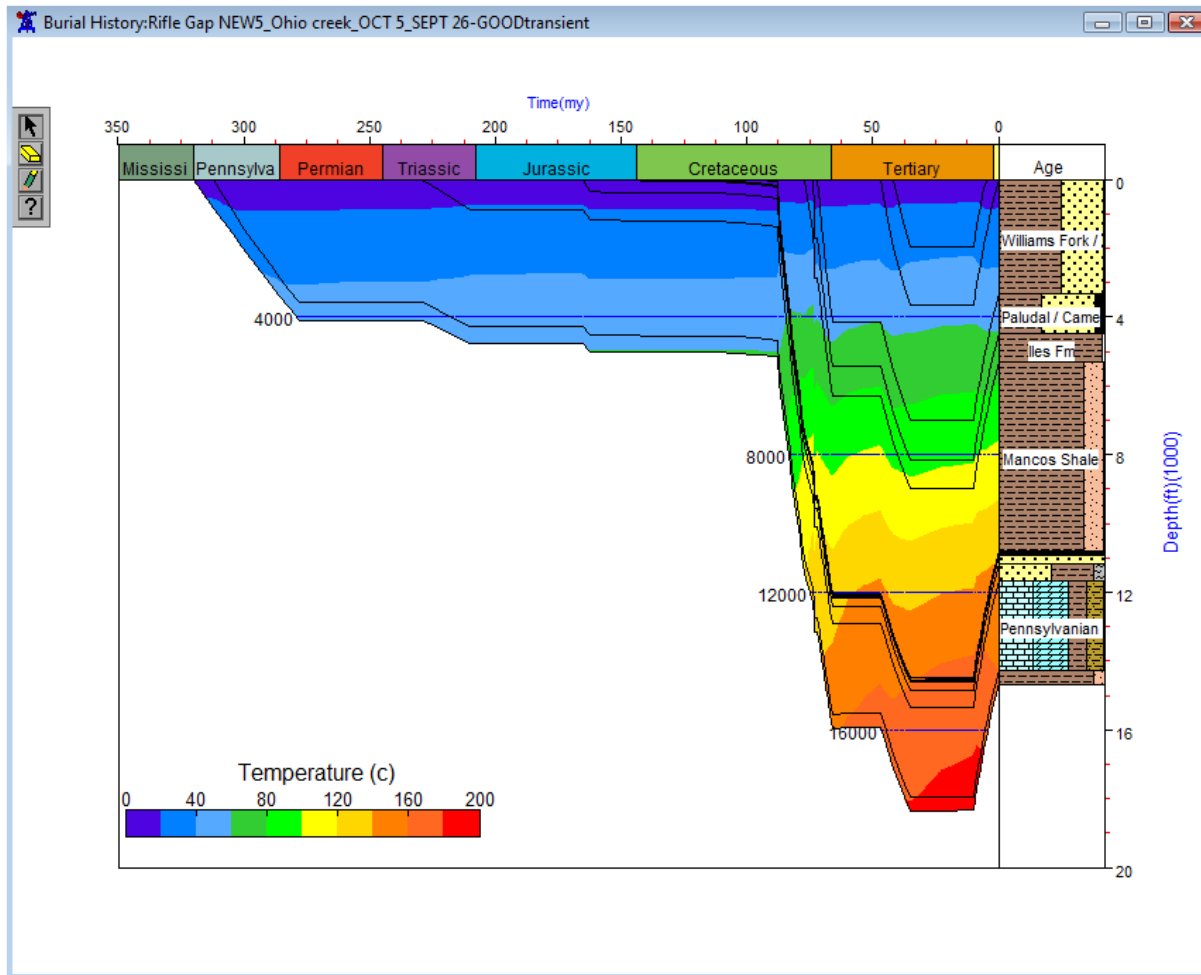


Figure 2.8. (A) (ctd) Representative burial history models generated with *Genesis*TM with overlay of predicted temperature history for Rifle Gap outcrop.

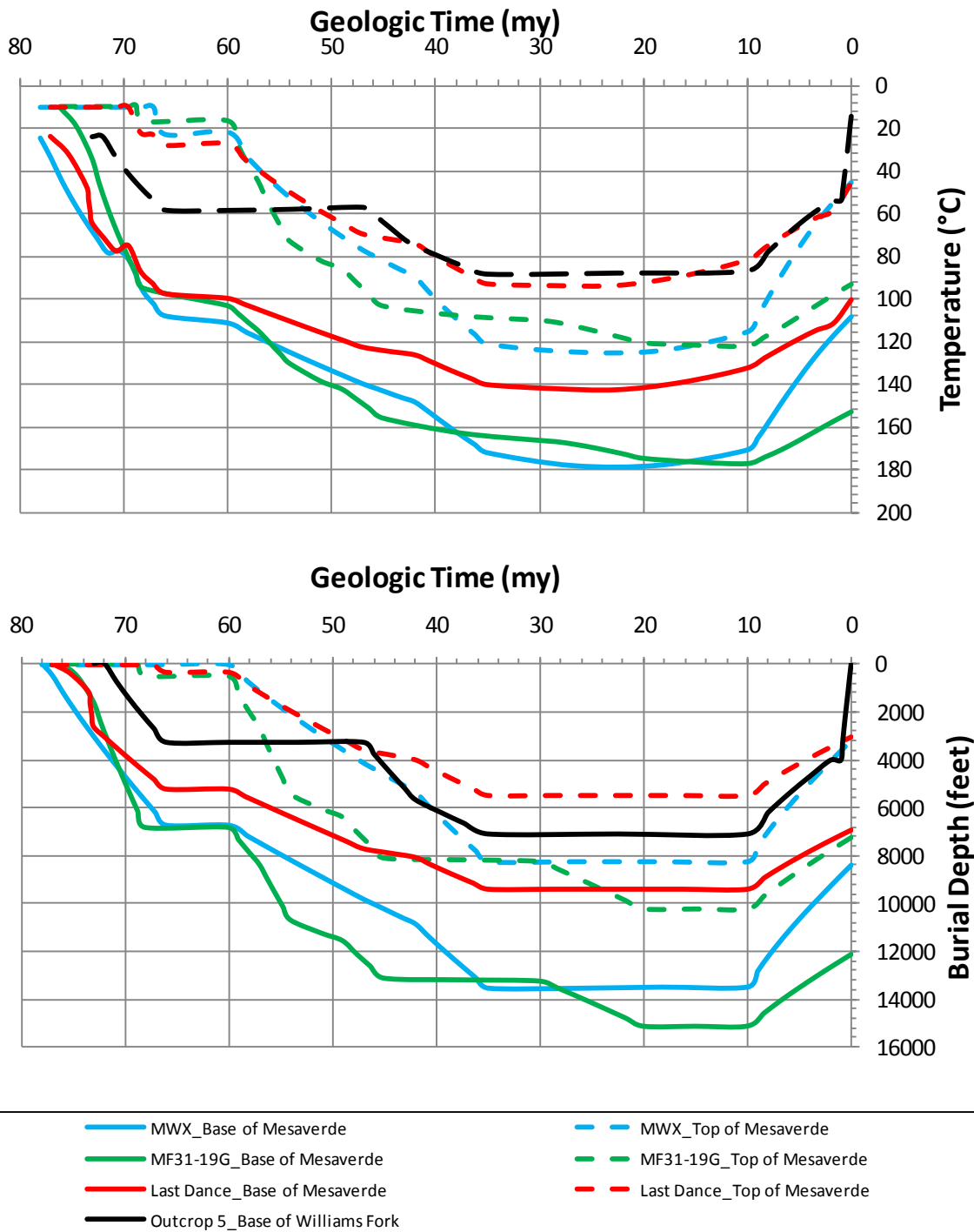


Figure 2.8. (B) Representative thermal and burial depth history curves for top and base of Mesaverde interval.

2.4. DISCUSSION: CONTROLS ON QUARTZ CEMENTATION

Outcrop samples experienced significantly less quartz cementation compared to most of the subsurface samples (Figure 2.5A). The burial history reconstructions illustrate that Mesaverde sandstone in the outcrop location experienced shallower maximum burial than the well sites and sandstones at the outcrop have not resided in the high temperature environments needed for quartz precipitation for very long; and therefore, the measured and predicted quartz cement is much less (up to 4%; Figure 2.5A). On the other hand, exposure to deeper burial and higher temperatures at the subsurface resulted in faster rates of quartz precipitation and greater quartz abundance (up to 14% quartz cement; Figure 2.5B).

As mentioned earlier, differences in the surface area for quartz nucleation are an additional cause of variation in quartz cement abundances. For a given set of sandstones with comparable grain size and thermal exposure, samples with thick and continuous grain-coats have lower quartz cement abundance. An example for emphasizing the importance of the surface area for quartz nucleation is subsurface sample LD (4016 ft) that has high grain-coat coverage with an outcrop sample with low grain coat coverage (WF-6) (Figures 2.9A and 2.9B). Although, the subsurface sandstone was exposed to temperatures as high as 120 °C at maximum burial depths of 7000 ft, the amount of quartz cement predicted for this sample is less than 1%. This estimate is nearly the same amount of quartz cement predicted for the outcrop sample WF-6 which had a cooler thermal history (~75 °C) around 4000 ft of maximum burial. Grain coat coverage explains the similarity of quartz cement estimates for these contrasting thermal histories. Sample LD 4016 ft has grain-coat coverage close to 98% whereas WF-6 had only ~30%

coverage. This example demonstrates the concept that even high temperatures cannot overcome the vital role of nucleation substrate.

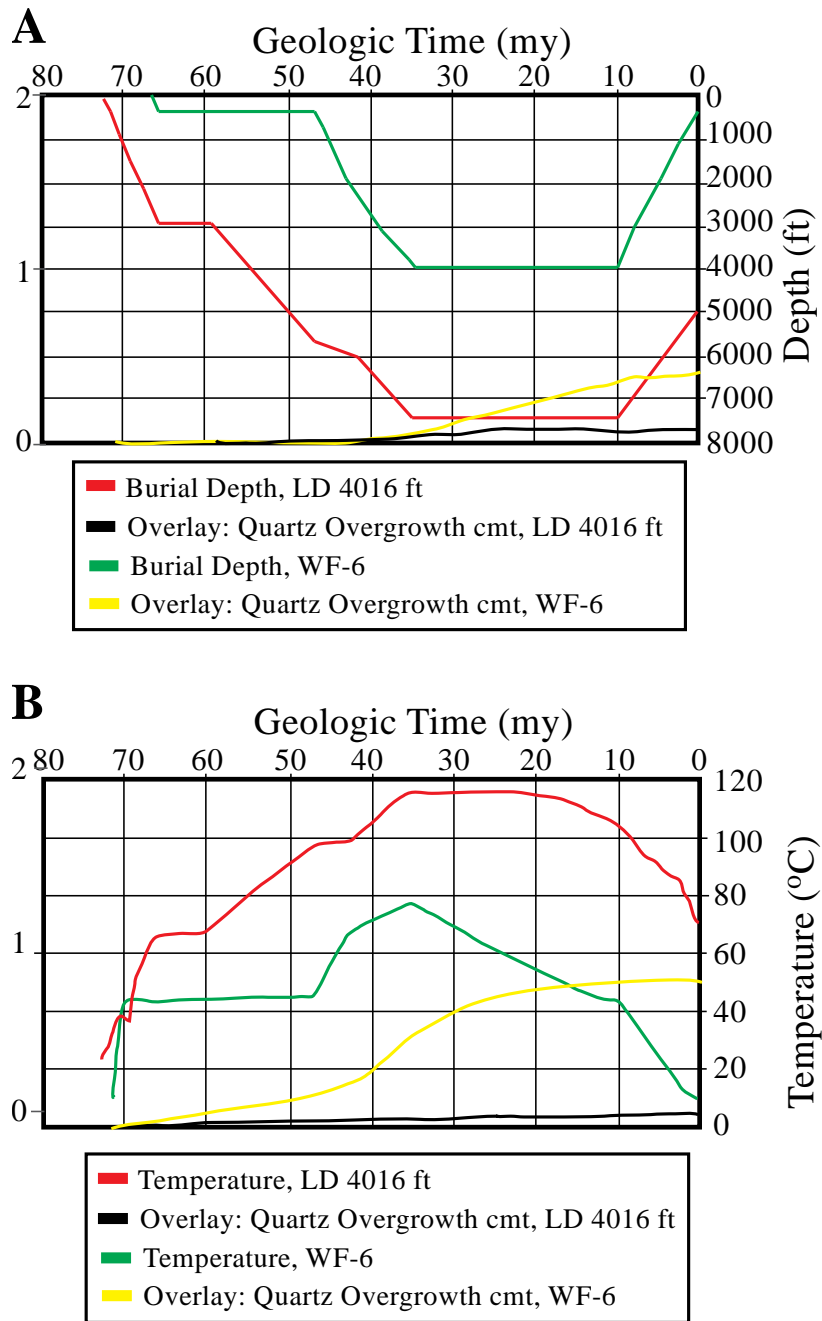


Figure 2.9. Comparison of quartz cementation evolution in geologic past for a sample from the outcrop (WF-6) and subsurface (LD 4016 ft). (A) Quartz cementation and burial depth with time. (B) Quartz cementation and temperature with time.

2.5. DISCUSSION: ESTIMATION OF REMOVED OVERBURDEN

The key issue in reconstructing the Piceance Basin's burial history is estimating the original thickness and the age of missing Tertiary section (Johnson and Nuccio, 1986). Apatite fission-track and thermal maturation studies suggest that maximum burial generally occurred between 45 and 20 Ma in the Piceance Basin, and that uplift began approximately 10 Ma as the Colorado River system eroded large quantities of sediment, estimated to vary between 1800 and 5000 feet (Bostick and Freeman, 1984; Johnson and Nuccio, 1986; Barker, 1990; Kelley and Blackwell, 1990; Wilson et al., 1998; Nuccio and Roberts, 2003, Yurewicz et al., 2003). The stratigraphic section from the Mancos to Green River formations is well established from well and outcrop studies but the section above the Green River and Uinta formations is less certain. Within the Piceance Basin, erosion over the past 30 m.y. has completely removed the Oligocene through Pliocene section (Yurewicz et al., 2003).

To estimate the thickness of removed overburden in the Piceance Basin, two approaches were used previously by numerous authors (Table 2.3): (1) stratigraphic projections (geologic inference), and (2) extrapolation of vitrinite reflectance versus depth profiles to vitrinite reflectance (R_o) values of 0.2% and 0.3% or extrapolation of $\log R_o$ -depth to R_o value of 0.2% (Table 2.3). There are uncertainties involved with both approaches. The stratigraphical approach utilizes the assumption that the missing Tertiary section was uniform in thickness and that differences in present-day topography represent differential erosion by the Colorado river system. Burial and thermal reconstructions are calibrated by adjusting input parameters so that predicted and observed present-day properties (maturation, temperature, pressure, etc.) match; however, numerous input

parameters (stratigraphy, heating events, rock properties, etc.) can match present-day properties (Payne et al., 2000).

In this section I used the approach of constraining the burial and thermal histories of the Piceance Basin with diagenetic modeling of quartz cementation. Diagenetic modeling was previously applied to assess thermal history reconstructions by Awwiller and Summa 1997, 1998 (Eocene of Western Venezuela) and Lander et al., 1997 (Miocene of Gulf of Mexico, Jurassic of North Sea, and Cambrian of Baltic region). Quartz cement is valuable as a paleotemperature indicator, because it is sensitive to both time and temperature: modeled quartz precipitation rates increase nearly exponentially with temperature and at a given temperature, the amount of quartz cement increases nearly linearly with time as long as nucleation sites are available. The approach has the limitation that finite pore space is available; once porosity is entirely occluded this gauge is insensitive to recording further thermal exposure unless other pore space becomes available (secondary pores, fractures).

In the following section, I summarize the different approaches to estimate the overburden. Overburden removal estimates by numerous studies are presented in Table 2.3, including results of the diagenetic approach taken here.

Table 2.3. Amount of Tertiary section removed at the study wells and outcrop location. Published interpretations of the burial history for the Piceance Basin are summarized below (AFT: Apatite Fission Track; FI: Fluid Inclusion; Ro: Vitrinite Reflectance (%)).

	MWX-1	MF31-19G (Mobil Oil, T52-19G)	Last Dance (O`Connell F11X-34P)	Outcrop Rifle Gap
Nuccio and Roberts, 2003 Basin models	4700 ft			
Nuccio and Johnson, 1992 Ro-depth extrapolation to 0.2 -0.3%	6100 ft Ro = 0.2% 3800 ft Ro = 0.3%	7200 ft Ro = 0.2% 3700 ft Ro = 0.3%		3800 - 4000 ft (Harvey Gap, White River Uplift)
Zhang et al, 2008 Basin models by using Ro values estimated from pyrolysis analyses		9166 ft		
Kelley and Blackwell, 1990 AFT	Max burial at 10 Ma			
Johnson and Nuccio, 1986	4600 ft.			
Barker, 1990 Ro and FIs	4600 ft			
Bostick and Freeman, 1984 Ro	4000 – 5000 ft			
Wilson et al., 1998 AFT, Ro and FI			4460 ft	
This study Quartz cement Paleothermometer	5147 – 5200 ft	3157 ft	5068- 5400 ft	3000 ft

2.5.1. Estimation of Sediment Removal with Stratigraphic Inference

The Piceance and Uinta Basins were uplifted regionally starting at about 10 Ma and eroded so extensively that only scattered remnants of pre-uplift surface is identified beneath 9.7 my basalt flows in the south central part of the Piceance Basin and 24 my basalt flows in the White River uplift east of the Piceance Basin (Nuccio and Roberts, 1992). This pre-uplift surface stands at 10,000 feet above sea-level at present day at these locations, which approximates the surface of maximum aggradation based on the

stratigraphic projections and geologic inference. The 24 Ma erosional surface beneath the basalt flows, which probably covered most of the area prior to regional uplift and 10 Ma downcutting, truncates upper Eocene rocks toward the southern margin of the Piceance Basin and may have begun to form in the late Eocene during the final stages of Laramide orogeny (Johnson and Nuccio, 1986). Nuccio and Johnson (1992) claimed that White River uplift could have been eroded to about the same elevation of as the Piceance Basin prior to deposition of basalt at 24 Ma.

2.5.2. Estimation of Sediment Removal from Vitrinite Reflectance Evidence

Vitrinite reflectance (R_o) values in the Piceance and Uinta Basins are mainly controlled by structure and thermal gradients. In general, planes of equal vitrinite reflectance dip toward the structural troughs of the two basins, but at a gentler dip than the structure except for the White River dome uplift in Piceance Basin near Meeker and Rangely, Colorado, perhaps due to a change in thermal gradient near the uplift (Johnson and Nuccio, 1986). Yurewicz et al. (2008) demonstrated a spatial correspondence between the thickness of the gas-charged interval and the extent of gas generation predicted from source maturation modeling and Zhang et al. (2008) found a correlation with the coal rank and depth of burial (higher coal ranks in the deeply buried areas except for Southwestern corner of Piceance where heat flow was increased due to igneous activity which resulted in higher coal ranks).

Nuccio and Johnson (1992) combined the surface R_o values with the subsurface R_o to create R_o -depth plots to estimate the thickness of overburden. These plots were extrapolated to R_o values of 0.2% and 0.3%, which are believed to be R_o values for

vitritine near the surface in a Basin that has not undergone erosion. Zhang et al. (2008) plotted log Ro-depth plots (Dow, 1977) and extrapolated the vitritine profile to an Ro value of 0.2% to estimate the maximum thickness of overburden in each borehole location. They assumed the burial histories were correct and adjusted the heat flow against both present-day and paleo- thermal constraints. Their results are presented in Table 2.5 with other estimations.

2.5.3. Estimation of Sediment Removal with Diagenetic Models: Subsurface

I was able to test the accuracy of the predicted temperature and pressure models with the diagenetic parameters of IGV and quartz cement. First, I used data from the literature as initial values for the removed sediments and changed the thickness of the Tertiary strata to get a better fit to the thermal maturity parameters and pressure data for a given well. After all the adjustments, burial, temperature, and pressure histories were provided as inputs to the diagenetic models and the best fit scenario was selected as the representative burial reconstruction. Amounts of uplift were estimated by subtracting the present day depth of the units from their depth at maximum burial. The basin models I built and refined with the help of diagenetic models indicate deepest burial estimates at the base of Mesaverde Formation are 13,575 feet for the MWX, 13,067 feet for the Last Dance / O`Connell 31x wells, and 15,763 feet for the MF31-19G / T52-19G wells. Estimated removed overburden amounts are around 5,147 ft for the MWX, 5,068 ft for the Last Dance / O`Connell 31x and 3,157 ft for the MF31-19G / T52-19G wells. The burial histories reconstructed with other methods (stratigraphic inference, vitritine reflectance and basin modeling) are highly variable; the estimation of sediment removal

at the MWX well site ranges from 3800 to 6100 ft, and varies from 3700 to 9166 ft at the T51-19G / MF31-19G well sites. The comparison of the outcome of my approach and other approaches is given in Table 2.5.

The estimated amount of eroded section in the literature varies from 3800 ft to 6100 ft for the MWX well, from 3700 ft to 9167 ft for the MF31-19G well and 4400 ft near the Last Dance well location in the literature (Bostick and Freeman, 1984 (Ro); Nuccio and Roberts, 1992 (Vitrinite reflectance (Ro)-depth extrapolation to Ro of 0.2% - 0.3%); Wilson et al., 1998 (Apatite Fission Track, Ro, and fluid inclusions); Nuccio and Roberts, 2003 (Basin modeling); and Zhang et al., 2008 (Basin modeling by using Ro data from pyrolysis experiments). Using quartz cement as paleothermometer was helpful in pinning down the amount of erosion. My estimations of the maximum burial depth and removed overburden are respectively: 13,575 ft and 5,147 ft for the MWX, 13,067 ft and 5,068 ft for the Last Dance and 15,163 ft and 3,157 ft for the MF31-19G. My estimations are in agreement with method of Ro-depth extrapolation to Ro value of 0.3% and some of the basin models that use the measured Ro values from well sites. My estimation for the MF31-19G well has a large discrepancy with estimation of Zhang et al. (2008) for a nearby well (T52-19G). While building their basin models they used experimental Ro results from sealed gold tube pyrolysis tests as temperature constraints, and claimed that experimental results are not adequately predicted by the published Ro kinetics. However, their basin modeling results suggest much hotter thermal histories than what I predict with quartz cementation approach and also published Ro values.

2.5.4. Estimation of Sediment Removal with Diagenetic Models: Outcrop

A study of surface and near-surface vitrinite reflectance in the Piceance and Uinta Basins in order to investigate the development of these Laramide-aged (Late Cretaceous through Eocene) basins and uplifts were made by Johnson and Nuccio (1992). They stated that the extrapolation method (as explained in section 2.5.2) was difficult to apply because of removal of tens of thousands of feet of section at the uplifts and absence of subsurface vitrinite reflectance data due to scarce drilling activity near the outcrops. Additionally, they report problems associated with the use of surface vitrinite reflectance values; such as, reworking of the older vitrinite, oxidation during diagenesis or near surface weathering giving anomalously high readings. They also mention interpretation problems because of poorly constrained timing of events for burial history reconstruction, unknown lithology of the eroded section, and unrecognizable kinks in vitrinite reflectance profiles.

I applied the diagenetic modeling approach to get an estimate of the amount of sediment removed at the Rifle Gap outcrop (Figure 2.1). I used the R_o value of 0.66% for Cameo coal zone at the Rifle Gap area as a thermal constraint for burial reconstruction (R_o data from Nuccio and Roberts, 1992). I tried two different scenarios for the outcrop burial reconstructions:

Scenario 1: Uplift at 55 Ma immediately after reaching the deepest burial. This scenario was built following the Piceance Basin paleogeographic reconstructions of Johnson and Flores (2003) indicating that White River Uplift was already emerging during the latest Paleocene and earliest Eocene (approximately 55 Ma). A burial reconstruction suggested by Johnson and Nuccio (2003) also follows a similar burial

reconstruction scenario for a location near the White River Uplift in the northern Piceance Basin.

Scenario 2: Deepest burial reached around 50 Ma ago and uplift started around ~35 Ma. This scenario is developed in accordance with Verbeek and Grout (1984)'s paleogeographic reconstruction suggesting the formation of Grand Hogback at 34 Ma. I assumed the deepest burial reached at the base of the Williams Fork is ~8500 feet in **Scenario 2a**, and as ~7000 feet **Scenario 2b** (Figure 2.10).

The quartz cement calibration plot illustrates how *Touchstone*TM models performed on quartz cement predictions (Figure 2.10) with different burial reconstruction scenario inputs. Scenario 1 underpredicted the abundance of quartz cement in the sandstones from the Upper Williams Fork. Scenario 2b overpredicted the amount of quartz cement especially for the Lower Williams Fork interval. It appears that the scenario that gives the best prediction of quartz cement volume is Scenario 2a with 7000 ft. depth of burial at the base of Williams Fork.

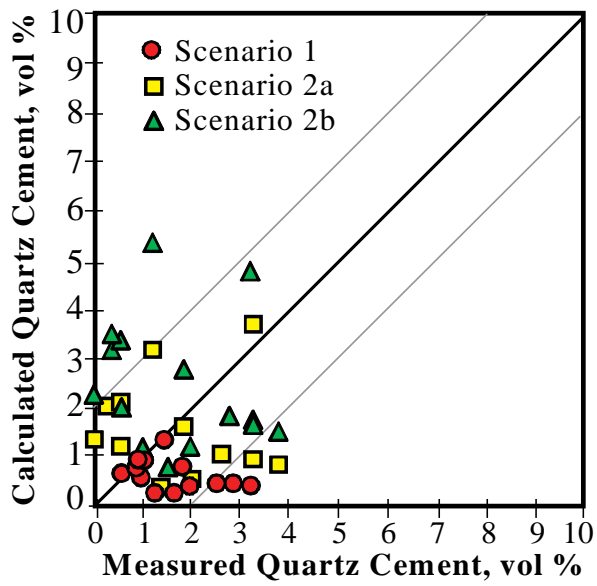


Figure 2.10. (A) Quartz cement calibrations for different burial history inputs at the Rifle Gap locality. Alternative burial and thermal history scenarios used for the calibrations are shown for the Cameo coal zone in Figure 2.10B.

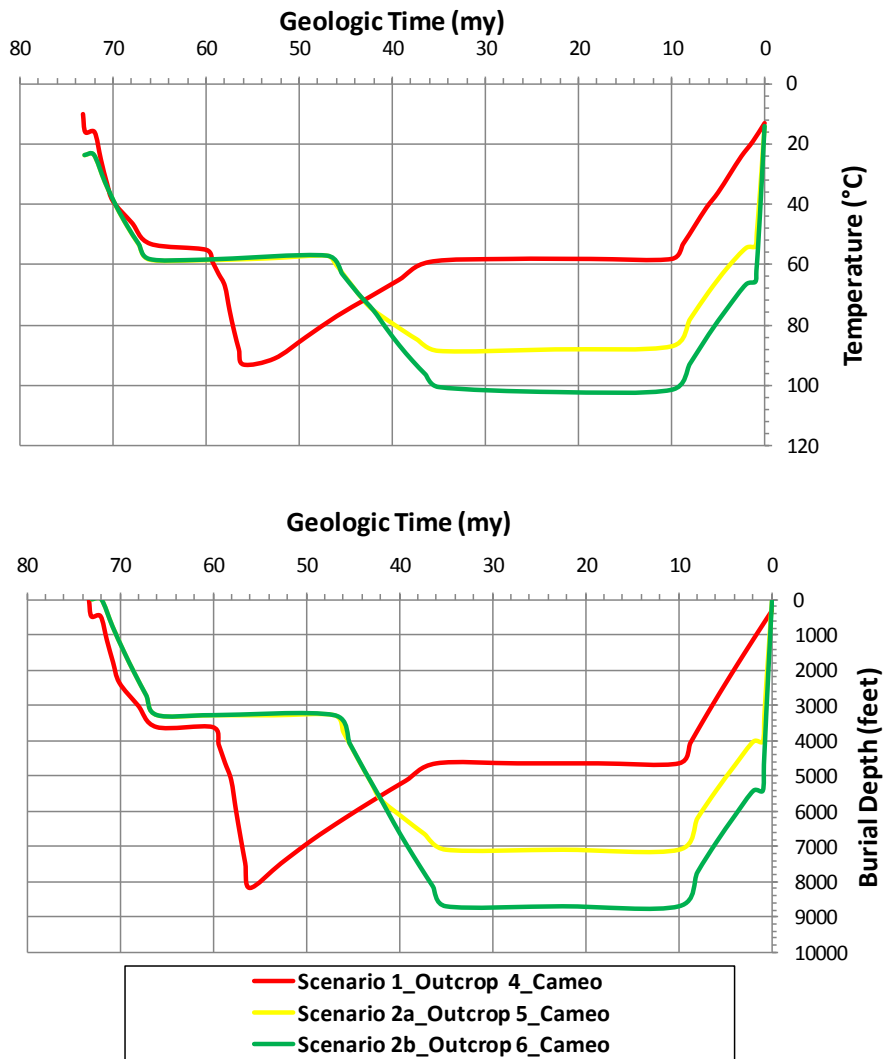


Figure 2.10. (B) Alternative burial and thermal history scenarios used for the calibrations are shown for the Cameo coal zone.

2.6. CONCLUSIONS: BASIN HISTORY ASSESSMENT WITH DIAGENETIC MODELING

In this chapter I used diagenetic models to constrain the erosional history of the Late Cretaceous Mesaverde Sandstones of the Piceance Basin. These sandstones underwent a deep burial and uplift cycle, but conventional burial history indicators do not unambiguously constrain the magnitude of burial and uplift or the timing of the event or events. Vitrinite reflectance indicates that maximum burial temperatures of 150 to 200 °C were reached and fluid inclusion homogenization temperatures suggest that the rocks reached temperatures of at least 140 to 180 °C and the actual temperatures the rock reached could be higher. Cooling below the annealing temperature of apatite occurred around 9 Ma in the subsurface according to the measurements at the MWX site. Although published estimates of the timing and amount of removed Tertiary overburden are highly variable (Table 2.5), these data were helpful in defining the initial input parameters (stratigraphic thickness, timing of the uplift etc.).

I petrographically analyzed the subsurface and outcrop Mesaverde sandstones and gathered modal analyses data (point count and textural data). I reconstructed various scenarios of burial at the study locations. I selected the burial scenario that led to best calibration of quartz cement model as the representative burial curve for a given locality. According to the models I developed, eroded Tertiary overburden is estimated to be around 5,100 feet for the MWX and Last Dance wells, 3,157 feet for the MF31-19G, and 3,000 feet for the Rifle Gap outcrop. The maximum burial depths at the base of Mesaverde are found to be 13,575 feet for the MWX well, 15,763 feet for the MF31-19G well, 13,067 feet for the Last Dance well, and 7000 feet for the outcrop at Cameo coal zone.

Accurate estimation of the Tertiary section is important for documenting the maximum depth of burial for the Williams Fork sandstones. Loading history controls the thermal exposure and pressure history which in turn influence the timing and amount of gas generation, overpressuring and resulting fracturing, and the evolution of quartz cementation which controls the rock mechanical properties and therefore fracture distribution. As stated in the introduction chapter, studies of these interactions show that diagenesis modifies mechanical stratigraphy (Marin et al., 1993; Laubach et al., 2009), fracture mechanics attributes (Rijken et al., 2002), fracture porosity and fracture porosity history (Laubach and Diaz-Tushman, 2009), the location and heterogeneity of patterns of open and sealed fractures (Laubach, 2003; Laubach and Ward, 2005), fracture system connectivity and permeability (Philip et al., 2005; Olson et al., 2009), fracture stiffness and propensity of fractures to close (Laubach et al., 2004a), and fracture seismic response (Marrett et al., 2007; Sayers et al., 2009).

Although using quartz cement model was helpful in narrowing the range of estimations for the removed Tertiary rocks, the approach has the limitation that finite pore space is available; once porosity is entirely occluded this gauge is insensitive to recording further thermal exposure unless other pore space becomes available (secondary pores, fractures). Therefore, quartz cementation can be useful when used in conjunction with other paleothermometers (such as vitrinite reflectance, fluid inclusions) in these deeply buried tight gas reservoirs. Progressive accumulation of quartz in fracture sets after the primary pore space is filled, has been documented and used to infer burial history conditions by Laubach and Ward, 2006 and Laubach and Diaz-Tushman, 2009.

Using diagenetic modeling approach for assessing basin history was helpful for constraining the burial history of the outcrop where thermal constraints are scarce (but not absent). Two possible scenarios were tested. Quartz cement volume predictions suggested that Scenario 2b with uplift around 35 Ma with maximum burial depths of 7000 feet is the most likely option. Although the limitation of available pore space for quartz precipitation was not a problem for the outcrop samples, presence of other cements such as kaolinite, calcite and Fe-oxide which could be related to outcrop weathering complicates the diagenetic story.

CHAPTER 3: PREDICTION OF LITHOFACIES AND RESERVOIR QUALITY USING WELL LOGS, WILLIAMS FORK FORMATION, MAMM CREEK FIELD, PICEANCE BASIN

3.1. INTRODUCTION: LITHOFACIES CLASSIFICATION

Gas production in the Piceance Basin is obtained mostly from discontinuous fluvial deposits of the Upper Cretaceous Williams Fork Formation. Understanding the controls and distribution of reservoir quality is important for the economic success of such tight-gas reservoirs in which diagenesis interacts with primary depositional variations in environment and texture to exert a strong control on pore networks, rock mechanical properties, and natural fractures.

Sandstone in the Williams Fork is feldspathic litharenite to litharenite cemented by varying amounts of quartz, calcite, Fe-dolomite, illite/smectite, chlorite, and sparse siderite, pyrite, Fe-calcite, kaolinite, sphene, zeolite, and gypsum. Framework grain composition is a major control on the degree of compaction and on the authigenic phases precipitated. Grain-coating clays are more common in the volcanic grain-rich Upper Williams Fork where alteration of these grains caused the precipitation of authigenic clays. Fe-dolomite cement is found only in the deeper marine-influenced intervals in which dolostone fragments are present. Compaction was more effective in the samples rich in micas, argillaceous grains, and low-grade metamorphic fragments.

I identified twelve lithofacies based on cement types, grain populations, and clay matrix content. The most common lithofacies are chlorite-cemented sandstones, illite/smectite-cemented sandstones, tightly calcite-cemented sandstones, tightly Fe-dolomite-cemented sandstones, clay matrix- or pseudomatrix-rich sandstones, quartz-

cemented sandstones and siltstones with mica-rich laminations, coarse-grained sandstones with thin detrital clay coats and abundant quartz cement (Ohio Creek samples), and quartz- and Fe-dolomite-cemented, hydrocarbon-stained sandstones with common dolostone, metamorphic and argillaceous rock fragments. Sandstones with the poorest reservoir qualities are tightly cemented with carbonates and quartz or are rich in clay matrix. The best reservoir quality sandstones are those with grain-coating clays which inhibited precipitation of quartz cement and preserved primary pores.

I correlated the lithofacies identified from petrographic observations to log responses to create a model that can be used to predict reservoir quality directly from well logs. Sandstones with the best reservoir quality can easily be identified based on low bulk-density log values. Intervals cemented with carbonates are identified by high bulk densities. Clay matrix- and mica-rich samples have high gamma-ray and bulk-density values. Presence of abundant potassium feldspars in the upper intervals results in high gamma-ray readings even in the clean (clay-matrix free) sandstones. This study suggests that careful petrographic assessment of lithofacies heterogeneity can be up-scaled by correlation with log properties to yield tools for field-scale reservoir quality prediction.

3.2. BACKGROUND INFORMATION ON FACIES CLASSIFICATION

The Upper Cretaceous Williams Fork Formation of the Mesaverde Group is the most important tight gas producer in the Piceance Basin, Colorado (Figure 3.1). Effective resource exploitation requires comprehensive reservoir description and characterization to quantify gas in place and to identify the reservoir properties that control production in such diagenetically heterogeneous sandstones.

Aspects of Mesaverde diagenesis have been described by Eatough (1983), Pitman and Sprunt (1986), Crossey and Larsen (1992), Hansley and Johnson (1980), Pitman et al. (1989), and Pollastro (1984). However, diagenetic variations have not been correlated previously with core petrophysics and well-log response. The Williams Fork is composed of tightly cemented, very fine- to medium-grained, lithic-rich sandstones, siltstones and mudrocks deposited in fluvial to coastal-plain settings. The reservoir is characterized by low klinkenberg permeabilities (geometric mean: 0.025 mD; range: 0.001–1.87 mD) and low measured helium porosities (average: 6.46%; range: 1.98 – 14.7%) in the study well. The average core porosity value for the study well is lower than the log-derived porosity representative of the Williams Fork in the Mamm Creek field, which is around 9%. The observed range in reservoir quality in the Williams Fork reflects the variable diagenetic histories across primary variations in provenance (grain composition), depositional systems, and textures. Most of the intergranular pore space is lost to cementation by varying amounts of quartz, calcite, Fe-dolomite, mixed-layer illite/smectite, and chlorite, and sparse siderite, pyrite, ferroan calcite, kaolinite, sphene, zeolite, and gypsum. Porosity consists mainly of micropores, along with minor primary intergranular pores, secondary intragranular pores, and rare fracture pores. Natural opening-mode fractures and small faults are present and locally abundant in core (Lorenz and Finley, 1991; Hooker et al., 2009). Fractures have a wide range of sizes and most contain deposits of quartz and/or calcite and locally clay minerals (Lorenz and Finley, 1991; Laubach, 2003).

Core samples and cuttings are used in determination of subsurface lithology. However, in most cases, high cost allows coring within only a limited part of the total drilled interval. It is very likely that a cored interval does not represent all of the

lithologies in a well. Well logs, on the other hand, provide a continuous survey of the well interval. By studying rock types in an extensively cored well and translating these facies to log responses, it is possible to generate a model that can be used to predict the likely lithofacies in nearby wells in a given field. The study well used here provides an excellent opportunity for such an approach, because all sandstone intervals were cored and thin sectioned (400.5 ft core with 275 thin sections), and laboratory measurements of petrophysical properties were obtained. Lithofacies were identified by systematic description of the petrographic features. Reservoir qualities of different lithofacies were determined from the core analysis data. The lithofacies were then correlated with their well-log signatures.

Lithofacies are defined as mappable stratigraphic units, laterally distinguishable from the adjacent intervals based upon lithologic characteristics such as mineralogical, petrographical, and paleontological signatures that are related with the appearance, texture, or composition of the rock (Porras et al., 1999 and Perez et al., 2003), *petrofacies* are intervals of rock with similar average pore throat radius, thus having similar fluid-flow characteristics (Porras et al., 1999), and *electrofacies* are similar log responses that characterize a specific rock type and allow it to be distinguished from other rocks (Perez, et al., 2003). Rushing et al. (2008) emphasized the importance of pore-scale description of tight gas reservoirs and suggested a rock-typing work-flow with *depositional* (core-based descriptions of genetic units), *petrographic* (pore-scale descriptions) and *hydraulic* (physical flow and storage properties) approaches. I use a similar approach.

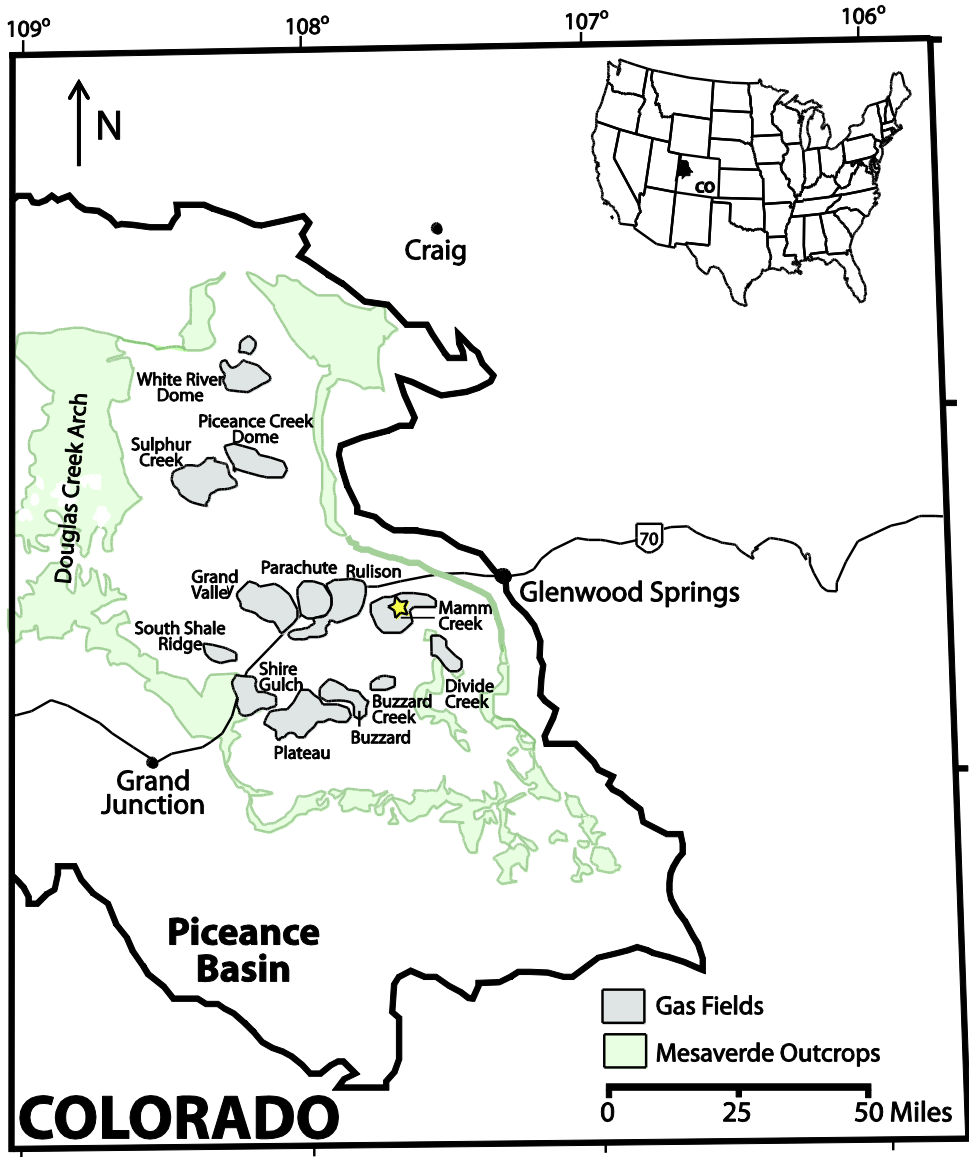


Figure 3.1. Map showing important gas fields in Piceance Basin. The study well (shown with a star) is located in the Mamm Creek field, Garfield County, Colorado (modified from Johnson and Roberts, 2003).

I evaluate the possibility of predicting core-derived porosity and permeability from log-derived porosity. I also determine the most characteristic log types for building an algorithm for field scale application of lithofacies and reservoir quality prediction

model. Sedimentary structures, grain size, sorting, and amount of clay matrix, which are reflections of the depositional environment and provenance, have control over depositional pore structures. During the course of burial, diagenetic events including compaction, precipitation, and dissolution modify the original pore system. In tight gas reservoirs diagenetic modification such as extreme physical compaction and extensive cement deposits can obscure the depositional imprints. Yet in the Williams Fork sandstones, despite deep burial and high temperatures reached, relict pore systems that reflect detrital grain assemblages and depositional setting still clearly influence pore geometry. Therefore, in this paper I build a classification encompassing not only pore-filling phases and pore types, but also the distribution of framework grains. Although, my detailed *petrographical* approach falls into lithofacies classification as defined by Rushing et al. (2008), it also has implications to pore network (*hydraulic*) characteristics as the rock types were defined with their petrophysical features (porosity and permeabilities).

3.3. DEPOSITIONAL HISTORY OF THE WILLIAMS FORK FORMATION

The Late Cretaceous Mesaverde Group is composed of the Iles and Williams Fork formations (Figure 3.2). The Iles Formation, 100 to 400 m (328 – 1312 ft) thick, overlies the marine Mancos Shale and includes regressive marine sandstone cycles of the Corcoran, Cozzette, and Rollins members which are separated by tongues of marine Mancos Shale. The sandstones in these cycles are laterally continuous and can be correlated across much of the southern and eastern Piceance. The Williams Fork Formation, 700 to 1500 m (2297 – 4921) thick, is composed of coastal plain, fluvial and

flood-plain deposits. In the southeastern part of the Piceance Basin, marine sandstones are also present above the Rollins; the informally named Upper and Middle Sandstones of the Williams Fork were deposited as regressive cycles following the transgression of the Rollins coastline westward. The rest of the Williams Fork, including Ohio Creek Member, was deposited as non-marine sequences. Stratigraphy of the Mesaverde Group is presented by Johnson and May (1980), Johnson (1989), Cole and Cumella (2003), Hettinger and Kirschbaum (2003), and Pranter et al. (2007).

3.4. METHODS FOR LITHOFACIES CLASSIFICATION

A total of 122 meters (400.5 feet) core from the Williams Fork Formation was available from the study well located in Mamm Creek field, Piceance Basin (Figure 3.1). The cores were collected between 853 and 1926 meters (2800 and 6321 ft) at 11 different intervals representing Ohio Creek, Upper Williams Fork, and Lower Williams Fork units (including Upper and Middle Sandstone Members and Cameo interval deposits, Figure 3.3). 275 thin sections were available for petrographic analyses. Thin sections were stained with sodium cobaltnitrite for potassium feldspar and alizarin red and potassium ferricyanide for carbonate identification.

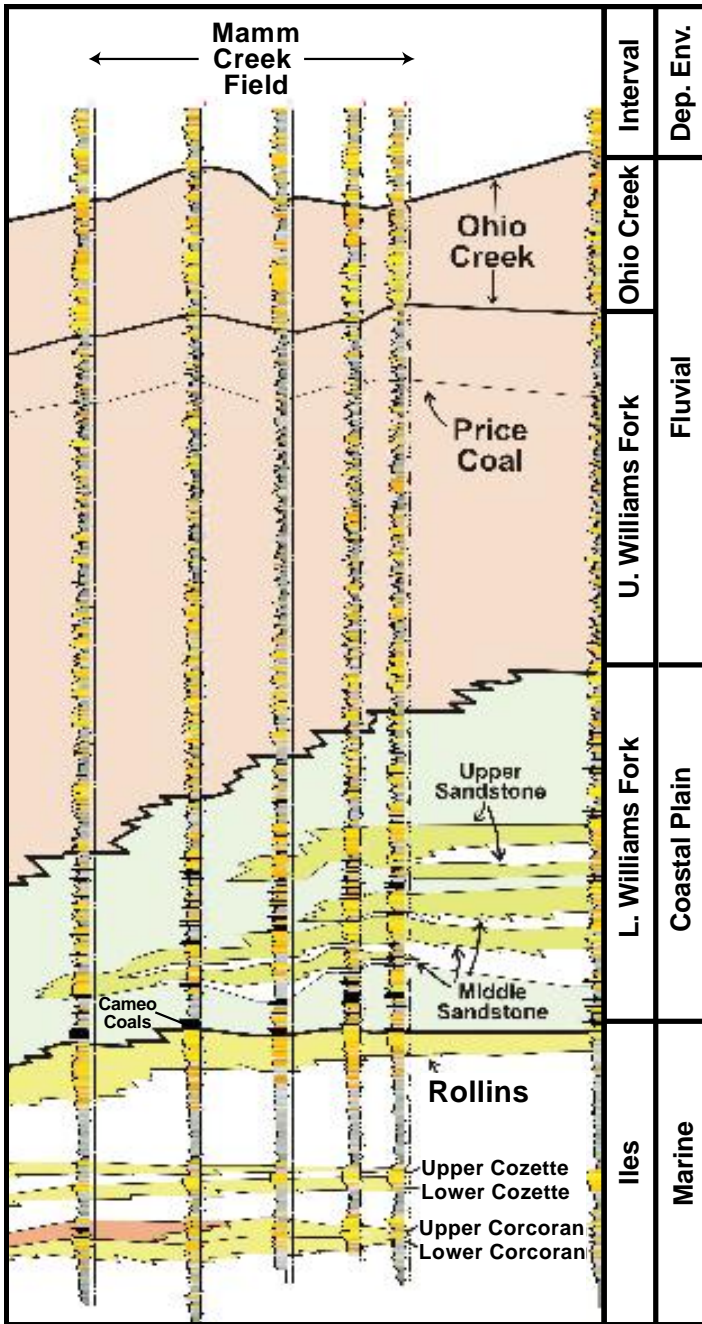


Figure 3.2. Stratigraphic column showing the distribution of Mesaverde depositional environments in the southern Piceance Basin (modified from Cumella and Scheevel, 2008). Fourth well from the right is the approximate location of the study well.

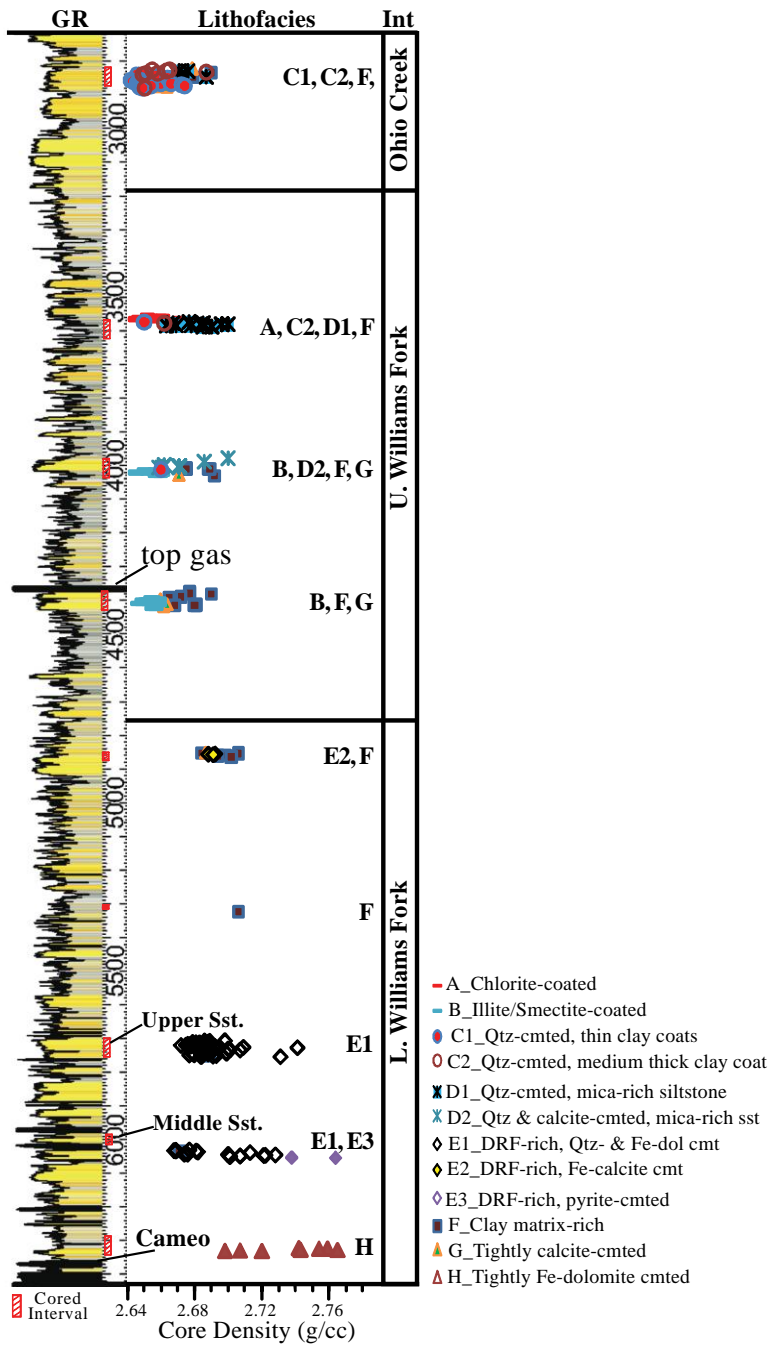


Figure 3.3. Distribution of Williams Fork lithofacies and their core-measured densities at different intervals of the study well. Cored intervals shown in red in the depth track of the log. Gamma ray log is color filled to show sandstones (yellow), shales (gray), and coals (black).

I point-counted twenty-two representative samples (400 points / slide) with conventional petrographic microscope to determine framework grains, cement types, clay-matrix content, and pore types. I examined the selected samples with JEOL JSM-6490 LV scanning electron microscope (SEM) with an energy-dispersive X-ray system (EDS), a cathodoluminescence (CL) detector attached to a Philips XL30 ESEM, and a JEOL JXA-8200 electron microprobe for determining cement distribution and composition. I measured grain size on the long axis of 100 randomly selected grains in each thin section.

Routine core analyses (permeability, porosity, and grain density) performed at 800 psi net effective stress were obtained for 257 samples by Core Laboratories. Core description was available from Discovery Group. A log suite, comprising dual-induction, gamma-ray, bulk-density, compensated-neutron, borehole-compensated sonic, spontaneous-potential, and image logs, was acquired which allowed the correlation of thin-section observations, core analyses data, and reservoir quality of lithofacies with log response.

3.5. FRAMEWORK COMPOSITION AND TEXTURE OF THE WILLIAMS FORK SANDSTONES

The Williams Fork sandstones are mostly lower fine-grained (average 165 μm), well-sorted (average $\sigma = 0.49$) lithic-rich sandstones. Grain size ranges from silt-size (44 μm) to coarse-grained sand (376 μm) and the sorting ranges from very well ($\sigma = 0.33$) to poorly-sorted ($\sigma = 1.47$). The composition varies from lithic arkose to litharenite according to Folk's classification scheme (1980). The average composition is $Q_{51.2}F_{14.8}L_{33.9}$ (Figure 3.4). Monocrystalline quartz with straight to slightly undulose

extinction is the dominant grain type. Both potassium feldspar and plagioclase are present. Potassium feldspars are mostly microcline to perthite. Extensive mechanical deformation by compactional grain crushing is clearly observed in the coarse-grained feldspars of the shallower intervals. Both twinned and untwinned varieties of plagioclase are present. Both potassium feldspars and plagioclases show varying degrees of sericitization and dissolution. Potassium feldspar constitutes 70 - 90 of the feldspar content in the upper Williams Fork interval and constitutes only 8 - 71% in the lower Williams Fork. The Williams Fork sandstones are lithic-rich but the type and abundance of lithics vary at different intervals. Lithic populations include granitic, volcanic, low-grade metamorphic (mostly phyllite), schist, argillaceous, chert, dolostone, and rare limestone and quartzite fragments. Accessory minerals include biotite, muscovite, and heavy minerals. Heavy minerals include garnet, zircon, sphene, tourmaline, opaques, epidote, and Fe-oxides. Elongated fragments of organic material are present mostly in the finer-grained, matrix-rich intervals. All of these accessory minerals are found most commonly as concentrations parallel to bedding planes. Trace to minor amounts of glauconite, phosphatic grains, and fossil fragments are observed in the marine-influenced intervals.

Provenance and depositional setting appear to control the distribution of framework grains at varying intervals (Figure 3.5A - C). Feldspars are common (11.5 - 28%) in the upper fluvial intervals and minor to moderate (2.8 - 8.3%) in the rest of the section (Figure 3.4). Volcanic and granitic grains and large biotite grains (up to 0.5 mm in size) are more common in the upper Williams Fork (Figure 3.5A). A shift in the provenance to igneous rocks (granitic, andesitic, and rare porphyritic felsic types and

coarse biotite flakes) in the southeast Piceance Basin was also pointed out by Hansley and Johnson (1980) in their study of outcrop and core samples of the Ohio Creek member of Upper Williams Fork interval. Laminations defined by small muscovite and biotite grains are most commonly observed within crevasse-splay deposits of the fluvial Upper Williams Fork.

Dolostone grains (DRFs) are present below 1478 meters (4850 ft) where the depositional environment is marine-influenced. This suggests an intrabasinal source for dolostone fragments. Cumella (1981) also observed occurrence of DRFs in vertical successions related to marine facies in his study of the Pictured Cliffs sandstones. Presence of DRFs in over 40 Western Interior Cretaceous formations was reported by Sabin (1962). A change in the provenance is also a possibility on the distribution of DRFs.

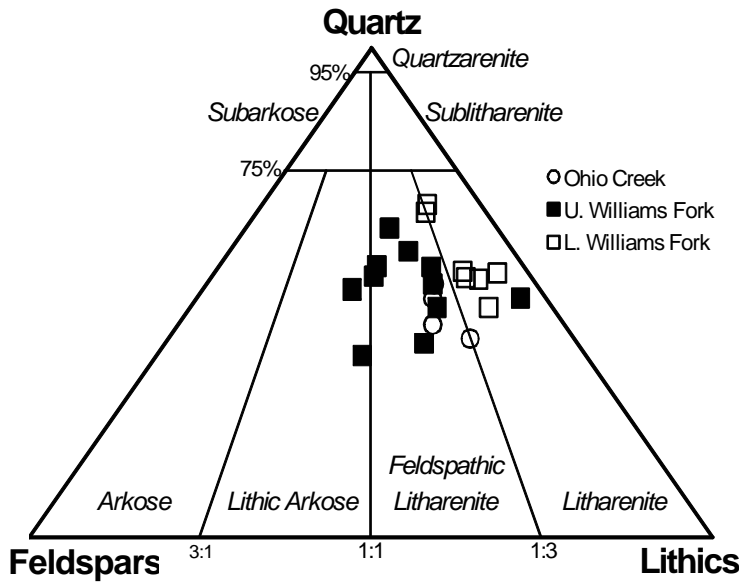


Figure 3.4. Ternary diagram illustrating detrital composition of sandstones based on ratios of detrital quartz, feldspar, and lithic fragments (Q:F:L). Sandstone clans are designated according to the classification of Folk (1980).

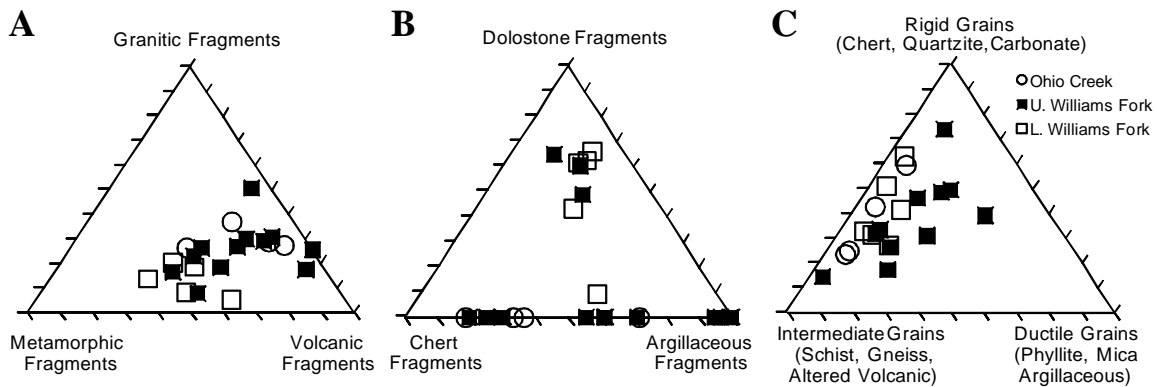


Figure 3.5. Distribution of rock fragments in the Ohio Creek, Lower Williams Fork and Upper Williams Fork intervals: (A) Crystalline fragments. (B) Sedimentary fragments. (C) Rock fragments according to their rigidity.

3.6. DIAGENESIS OF THE WILLIAMS FORK SANDSTONES

3.6.1. Compaction

Compaction resulted in deformation of ductile grains and fracturing of rigid grains (Figure 3.7E). Compaction is more penetrative where ductile grains (argillaceous fragments, phyllite, micas, and glassy volcanic fragments) are abundant. Extensive compaction on argillaceous fragments and low grade metamorphic grains resulted in formation of pseudomatrix. The IGV (Intergranular Volume) is reported as a percentage of the rock volume and is the sum of detrital matrix, primary porosity, and the volume of cement that fills primary pore space (Paxton et al., 2002). In the absence of detrital matrix, IGV is equivalent to pre-cement porosity. A plot of cements vs. IGV indicates most of the IGV is contributed by cements and contribution by primary pores is minor (Figure 3.6A). Ductile components (micas + phyllite + argillaceous clasts) as a percentage of the whole rock have a rough negative correlation with IGV which indicates the importance of compaction in porosity loss (Figure 3.6B).

IGV, compactional porosity loss (COPL) and cementational porosity loss (CEPL) are calculated from the point-count data following established conventions (Paxton et al., 2002; Lundegard, 1992; Ehrenberg, 1995). The COPL and CEPL are calculated from the assumed initial porosity, $P_i = 40\%$, the IGV, and the volume of cement, C , that fills primary porosity. Index of compaction (Icomp) is the ratio of compactional porosity loss to total porosity loss (I comp). I comp values are greater than 0.5 for all samples, and highest for the Upper Williams Fork samples (Figure 3.6C). As shown in Figure 3.4C, Upper Williams Fork samples have the greatest ductile lithic component.

$$CEPL = \left[(P_i - COPL) \times \frac{C}{IGV} \right] \quad (\text{equation 3.1; Ehrenberg, 1989})$$

$$COPL = P_i - \left\{ \frac{[(100 - P_i) \times IGV]}{100 - IGV} \right\} \quad (\text{equation 3.2; Ehrenberg, 1989})$$

$$I_{comp} = \frac{COPL}{COPL + CEPL} \quad (\text{equation 3.3; Lundegard, 1992})$$

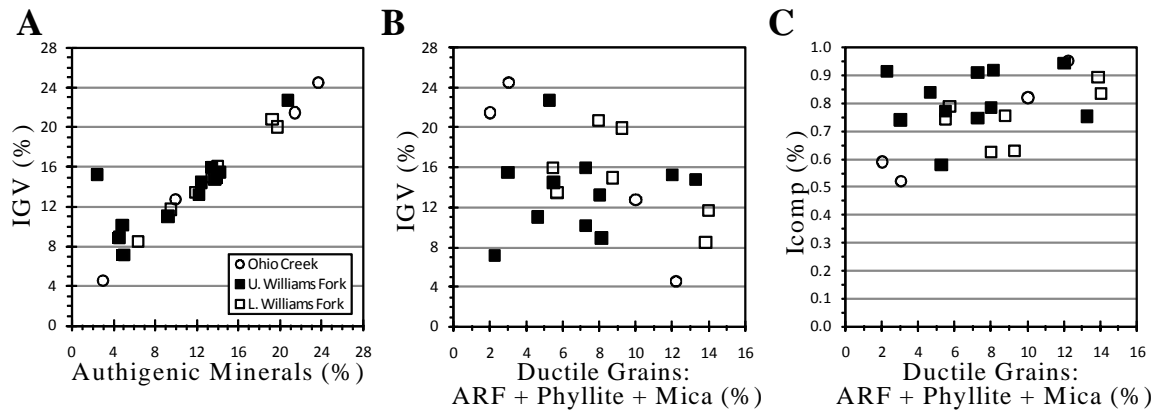


Figure 3.6. (A) Most of the intergranular volume (IGV) is contributed by authigenic minerals, contribution from primary pores and matrix is minor. Evidence of control on compaction by the content of ductile detrital components: intergranular volume (IGV) is lower where ductile grain content is highest (B) and compaction index (I_{comp}) is greatest for the ductile grain-rich samples (C). (ARF: Argillaceous Rock Fragments).

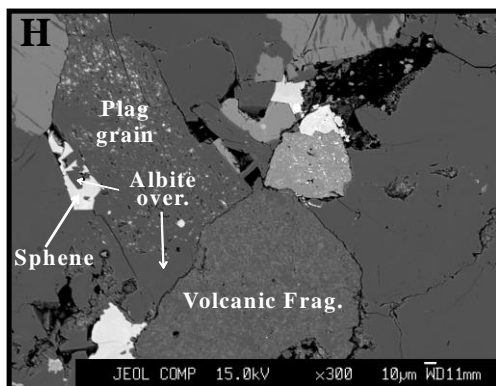
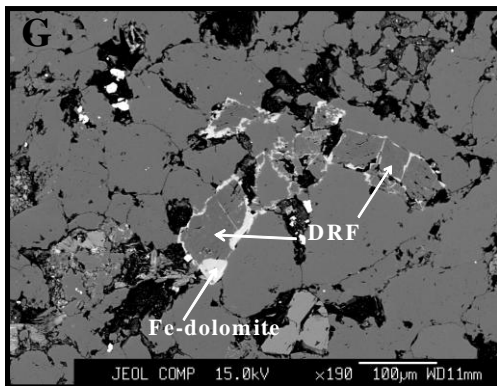
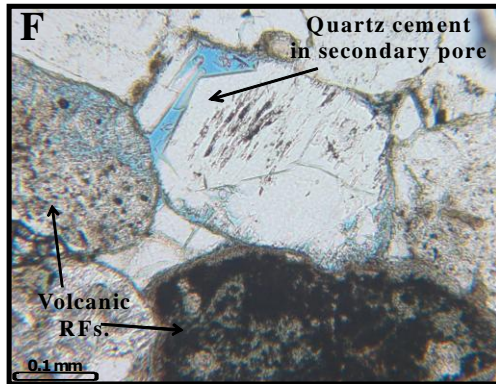
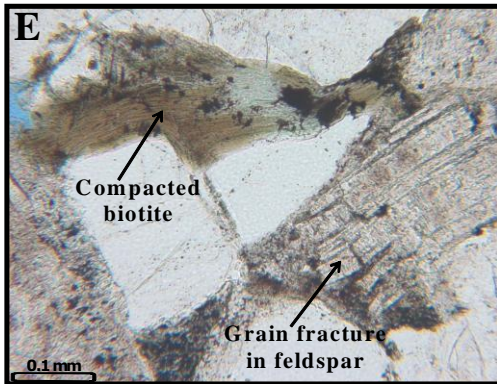
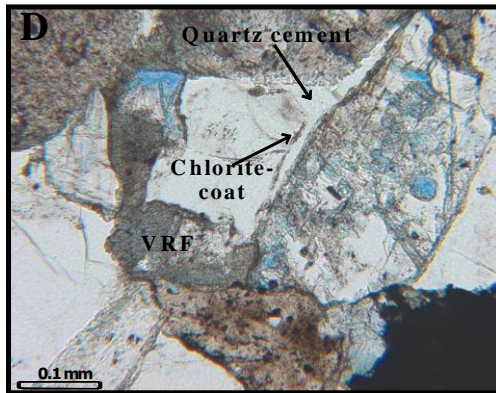
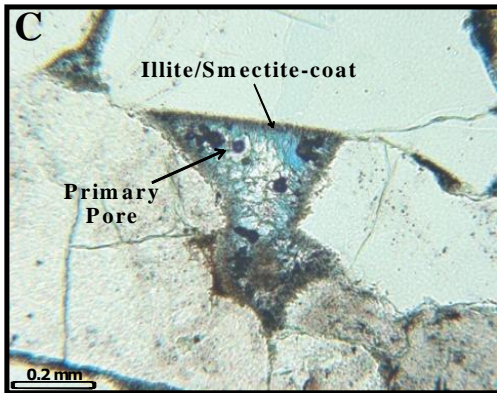
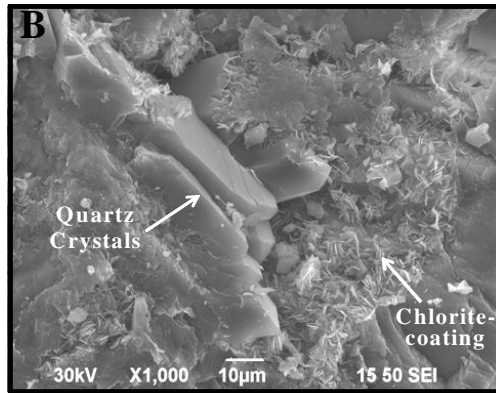
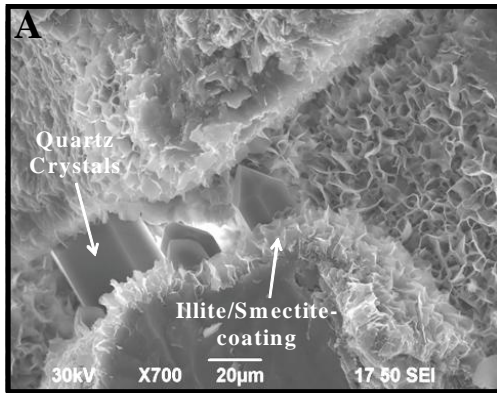


Figure 3.7. (A) SEM image showing pore-lining illite-smectite (I/S) with honeycomb morphology. Quartz cementation was inhibited due to thick I/S-coats; quartz was able to grow as small crystals where there is break in the clay coats. Sample depth = 4016 ft. (B) SEM image showing plates of chlorite cement lining the pores were not as effective inhibiting quartz cementation. Quartz crystals were able to grow larger. Sample depth = 3562 ft. (C) Well preserved primary pore in the I/S-coated sandstones (blue color represents epoxy-filled pore space). Sample depth = 4016 ft. (D) Chlorite-cemented sample with more quartz overgrowths. Note the chloritized volcanic rock fragment (VRF). Sample depth = 3562 ft. (E) Compaction resulted in deformation of ductile grains and fracturing of rigid grains. (F) Quartz cement is growing into a secondary pore formed by dissolution of a feldspar grain. Volcanic fragment in the mid-right position is felsitic and bottom-center is glassy. (G) Backscattered image showing Fe-dolomite cement forming overgrowths around detrital dolomite (DRF). Sample Depth = 5733 ft. (H) Sphene is found as authigenic mineral in the primary and secondary pores. Note that sphene encloses albite and pyrite crystals indicating that it postdates these two phases. Sample Depth = 3561 ft.

3.6.2. Authigenic Minerals in Pores and Fractures

The most common cements are quartz overgrowths, grain-coating clay minerals (mixed-layer illite/smectite, I/S and chlorite) and calcite, along with trace to minor amounts of potassium feldspar overgrowths, albite, pyrite, titanite, Ti-oxide, zeolite, and gypsum (Figure 3.7A-H). In this core, calcite cement is volumetrically the main constituent of fracture-fills. Minor amounts of quartz crystals that grew as veneers along the fracture walls are also present. Quartz cement entirely fills only microfractures (width less than 0.1 mm) and hair-line (width less than 0.33 mm) macroscopic fractures.

SEM analyses reveal that illitic clays and chlorite occur in the form of grain-coats and grain-replacements (Figure 3.7A & B). Illitic clays additionally occur as pore-bridges and pore-fills. Where clay coats are abundant, they inhibited the precipitation of quartz overgrowths and preserved the intergranular pore space. In the study well I/S grain-coats were more effective than chlorite-coats in preventing quartz cementation because they were thicker and more continuous (Figure 3.7A-D).

Quartz cement mostly forms as large euhedral overgrowths. If grain-coating clays are thick and continuous, quartz cement does not precipitate due to lack of nucleation sites. If there are breaks in the grain-coat, quartz grows as small prismatic crystals through the breaks in the coat. Prismatic quartz crystals are also observed in secondary pores. Free standing quartz crystals within calcite cement indicate a later-stage calcite phase postdating the precipitation of quartz cement. An interesting observation in the clay-coated intervals was growth of quartz cement not in optical continuity with the

quartz grain (not syntaxial). This might be due to growth of a large overgrowth of quartz cement nucleated on a grain that is out of the plane of the thin section.

Calcite cement mostly forms as sparse pore-fills and grain-replacements. Locally, it makes about half of the total rock volume in the form of poikilotopic crystals. In the extensively calcite-cemented zones, some of the grains are totally replaced by calcite leaving remnant outlines (dust lines or clay coats) within the cement. Calcite cement picks up light purple stain in the transition zone from lowermost fluvial intervals to coastal plain environment which indicates presence of Fe-calcite.

In order to understand the distribution patterns of calcite cement, the intervals adjacent to extensively calcite-cemented samples ($\frac{1}{2}$ -1 foot above or below) were examined. Mostly the abundance of calcite cement drops from extensive amounts to minor amounts in the adjacent samples. This suggests that calcite cement has a highly localized distribution, confined to thin beds or concretions.

Fe-dolomite does not form large poikilotopic cement deposits, but occurs in small discrete areas (20-70 μm). It is mainly in the form of rhombic overgrowths around dolostone rock fragments (DRFs). Compositional zoning (Fe-rich / Fe-poor) in the overgrowths are locally observed by backscattered electron (BSE) imaging. Fe-dolomite is also found as grain replacement. Rhombic crystals of dolomite replacing chert grains are observed which probably is inherited from the source area. Detrital grains of dolostone can be easily identified from Fe-dolomite overgrowths with the help of carbonate-stain and with the help of BSE images where DRFs exhibit sub-rounded shapes and contrasting Fe-poor compositions compared to the overgrowths (Figure 3.7G).

Hydrocarbon in the form of dead oil is observed in the coastal-plain deposits which are the organic material-rich intervals. Dead oil is reported within fractures in the nearby Rulison field (MWX wells) along with quartz, calcite, and locally, clay minerals (dickite) by Eatough (1982) and Lorenz and Finley (1991).

Grain replacing phases include albite, titanite, pyrite and siderite; as they form in trace amounts they are not major factors in reservoir quality reduction.

3.6.3. Controls on Diagenesis: Provenance

The provenance of the Williams Fork is an important influence on the path of diagenesis. Authigenic clay minerals are more common in the volcanic grain-rich, upper fluvial deposits (Figure 3.8). The clays probably formed by alteration and breakdown of the volcanic fragments (Figure 3.7D & 3.7F). Amount of clay coats present affected, in turn, the degree of quartz cementation owing to inhibition of quartz precipitation by grain-coats.

Two different types of clay coats are observed within the fluvial interval, only 152 m (500 ft) apart from each other (Figure 3.8). Chlorite-coats dominate the sandstone interval around 1066 m (3500 ft) and I/S-coats dominate the sandstones close to 1219 m (4000 ft). Sandstones rich in biotite, feldspar, felsic volcanic (?), and granitic rock fragments contain chlorite; in contrast, samples rich in glassy volcanic fragments have I/S cement precipitated. As these intervals are only 152 m (500 ft) apart from each other, temperature is not a likely control. More likely, contrasting alteration of different framework constituents has the largest influence on this diagenetic difference.

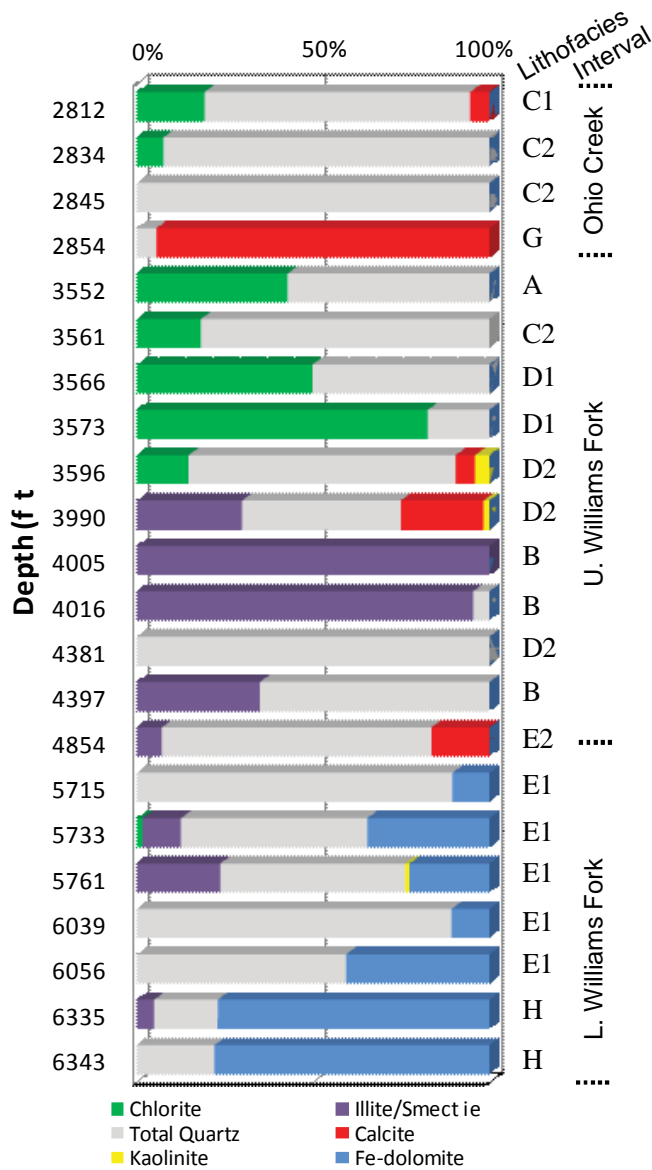


Figure 3.8. Distribution of authigenic minerals at different Williams Fork Intervals (authigenic mineral components are normalized to 100%). Grain-coating clays are chlorite in the shallower intervals and illite/smectite in the deeper intervals. Amount of quartz cement varies with the abundance, thickness, and continuity of the clay coats. Fe-dolomite cement is present in the marine-influenced Lower Williams Fork interval.

3.6.4. Controls on Diagenesis: Depositional Environment

In this set of samples, I observed Fe-dolomite cement only in the coastal-plain deposits (Figure 3.7) where detrital dolostone fragments (DRFs) are present. These DRFs could be intrabasinal clasts; contributed by reworking of dolomitic hardground crusts. These fragments act as nucleation sites for Fe-dolomite cement. The amount of Fe-dolomite cement generally correlates positively with the amount of DRFs in this set of Williams Fork samples (Figure 3.9). Dolostone fragments may be a necessary substrate for precipitation of Fe-dolomite as indicated by absence of Fe-dolomite cement in sandstones having no DRFs. Crossey and Larsen (1992) noted close spatial association of pervasive Fe-dolomite with high organic contents in the paludal intervals in the neighboring Rulison field, suggesting that organic acids might facilitate Fe-dolomite cement.

3.7. PORE TYPES AND DISTRIBUTIONS

Porosity consists mainly of micropores, along with minor primary intergranular and secondary intragranular pores (Figure 3.10A & B). Comparison of thin section macroporosity with core helium porosity indicates that micropores make up 67-100% of the total porosity (Figure 3.11A & B). Micropores are associated with authigenic and detrital clays, argillaceous, metamorphic, and altered volcanic grains. Presence of grain-coating, pore-bridging and pore-filling authigenic clays narrows the pore throats and reduces the intergranular pore space. However, where they are present in the form of grain coats they inhibited precipitation of quartz overgrowths, and preserved intergranular pore space. Sandstones with the highest porosities are the ones with relatively thick and continuous grain-coating clays. Lowest porosities are associated with

sandstones tightly cemented with carbonates or rich in clay matrix. Secondary intragranular to moldic pores were formed mainly by the dissolution of feldspar grains (Figure 3.7D). Intragranular pores are rarely observed within chert, volcanic, and metamorphic grains.

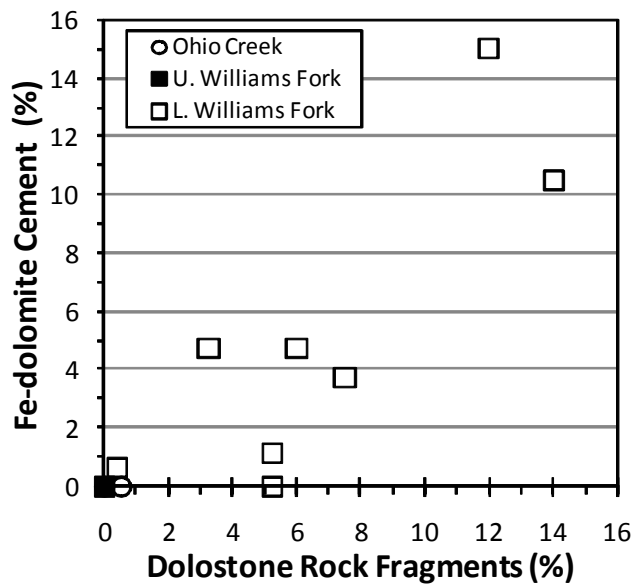


Figure 3.9. Abundance of Fe-dolomite cement and Dolostone Rock Fragments (DRFs) correlates positively.

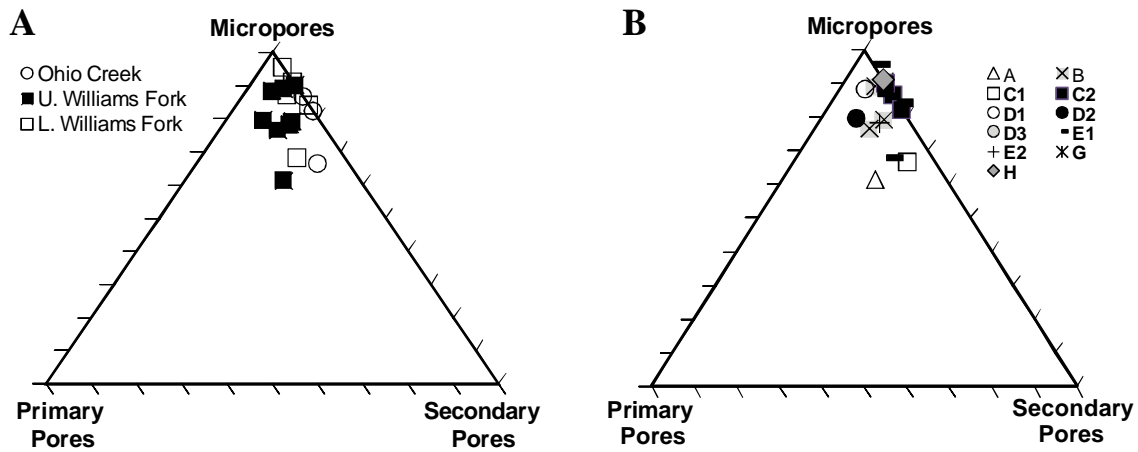


Figure 3.10. Distribution of pore types between (A) Ohio Creek, Upper Williams Fork and Lower Williams Fork intervals and (B) Williams Fork lithofacies. Micropores = core-measured porosity – total visible point-count porosity.

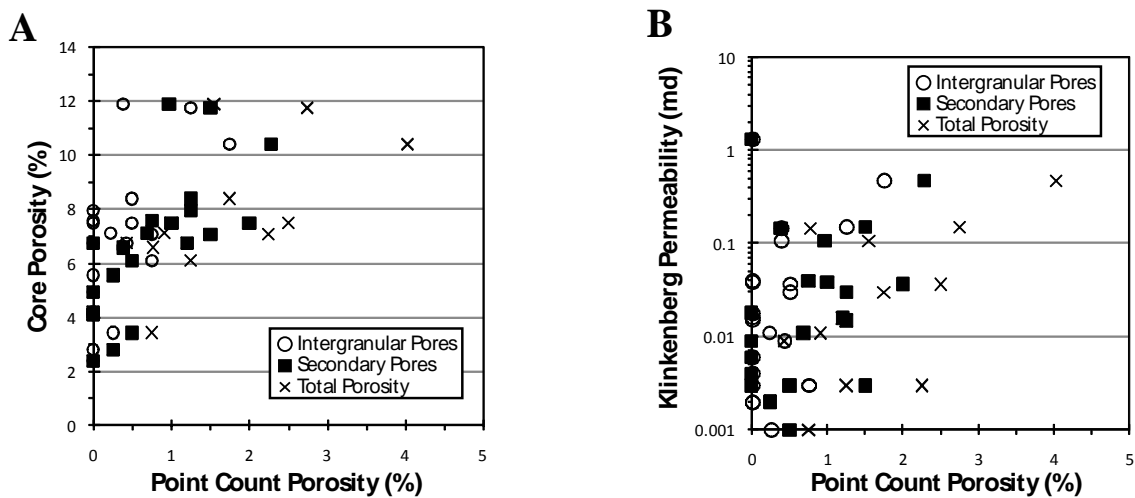


Figure 3.11. (A) Comparison of point-count porosity with core-measured porosity. (B) Plot showing the relationship between point-count porosity and permeability. The low permeability values are due to abundance of micropores.

Point count and core-measured porosities are lower in the marine-influenced Lower Williams Fork deposits compared to most of the samples in the fluvial intervals. Coastal plain deposits are tightly cemented with Fe-dolomite and/or quartz cements which are not microporous; they also lack the microporosity contributed by grain-coating clays and some of the microporous framework grains that are present in the fluvial sections.

3.8. RESERVOIR QUALITY

The quality of a reservoir is a function of both its porosity and permeability. In tight gas sandstones reservoir quality reflects initial sediment composition and subsequent modification. Modification typically includes physical and chemical compaction, cement deposits and dissolution, and fracturing. In my study to assess porosity and permeability routine core analysis data measured at 800 psi net effective stress were available for 257 samples. The mean (geometric) klinkenberg permeability of the sandstones is 0.025 mD (range: 0.001 – 1.87 mD) and average helium porosity is 6.46% (range: 1.98 – 14.7%). The low permeability is mainly due to micropores dominating the pore system as confirmed by petrography and SEM studies. Only four samples have permeabilities greater than 1 mD and two of them were fractured samples (Figure 3.12). In a given lithofacies fractured samples exhibit permeabilities that are as much as an order of magnitude greater for a given porosity than the average. Although the fractures in these samples may be artifacts of sample handling, their effects are comparable to those expected from natural fractures in the subsurface (Philip et al., 2005).

3.8.1. Diagenetic Controls on Reservoir Quality

Although measured core porosities are lower in the chlorite-coated sandstones, they have slightly higher permeability values compared to I/S-coated sandstones (Figure 3.12). This variation is due to differences in their pore networks. In the chlorite-cemented zones, where the coats are thinner and discontinuous, more quartz cement was able to precipitate reducing the primary pore space relative to I/S-cemented sandstones with thicker and more continuous coats (Figure 3.7A-D). Although the pores in the I/S-cemented zones were spared from the precipitation of quartz cement, I/S cement locally formed as pore-bridges and pore-fills in the available pore space reducing the size of the intergranular pores and turning them into micropores. In contrast, chlorite cement formed only as grain-coats, as a result primary pores are “cleaner” in the chlorite-cemented zones. In addition, due to their high surface area compared to chlorite cement, I/S tend to reduce the permeability more effectively.

3.8.2. Textural Controls on the Reservoir Quality

The porosity and permeability values tend to be higher in the coarser-grained sandstones (Figures 3.13A & 3.13B). The wide variation is due to diagenesis changing the initial pore network controlled by grain size distribution which is mainly linked to the energy of the depositional environment. The sandstones with grain-coating I/S and chlorite do not fit to this general trend, because in these sandstones the reservoir quality is controlled by the amount and continuity of the grain-coating clays that inhibit quartz precipitation.

Crevasse splay deposits are dominated by siltstone and sandstones with abundant clay matrix or siltstones with mica-rich laminations. Permeability is low in sandstones with abundant clay matrix. Reservoir quality is also low in the sandstones and where compaction was penetrative.

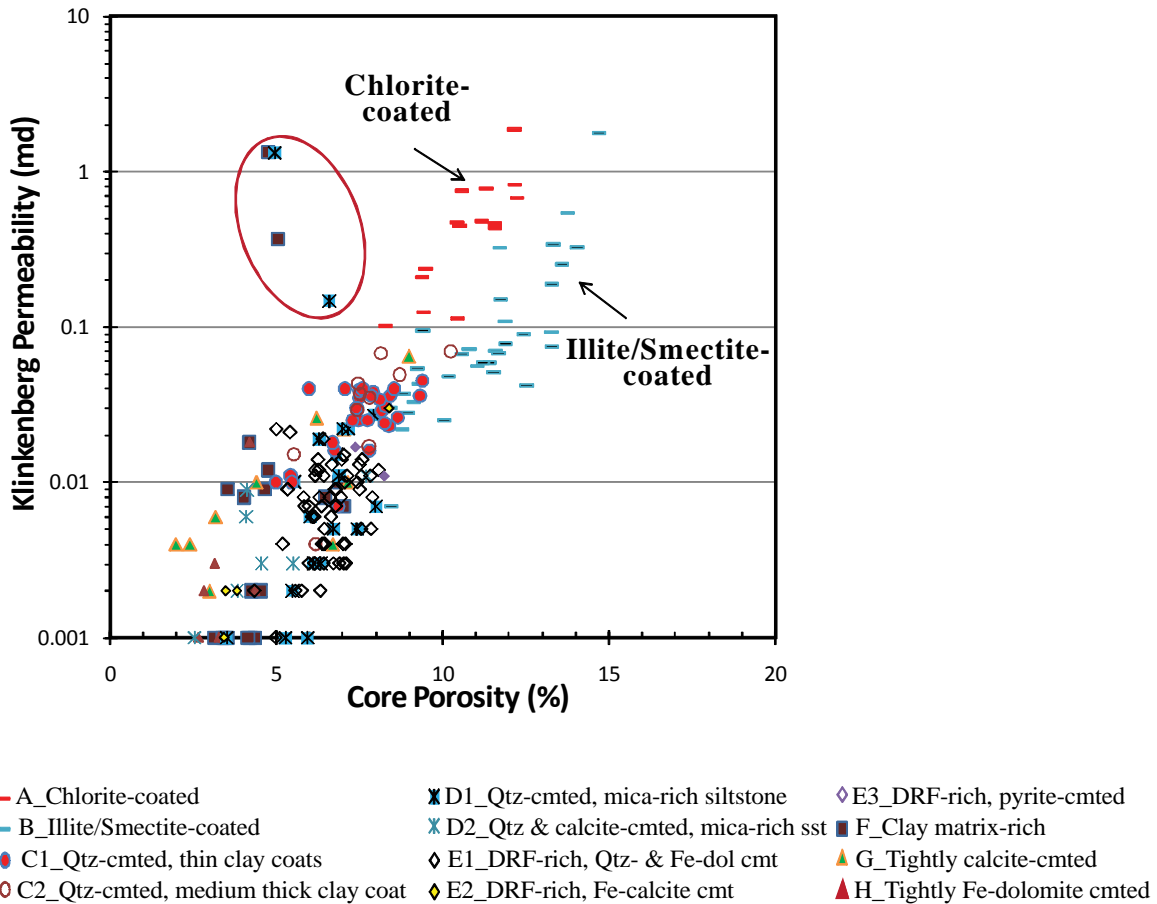


Figure 3.12. Core-measured porosity versus klinkenberg gas permeability crossplot for routine core analysis data measured at 800 psi net effective stress. The samples marked with black circle have microfractures. Clay-coated sandstones have the best reservoir quality.

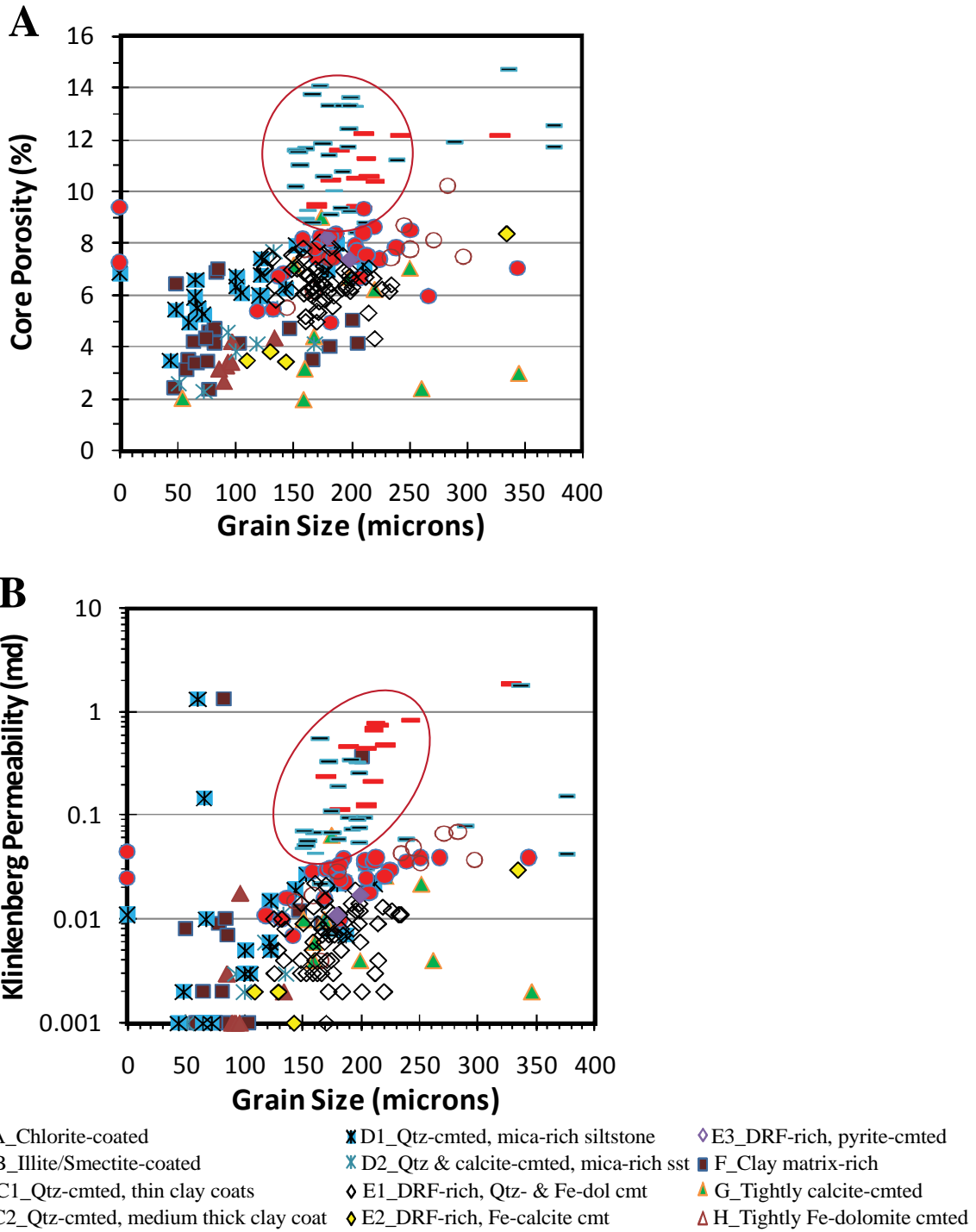


Figure 3.13. Effects of grain size on (A) core porosity and (B) permeability. Outlier samples (marked with circles) have grain-coating clays.

3.9. LITHOFACIES IDENTIFIED IN THE WILLIAMS FORK SANDSTONES

My lithofacies classification is designed to facilitate correlation of diagenetic facies with petrophysical properties. Twelve lithofacies are identified based on petrographic observations including framework constituents, authigenic minerals, grain size and sorting, clay-matrix content and pore types. Core analyses and log responses are ignored while establishing the lithofacies classification. Petrographic features of these lithofacies are provided in Table 3.1 and photographs representative of the most abundant lithofacies are given in Figure 3.14. Distribution of these lithofacies through the cored intervals is shown in Figure 3.3.

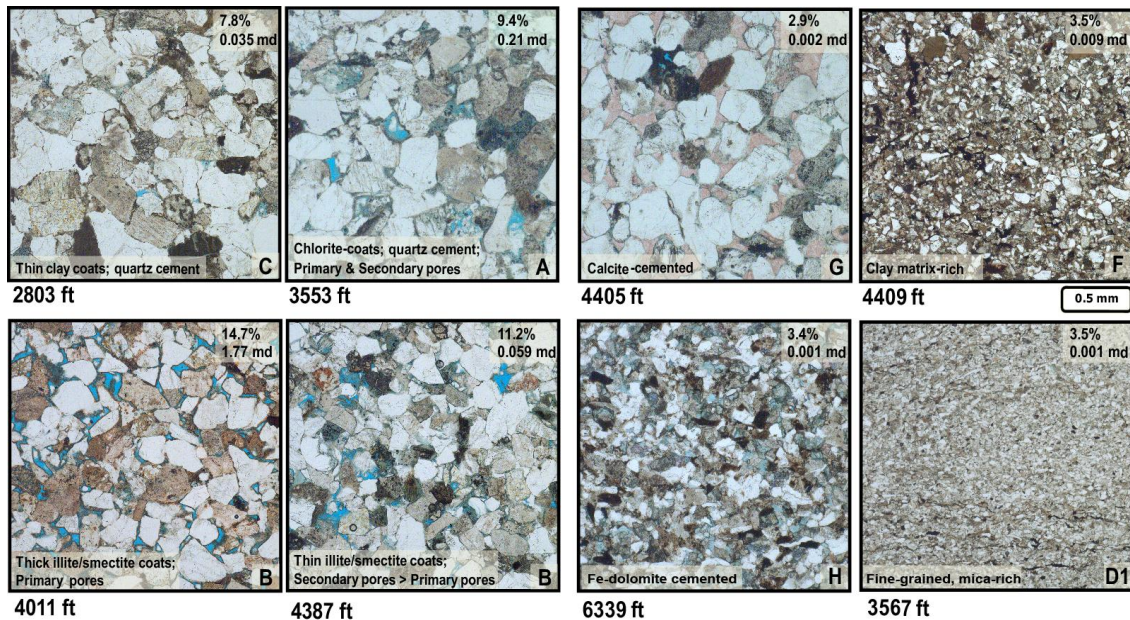


Figure 3.14. Photomicrographs illustrating characteristics of various lithofacies. Bright blue indicates epoxy filling pore spaces, calcite is stained pink and Fe-dolomite is stained turquoise blue. The images are taken at the same magnification.

Table 3.1. Summary of petrographic, petrophysical and log characteristics of the Williams Fork sandstones.

LITHOFACIES		DISTRIBUTION			PETROGRAPHY				
		#	Unit	Deposit. Environ.	Mean Grain Size (µm)	Sorting	Pore-fill	Comp	Rock Frags.
A	Chlorite-coated	15	U. W. Fork	Fluvial Channel	216	MW-W	Chlorite > Qtz	Felds. Lith.	GRF > VRF
B	Illite/Smectite-coated	33	U. W. Fork	Fluvial Channel	202	W	Illite / Smectite	Felds. Lith.	VRF >GRF
C1	Qtz-cemented; medium thick detrital clay coats (Ohio Creek)	9	Ohio Creek	Fluvial Channel	230	W	Quartz > Chlorite	Lithic Arkose	GRF > VRF
C2	Qtz-cemented; thin detrital clay coats (Ohio Creek)	30	Ohio Creek	Fluvial Channel	202	MW-W	Quartz > Chlorite	F. Lith. to L. Ark.	GRF > VRF
D1	Qtz-cemented; mica-rich; sst/siltst	19	Ohio Creek	Fluvial Channel	109	W	Quartz > Chlorite	Felds. Lith.	ARF, micas
D2	Qtz-cemented; thin clay coats, mica rich with CRFs	8	L. W. Fork	Crevasse Splay	109	M-W	Qtz	Felds. Lith.	ARF, micas
E1	Dolostone grain-rich, Qtz- & Fe-dolomite-cemented	60	L. W. Fork	Coastal Plain	176	W-VW	Qtz, Fe-dol, dead oil	Lithar enite	DRF
E2	Dolostone grain-rich, Qtz- & Fe-calcite cemented	3	L. W. Fork	Coastal Plain	127	W	Qtz, Fe-cc, Fe-dol	Lithar enite	DRF
E3	Dolostone grain-rich, Qtz- & pyrite-cemented	2	L. W. Fork	Coastal Plain	189	W-VW	Qtz, Pyrite, Fe-dol	Lithar enite	DRF
F	Clay matrix- rich sst	23	All	Crevasse Splay	100	MW-W	Clay-matrix	Lithar enite	ARF
G	Tightly calcite-cemented	11	All	All	195	MW-W	Calcite	Lithar enite	variable
H	Fe-dol cemented; Dolostone grain & Qtz-rich	8	L. W. Fork	Coastal Plain	98	W	Fe-dol	Lithar enite	DRF

Table 3.1. (ctd)

Lithofacies	PETROPHYSICS (@800 psi)								
	Density (g/cm ³)			Porosity (%)			Geomean Kinf (md)		
	Ave	Min	Max	Ave	Min	Max	Ave	Min	Max
A	2.65	2.63	2.68	10.7	8.3	12.2	0.396	0.102	1.870
B	2.65	2.65	2.66	11.3	8.4	14.7	0.080	0.007	1.770
C1	2.66	2.65	2.69	7.8	5.5	10.2	0.036	0.015	0.069
C2	2.65	2.64	2.67	7.5	5.0	9.4	0.025	0.007	0.045
D1	2.68	2.65	2.70	6.3	3.5	8.0	0.009	0.001	1.320
D2	2.67	2.66	2.70	4.3	2.3	7.7	0.004	0.001	0.011
E1	2.69	2.67	2.74	6.5	4.3	8.1	0.007	0.001	0.022
E2	2.69	2.69	2.69	3.6	3.4	3.8	0.002	0.001	0.002
E3	2.75	2.74	2.76	7.8	7.4	8.2	0.014	0.011	0.017
F	2.68	2.67	2.71	4.3	2.4	7.0	0.006	0.001	1.340
G	2.67	2.66	2.69	4.8	2.0	9.0	0.009	0.002	0.065
H	2.74	2.70	2.77	3.4	2.7	4.4	0.002	0.001	0.018

Lithofacies	LOG CHARACTERISTICS											
	SPHI			PE			HDRS			HMRS		
	Ave	Min	Max	Ave	Min	Max	Ave	Min	Max	Ave	Min	Max
A	0.14	0.12	0.15	2.46	2.33	2.66	112	83	157	120	88	162
B	0.17	0.13	0.22	2.07	1.82	2.56	43	29	84	46	31	96
C1	0.14	0.09	0.21	2.56	2.25	3.32	51	27	126	55	28	147
C2	0.14	0.11	0.17	2.33	2.07	2.86	43	29	112	46	31	145
D1	0.12	0.11	0.14	2.81	2.14	3.28	59	37	131	63	39	136
D2	0.13	0.08	0.20	2.62	2.31	3.13	43	16	64	49	17	79
E1	0.12	0.08	0.14	2.32	1.92	3.96	39	28	70	44	30	79
E2	0.10	0.07	0.12	2.45	2.28	2.68	62	50	67	78	59	92
E3	0.13	0.13	0.14	2.68	2.55	2.80	30	28	32	35	34	36
F	0.12	0.07	0.16	2.67	2.26	3.40	37	23	50	40	23	60
G	0.12	0.07	0.19	2.75	2.37	3.12	59	43	92	69	46	123
H	0.09	0.06	0.13	2.93	2.63	3.22	52	39	86	62	43	103

Table 3.1. (ctd)

Lithofacies	LOG CHARACTERISTICS											
	GR			RHOB			DPHI			NPHI		
	Ave	Min	Max	Ave	Min	Max	Ave	Min	Max	Ave	Min	Max
A	95	86	101	2.47	2.43	2.52	0.13	0.10	0.15	0.13	0.12	0.14
B	67	55	90	2.44	2.38	2.52	0.14	0.09	0.18	0.13	0.08	0.18
C1	108	83	159	2.54	2.50	2.65	0.08	0.02	0.11	0.13	0.09	0.16
C2	92	62	118	2.53	2.49	2.58	0.09	0.06	0.11	0.12	0.10	0.16
D1	125	90	162	2.56	2.51	2.62	0.07	0.04	0.10	0.13	0.09	0.15
D2	89	64	173	2.57	2.53	2.63	0.07	0.03	0.09	0.15	0.11	0.29
E1	82	55	160	2.55	2.51	2.63	0.08	0.03	0.10	0.09	0.07	0.14
E2	76	75	76	2.65	2.64	2.66	0.02	0.01	0.02	0.08	0.06	0.09
E3	147	101	193	2.58	2.56	2.60	0.06	0.05	0.07	0.14	0.13	0.15
F	108	83	136	2.59	2.54	2.65	0.05	0.02	0.08	0.14	0.10	0.19
G	89	57	122	2.55	2.41	2.63	0.08	0.03	0.16	0.09	0.05	0.13
H	72	60	82	2.64	2.60	2.69	0.02	0.01	0.05	0.09	0.08	0.11

3.10. LOG ANALYSES

3.10.1. Lithology Identification

The open-hole logs available for this well include dual-induction, gamma-ray, bulk-density, compensated neutron, borehole-compensated sonic, spontaneous potential, and image logs. The diagenetic facies are defined by a set of log responses. A database was built with the value ranges of bulk-density, neutron, sonic, and gamma-ray logs for each lithofacies (Table 3.1). Porosity and permeability ranges for each lithofacies were determined from core analyses to prepare a key for reservoir quality prediction.

Bulk density is plotted against gamma ray, deep resistivity and neutron porosity. Because each diagenetic facies is defined by a distinct range in density values and clay matrix content, high-resolution bulk-density and gamma-ray logs are the most helpful tools in predicting Williams Fork lithofacies (Figure 3.15A, Table 3.1). Lithofacies rich in authigenic and detrital carbonate minerals are relatively easy to identify with their high bulk density (calcite-cemented intervals (G): 2.655–2.687 g/cc, Fe-dolomite cemented intervals (H): 2.698–2.765 g/cc, and dolostone rock fragment-rich intervals (E): 2.668–2.741 g/cc). Clay matrix- and pseudomatrix-rich sandstones (F) and mica-rich sandstones (D) also have high bulk densities but their gamma-ray values are significantly higher than dolostone rock fragment-rich (E) and carbonate-cemented intervals (G & H). Sandstones with best reservoir qualities (A & B) can easily be identified with their low bulk grain densities (<2.55 g/cc).

Samples with mica-rich laminations (D) tend to have the greatest GR values ranging between 95 -160 API. Clay-matrix rich sandstones; on the other hand, have GR

values ranging from 95 – 115 API. Calculating a shale-cutoff value is difficult for this set of sandstones. In general, clean sandstones (clay matrix-free) tend to have lower GR readings; however, presence of abundant potassium feldspars in the Upper Williams Fork sandstones results in relatively high GR values (85 -106 API).

The contribution of potassium feldspars to the radioactivity can be best explained by comparing the chlorite- and I/S-cemented lithofacies: the two highest porosity lithofacies devoid of clay matrix. Chlorite-coated sandstones have 18-30% feldspars, and their gamma-ray signature is between 85-106 API and smectite-coated sandstones have 8-12% feldspars and their GR reading is between 55-90 API. The amount of chlorite and I/S cements in these sandstones are, respectively, 0–4% and 2-13% which is volumetrically not enough to contribute the radioactivity needed to reach the GR readings.

Overall, the facies best identified with bulk-density and GR logs are A, B, C1, D1, E1, F and G. As it can be seen in figures 3.15 A and B, some of the lithofacies have similar log characteristics. In order to further delineate lithofacies in spite of this overlap, I added other variables and ratios (DPHI, NPHI and SPHI) to the lithofacies prediction spreadsheet in *ExcelTM*. I built the spreadsheet by *nested if function* using the minimum and maximum values for well-log parameters and their ratios for each lithofacies. The range of well-log parameters is provided in Table 3.1. The lithofacies best predicted with the method were chlorite-coated sandstones (A), I/S-coated sandstones (B), and dolostone grain-rich, quartz- and Fe-dolomite-cemented sandstones (E1). The lithofacies prediction spreadsheet had difficulty distinguishing between quartz-cemented sandstones with detrital clay coats (C1 and C2) and quartz-cemented sandstones with biotite rich

laminations (D1). Actual lithofacies and predicted lithofacies at different depths are listed in Table 3.2. A statistical representation of the performance of the prediction model is presented in Table 3.3 and Figure 3.16.

Coal beds and other rocks containing extensive coal fragments were not classified separately as a lithofacies, but their identification is important. In this well, the thickest coal zone within the 1940.1 – 1942.8 m (6365 -6374 ft) interval is defined by very low bulk-density (1.22 to 1.30 g/cm³), low gamma-ray (17 to 28 API) and high neutron porosity (NPHI: 60 to 75 pu). The log characteristics of coal-rich intervals in the Piceance basin were reported by Yurewicz et al. (2008) as following: GR < 75 API units; RHOB ≤ 1.9 g/cm³; NPHI > 45 pu; Sonic (DT) > 120 μs/ft; and high resistivity ≥10 ohms.

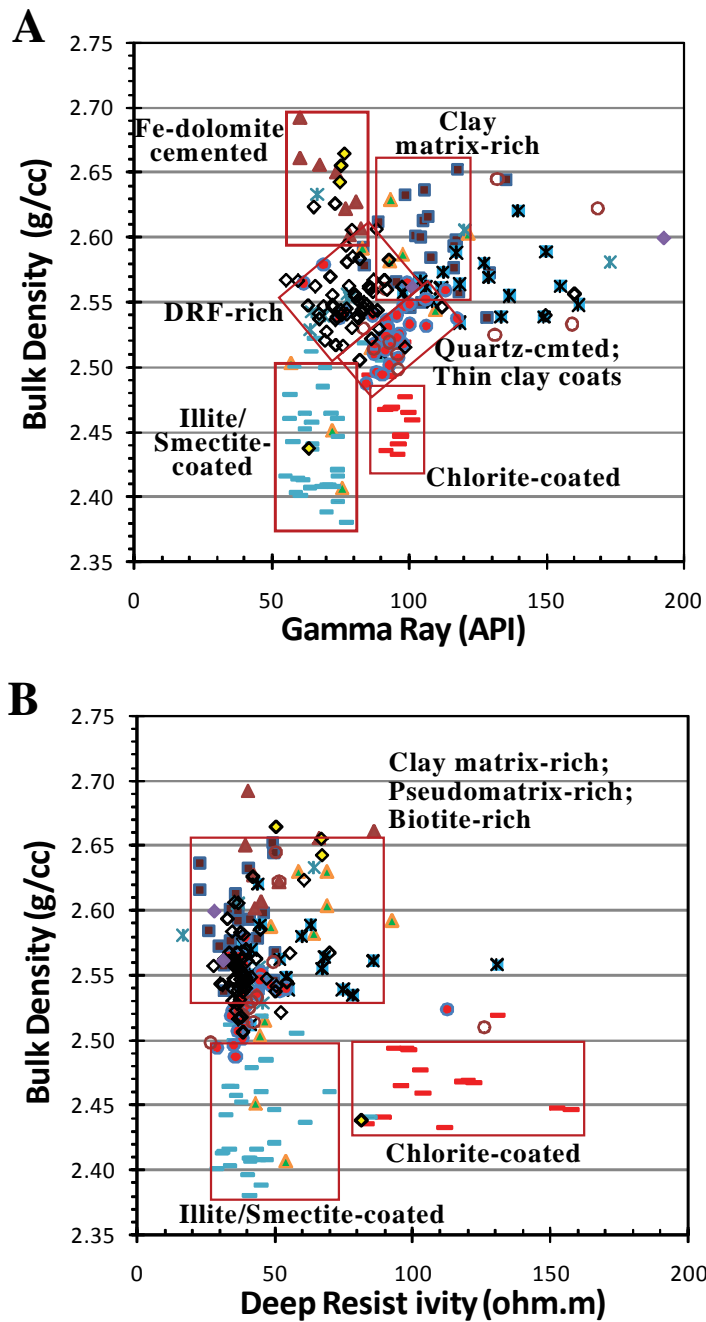


Figure 3.15. Plots of bulk density versus (A) gamma ray and (B) deep resistivity. Resistivity responds more to fluids than matrix; therefore, bulk density versus resistivity crossplot could be misleading in identifying the lithofacies. Legend is shown in figure 3.12.

Table 3.2. Comparison of actual (assigned) lithofacies and predicted lithofacies in the study well.

Depth (ft)	Lithofacies	Prediction		Depth (ft)	Lithofacies	Prediction
4002.8	A	A		3543.0	B	B C2
4003.9	A	A		3545.0	B	B C2
4004.9	A	A		3546.0	B	B C2
4005.9	A	A		3547.0	B	B
4007.1	A	A		3548.0	B	B
4387.0	A	A		3549.0	B	B
4387.9	A	A		3550.5	B	B
4389.0	A	A		3551.9	B	B
4390.0	A	A		3553.3	B	B
4391.0	A	A		3554.0	B	B
4416.0	A	A		3554.9	B	B
4393.0	A	A G		3556.0	B	B
4394.0	A	A G		3556.9	B	B
4394.9	A	A		2815.0	C1	C1 C2
4396.0	A	A		2858.0	C1	C1
4398.2	A	A		3562.0	C1	C1
4399.0	A	A G		2802.0	C1	C1 C2 E1
4402.0	A	A G		2803.0	C1	C 1D1 E1
4403.0	A	A G		2804.0	C1	C1
4403.9	A	A		2809.8	C1	C1 F
4406.1	A	A E1 G		2812.0	C1	C1 C2 D2
4008.0	A	A		2813.1	C1	A C1 C2
4008.9	A	A		2832.0	C2	C1 C2 E1
4010.0	A	A		2844.0	C2	C1 C2
4011.0	A	A		2817.0	C2	C2
4011.9	A	A		2818.0	C2	C2 G
4012.9	A	A		2819.0	C2	C2
4013.9	A	A		2827.0	C2	C1 C2 D1 E1 F
4014.9	A	A		2833.1	C2	C1 C2 D1 E1 F
4016.0	A	A		2834.0	C2	C1 C2 D1 E1 F
4016.9	A	A		2835.0	C2	C1 C2 D1 E1
4018.9	A	A G		2837.0	C2	C1 C2
4417.0	A	A		2838.0	C2	C1 C2 F
3540.0	B	B		2839.0	C2	C1 C2
3542.0	B	B		2840.0	C2	C1 C2

Table 3.2. (ctd) Comparison of actual (assigned) lithofacies and predicted lithofacies in the study well.

Depth (ft)	Lithofacies	Prediction	Depth (ft)	Lithofacies	Prediction
2841.0	C2	C1 C2	2831.0	D1	D1 E1 G
2842.0	C2	C1 C2	3964.0	D2	D2
2843.0	C2	C1 C2	3974.6	D2	D2 F
2845.0	C2	C1 C2 F	3989.6	D2	D2
2846.0	C2	C1 C2	3992.0	D2	D2 E1 G
2847.0	C2	C1 C2	3992.8	D2	C2 D2 G
2848.0	C2	C2	3994.0	D2	C2 D2 G
2849.0	C2	C1 C2	3995.0	D2	D2 G
2850.0	C2	C1 C2	3995.8	D2	C2 D2 E1 G
2851.0	C2	C1 C2	5712.9	E1	A E1 G
2852.0	C2	C1 C2 E1	5714.0	E1	E1 G
2853.0	C2	C2 E1 G	5715.2	E1	E1 G
2856.0	C2	C1 C2 E1	5717.0	E1	E1 G
2857.0	C2	C2	5718.2	E1	E1
3561.0	C2	C1 C2	5719.0	E1	E1
4000.9	C2	C2	5719.9	E1	E1
4001.8	C2	C2	5721.2	E1	E1
3564.0	D1	C1 D1 E1	5722.2	E1	E1
3569.6	D1	C1 C2 D1 G	5723.0	E1	E1
3571.0	D1	D1	5724.0	E1	E1
3566.2	D1	C1 D1 E1	5725.0	E1	E1
3571.9	D1	C1 D1 E1	5725.9	E1	E1
3573.1	D1	C1 D1	5726.9	E1	E1
3563.0	D1	C1 D1 G	5727.9	E1	E1
3560.0	D1	C1 D1 E1 G	5728.7	E1	E1
2807.0	D1	C1 D1 E1	5729.8	E1	E1
2808.0	D1	C1 D1	5730.9	E1	E1
2836.0	D1	C1 C2 D1 D3	5732.4	E1	A E1
3565.0	D1	D1	5733.1	E1	C2 E1
3567.1	D1	D1	5734.2	E1	C2 E1
3568.0	D1	C1 D1 E1	5735.0	E1	C2 E1
2824.0	D1	C1 D1 D3 F	5735.8	E1	C2 E1
2825.0	D1	C1 D1 E1 F	5736.9	E1	C2 E1
2826.0	D1	C1 D1 E1 F	5738.0	E1	E1
2828.0	D1	C1 C2 D1 E1 F	5739.0	E1	D3 E1

Table 3.2. (ctd) Comparison of actual (assigned) lithofacies and predicted lithofacies in the study well.

Depth (ft)	Lithofacies	Prediction		Depth (ft)	Lithofacies	Prediction
5739.9	E1	E1		4370.0	F	F
5741.0	E1	E1		6044.0	F	D1 F
5743.4	E1	C1 E1 F		5328.0	F	F
5745.0	E1	C2 E1		2811.0	F	F
5745.9	E1	C2 E1		3996.9	F	F
5747.1	E1	C2 E1		3998.0	F	F
5749.0	E1	E1		3998.9	F	D2 F
5750.3	E1	E1		3999.9	F	C2 E1 F G
5751.1	E1	E1		4374.0	F	C1 C2 D1 E1 F
5752.1	E1	E1		4374.9	F	C1 E1 F
5753.3	E1	E1		4384.0	F	C1 C2 E1 F
5755.0	E1	C2 E1		4384.9	F	C1 C2 F
5756.0	E1	E1		4408.1	F	C1 D1 E1 F
5757.4	E1	E1		4409.0	F	C1 D1 E1 F
5759.4	E1	C1 D1 E1 F		4410.0	F	C1 D1 E1 F
5760.3	E1	D3E1		4851.9	F	F
5761.3	E1	D3E1		4853.1	F	F
6039.1	E1	C2E1		4857.0	F	F
6040.1	E1	C2E1		4859.0	F	D2 F
6041.0	E1	E1		4863.0	F	F
6042.0	E1	E1		2800.2	G	G
6043.0	E1	C1 E1 F		2801.0	G	E1 G
6044.9	E1	D2 E1		2854.1	G	G
6047.1	E1	C2 E1		4017.9	G	A G
6051.0	E1	E1 G		4391.9	G	A G
6052.0	E1	E1 G		4405.0	G	A G
6052.9	E1	E1		4412.9	G	A C1 C2 G
6054.1	E1	E1 H		2830.3	G	G
6054.9	E1	D2 E1		2855.0	G	G
6055.8	E1	C2 E1		4407.1	G	C1 C2 D1 E1 G
6057.0	E1	A C2 E1		4850.9	G	C1 G
6058.0	E1	C2 E1		6334.0	H	H
6059.0	E1	E1		6335.0	H	H
4854.1	E2	E2		6335.9	H	E1 G H
4855.0	E2	E2		6339.9	H	H
5758.4	F	C1 E1 F		6342.0	H	E1 H

Table 3.3. Evaluation of the performance of the Williams Fork lithofacies classification tool in the study well (success: when the tool successfully predicted the lithofacies at a given depth; overlap: the tool predicted more than one lithofacies at a given depth).

Lithofacies	Percentage (%)					
	Success	Overlap 1	Overlap 2	Overlap 3	Overlap 4	Overlap 5
A	79	18	3	3	0	0
B	80	20	0	0	0	0
C1	33	22	44	44	0	0
C2	20	47	20	20	3	1
D1	16	11	47	47	21	1
D2	25	25	38	38	13	0
E1	53	39	7	7	2	0
E2	100	0	0	0	0	0
F	48	13	13	13	22	0
G	36	45	0	0	9	1
H	50	33	17	17	0	0

Lithofacies	Number of Samples					
	Success	Overlap 1	Overlap 2	Overlap 3	Overlap 4	Overlap 5
A	26	6	1	1	0	0
B	12	3	0	0	0	0
C1	3	2	4	4	0	0
C2	6	14	6	6	1	3
D1	3	2	9	9	4	1
D2	2	2	3	3	1	0
E1	31	23	4	4	1	0
E2	3	0	0	0	0	0
F	11	3	3	3	5	1
G	4	5	0	0	1	1
H	3	2	1	1	0	0

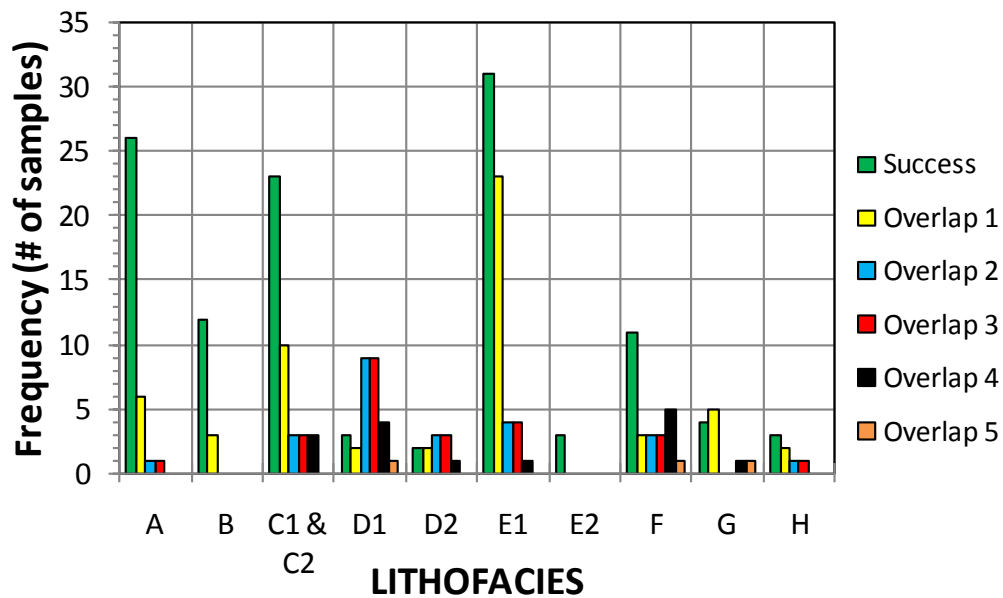
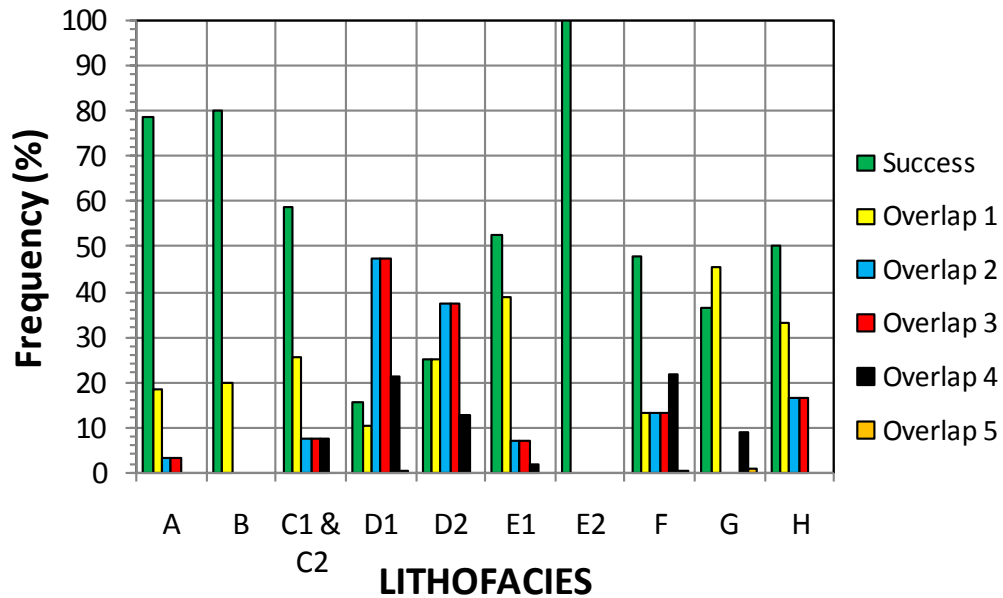


Figure 3.16 Distribution bar graph showing the performance of the Williams Fork lithofacies classification tool in the study well (success: when the tool successfully predicted the lithofacies at a given depth; overlap: the tool predicted more than one lithofacies at a given depth.)

3.10.2. Assessing Reservoir Quality from Well Logs

3.10.2.1. Controls on Grain Density

Grain density values are generally higher in the samples rich in carbonate and pyrite cements, and also in those rich in DRFs. The sandstones with the highest porosities are found in the fluvial intervals and they have the lowest grain densities (2.64-2.65 g/cm³). Locally abundant calcite cement in these fluvial samples results in higher grain densities (2.66-2.67 g/cm³). Grain densities are relatively higher in the deeper, marine-influenced Upper and Middle Sandstones (2.67 -2.68 g/cm³) and Cameo zone (2.70 -2.76 g/cm³) due to presence of dolostone fragments and Fe-dolomite cement.

Comparison of standard bulk-density log values with core-measured densities indicates very poor correlation for highly porous (and lightest) sandstones (Figure 3.17). However, bulk-density readings for the best reservoir quality sandstones are clearly the lowest which makes their identification very easy.

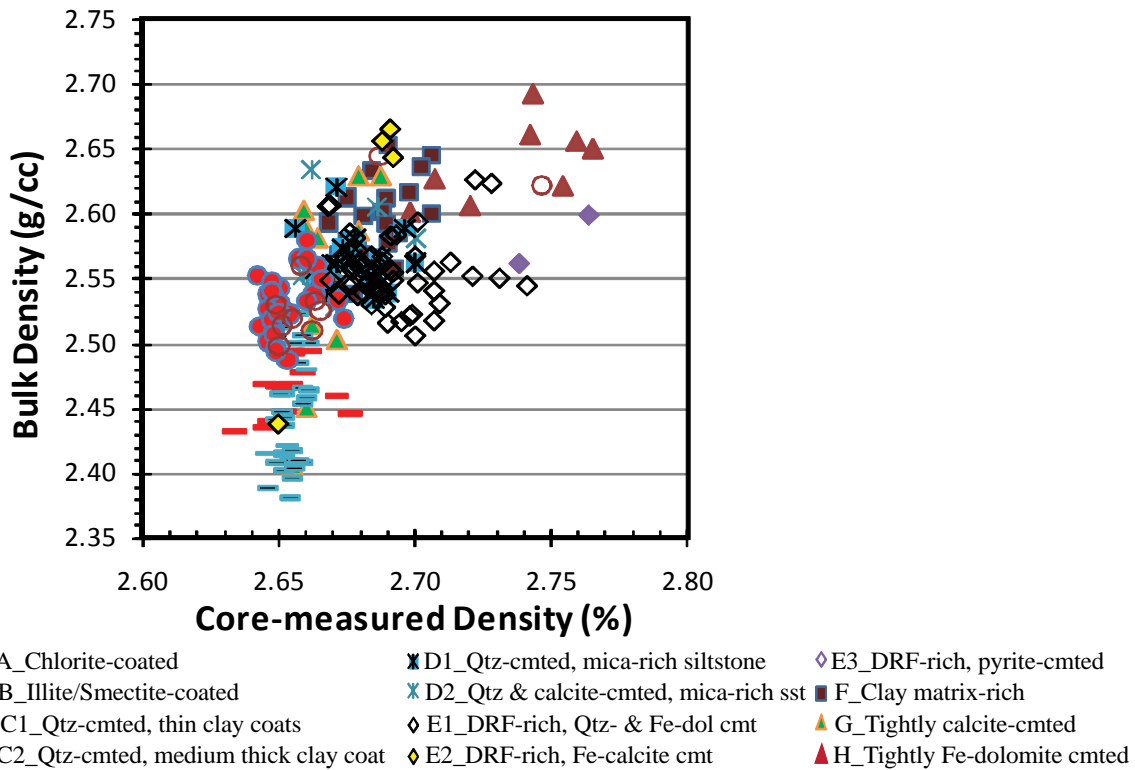


Figure 3.17. Comparison of density derived from bulk-density logs and core measurements. The sandstones with the lowest bulk-density values are clay-coated intervals with best reservoir qualities.

3.10.2.2. Reservoir Quality Prediction

In order to assess the core porosity prediction success from well logs, log-derived porosity values (sonic, neutron, density, and average neutron-density porosity) were compared with core measured porosities (Figure 3.18A, B, C and D). Sonic porosity overestimates the core-measured porosities of all rock types from 3% to 9%. Log-derived density porosity estimates the core porosities within a range of $\pm 4\%$ for most of the lithofacies except for those with highest reservoir qualities for which an overestimation $>6\%$ is obtained. Due to clay effects, neutron porosity gives unreasonably high porosities

in clay matrix- and pseudomatrix-rich sandstones and fine-grained mica-rich lithofacies in which overprediction reaches >10%. Neutron porosity estimates the rest of the samples 0-5% higher than the core porosities. In order to eliminate the gas effects, average neutron-density porosity is calculated and best correlation with the core-measured porosity is observed with this calculated average neutron-density porosity (Figure 3.18D).

Vertical density log resolution is about 16 inches and density porosity was calculated with the standard formula below by using matrix grain density of 2.68 g/cm³ and a fluid density of 1.0 g/cm³. As explained above, the upper fluvial and lower coastal plain deposits of Williams Fork intervals have distinct differences in their grain densities (Figure 3.3; average of 2.67 ± 0.024 g/cm³ for the cored interval). When a single matrix grain density value is used to calculate the porosity with this formula, log-derived density porosity is overestimated in the lighter sandstones and underestimated in the heaviest ones (Figure 3.18C). By using variable matrix density values that are closer to the core-measured densities, density porosity estimations can be greatly improved (Figure 3.19; Table 3.4).

$$\text{Porosity} = (\text{matrix density} - \text{bulk-density}) / (\text{matrix density} - \text{fluid density})$$

Gas has very low density and a very low hydrogen index compared to water; therefore, presence of gas causes the neutron porosity to read too low and the density porosity to read too high, giving a large separation (crossover) of the neutron-density log combination. In the gas-producing zones of lower Williams Fork, this crossover effect is locally subdued. The gas effect is suppressed due to the higher matrix densities that result from the presence of dolomite grains and carbonate cements. Because the matrix densities in these intervals are higher than the 2.68 g/cm³ that is used to calculate the

density porosity, the density porosity reads too low and the neutron-density crossover is suppressed or absent, even though the sandstones are gas saturated.

Permeability prediction with log-based porosity is possible only for the highest and lowest permeability sandstones (Figure 3.18E, F, G and H). Table 3.1 shows the parameter ranges for successful permeability prediction from logs. More accurate porosity and permeability prediction is possible by identifying the lithofacies rather than using cross plots of log-derived porosity vs. core-measured porosity and permeability.

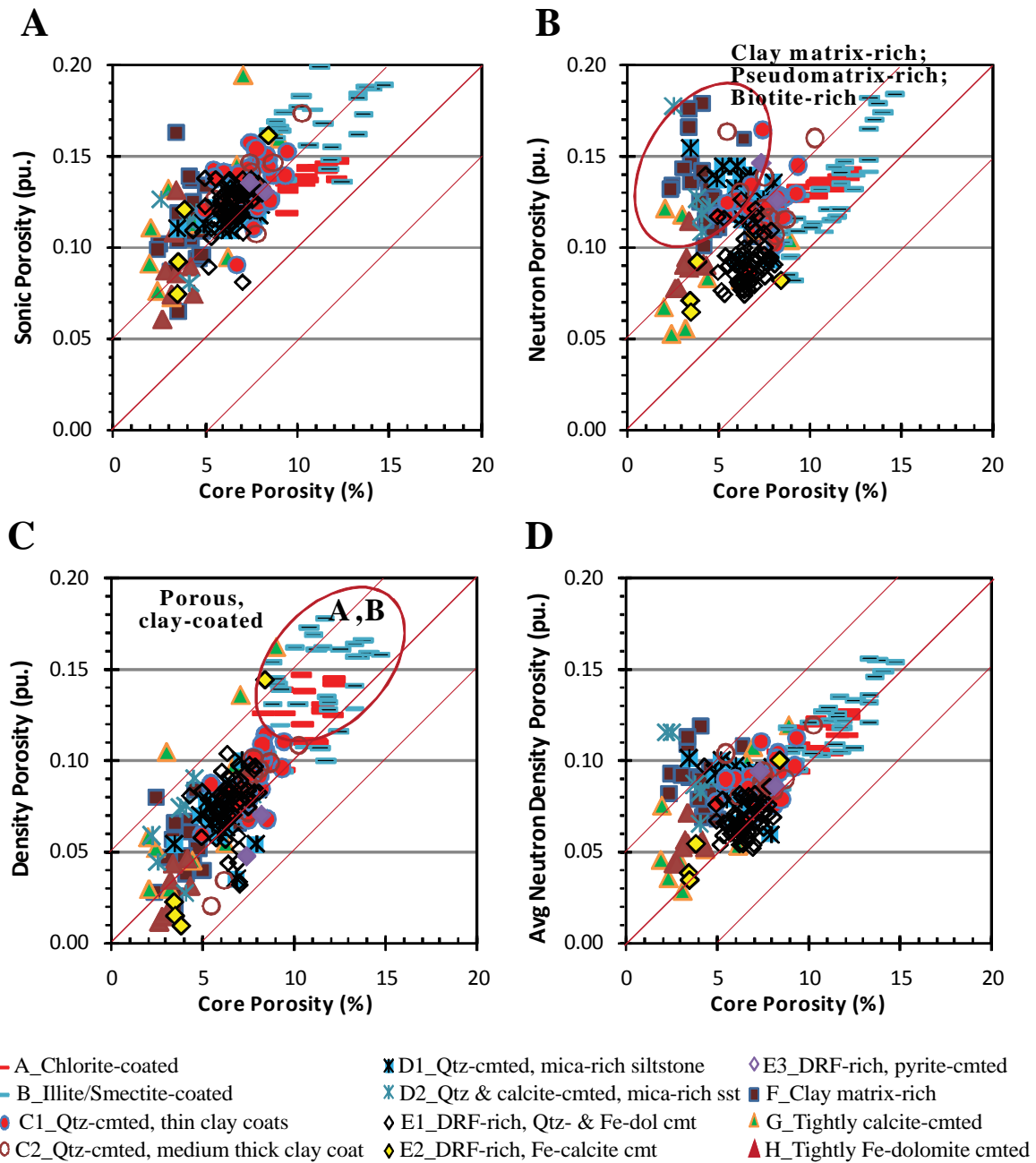


Figure 3.18. Prediction of core porosity and permeability with sonic porosity (A, E), neutron porosity (B, F), density porosity (C, G), and average neutron density porosity (D, H). Avg: average.

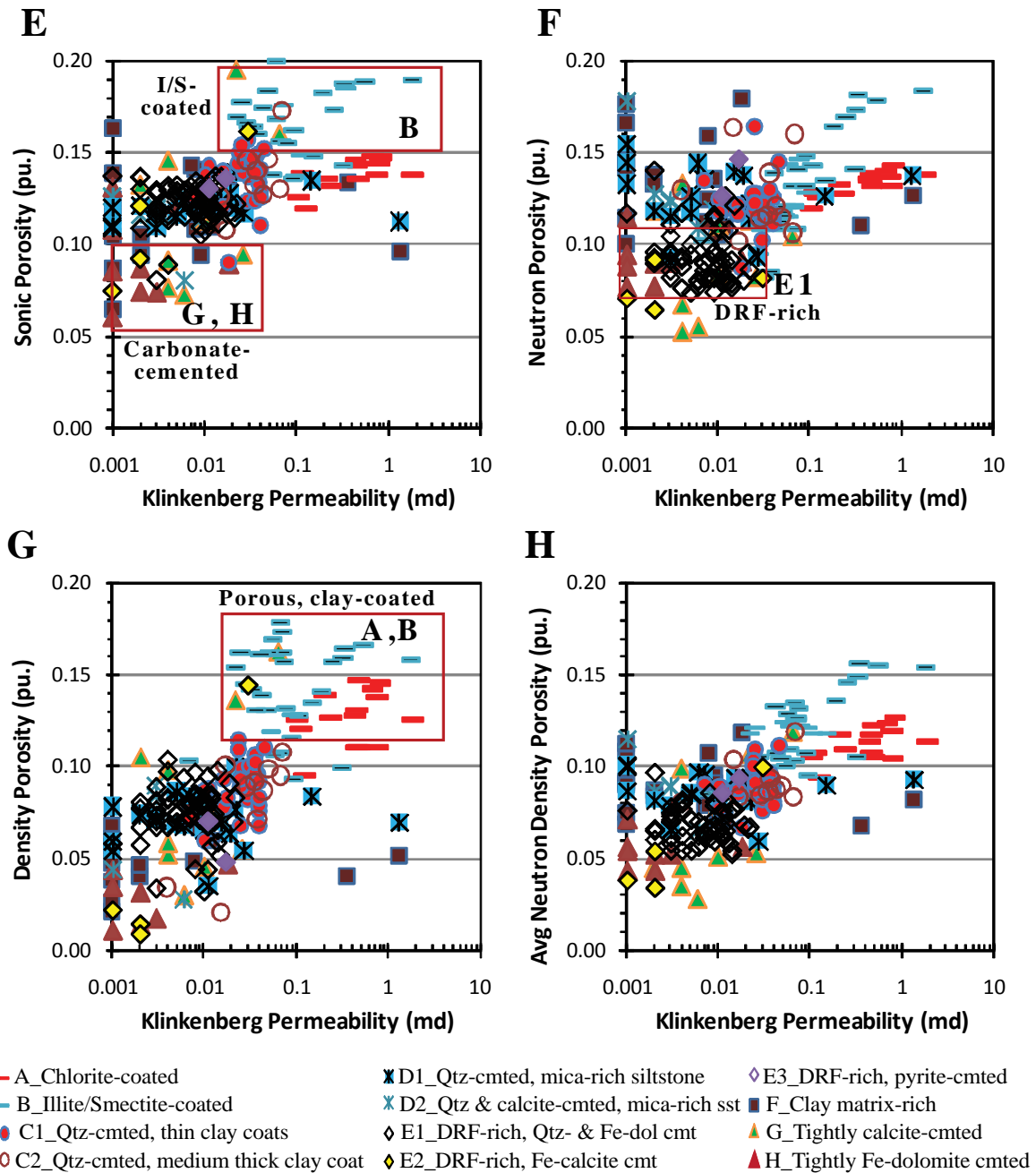


Figure 3.18. (ctd) Prediction of core porosity and permeability with sonic porosity (A, E), neutron porosity (B, F), density porosity (C, G), and average neutron density porosity (D, H). Avg: average.

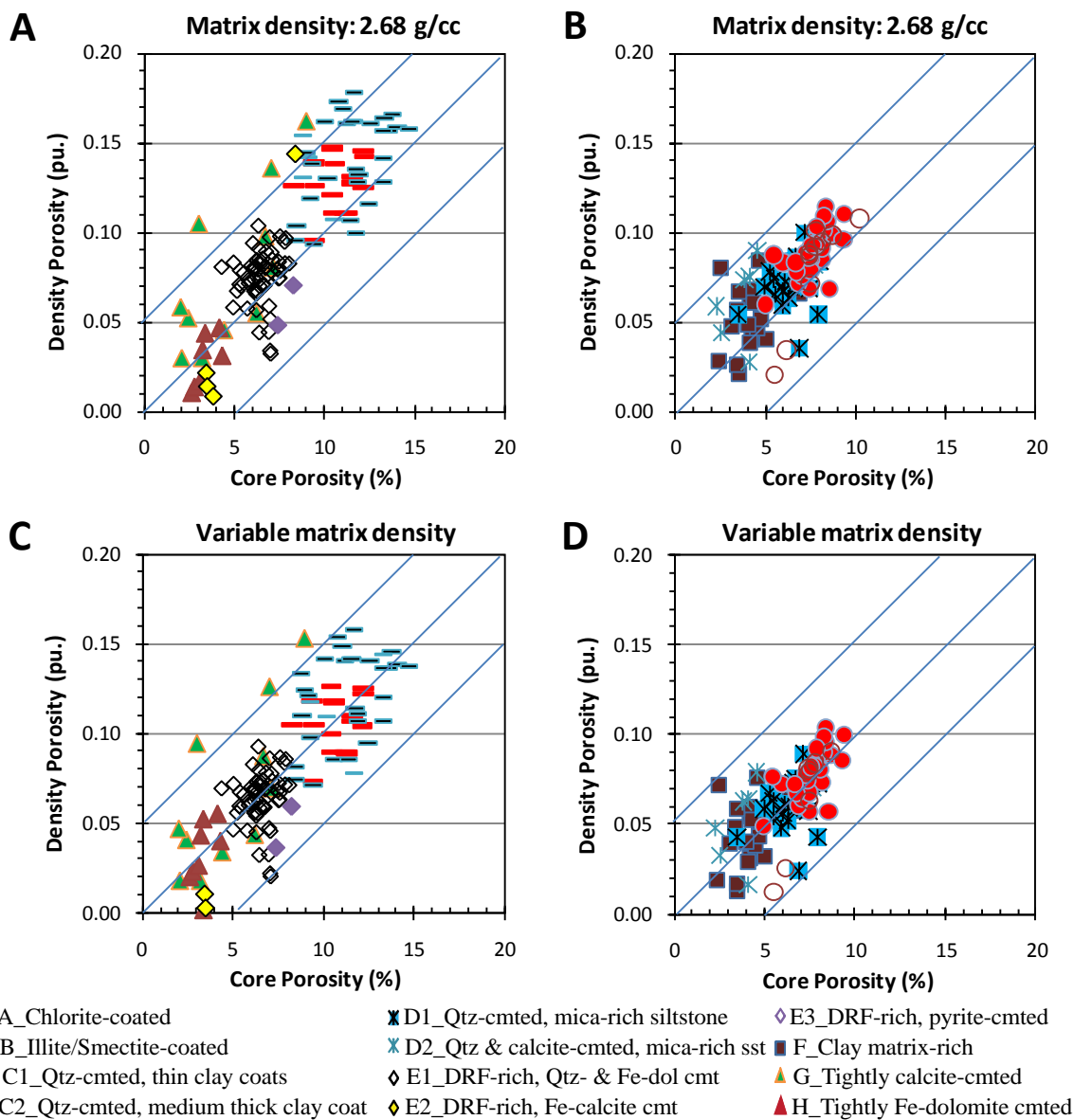


Figure 3.19. Comparison of density porosity calculated by using matrix density of 2.68 g/cc for all interval (A and B) and variable matrix densities close to the core-measured densities (data is available in Table 3.2).

Table 3.4. List of core-measured density and matrix density that is used to improve density porosity calculation.

Lithofacies		Core-Density (g/cm ³)			Matrix Density (g/cm ³)	
		Ave	Min	Max	Original Calculation	Improved Calculation
A	Chlorite-coated	2.65	2.63	2.68	2.68	2.64
B	Illite/Smectite-coated	2.65	2.65	2.66	2.68	2.64
C1	Qtz-cemented; medium thick detrital clay coats (Ohio Creek)	2.66	2.65	2.69	2.68	2.66
C2	Qtz-cemented; thin detrital clay coats (Ohio Creek)	2.65	2.64	2.67	2.68	2.66
D1	Qtz-cemented; mica-rich; sst/siltst	2.68	2.65	2.70	2.68	2.66
D2	Qtz-cemented; thin clay coats, mica rich with CRFs	2.67	2.66	2.70	2.68	2.66
E1	Dolostone grain-rich, Qtz- & Fe-dolomite-cemented	2.69	2.67	2.74	2.68	2.66
E2	Dolostone grain-rich, Qtz- & Fe-calcite cemented	2.69	2.69	2.69	2.68	2.71
E3	Dolostone grain-rich, Qtz- & pyrite-cemented	2.75	2.74	2.76	2.68	2.66
F	Clay matrix- rich sst	2.68	2.67	2.71	2.68	2.665
G	Tightly calcite-cemented	2.67	2.66	2.69	2.68	2.66
H	Fe-dol cemented; Dolostone grain & Qtz-rich	2.74	2.70	2.77	2.68	2.695

3.11. CONCLUSIONS: LITHOFACIES CLASSIFICATION APPROACH

In Williams Fork sandstones, pore network and permeability distribution are strongly influenced by diagenesis, depositional texture, and environment. Framework grain composition is a major control on degree of compaction and authigenic phases precipitated. Grain-coating clays are more common in the volcanic grain-rich Upper Williams Fork where alteration of these grains caused the precipitation of authigenic clays. Fe-dolomite cement is found only in the deeper marine-influenced intervals in which dolostone fragments are present. Compaction was more effective in the samples rich in micas, argillaceous grains, and low-grade metamorphic fragments.

Based on cement type, grain population, and clay-matrix content, twelve lithofacies are identified in the Williams Fork reservoir. Examination of core analysis data indicates these lithofacies have distinct porosity, permeability and density ranges. The best reservoir quality is observed in sandstones with grain-coating chlorite and illite/smectite. Primary pores were better preserved in these sandstones due to inhibition of quartz precipitation by grain-coating clays.

A model that uses gamma-ray, bulk-density, neutron, and sonic logs and their ratios as variables was built to identify diagenetically significant lithofacies and predict the reservoir quality from well logs. With this model better calculation of net sandstone thickness and permeability thickness is possible.

Correlation of petrographically identified lithofacies with log responses indicates that bulk-density and gamma-ray logs, alone or combined, can be a tool for predicting the best and poorest reservoir quality sandstones in this system. Sandstones with the best reservoir quality can easily be identified based on low bulk-density log values. Intervals cemented with carbonate minerals are identified by high bulk densities. Clay matrix- and mica-rich samples have high gamma-ray and bulk-density values. The lithofacies with overlapping gamma-ray and grain density log values can be differentiated by adding other log info as variables such as resistivity, neutron porosity and sonic logs. The lithofacies best predicted with the lithofacies prediction spreadsheet were chlorite-coated sandstones (A), I/S-coated sandstones (B), and dolostone grain-rich, quartz- and Fe-dolomite-cemented sandstones (E1, E2). Predictive tool did poorly distinguishing between quartz-cemented sandstones with detrital clay coats (C1 and C2) and quartz-cemented sandstones with biotite rich laminations (D1).

This study suggests that careful petrographic assessment of lithofacies heterogeneity can be up-scaled by correlation with log properties to yield tools for field scale reservoir quality prediction.

Lithofacies prediction with log responses can also be a helpful tool in determining some of the depositional facies. Marine-influenced deposits of lower Williams Fork are associated with dolostone fragment-rich lithofacies and crevasse splay deposits within the fluvial upper Williams Fork are mostly associated with clay matrix-rich sandstones and mica-rich siltstones to fine-grained sandstones.

Quartz and calcite cements in Williams Fork sandstones vary to some extent with depositional composition. These same cements are found propping open or sealing natural fractures. It remains to be determined if lithofacies approaches can shed light on the natural fracture component of reservoir quality.

CHAPTER 4: INFLUENCE OF DIAGENESIS ON ROCK MECHANICAL PROPERTIES

4.1 INTRODUCTION: ROCK MECHANICAL PROPERTIES AND FRACTURING

Fracture network prediction is especially important in tight gas sandstones where matrix permeabilities are very low and fractures, being permeability pathways, are the main contributors of gas production. Because it is difficult to sample vertical fractures with vertical wells, many of the fracture characteristics remain poorly known in the deep subsurface (Laubach, 1997). The characteristics such as aperture size, length, aperture and length distributions, connectivity, clustering, number of fracture sets and orientations carry importance as they influence fluid flow in the reservoirs, therefore, geostatistical and geomechanical models are used to determine distribution of these parameters. Geostatistical approaches that use the fracture attributes collected from rock samples are commonly applied to predict fracture spacing, length and aperture distributions (Rives et al., 1992; Marrett, 1997; Ortega et al., 2006). Geomechanical models have proven useful in generating fracture networks with realistic fracture spacing, aperture and length distributions using measurable rock parameters such as subcritical crack index, Young's modulus, mechanical layer thickness and tectonic strain (Olson et al., 2001; Olson, 2004). My study provides tool for making predictions of a rock's fracturing behavior at different times in the burial history by presenting how evolution of quartz cementation through geological time can be effectively modeled, and how mechanical parameters can therefore also be modeled at different times in a rock's burial history.

Subcritical crack index is a mechanical rock property that influences fracture characteristics, which in turn controls the aperture distributions and clustering (Olson et al., 2001). Subcritical growth can occur in systems subject to long-term loading, where

cracks can propagate at stress intensity factors lower than fracture toughness, at velocities several orders of magnitude lower than the rupture velocity (Atkinson, 1984). Subcritical crack growth was observed in glass by Grenet (1899), ceramics (Wiederhorn, 1974) and in rocks and minerals (Atkinson, 1982; 1984). Subcritical crack index can be measured in the lab environment and index results were reported for a range of rocks and testing environments by Atkinson and Meredith (1981), Holder et al. (2001), Olson et al. (2001), Rijken et al. (2002), Rijken (2005), and Gale et al. (2007).

I conducted fracture path analyses in order to quantify a fracture's behavior going through a sandstone and understand how the microscale textural differences in the growth mechanisms of pore-filling cements affect this path and the subcritical crack index (Section 4.2). For pure opening mode (or mode I), the displacement discontinuity across the fracture is normal to the fracture face. Opening mode fractures typically propagate as planes perpendicular to the least compressive principal stress, S_3 (Lawn and Wilshaw, 1975; Pollard and Aydin, 1988). Fractures are assumed to take the least resistant path in the rock (Kranz, 1983): instead of cracking through intact grains they can be expected to follow intergranular paths which might constitute areas of relatively low cohesion and thus flaws in sandstones. Natural fracture paths in some well-cemented sandstones follow grain boundaries for parts of their trajectories rather than cutting across grains, producing tortuous microscopic fracture paths (Laubach, 1988). A tightly quartz-cemented and a tightly calcite-cemented sandstone were subjected to subcritical crack testing and the cracks introduced by the test were imaged with cathodoluminescence for fracture path analyses. The fracture path was traced and lengths of the intergranular (grain-grain, grain-cement, cement-cement) and intragranular (intragrain and intracement) paths along the fractures were measured. The results of these measurements are the focus of section 4.2 of this chapter.

In order to quantify the effects of diagenesis on the mechanical properties of the sandstones subsurface samples I compared subsurface samples with outcrop samples (section 4.3). The influence of rock type, cement type and volume, porosity, tortuosity, and grain size on subcritical crack index was examined for a large set of sedimentary rocks by Olson et al. (2001), Rijken et al. (2002), and Rijken (2005). They found clear differences in the mechanical properties of carbonates and sandstones. However, their studies in sandstones point out the difficulty of isolating the effect of an individual rock property (porosity, grain size, cement type) on subcritical crack behavior due to large numbers of combinations of framework grain composition, grain size and shape, and diagenetic overprint. In order to overcome the heterogeneity problem, I try to isolate the effects of cementation and porosity by comparing the subsurface and outcrop samples of the same formation with similar framework mineralogies. Williams Fork samples from the Piceance Basin provide a good set of samples for this study because the degree of lithification is different for the subsurface and outcrop samples owing to contrasting burial and thermal histories related to the Laramide orogeny. Subsurface samples from the Mamm Creek field went through deeper burial and were exposed to higher temperatures which led to precipitation of considerably more quartz cement. While deeply buried subsurface samples represent well-consolidated end-members, their outcrop equivalents can be used as contrasting, poorly to moderately consolidated end-members for subcritical crack index measurements. The approach taken here not only helps us quantify the effects of diagenesis on the mechanical properties of the sandstones, also it helps us to determine a range subcritical crack index values for sandstones of given framework composition. The details of this work are explained in section 4.3.

Subcritical crack index measurements done on the sandstones yield a value for the present day characteristics of the rock. At the time of fracturing the sandstone might have

been at a different diagenetic stage (degree of compaction, cementation, porosity, permeability, etc.). As the degree of lithification changes during burial through compaction and cementation, the rock's response to fracturing changes in concert. Determination of the compaction and cementation state of a sandstone at the time of fracturing is possible with the aid of diagenetic modeling programs (*TouchstoneTM*) which can predict the degree of compaction, porosity loss and amount of quartz precipitation at a given geologic time (for example, some time in the past) by using burial history and present day petrography data. Microthermometry (isotope and fluid inclusions) on the fracture-filling quartz and carbonate cement with crack-seal textures can yield temperature ranges of fracture opening (Laubach et al., 2009; Becker et al., 2009b). Timing of the fracture opening can be determined by linking this data to the burial and thermal histories obtained from basin models. In this case study, the effects of subcritical crack index, bulk rock mechanical parameters, Young's modulus, and Poisson's ratios, on the degree of fracturing are also discussed.

4.1.1. Subcritical Crack Growth

Mechanical rupture of a material occurs when the mode I (normal opening) stress intensity factor, K_I , is equal to the critical stress intensity factor or fracture toughness, K_{IC} , at which time the fracture propagates with a velocity slightly below the shear-wave velocity (Figure 4.1). However, fractures can also propagate at stresses well below this level at velocities several orders of magnitude slower than the rupture velocity (Atkinson, 1984). In tectonically stressed crustal rocks subcritical crack growth can be significant (Olson et al., 2001).

Fracture toughness describes the ability of a material containing a crack to resist fracturing. It is denoted K_{Ic} and has the units of $\text{Mpa}\cdot\sqrt{\text{m}}$. The subscript 'Ic' denotes mode I crack opening under a normal tensile stress perpendicular to the crack, since the

material can be made thick enough to resist shear (mode II) or tear (mode III). If a material has a large value of fracture toughness it will probably undergo ductile fracture. Brittle fracture is the characteristic of materials with a low fracture toughness value (Griffith, 1921).

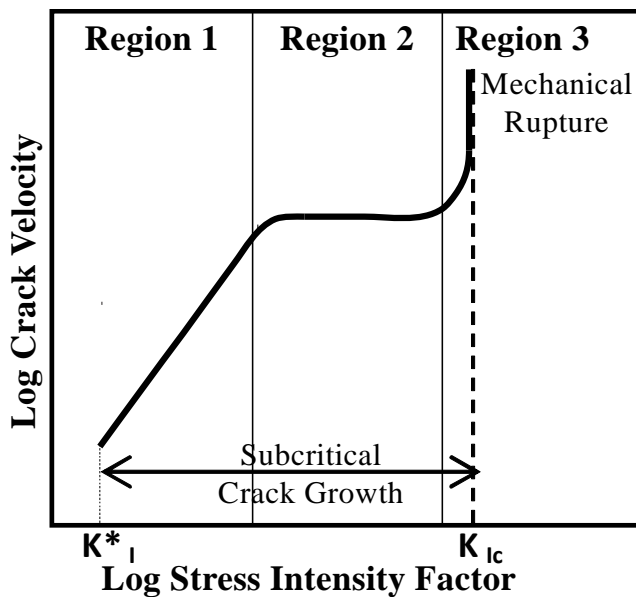


Figure 4.1. Three regions of crack propagation. Region I is dominated by stress corrosion. Region II is controlled by the transport of reactive species to the crack tip; and Region III is where mechanical rupture occurs. Subcritical fracture growth occurs between the stress corrosion limit, K^*_I and the fracture toughness, K_{Ic} (Wiederhorn, 1967). The slope of the curve in Region 1 is the subcritical crack index. (Figure after Atkinson and Meredith, 1981).

During subcritical crack growth, the material is strained at levels below that necessary for breaking bonds, but the strained bonds are weaker and more prone to chemical attack (Lawn, 1975; Atkinson and Meredith, 1981). The bonds are further weakened and ultimately broken by thermally activated chemical interactions. An empirical power law provides a good correlation between subcritical fracture velocity

(Charles, 1958), V , and the stress intensity factor (or, because of its proportionality to K_I , applied load, P):

$$V = k_o \left(\frac{K_I}{K_{IC}} \right)^n = AP_n \quad (\text{equation 4.1; Charles, 1958})$$

where n is the subcritical crack index, and k_o and A are constants.

Values for the subcritical indices are determined from measurements of load decay in a dual torsion beam configuration at constant displacement (Williams and Evans, 1973). This technique is based on empirical evidence that the effective specimen compliance, S , is a linear function of crack length, a . This is equivalent to the ratio of displacement normal to the plane of the test specimen, y , to the normal load, P :

$$S = \frac{y}{P} = S_o + Ba \quad (\text{equation 4.2; Williams and Evans, 1973})$$

In this expression, B is a constant; S_o is compliance when $a = 0$; and the crack velocity, V , is given by the time derivative of a . For a constant normal displacement, y_0 , the crack propagation velocity is determined by the rate of change of the load, P .

$$V = - \frac{C}{P^2} \left(\frac{\partial P}{\partial t} \right) \quad (\text{equation 4.3; Williams and Evans, 1973})$$

where C is another constant. The crack velocity can then be determined from numerical differentiation.

Studies have proven that subcritical index values vary with rock type (Atkinson and Meredith, 1989; Rijken et al., 2002; Rijken, 2005) and differences in subcritical crack index of the rock has control on fracture attributes such as length, spacing (Olson 1993; Renshaw and Pollard, 1994; Olson et al., 2001) and connectivity (Renshaw, 1996; Olson, 1997) at a given chemical environment.

Output of the geomechanical models by Olson et al. (2001) illustrates the effects of the subcritical index on fracture-spacing length distributions, connectivity, and fracture aperture can be controlled by this process (Olson et al., 2001). For low values of ($n < 20$), computed natural fracture patterns exhibit small spacing relative to bed thickness. At high values ($n \geq 80$), fractures are spatially arranged in widely spaced swarms or clusters. Intermediate values (20–80) result in more regular fracture spacing that is roughly proportional to layer thickness.

Discrete fracture flow modeling of geomechanically generated fracture patterns has demonstrated variations in effective permeability with subcritical index, primarily through its influence on fracture length distributions (Philip et al., 2005; Rijken, 2005).

Atkinson and Meredith's (1989) experimental data on single crystals and polycrystalline ceramics, show that subcritical fracture growth is influenced by strain energy release rate, temperature, chemical environment, pressure, rock microstructure, and residual internal strains. This data however was reported for metals, ceramics and glass which have much simpler microstructures than rocks. Sandstones can have very heterogeneous microstructures due to textures inherited from depositional environment, including porosity in various configurations, grain size, sorting, and amount of clay matrix which control the pore sizes and distributions. Effects of diagenesis can further complicate these inherited textural heterogeneities. The presence of porosity and other compliant constituents in sedimentary rock requires special testing procedures to measure subcritical crack index (Holder et al., 2001). Using these methods, Rijken et al. (2002) attempted to quantify sedimentary composition and texture effects on subcritical

fracture behavior. However, due to microstructural complexity of the tested sandstones it was not possible to isolate the individual effects of mineralogy and texture.

Park (2006) performed a numerical study of subcritical crack growth using the Discrete Element Method (DEM) to model laboratory test behavior, individually assessing the sensitivity of results to cement volume, time dependent cement properties, grain/cement mineralogy, and confining pressure. He implemented the time dependent properties of subcritical crack growth by incorporating stress corrosion. The stress corrosion rate was quantified by the activation energy and volume of quartz. For his models, he used lab-measured fracture toughness and subcritical index values of Berea sandstone and extended the results to weaker rocks by reducing cement volume. He reported when intergranular cement volume is reduced, fracture toughness, relative fracture strength, and subcritical index decrease.

Zou et al. (2009) studied the effects of temperature on rock mechanical properties. They reported that fracture toughness value increases exponentially when the range of the temperature is from 25 to 150°C, but decreases exponentially when the range of the temperature is from 150 to 300°C.

4.1.2. Subcritical Crack Index Testing

In order to quantify the link between petrographical properties and rock mechanical properties, the samples were analyzed petrographically and subjected to SCI testing. For SCI testing, the samples were cut into thin section size slabs (2.5 cm × 5 cm × 1.5 mm (1 × 2 × 0.6 in.)) parallel to bedding. Well consolidated samples were cut with a saw that uses water as a coolant. Poorly consolidated samples (particularly clay-cemented

sandstones), however, fell apart with the use of water-saw, therefore they were cut dry. The samples were polished on one side to aid easier identification of crack propagation path, and grooved along the center of the nonpolished surface as part of the testing procedure described by Holder et al. (2001).

The experiments are conducted in ambient laboratory conditions (22 °C and 51% relative humidity) at zero depth. This should not affect the measurements, because theoretically subcritical crack index's governing equation is only marginally affected by confining pressure (J. Holder, personal communication, 2008; Gale et al., 2007).

Total crack propagation during a single load decay is usually less than length of the specimen, which allows application of multiple tests on the same specimen. For most specimens two or three subcritical crack measurements were carried out under dry conditions (in air). Subcritical index values vary with the ambient fluid within the crack. As some of the outcrop samples were cemented with clays, measuring the SCI values under water was not attempted for any of the samples. Difficulty of subcritical index measurements under water conditions for clay-cemented sandstones was mentioned in Rijken et al. (2002).

The test sequence described in Holder et al. (2001) and Gale et al. (2007) was followed for the subcritical crack propagation tests:

- The specimen is loaded in steps of approximately 0.23 kg (0.5 lb), holding the applied load constant during each interval by means of a programmed stepper motor.
- When crack formation and propagation were indicated by increases in vertical displacement of the loading ram, further displacements were stopped.

- The load was allowed to decay for about 10 minutes, attaining an approximately constant value.

Microsoft Excel's SOLVE option was used to determine the parameters from a least-squares fit of all load decay data. This process is set up in an Excel template, and the entire fitting procedure is conducted in a few seconds.

4.2. MICROSCALE TEXTURAL CONTROLS ON SUBCRITICAL CRACK INDEX

In order to determine the mineralogical and textural controls exerted on subcritical crack behavior, subcritical crack index (SCI) was measured for a group of sandstones with varying framework compositions, pore-filling cements, and porosity. Despite the differences in sandstone composition and amount and type of pore-filling cements, SCI increased with increasing content of total cement while total porosity has the opposite effect on the SCI. The overall data distribution suggests that SCI decreases as grain size becomes coarser (the largest grain size in the sample set is 0.39 mm).

In order to understand and quantify the microscale textural effects of pore-filling cement mineralogy on fracture paths, the fractures introduced by SCI testing were imaged with cathodoluminescence for a tightly quartz-cemented sandstone (31.7% quartz cement) and a tightly calcite-cemented sandstone (27.3% calcite cement). The path the fracture took was traced and lengths of the intergranular (grain-grain, grain-cement, cement-cement) and intragranular (intra-grain and intra-cement) paths along the fracture was measured. Fractures might be expected to follow the least resistant path, which could be the intergranular boundaries. After the measurements, however, the ratio of intergranular/intragranular path along the fracture is found to be close to 1:1.

Microscale textural effects exerted by growth mechanisms of cements were also examined as a potential control on crack trajectory by examination of the cathodoluminescence images. The syntaxial growth of quartz cement around quartz grains is often a weak mechanical junction owing to natural impurities and inclusions on the grain surface. This weak junction has been used by isotope geochemists to mechanically separate grains from cement. Thus, quartz cement deposition results in introduction of more flaws into the sandstone body in the form of overgrowth-overgrowth contacts and contacts between grains and cement. Calcite cement, on the other hand, forms very large crystals that enclose multiple grains and the surface area of crystal-crystal contacts for these calcite bodies is much less. Fracture path analyses indicate that for similar amounts of pore-filling cements, only 18% of the total fracture length cuts through quartz-overgrowths while it reaches to 38% intra-calcite cement path. Probably, when the fracture comes across a quartz overgrowth, it picks the least resistant path: overgrowth-overgrowth or grain-overgrowth contacts.

Overall, cement growth textures introduce more flaws in the case of quartz precipitation which might help to explain its lower SCI values (60, 71) compared to calcite-cemented sandstone (89, 101). The energy required to create a fracture is proportional to the fracture surface area and its specific surface energy (Lawn and Wilshaw, 1975). The differences in the microstructure of the quartz- and calcite-cemented sandstones alter the length and tortuosity of fracture paths, energy balance; and thus the subcritical index, as discussed further below.

4.2.1. Methods for Determining Microscale Textural Controls on SCI

Quantifying the link between petrographical properties and SCI could lead to increased predictive capability of the rock mechanical properties and fracture distribution patterns in the subsurface. In order to quantify the link between petrographical properties and rock mechanical properties, the following samples were analyzed petrographically and subjected to SCI testing: four outcrop samples from the Cambrian Flathead, Wyoming and Montana, four samples from the Cretaceous Frontier Formation, Wyoming, and thirty-one samples representing Williams Fork, Cozzette, and Rollins intervals of the Mesaverde Group (outcrop samples from the Rifle Gap, Colorado (16) and subsurface samples from the Last Dance well (8), Colorado, the Shell Brotherson 1-11 Well, Utah (2), and the MF31-19G well, Colorado (5)).

These samples were point counted (400 points/slide) with conventional petrographic microscope to determine framework grains, cement types, clay matrix content, and pore types. Selected samples were further examined with JEOL JSM-6490 LV scanning electron microscope (SEM) with an energy-dispersive X-ray system (EDS) for determining distribution and composition of cements. Cathodoluminescence (CL) attached to a Philips XL30 ESEM was used to image the SCI-induced fracture path on two samples. Fracture path analyses were done on the photomosaics of CL and accompanying secondary electron images (SEI) by using measurement tool in the Adobe PhotoshopTM program. Grain size was measured on the long axis of 100 random grains in each thin section.

4.2.2. Controls on the Subcritical Crack Index

4.2.2.1. Effects of Sandstone Texture on Fracture Propagation

The energy required to create a fracture is proportional to the fracture surface area and its specific surface energy (Lawn and Wilshaw, 1975). Fracture wandering, microcracking, and fracture branching are the three processes that increase the energy necessary for fracture propagation within granular material. *Fracture wandering* occurs because fracturing takes place in intergranular spaces; the crack-path is not straight and therefore longer than a comparable planar feature (Wu et al., 1978; Gesing and Bradt, 1983). *Microcracking* takes place because numerous microcracks develop within the crack-tip stress field (Gesing and Bradt, 1983). *Fracture branching* is formation of fractures in two or more separate branches (Wu et al., 1978).

A fracture propagates along the grain boundaries in intergranular fracturing and through the grains in transgranular fracturing. The propagation of a fracture following an intergranular path or transgranular path depends on flaw/grain size ratio in polycrystalline materials, when the ratio of flaw/grain size increases, the proportion of intergranular fracture with respect to transgranular fracture increases (Rice et al., 1980; Mussler et al., 1982). Olson et al. (2001) reported intergranular fracture growth being more common in sedimentary rocks. Because it provides the least resistant path intergranular growth is likely to be more prevalent than transgranular fracture growth in sedimentary rocks. However, the mineralogy and distribution pattern of authigenic minerals between grains can alter the intergranular contacts and therefore fracture paths in sandstones.

According to fracture propagation theory described by Gesing and Bradt (1983), large fractures (macrofractures) will propagate only when the local stress intensity factor

at all the micro-flaws exceeds the stress intensity necessary for the micro-flaws to propagate. This condition is satisfied when the apparent crack extension force equals the average extension force for all micro-flaw sizes. The flaws, which link to form the main crack, are always one grain facet, d , away from the crack tip since the crack is assumed to propagate along the grain boundaries. The crack extension force that has to be applied to the main crack in order to extend a flaw, a , can be calculated from the stress field analysis around the crack tip. With the assumption that the crack extends, on average, with subcritical fracture velocity until the local fracture toughness is exceeded, the subcritical index is predicted to be:

$$n = c \times \frac{a}{d} \times \frac{G}{G_0} \quad (\text{equation 4.4; Gesing and Bradt, 1983})$$

a = flaw length; d = grain size (facet); G = applied crack extension force, G_0 = critical crack extension force (material property), c = constant.

Following this equation, subcritical index of a material would decrease when the grain size of the material increases at a given condition.

In addition, a decrease in surface energy is expected to increase the subcritical index value. Surface energy is 1.34 J m^{-2} for quartz cement and 0.27 J. m^{-2} for calcite cement (Atkinson and Avdis, 1980).

4.2.2.2. Effects of Chemical Environment on SCI: Water Saturation

Chemical processes that weaken the bonds play an important role in subcritical cracking (stress corrosion cracking), therefore, fluid type present in the system is important (Atkinson and Meredith, 1981). In order to characterize fluid effects on SCI, Rijken et al. (2002) compared the SCI values tested under dry (ambient air) conditions

and submerged in water and oil. Although, a decrease in subcritical index was expected under water saturated conditions due to presence of water which is a reactive fluid (Meredith and Atkinson, 1989), they found out that the SCI value decreased for the finer-grained samples but increased for the coarser-grain size sandstones. They reported that the index values generally increased with oil content. Oil droplets decrease the accessibility of water to the silica bonds, thus allowing fewer of the bonds to be excited. Within petroleum reservoirs fluid saturation and distribution are variable, which may change the subcritical index value and, in turn, may alter the ultimate fracture pattern.

4.2.3. Results of Subcritical Crack Index Measurements

Fracture toughness and subcritical index are two parameters of particular importance in the fracturing process. There is a fair amount of experimental data on different rock types for these parameters; however, the degree that mineralogy and texture can control their magnitude is not well understood because it is difficult to isolate the effects of mineralogy and texture.

In order to elucidate the impact of mineralogical differences on rock mechanical properties, first a large group of samples were tested. The selected sample set includes: 1) quartz-rich, mainly quartz-cemented Flathead sandstones, 2) rigid lithic grain-rich, partially quartz-cemented Frontier Sandstones and 3) lithic-rich (ductile and rigid), outcrop and subsurface sandstones of Williams Fork cemented with varying amounts of clays, calcite, quartz, and Fe-dolomite. Results of SCI values measured in air and fracture toughness values calculated by the spreadsheet that is used for SCI calculations are listed in Table 4.1 and their distributions are plotted in Figure 4.2.

Table 4.1. Summary of subcritical crack index results for the Flathead, Frontier and Williams Fork samples (* Measurements from Rijken, 2005). SCI (n): Subcritical Crack Index; KIC: fracture toughness.

Sample	Formation	Type	Locality / Well	SCI (n)	KIC
WF-46	U. Williams Fork	Outcrop	Rifle Gap, CO	44.1	0.8
WF-44	U. Williams Fork	Outcrop	Rifle Gap, CO	30.5	0.2
WF-44	U. Williams Fork	Outcrop	Rifle Gap, CO	38.9	0.9
WF-44	U. Williams Fork	Outcrop	Rifle Gap, CO	36.9	0.8
WF-44	U. Williams Fork	Outcrop	Rifle Gap, CO	20.0	0.4
WF-43	U. Williams Fork	Outcrop	Rifle Gap, CO	46.8	0.2
WF-43	U. Williams Fork	Outcrop	Rifle Gap, CO	62.4	0.2
WF-41	U. Williams Fork	Outcrop	Rifle Gap, CO	52.4	0.1
WF-39	U. Williams Fork	Outcrop	Rifle Gap, CO	47.6	0.8
WF-39	U. Williams Fork	Outcrop	Rifle Gap, CO	48.2	0.9
WF-39	U. Williams Fork	Outcrop	Rifle Gap, CO	48.2	0.9
WF-39	U. Williams Fork	Outcrop	Rifle Gap, CO	43.2	0.7
WF-39	U. Williams Fork	Outcrop	Rifle Gap, CO	56.8	0.7
WF-38	U. Williams Fork	Outcrop	Rifle Gap, CO	14.8	0.4
WF-38	U. Williams Fork	Outcrop	Rifle Gap, CO	24.5	0.5
WF-38	U. Williams Fork	Outcrop	Rifle Gap, CO	21.0	0.4
WF-8	L. Williams Fork	Outcrop	Rifle Gap, CO	68.2	3.5
WF-8	L. Williams Fork	Outcrop	Rifle Gap, CO	126.3	2.3
WF-8	L. Williams Fork	Outcrop	Rifle Gap, CO	71.2	3.4
WF-7	L. Williams Fork	Outcrop	Rifle Gap, CO	10.8	0.1
WF-7	L. Williams Fork	Outcrop	Rifle Gap, CO	24.7	0.1
WF-7	L. Williams Fork	Outcrop	Rifle Gap, CO	22.9	0.1
WF-7	L. Williams Fork	Outcrop	Rifle Gap, CO	17.2	0.2
WF-6	L. Williams Fork	Outcrop	Rifle Gap, CO	18.6	1.1
WF-4	L. Williams Fork	Outcrop	Rifle Gap, CO	42.2	0.7
WF-4	L. Williams Fork	Outcrop	Rifle Gap, CO	17.4	0.9
WF-4	L. Williams Fork	Outcrop	Rifle Gap, CO	35.0	0.9
WF-3	L. Williams Fork	Outcrop	Rifle Gap, CO	44.6	1.1
WF-3	L. Williams Fork	Outcrop	Rifle Gap, CO	64.7	0.5
WF-3	L. Williams Fork	Outcrop	Rifle Gap, CO	71.2	0.8
WF-3	L. Williams Fork	Outcrop	Rifle Gap, CO	69.4	0.3
WF-2	L. Williams Fork	Outcrop	Rifle Gap, CO	30.7	0.2
WF-1	L. Williams Fork	Outcrop	Rifle Gap, CO	66.4	2.9
WF-1	L. Williams Fork	Outcrop	Rifle Gap, CO	27.0	3.1

Table 4.1. (ctd)

Sample	Formation	Type	Locality / Well	SCI (n)	KIC
RCC-1	Rollins	Outcrop	Rifle Gap, CO	49.7	0.3
RCC-1	Rollins	Outcrop	Rifle Gap, CO	43.6	0.3
RCC-1	Rollins	Outcrop	Rifle Gap, CO	25.2	0.5
RCC-1	Rollins	Outcrop	Rifle Gap, CO	43.1	0.2
RCCC-2	Rollins	Outcrop	Rifle Gap, CO	24.2	0.1
RCCC-2	Rollins	Outcrop	Rifle Gap, CO	35.0	0.1
CZTC-1	Cozette	Outcrop	Rifle Gap, CO	40.6	3.1
CZTC-1	Cozette	Outcrop	Rifle Gap, CO	45.4	2.8
CZTC-1	Cozette	Outcrop	Rifle Gap, CO	46.7	2.4
LD 2854	U. Williams Fork	Core	Last Dance, CO	101.1	2.7
LD 2854	U. Williams Fork	Core	Last Dance, CO	89.7	2.9
LD 3585.9	U. Williams Fork	Core	Last Dance, CO	145.2	3.8
LD 3585.9	U. Williams Fork	Core	Last Dance, CO	168.5	3.6
LD 3585.9	U. Williams Fork	Core	Last Dance, CO	67.8	5.7
LD 4016.9	U. Williams Fork	Core	Last Dance, CO	61.8	1.7
LD 4016.9	U. Williams Fork	Core	Last Dance, CO	59.1	1.3
LD 4016.9	U. Williams Fork	Core	Last Dance, CO	78.7	1.9
LD 4016.9	U. Williams Fork	Core	Last Dance, CO	62.6	1.5
LD 4381	U. Williams Fork	Core	Last Dance, CO	86.0	3.7
LD 4381	U. Williams Fork	Core	Last Dance, CO	53.9	3.5
LD 4381	U. Williams Fork	Core	Last Dance, CO	78.8	3.1
LD 5722.7	L. Williams Fork	Core	Last Dance, CO	51.8	3.0
LD 5722.7	L. Williams Fork	Core	Last Dance, CO	52.8	2.5
LD 5736.8	L. Williams Fork	Core	Last Dance, CO	56.1	2.6
LD 5736.8	L. Williams Fork	Core	Last Dance, CO	50.1	3.2
LD 5740	L. Williams Fork	Core	Last Dance, CO	37.2	3.5
LD 6332.7	L. Williams Fork	Core	Last Dance, CO	65.2	2.8
LD 6332.7	L. Williams Fork	Core	Last Dance, CO	55.5	3.8
LD 6332.7	L. Williams Fork	Core	Last Dance, CO	58.8	5.0
SB 12372	Cozette	Core	Shell Brotherson, UT	56.6	4.9
SB 12372	Cozette	Core	Shell Brotherson, UT	37.3	4.1
SB 12374.5	Cozette	Core	Shell Brotherson, UT	44.3	5.7
SB 12374.5	Cozette	Core	Shell Brotherson, UT	30.0	5.4
MF31 7333.7	Williams Fork	Core	MF31-19G, CO	91.5	3.0
MF31 7333.7	Williams Fork	Core	MF31-19G, CO	65.1	3.3
MF31 7333.7	Williams Fork	Core	MF31-19G, CO	78.7	2.9

Table 4.1. (ctd)

Sample Name	Formation	Type	Locality / Well	SCI (n)	KIC
MF31 7362	Williams Fork	Core	MF31-19G, CO	63.9	1.8
MF31 7362	Williams Fork	Core	MF31-19G, CO	51.2	0.4
MF31 10293	Williams Fork	Core	MF31-19G, CO	62.5	2.6
MF31 10293	Williams Fork	Core	MF31-19G, CO	69.9	2.5
MF31 10299	Williams Fork	Core	MF31-19G, CO	53.8	2.5
MF31 10299	Williams Fork	Core	MF31-19G, CO	64.3	2.2
MF31 10302.2	Williams Fork	Core	MF31-19G, CO	62.8	3.3
MF31 10302.2	Williams Fork	Core	MF31-19G, CO	77.4	
MF31 10302.2	Williams Fork	Core	MF31-19G, CO	78.0	3.4
CF-12	Flathead	Outcrop	Canyon Ferry, MT	60.9	6.6
CF-12	Flathead	Outcrop	Canyon Ferry, MT	71.3	7.2
TP-4	Flathead	Outcrop	Canyon Ferry, MT	82.4	3.0
TP-4	Flathead	Outcrop	Canyon Ferry, MT	79.0	3.2
TP-4	Flathead	Outcrop	Canyon Ferry, MT	66.9	3.5
SB-7	Flathead	Outcrop	Canyon Ferry, MT	38.4	4.4
SB-7	Flathead	Outcrop	Canyon Ferry, MT	97.6	3.8
SB-7	Flathead	Outcrop	Canyon Ferry, MT	57.3	3.8
EHPO-16	Flathead	Outcrop	Canyon Ferry, MT	70.5	1.0
JO_F1	Frontier	Outcrop	WY	55.9	1.3
JO_F1	Frontier	Outcrop	WY	73.3	1.1
JO_F2	Frontier	Outcrop	WY	61.4	2.1
JO_F2	Frontier	Outcrop	WY	70.5	2.1
JO_F2	Frontier	Outcrop	WY	46.5	1.9
JO_F3	Frontier	Outcrop	WY	47.6	1.5
JO_F3	Frontier	Outcrop	WY	47.6	1.4
JO_F3	Frontier	Outcrop	WY	60.4	1.1
JO_F4	Frontier	Outcrop	WY	39.8	2.3
JO_F4	Frontier	Outcrop	WY	44.8	2.2
JO_F4	Frontier	Outcrop	WY	46.7	1.9
MWX-1 7892 *	MWX-1/Cozette	Core	MWX-1, CO	66 ± 17	Dry
MWX-1 7892 *	MWX-1/Cozette	Core	MWX-1, CO	64 ± 16	
	Flathead	Outcrop?	WY	77 ± 11	Dry
SHCT 7892 *	SHCT/Cozette	Core	SHCT, CO	66 ± 17	
SHCT 7892 *	SHCT/Cozette	Core	SHCT, CO	64 ± 16	
SHCT 9002 *	SHCT/Cozette	Core	SHCT, CO	58 ± 6	
SHCT 9041 *	SHCT/Cozette	Core	SHCT, CO	54 ± 16	
SHCT 9071 *	SHCT/Cozette	Core	SHCT, CO	50 ± 9	

Although the index values are highly variable between 14.8 and 168.5 for this set of sandstones, most of the data points fall within the range of 38 to 65 (Figures 4.2 and 4.3). Overall, outcrop samples from the Williams Fork, especially the ones with lowest amounts of cements, and therefore the poorest degrees of consolidation, have the lowest SCI and K_{Ic} values. Differences in SCI and K_{Ic} values of well-consolidated core (Last Dance) and poorly-consolidated outcrop (Rifle Gap) samples of the Williams Fork samples are well presented with distribution graphs.

SCI vs. fracture toughness plot leads to some interesting points. Although some outlier data exist, the general tendency is such that with increasing fracture toughness SCI increases. Tightly quartz-cemented Flathead samples have the highest fracture toughness values (6.1-7.2 MPa \sqrt{m}) and their SCI values are in the mid-range of 55 to 60, similar to values that Rijken (2005) found for tightly quartz-cemented Cretaceous Travis Peak Formation sandstones. On the other hand, tightly calcite-cemented sandstones have SCI values close to 100 with fracture toughness values in the mid-range (~ 3 MPa \sqrt{m}) (marked with circles in Figure 4.3). These differences indicate that quartz cement is better at increasing the overall rock strength than calcite cement.

Representative load decay curves for the tightly quartz-cemented and tightly calcite-cemented sandstones show that the ranges in load differ significantly between the two: quartz cemented-sandstone required higher loads for initializing the fracture than the calcite-cemented sandstone (Figure 4.4A). The load decay curves are numerically differentiated to obtain the velocities. Following the equation for subcritical crack index (n), the slopes of the curves in the log-log plot of velocity against load gives the SCI value (Equation 4.2, Figure 4.4B).

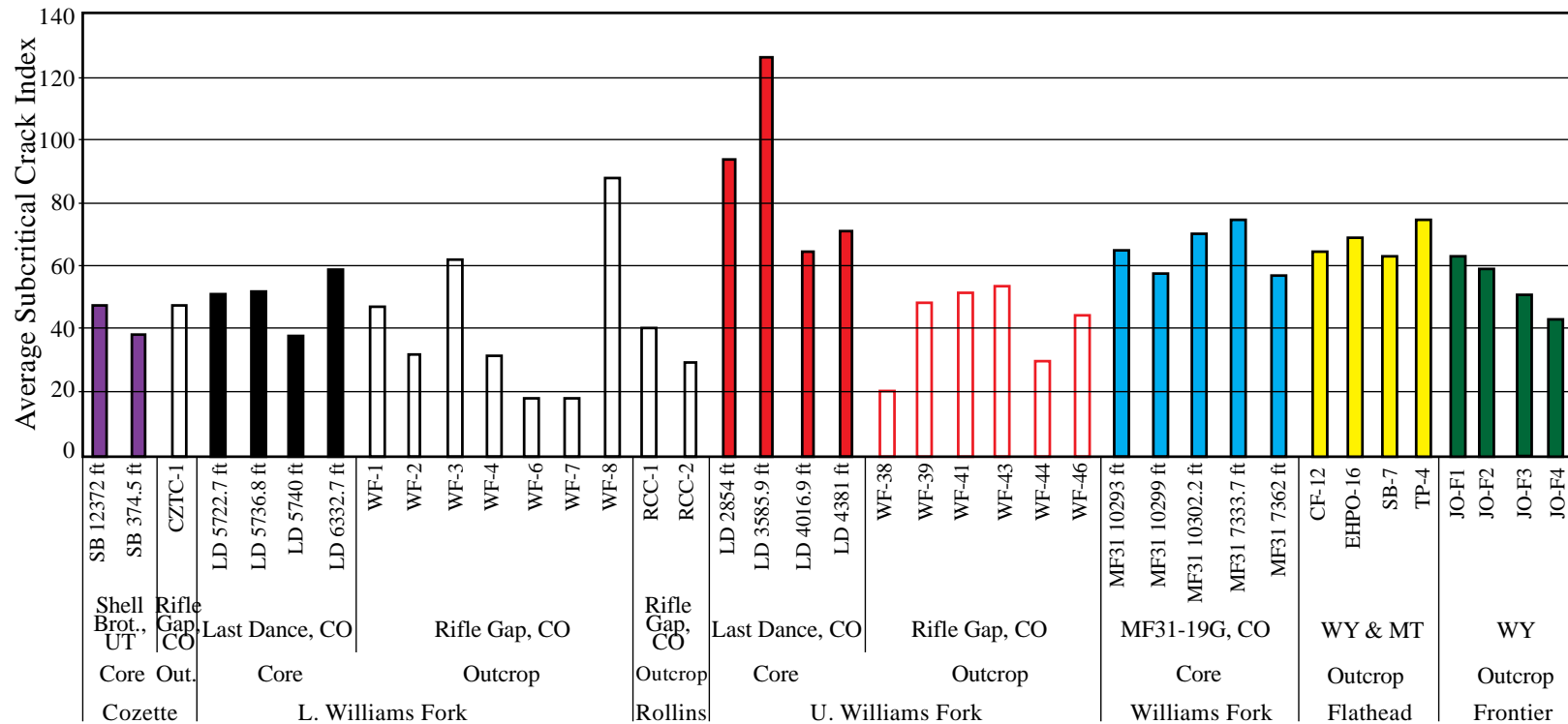


Figure 4.2. The distribution of subcritical crack index values and calculated fracture toughness for sandstones of different formations. The values plotted are the averages for each sample.

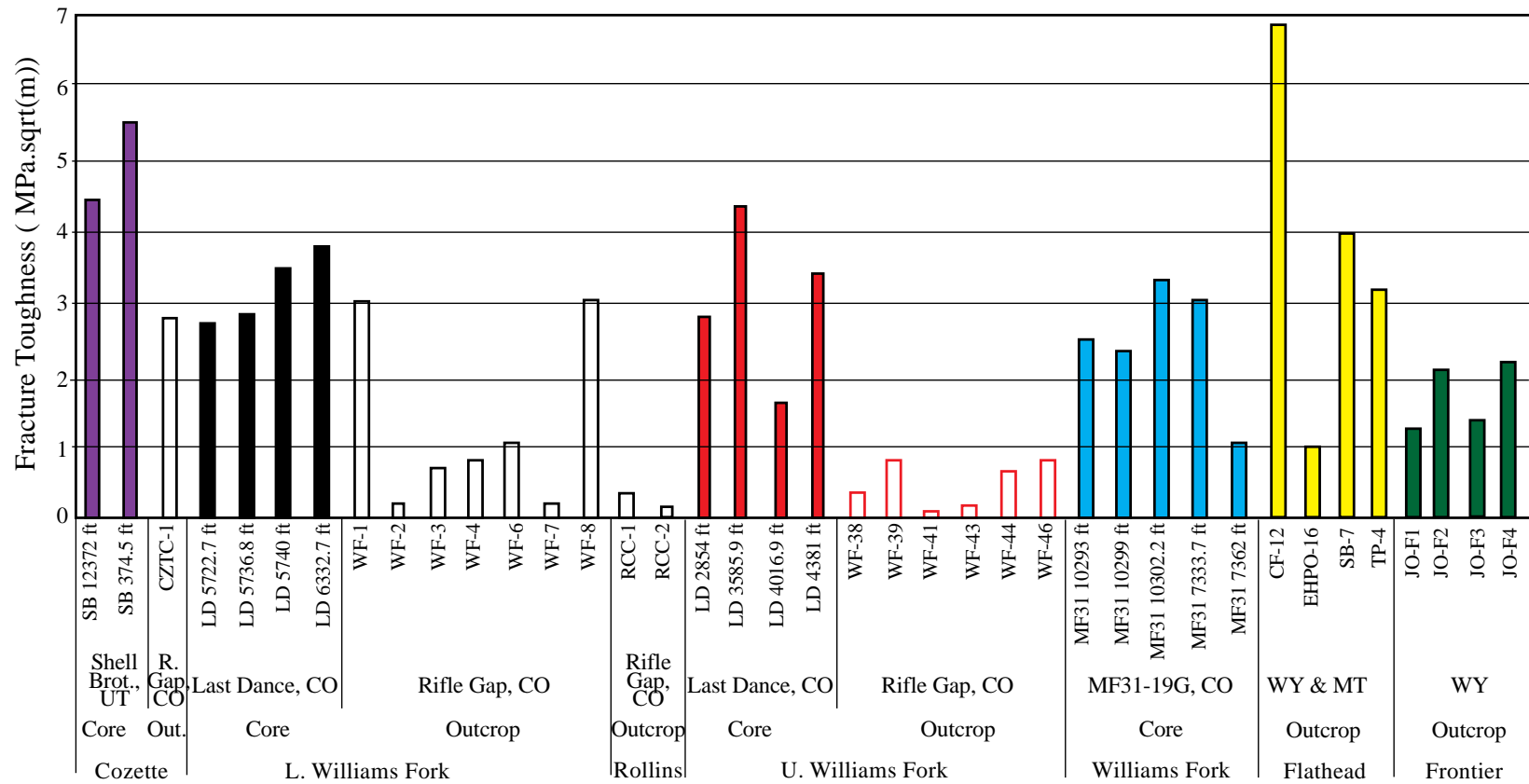


Figure 4.2. (ctd)

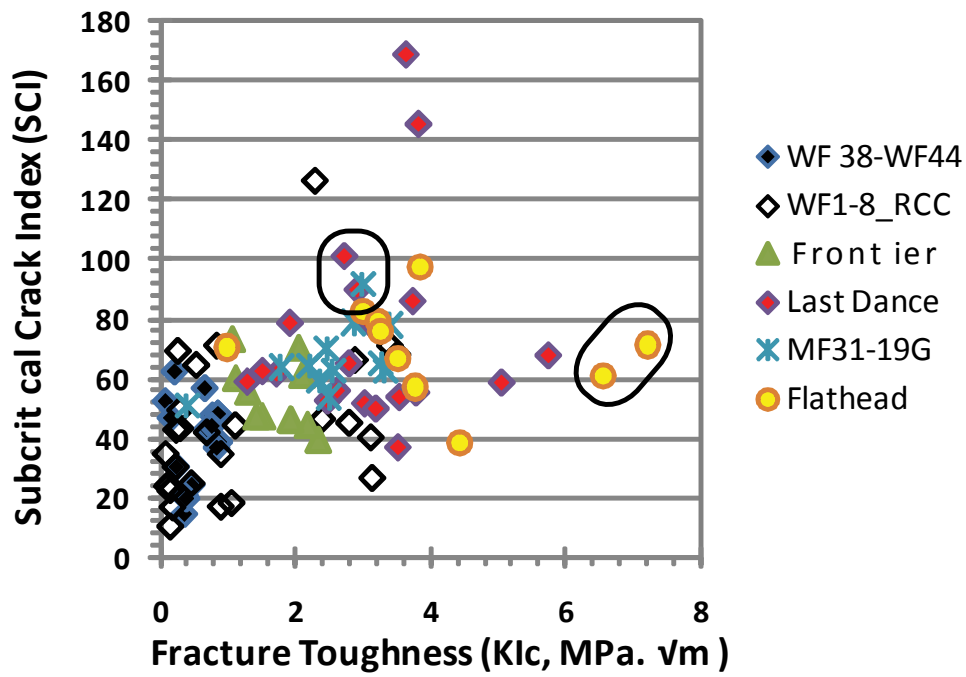


Figure 4.3. Plot of subcritical crack index versus fracture toughness. The toughness values are the predictions from the spreadsheet that is used to calculate the SCI. (UWF: Upper Williams Fork, LWF: Lower Williams Fork, Last Dance and MF31-19G (subsurface), Rifle (Rifle Gap outcrop)).

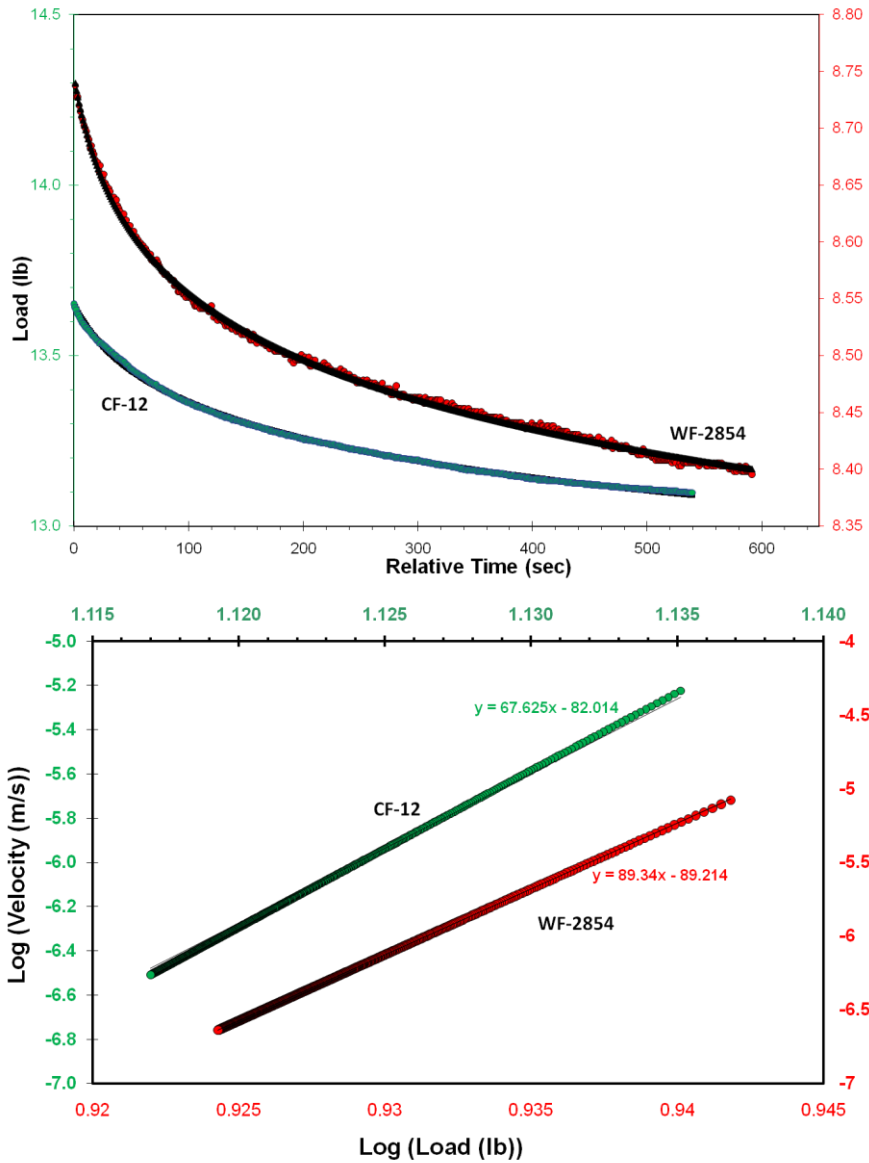


Figure 4.4. (A) Load decay curves measured for two samples. The total time for each test is approximately 10 min. The quartz-cemented Flathead Sandstone (CF12) has SCI of 67.6 and calcite-cemented Williams Fork (WF 2854 ft) has a value of 89.3. Test data points (red and green colored circles) and behavior predicted by equation 4.2 (black lines) indicate good agreement between expected and actual behavior. (B) Log-log plot of velocity (vertical axes), numerically computed from equation 4.3, against load (horizontal axes). The slopes of the two curves are the subcritical indices. The appropriate y (load)-axes are indicated by matching colors with data points (CF-12 for left axis and WF-2854 for right).

4.2.4. Discussion: Diagenetic Controls on SCI

The measurements on this set of sandstones are the first steps in investigating the systematics of subcritical index variations and assessment of how microscale structures influence subcritical index values. Many cross plots are provided in Figure 4.5; however, not all of them show clear patterns. The key observation is that despite the differences in sandstone composition and amount and type of pore-filling cements, SCI increased with increasing content of total cement. Total porosity has the opposite effect on the SCI (Figure 4.5). As cement content goes up and porosity goes down, subcritical crack index increases. More porous and less cemented samples probably have a higher number of less resistant paths for intergranular growth. Increasing cement content reduces the number, size and continuity of flaws, leads to better-consolidated sandstones and increases the SCI. Calcite appears to increase the SCI and for the outcrop Williams Fork samples presence of zeolite in the pore system leads to higher SCI values. Rijken et al. (2002) found an increase in index value with decreasing quartz cement, increasing carbonate cement (up to 8%), decreasing grain size and increasing pore size for constant chemical environment.

As explained earlier, the flaw lengths are longer in the coarser-grained samples if the fracture propagates through intergranular paths leading to lower SCI values which affect the fracture distribution patterns. Overall the data distribution agrees with this idea and suggests that SCI is lower in coarser grain size sandstones. However, when the data points are examined closely, Frontier and Flathead samples with more rigid framework grains have SCI values that increase with grain size and Williams Fork samples with both rigid and ductile grains hold to the opposite trend. The grain size issue carries importance

because most sedimentary deposits have gradations in grain size. If the coarser sandstones are expected to have lower SCI values, keeping other conditions the same, if other rock properties, bed thickness and loading conditions are the same, they are expected to have shorter and more closely spaced fracture distributions than those in fine-grained sandstones (Olson, 2004). The grain size effects need to be analyzed with more care perhaps using sample sets of same grain size but varying cements or using a set of sandstones with similar mineralogies but varying grain sizes.

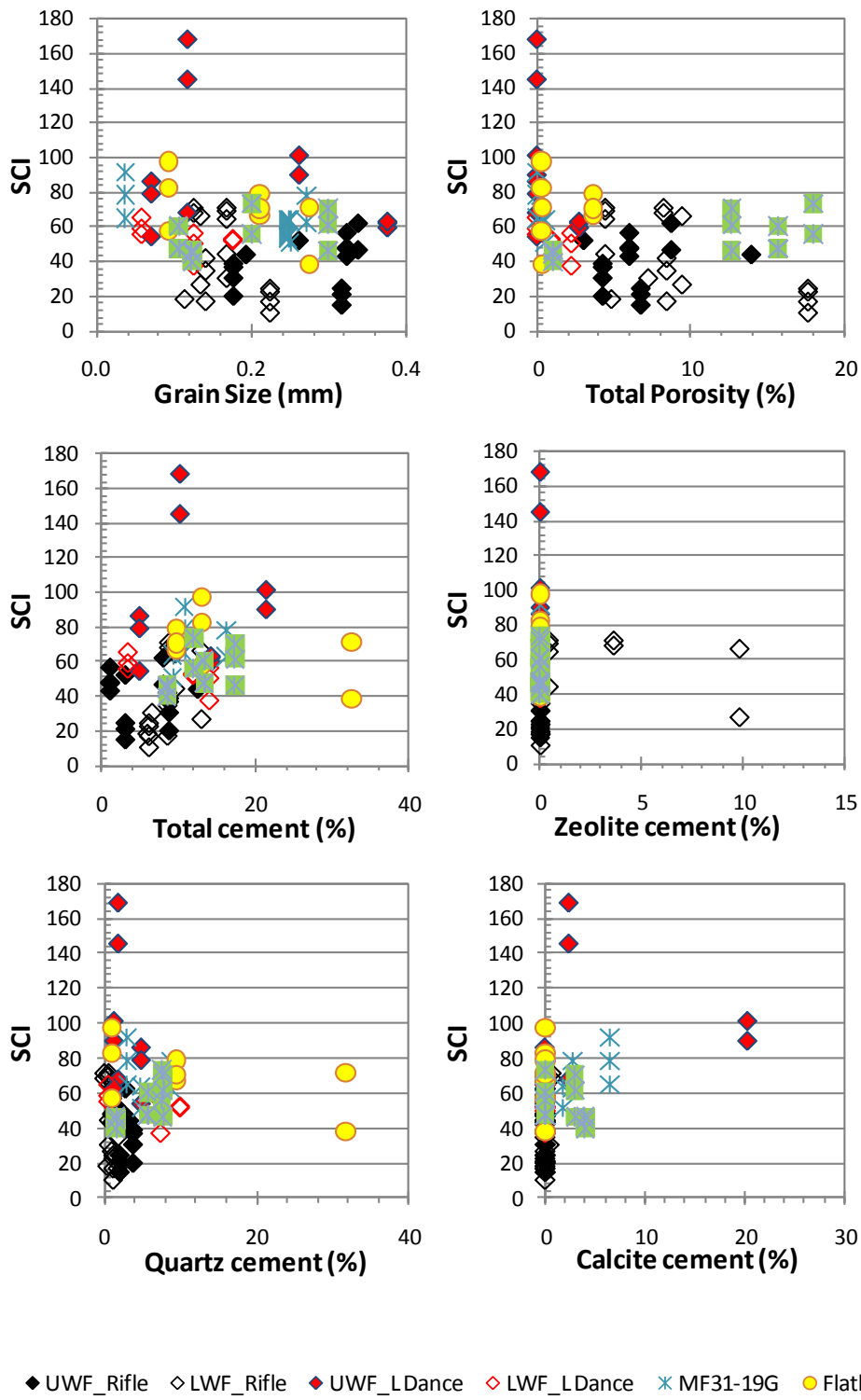


Figure 4.5. Plot of subcritical crack index versus petrographic parameters.

4.2.5. Discussion: Microscale Mineralogical and Textural Controls on SCI: Fracture Path Analyses in Quartz- and Calcite-cemented Sandstones

In order to understand the effects of pore-filling cement mineralogy on fracture paths, the fractures introduced by SCI testing were imaged with cathodoluminescence for a tightly quartz-cemented sandstone from the Flathead Formation (CF-12) and a tightly calcite-cemented sandstone from the Williams Fork Formation (LD 2854 ft). These samples had the fractures induced by the SCI testing, however, they were intact. The path the fracture took was traced and lengths of the grain/grain, grain/cement, cement/cement and intra-grain and intra-cement boundaries long the fracture path was noted (Figure 4.6). The results are listed in Table 4.2. Using CL was especially helpful for analyzing the quartz-cemented sandstone where differentiating between quartz grains and quartz overgrowths is difficult using other microscopy methods.

The amount of total framework grains (68.3% vs. 72.8%) and amount of pore-filling cements (31.7% vs. 27.3%) were pretty close for the quartz-cemented and calcite-cemented sandstones respectively (Table 4.2). Other than the induced fracture pores, samples had trace amounts of pore space. Measurements lead to SCI values of 60.9 & 71.3 for quartz-cemented sandstone and 101.1 and 89.7 for the carbonate-cemented sandstone. So, for about the same amount of pore-filling cement, we observe differences in the SCI values of the two samples. Lower surface energy of calcite (0.27 J m^{-2}) compared to quartz (1.34 J m^{-2}) helps to increase subcritical index values for calcite cement. In addition, authigenic mineral phases not only affect the SCI through differences in surface energy, but also they introduce microscale textural differences.

One should examine the microstructures introduced by the growth mechanisms of the two cements to understand their textural effects in the whole sandstone body. Quartz

cement tends to form syntaxial overgrowths around quartz grains -the most common grain in sandstones. Calcite cement, on the other hand, does not grow syntaxially over quartz grains. Calcite can occur in sizes of discrete pore-filling patches to very large crystals that encompass many grains within them (poikilotopic texture). When it forms in local patches carbonate-cemented sandstones could have highly variable microstructures. However, that it is not a problem for the analyzed sample because every single pore is filled with calcite cement.

In addition to grain-grain and grain-cement contacts, planar crystal contacts are present where two quartz overgrowths grow next to each other which introduce flaws to the rock system. In the case of poikilotopic calcite cement, contacts between crystals exist but due to large crystals sizes, overall surface area associated with such contacts would be smaller. Overall, there are more flaws available in the quartz-cemented sandstones which probably is the reason of the lower SCI compared to calcite-cemented sandstone.

Following this argument, if the tightly cementing carbonate was dolomite or Fe-dolomite which tends to make rhombic overgrowths (overgrowths around dolostone substrate or crystals attached to other grains) an index value less than a tightly calcite-cemented sandstone but similar to quartz-cemented sandstone would have been expected. In fact, a sandstone from the deep intervals of the Williams Fork has common amounts of Fe-dolomite cement (13%) and its index measurements are 55, 58 and 65 which agrees with this argument. Rijken (2005) reported average subcritical index value of 62 ± 25 for sandstones and 120 ± 87 for carbonates with the exceptions of vuggy carbonates, dolopackstones (Clear Fork Formation) and a dolowackestone (Clear Fork Formation)

which tend to have indices more similar to sandstones. She interpreted the outlier dolomite data being related to larger grain sizes, however, it could very well be related to the crystal growth textures.

For similar amounts of pore-filling quartz and calcite cements, only 18.1% of the total fracture length cuts through quartz-overgrowths while it reaches to 36% in intra-calcite fractures. One possibility, when the fracture comes across a quartz overgrowth, it picks the least resistant path and goes between the overgrowths or grain-overgrowth contacts.

When the total fracture path lengths were compared to the planar distances from start to end (tip to tip) of the fractures, tortuosity is found to be remarkably similar. In both cases, the fractures have wandered about 13% longer than if they had followed a straight tip-to-tip path. This is a surprising result because I would have expected a more tortuous pathway in the quartz-cemented sandstone because of the zig-zag path it takes between grains, cements etc. than the straighter, cement-cutting fracture of the calcite-cemented sample.

Overall, total intragranular paths (intragrain and intracement) were 42.6 % for the quartz-cemented sandstone and 47.8% for the calcite-cemented sandstone. So, intergranular paths are not as common as it would have been predicted with the idea that fracture would follow the least resistant path.

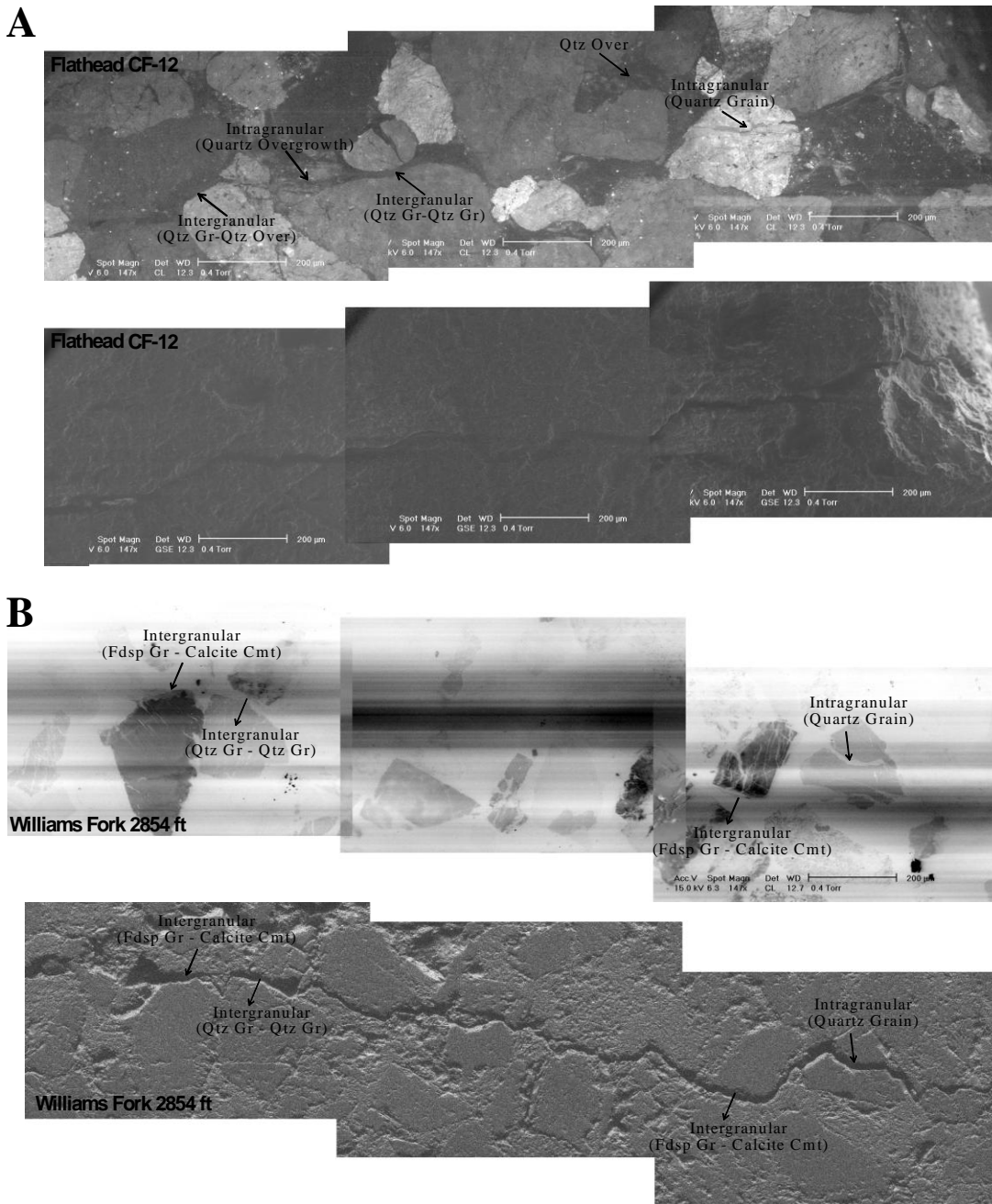


Figure 4.6. CL (Cathodoluminescence) and SEI (Secondary Electron Image) image pairsshowing the fracture propagation paths for the (A) tightly quartz-cemented Flathead sandstone (Canyon Ferry locality, Montana) and (B) tightly calcite-cemented Upper Williams Fork sandstone (Mamm Creek field, Piceance Basin).

Table 4.2. Results of fracture path analyses for quartz-cemented Flathead and calcite-cemented Williams Fork sample.

FRACTURE PATH THROUGH SANDSTONE		
	Flathead CF-12	Williams Fork 2854 ft
BETWEEN CEMENT & GRAIN (%)		
Quartz Grain - Quartz Over	29.6	
Quartz Grain - Calcite Cement		31.3
Feldspar Grain - Calcite Cement		12.5
BETWEEN CEMENTS (%)		
Quartz Over - Quartz Over	6.8	
BETWEEN GRAINS (%)		
Quartz Grain - Quartz Grain	21.0	8.4
Total Intergranular Path (%)	57.4	52.2
INTRA-CEMENT (%)		
Intra Quartz Overgrowth	18.1	
Intra Calcite Cement		36.0
INTRA-GRAIN (%)		
Intra Quartz Grain	24.5	6.2
Intra Feldspar Grain		1.5
Intra Lithic		4.1
Intra Lithic (rigid)		
Total Intragranular Path (%)	42.6	47.8
Total Fracture Length (microns)	28488	10303
Total Planar Length (microns)	25017	9133
Fracture Length / Planar Length (%)	13.9	12.3
Aperture (microns)	15.0	13.5

Table 4.2. (ctd)

PETROGRAPHY: MODAL ANALYSES (%)		
	Flathead CF-12	Williams Fork 2854 ft
FRAMEWORK GRAINS		
Quartz grains	67.2	30.5
Feldspar grains	0.0	13.5
Lithic grains	0.0	27.8
Accessory grains	1.1	1.0
Total	68.3	72.8
AUTHIGENIC MINERALS		
Quartz cement	31.7	1.3
Calcite cement	0.0	20.3
Calcite replacements	0.0	5.8
Total	31.7	27.3
MECHANICAL PROPERTIES		
SCI Values		
	60.9	101.1
	71.3	89.7
KIC (Mpa.\sqrt{m}, estimated)		
	6.6	2.7
	7.2	2.9

4.2.6. Conclusions: Crack-Path Mapping

In order to determine the mineralogical and textural controls exerted by different authigenic minerals on subcritical crack index (SCI), was measured for a group of sandstones with varying compositions, pore-filling cements, and porosity. Despite the differences in sandstone composition and amount and type of pore-filling cements, SCI increased with increasing content of total cement while total porosity had the opposite effect on the SCI. Overall data distribution suggests that SCI decreased with coarser grain size. Quantifying mineralogical effects on SCI is important because it could lead to prediction of SCI values for a given mineralogy of sandstone which in turn could provide implications for fracture distribution in the subsurface. As stated earlier, influence of subcritical crack index on fracture spacing, fracture-spacing length distributions, connectivity, and fracture aperture are illustrated in geomechanical models introduced by Olson et al. (2001).

The mineralogy and distribution pattern of authigenic minerals between grains can alter the intergranular contacts and flaw distribution, and therefore, fracture paths in sandstones. The unique paths that SCI-induced fractures followed through quartz-cemented and calcite-cemented sandstones suggest that microscale textural differences between cement growths can affect the fracture propagation and control the subcritical index. Subcritical index trends with varying volumes of calcite cement can be more difficult to predict because of textural differences in its occurrence.

Fe-dolomite is another important carbonate cement observed in the sandstones. The SCI values associated with Fe-dolomite-cemented sample are closer to quartz-

cemented sandstone and much less than calcite-cemented sandstone which might be an indication of textural controls over the subcritical fracture behavior.

4.3. QUANTIFICATION OF EFFECTS OF CEMENTATION ON SCI BY COMPARISON OF OUTCROP AND SUBSURFACE SAMPLES OF WILLIAMS FORK FORMATION

Subcritical crack index is a rock mechanical property that influences fracture characteristics (aperture distribution and clustering) (Olson et al., 2009). Subcritical crack index measurements performed on samples yield a value for the present day characteristics of the rock. At the time of fracturing sandstone might have been at a different diagenetic stage (degree of compaction, cementation, porosity, permeability, etc.) linked to its burial and thermal history. As the degree of lithification changes during burial through compaction and cementation, the rock's response to fracturing may change in concert.

In order to determine the range of subcritical crack index values for a sandstone of given framework composition at different diagenetic stages, measurements were made on a set of Williams Fork core samples and their outcrop equivalents. These core and outcrop samples have contrasting burial and thermal histories related to burial and uplift associated with the Late Cretaceous to Tertiary Laramide orogeny and subsequent orogenic movements (Cerveny and Steidtmann, 1993; Tristan-Gonzales et al., 2009; Lawton, 2008). Differences in thermal histories were clearly reflected in the amount of quartz cementation which mainly controlled the degree of consolidation. While deeply buried core samples represent well-consolidated end-members, their outcrop equivalents are used as contrasting, poorly to moderately consolidated end-members for subcritical crack index measurements. Wide variations between SCI values from outcrop and core

samples have proven the effects of diagenesis on rock mechanical properties and the need for integrating diagenesis into geomechanical models for more accurate prediction of fracture network characteristics.

The results of this study also indicate that caution is needed using the outcrop samples as petrographic analogs to subsurface rocks. The burial histories should be well understood and amount of quartz cement should be predicted for the subsurface, because quartz precipitation can alter the rock mechanical properties. In addition, outcrop alterations including kaolinite, Fe-oxide, zeolite, siderite, and calcite can change the diagenetic and mechanical characteristics of the rock a great deal.

4.3.1. Study Area, Piceance Basin, Colorado

Naturally fractured Late Cretaceous Mesaverde Group sandstones of the Piceance Basin (NW Colorado) were selected for this study due to their wide range in burial histories which control the diagenesis the sandstones go through: burial depths between 2 and 6 km and temperatures between 70 and 170 °C (Nuccio and Roberts, 2003). Diagenetic differences in these sandstones provide an opportunity to evaluate their effects on rock mechanical properties. Outcrop samples are from the Rifle Gap Locality (Figure 4.7) and the subsurface samples used are mainly from the study well (Last Dance) located in the Mamm Creek field, which is about 12 miles from the outcrop location (Figure 4.7). Although a few other samples were also analyzed from two other wells, the main comparison is between Rifle Gap outcrop samples and Last Dance well subsurface samples (Table 4.3). Proximity of these two locations provides reduced variation in the framework mineralogy of the sandstone between the two study areas. This sampling

strategy thus largely avoids compositional variability from provenance such as those reported in earlier studies that document a change in the sandstone framework composition due to provenance controls, specifically an increase in the amount of volcanic rock fragments in SW regions in close proximity to Mogollon Highlands (Johansen, 1986).

4.3.2. Depositional History

The Late Cretaceous Mesaverde Group is composed of the Iles and Williams Fork formations. The Iles Formation overlies the marine Mancos Shale and includes regressive marine sandstone cycles of the Corcoran, Cozzette, and Rollins members which are separated by tongues of marine Mancos Shale. The sandstones in these cycles are laterally continuous and can be correlated across much of the southern and eastern Piceance. The Williams Fork Formation is composed of coastal plain, fluvial and flood plain deposits. Details of the Mesaverde Group stratigraphy in the Piceance Basin can be found in Johnson and May (1980), Johnson (1989), Cole and Cumella (2003), Hettinger and Kirschbaum (2003), and Pranter et al. (2007).

4.3.3. Methods for Outcrop/Subsurface Comparison

Subsurface samples are from sandstone intervals of the study well (Last Dance, Mamm Creek field) between 853 and 1926 meters (2800 and 6321 ft) and outcrop samples were collected from 3800 feet of Williams Fork deposits at the Rifle Gap locality (Figures 4.7 and 4.8). 275 subsurface samples and 75 outcrop samples representing Ohio Creek, Upper Williams Fork, and Lower Williams Fork units (including Upper and

Middle Sandstone Members and Cameo interval deposits) were available for petrographical examination.

Samples tested for SCI were point counted (400 points / slide) with conventional petrographic microscope to determine framework grains, cement types, clay matrix content, and pore types. Selected samples were further examined with JEOL JSM-6490 LV scanning electron microscope (SEM) with an energy-dispersive X-ray system (EDS), cathodoluminescence (CL) attached to a Philips XL30 ESEM and JEOL JXA-8200 electron microprobe for determining cement distribution and composition. Grain size was measured on the long axis of 100 random grains in each thin section.

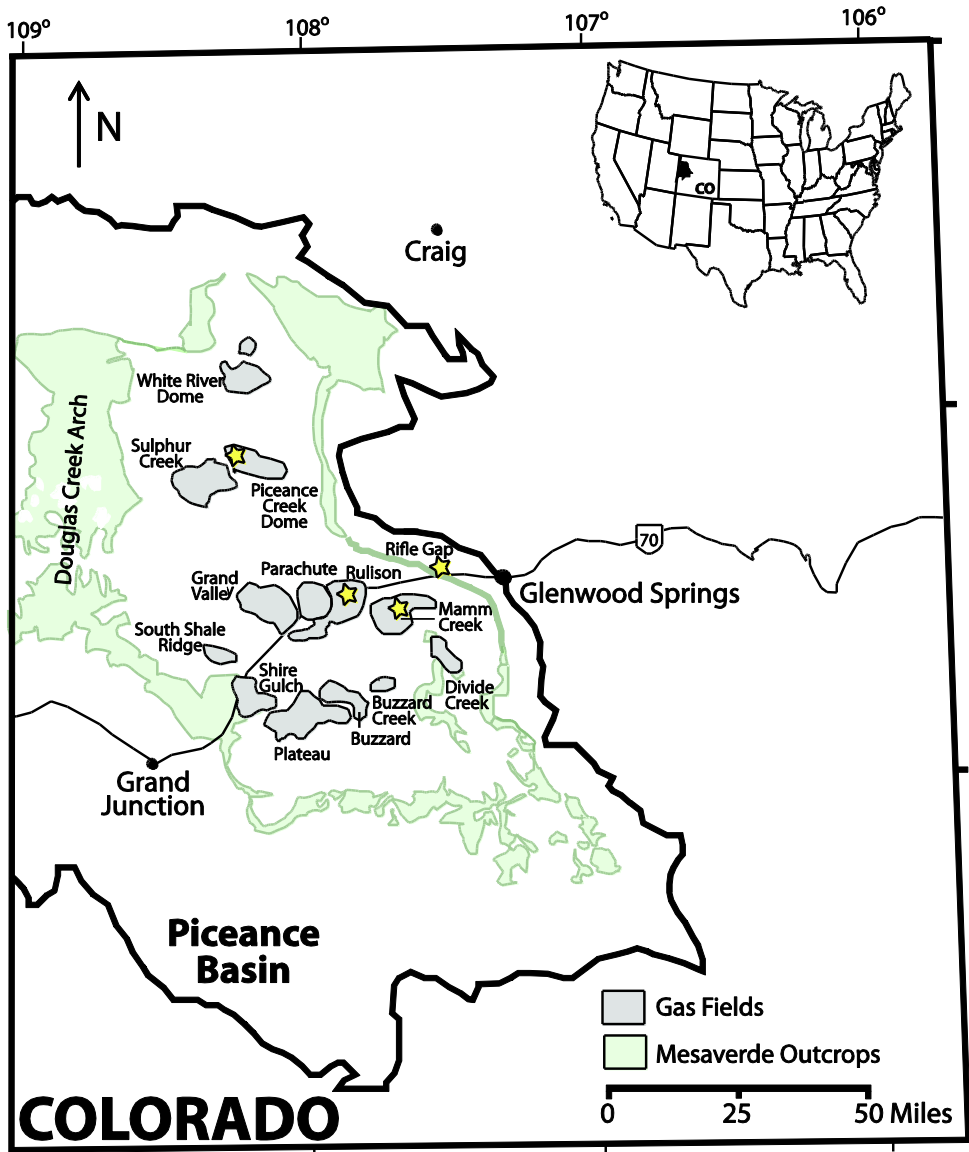


Figure 4.7. Map of Piceance Basin showing the location of well sites for the subsurface samples and outcrop sample location at Rifle Gap area.

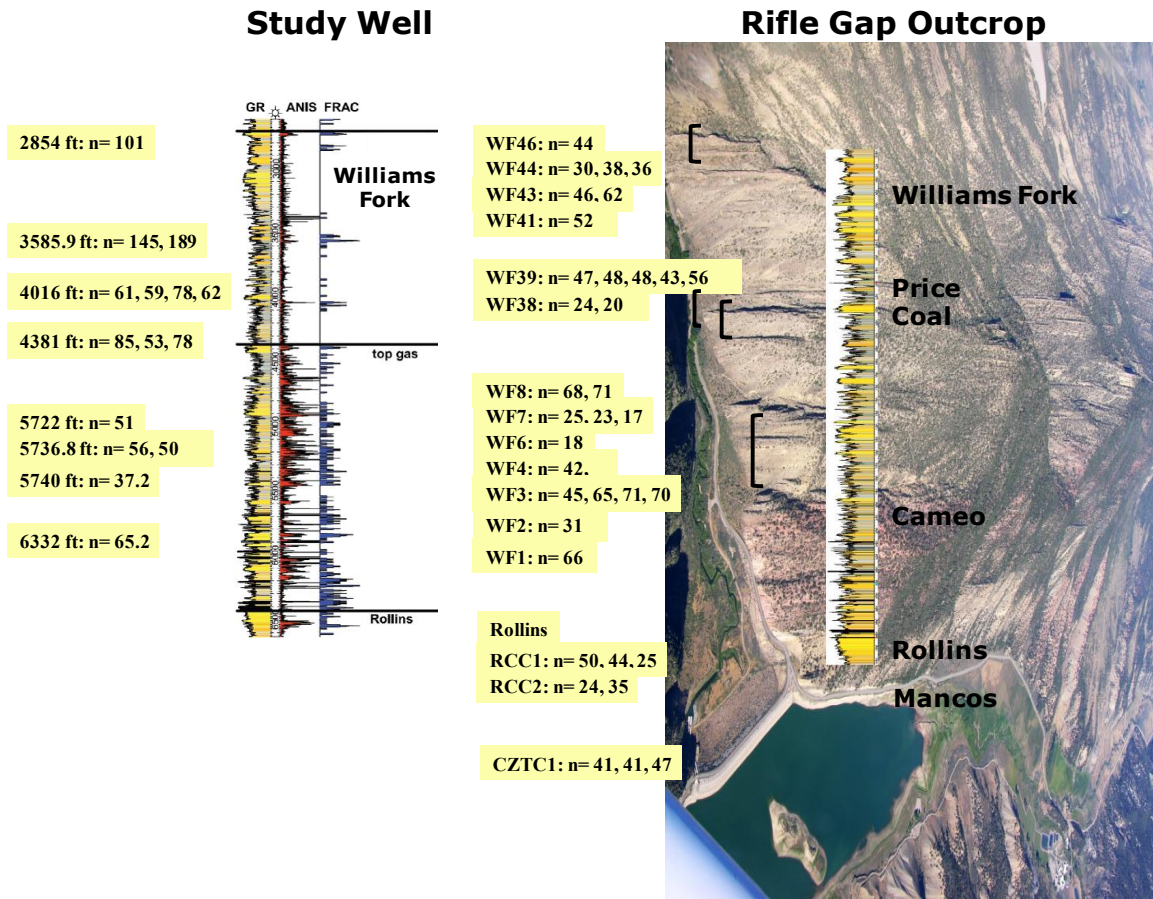


Figure 4.8. Gamma-ray curves for the study well (Last Dance) and well nearby the Rifle Gap outcrop were correlated in order to match the sandstone intervals. Subcritical crack index values are shown in yellow boxes.

4.3.4. Petrographical Comparison of Rocks

The Williams Fork is composed of very fine- to medium-grained, lithic-rich sandstones, siltstones and mudrocks deposited in fluvial to coastal-plain settings. The composition varies from lithic arkose to litharenite in the subsurface samples and litharenite to feldspathic litharenite in the outcrop samples according to Folk's classification scheme (1980) (Figure 4.9A). The less arkosic composition of the outcrop samples is probably a result of higher degree of grain dissolution. As it can be observed

in Figure 4.9B, there are differences in the distribution of the major lithic components as well. Mainly, outcrop samples are characterized by less abundant volcanic rock fragments. Petrographic examinations suggest that this is likely to be controlled by dissolution and alteration to clays.

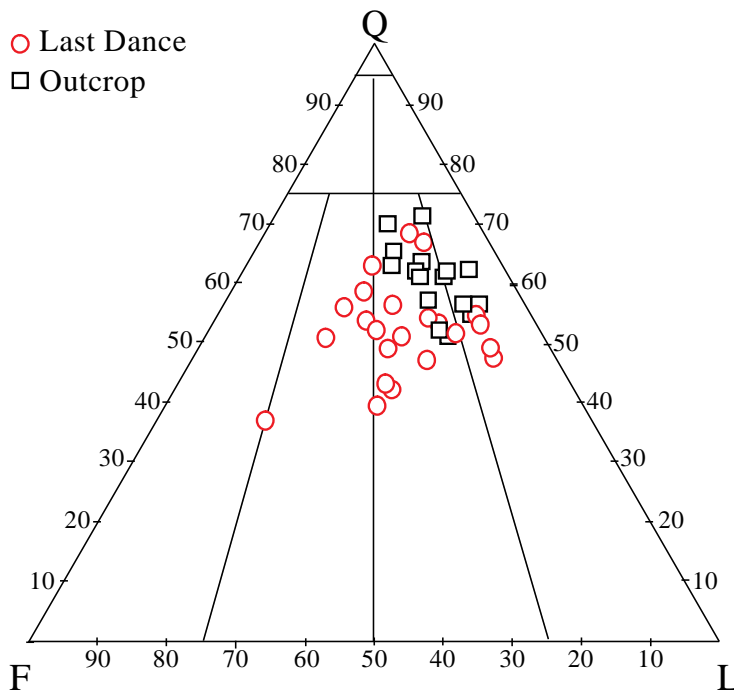


Figure 4.9. (A) Ternary diagram illustrating the differences in detrital composition of outcrop and subsurface sandstones based on ratios of detrital quartz, feldspar, and lithic fragments (Q:F:L). Sandstone clans are designated according to the classification of Folk (1980).

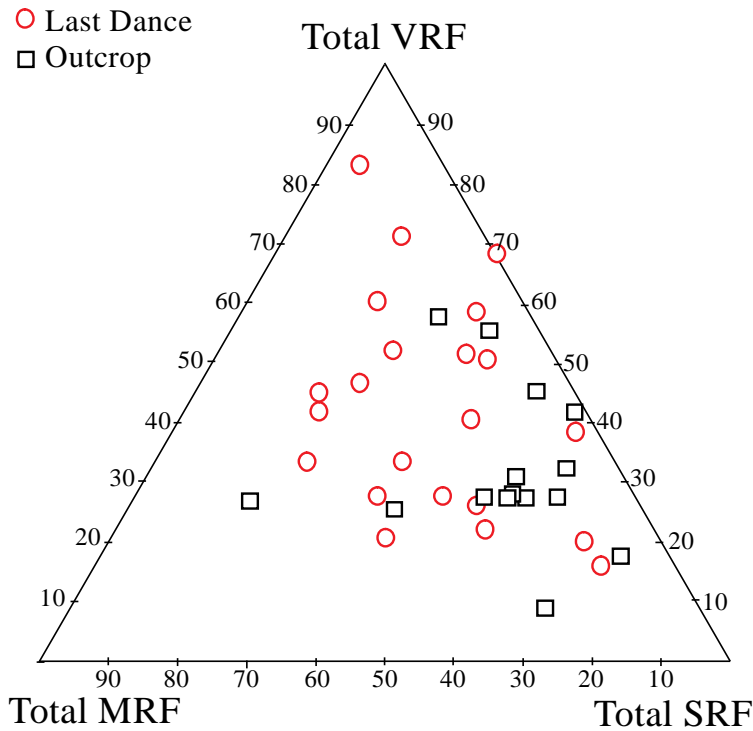


Figure 4.9. (B) Ternary diagram that illustrates the distribution of lithic grains (VRF: Volcanic Rock Fragments; MRF: Metamorphic Rock Fragments; SRF: Sedimentary Rock Fragments).

Although it is more pronounced at the subsurface, in both core and outcrop samples observed range in reservoir quality reflects the variable diagenetic histories across primary variations in provenance (grain composition), depositional systems, and textures. Comparison of subsurface samples with their outcrop equivalents has shown major differences in the type and amount of cement. At the subsurface Williams Fork is tightly cemented and well-consolidated, whereas at the outcrop it is characterized by much less cement and poor consolidation. In the subsurface most of the intergranular pore space is lost to cementation by varying amounts of quartz, calcite, Fe-dolomite,

mixed-layer illite/smectite, and chlorite, and sparse siderite, pyrite, ferroan calcite, kaolinite, sphene, zeolite, and gypsum. In the outcrop samples, on the other hand, quartz cement is noticeably less, and kaolinite, zeolite and siderite are more commonly observed. Upper Williams Fork is characterized by developments of chlorite and illite/smectite grain-coats in the subsurface samples according to my petrographic observations. The absence of grain-coating mixed-layer illite/smectite or chlorite in the outcrop is surprising, because according to the textural relations I observed in thin sections I interpreted the grain-coating clays to have formed relatively early in diagenesis before the burial histories of outcrop and subsurface samples diverged (Section 3.6.2). Grain-coating clays; therefore, likely formed later, during deeper or more protracted burial not experienced by rocks in outcrops. In place of grain-coating clays, zeolite cement was observed at the outcrop samples. While porosity consists mainly of micropores with only minor amounts of primary intergranular, secondary intragranular pores in the subsurface samples, outcrop samples have abundant primary pores and minor amounts of secondary pores.

4.3.5. Results of Subcritical Crack Index Measurements for Outcrop/Core Pairs

Petrographical heterogeneity is reflected on the subcritical crack index values, which are highly variable for both outcrop and subsurface samples (Table 4.3, Figures 4.10A & B). Outcrop samples from the Williams Fork, especially the ones with lowest amounts of cements, and therefore the poorest degrees of consolidation, have the lowest SCI and KIC values. Differences in SCI and KIC values of well-consolidated subsurface (Last Dance) and poorly-consolidated outcrop (Rifle Gap) samples of the Williams Fork

samples are clear in distribution graphs. Upper Williams Fork samples have greater SCI values compared to the Lowest Williams Fork samples both in the outcrop and subsurface. Subsurface samples from the MF31-19G well are characterized by tight calcite and quartz cementation which results in relatively high SCI values.

Figure 4.11 presents cross plots illustrating petrographic parameters against subcritical crack index. In general, SCI and KIC values follow a trend of increase with increasing amounts of total cement and decreasing pore space, probably because the introduction of cements results in a decrease in number of flaws. Calcite and zeolite cements appear to be more effective in increasing SCI than the quartz cement. For example, the outcrop samples WF-1 and WF-8 with relatively high SCI values have moderate amounts of zeolite cement, 9.8% and 3.6% respectively. The distribution of zeolite cement in the pore space is very similar to calcite cement: as small crystals filling individual pores or large patches of cement enclosing grains and filling multiple pores. This might be another example of microtextural controls on the SCI as well as mentioned in section 4.2.5. General relations with grain size is such that with increasing grain size both KIC and SCI decrease, but this trend exerted by grain size on SCI dissipates for the grain sizes larger than 0.18 mm.

Outcrop samples with high compaction indexes (Icomp) have more loss of pore spaces through compaction than cementation (COPL (Compactional Porosity Loss) > CEPL (Cementational Porosity Loss); calculation of these values are explained in Chapter 3). The plots show that the samples with the highest compaction indices have relatively lower SCI values. This illustrates having cements as binding agents is more effective than compaction in consolidating the sandstones.

Table 4.3. Results of subcritical crack index testing (SCI) and calculated fracture toughness (K_{Ic}) for the Mesaverde sandstones. The sample type, formation name, localities and number of measurements per sample are also listed.

Type	Formation	Well/Locality	Sample	Average K _{Ic}	Average SCI	No. of Samples	
Core	U. Williams Fork	Last Dance, CO	LD 2854 ft	2.80	95	2	
			LD 3585.9 ft	4.38	127	3	
			LD 4016.9 ft	1.59	66	4	
			LD 4381 ft	3.44	73	3	
	L. Williams Fork	Last Dance, CO	LD 5722.7 ft	2.73	52	2	
			LD 5736.8 ft	2.89	53	2	
			LD 5740 ft	3.50	37	1	
			LD 6332.7 ft	3.86	60	3	
	Williams Fork	MF31-19G, CO	MF31 7333.7 ft	3.04	78	2	
			MF31 7362 ft	1.10	58	3	
			MF31 10293 ft	2.50	66	2	
			MF31 10299 ft	2.35	59	2	
			MF31 10302.2 ft	3.36	73	2	
	Cozette	Shell Brotherson, UT	SB 12372 ft	4.48	47	2	
			SB 12374.5 ft	5.57	37	2	
	Outcrop	U. Williams Fork	Rifle Gap, CO	WF-46	0.77	44	3
WF-44				0.59	32	5	
WF-43				0.19	55	1	
WF-41				0.09	52	2	
WF-39				0.77	49	4	
WF-38				0.40	20	1	
L. Williams Fork				WF-8	3.06	89	2
				WF-7	0.15	19	1
				WF-6	1.05	19	4
				WF-4	0.82	32	3
Rollins			WF-3	0.68	62	1	
			WF-2	0.23	31	4	
			WF-1	3.00	47	3	
Cozette			RCC-1	0.32	40	4	
			RCCC-2	0.09	30	2	
				CZTC-1	2.76	44	3

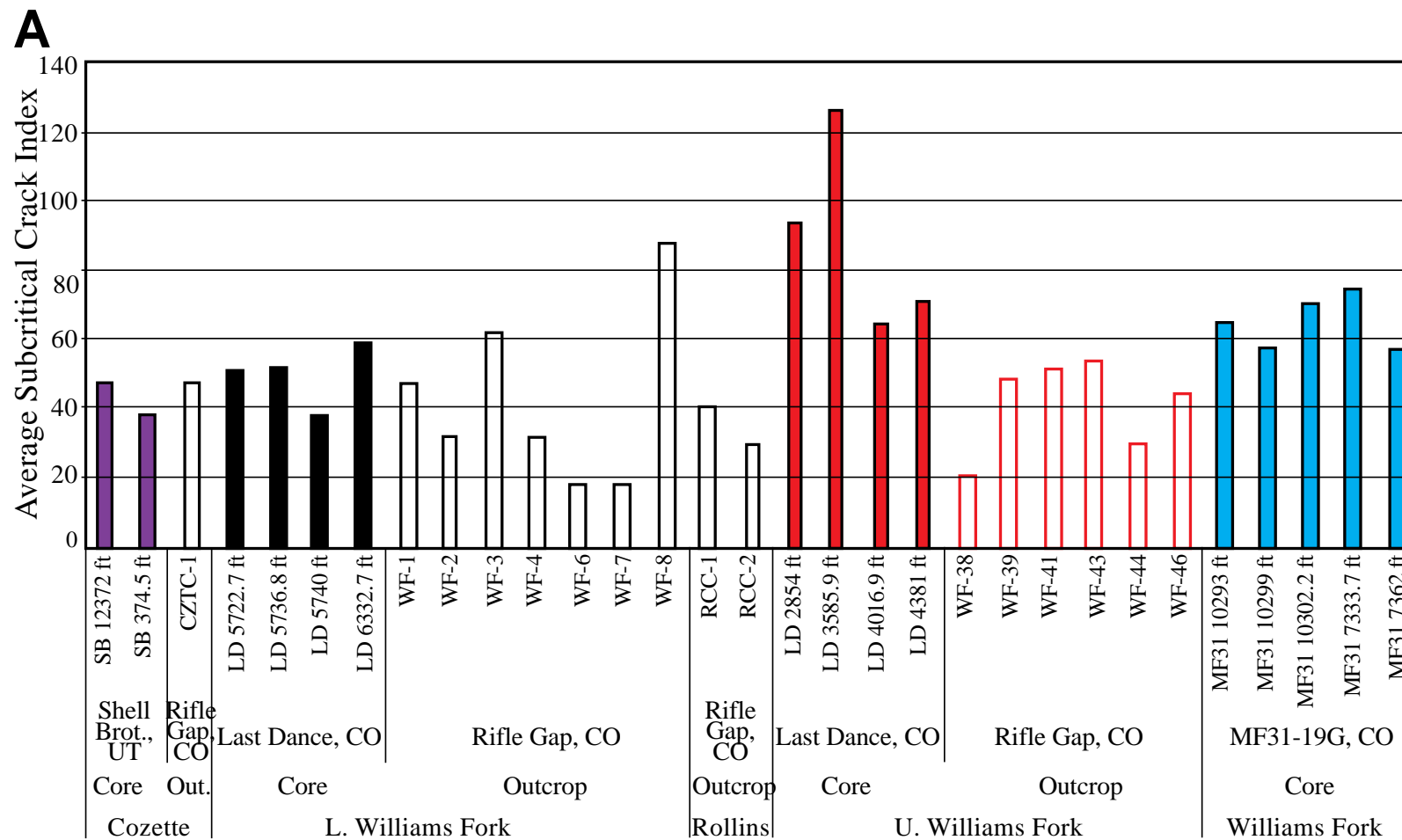


Figure 4.10. (A) Bar graph showing the distribution of measured-SCI values for the Mesaverde Group sandstones.

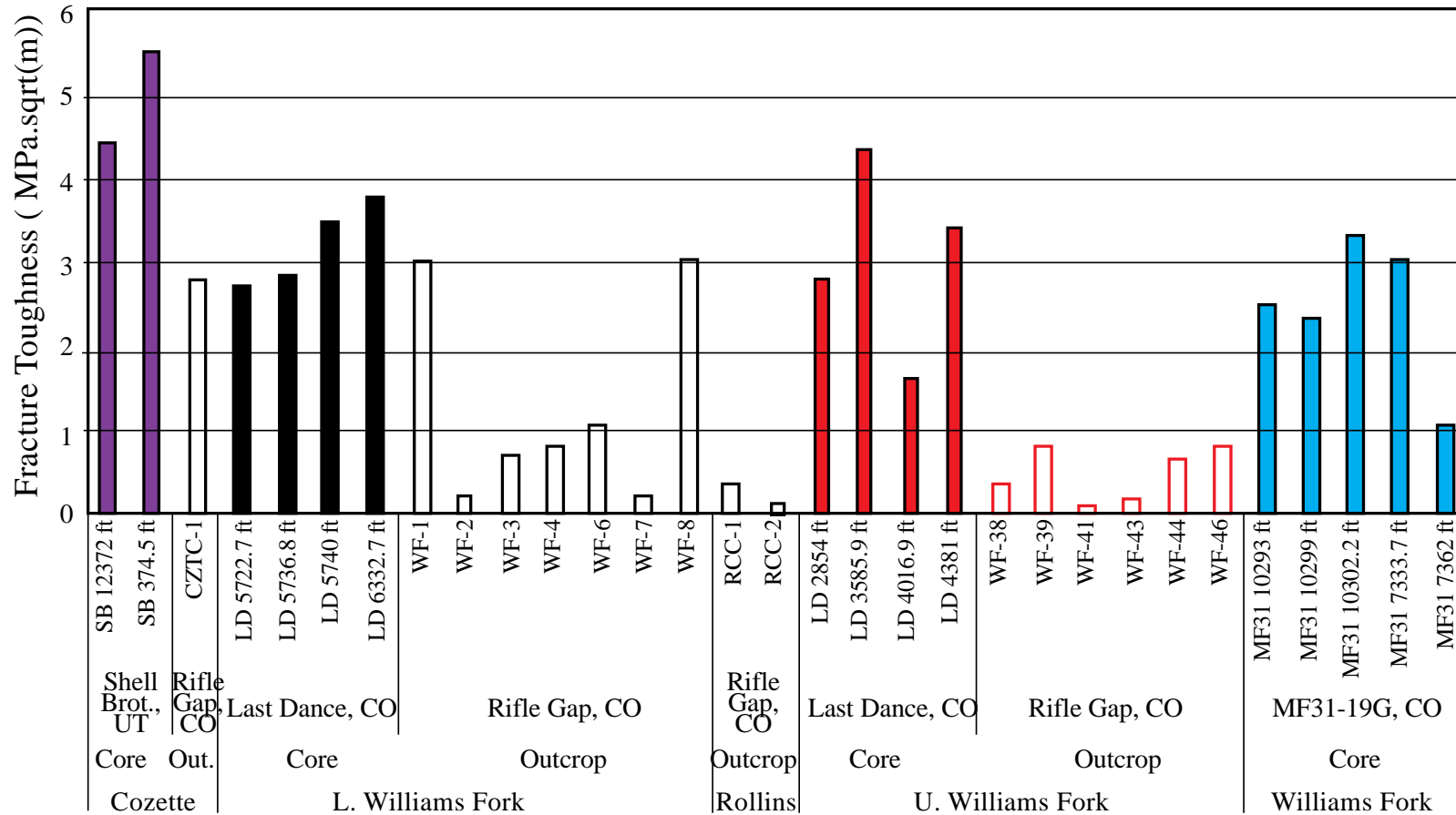
B

Figure 4.10. (B) Bar graph showing the distribution of calculated-fracture toughness values for the Mesaverde Group sandstones.

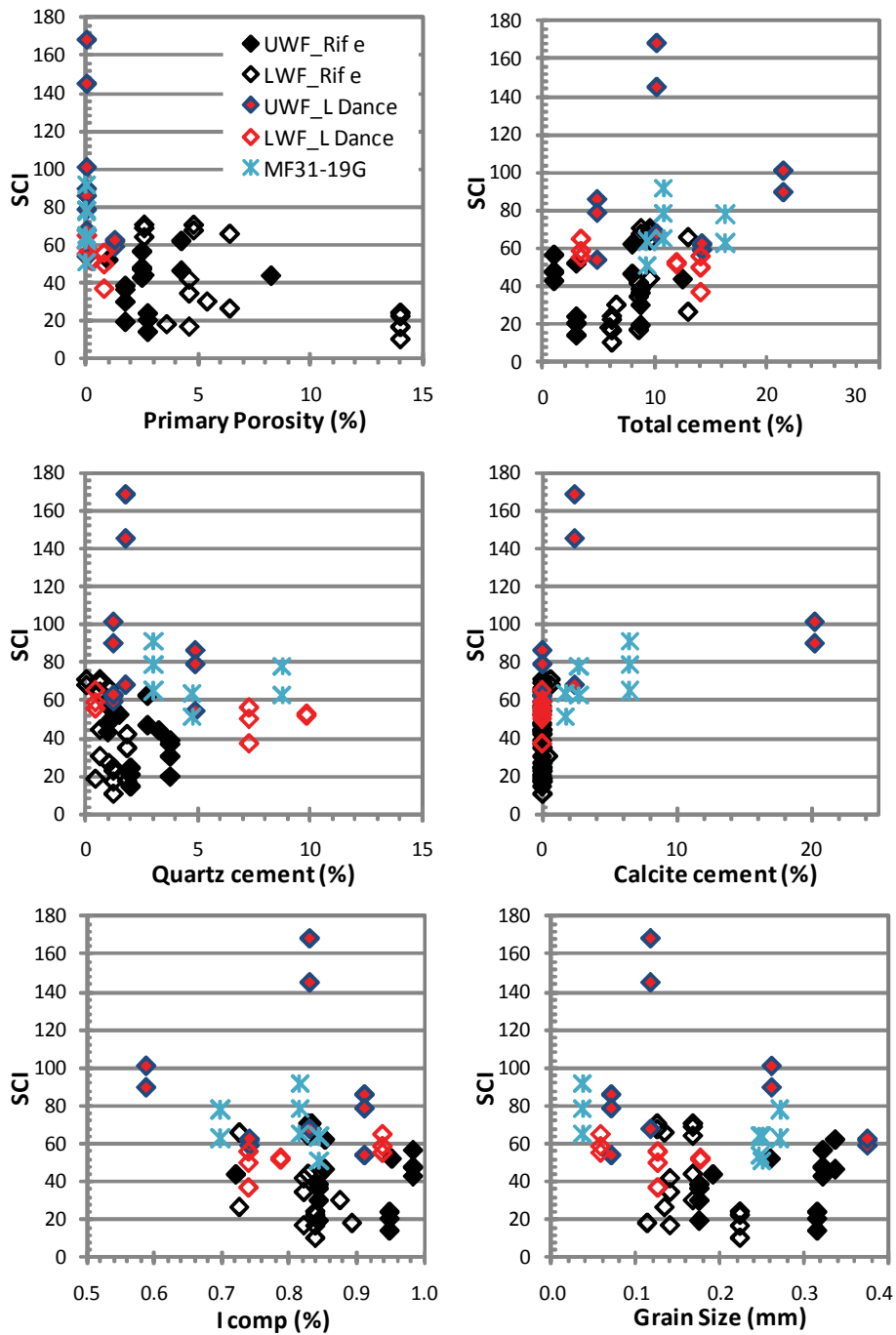


Figure 4.11. Cross plots of subcritical crack index versus petrographical parameters obtained from point count data. The terms COPL: Compactional porosity loss, CEPL: cementational porosity loss, and I_{Comp} : compaction index were described in section 3.6.1 of the previous chapter.

4.3.6. Rock Mechanical Comparison of Subsurface Samples and Their Outcrop Equivalents

In this section I search for an answer to the question of “Does quartz cementation have an effect on rock mechanical properties?” I believe it will because it influences the rock properties through binding the framework grains and increasing the overall rock strength. In order to test this hypothesis and quantify the effects of quartz cementation on rock mechanical properties, I compare the diagenetic and rock mechanical characteristics of subsurface and outcrop samples of the Williams Fork Formation from the Piceance Basin. I try to isolate the effects of cementation and porosity by comparing the subsurface and outcrop samples of the same formation with similar framework mineralogies. The Williams Fork lithofacies classification in Chapter 3 was based on detrital grain composition, amount and type of cements and pores, and detrital clay content. Because outcrop and subsurface samples clearly have gone through different diagenetic paths, the lithofacies observed in the outcrop and subsurface have differences in the amount and type of cements and pores. However, framework mineralogies are similar for a given subsurface lithofacies and its outcrop equivalent. Therefore, while pairing outcrop and subsurface samples for SCI comparisons their framework mineralogies were used. After selecting the subsurface sample and its outcrop equivalent, I compared their petrographical features and measured their subcritical crack indices to quantify the effects of diagenesis on SCI, a rock mechanical property.

Petrographical comparison of the samples to select the pairs of sandstones for subcritical crack index comparison led to pairing of the dolostone fragment-rich, quartz- and Fe-dolomite cemented lithofacies of the subsurface (E1, described in Chapter 3 on lithofacies of Williams Fork) with its outcrop equivalent. It was unfortunate not to find a

good correlation between the other samples; however, having found the best correlation on the lithofacies E1 was a great luck. Lithofacies E1 is the most important lithofacies because it dominates the Lower Williams Fork interval where the degree of fracturing and gas production are mentioned to be the highest (Cumella and Scheevel, 2008).

E1, a Lower Williams Fork lithofacies, is found to have the best match at the outcrop with similar framework mineralogy, but different amounts of quartz cement, Fe-dolomite cement and primary pores. Photomicrographs of the two illustrate well the differences in the amount of pore space (Figure 4.12, Table 4.4). In the Lower Williams Fork, differences in the burial histories are reflected mainly in the amount of quartz cement. Outcrop sample have only 1% percent quartz overgrowths, no Fe-dolomite and 4% kaolinite. Subsurface samples, on the other hand, have 7.3% quartz cement, 4.8% Fe-dolomite and trace amounts of kaolinite.

I was able to quantify the effect of quartz and Fe-dolomite cements on the SCI for a sandstone of given framework grain assembly by examining the influence of petrographical parameters on SCI (Figure 4.13). Quantification of the influence of quartz cement on SCI can aid determining this rock mechanical characteristic in the geologic past when the sandstone was at a diagenetically less mature state (i. e. when it had less quartz cement). The evolution of quartz cement in the geologic past can be modeled with diagenetic models.

Calculations indicate that adding 7.3% quartz and 4.8% Fe-dolomite cement into the pore system increased the subcritical crack index from 21.7 to 49.6. As explained in section 4.2.5 the microscale textures exerted by the growth of quartz and Fe-dolomite

overgrowths are similar to each other. Therefore, I interpret that additional 12.1% strong overgrowth cement increases the subcritical crack index a value of 30.7.

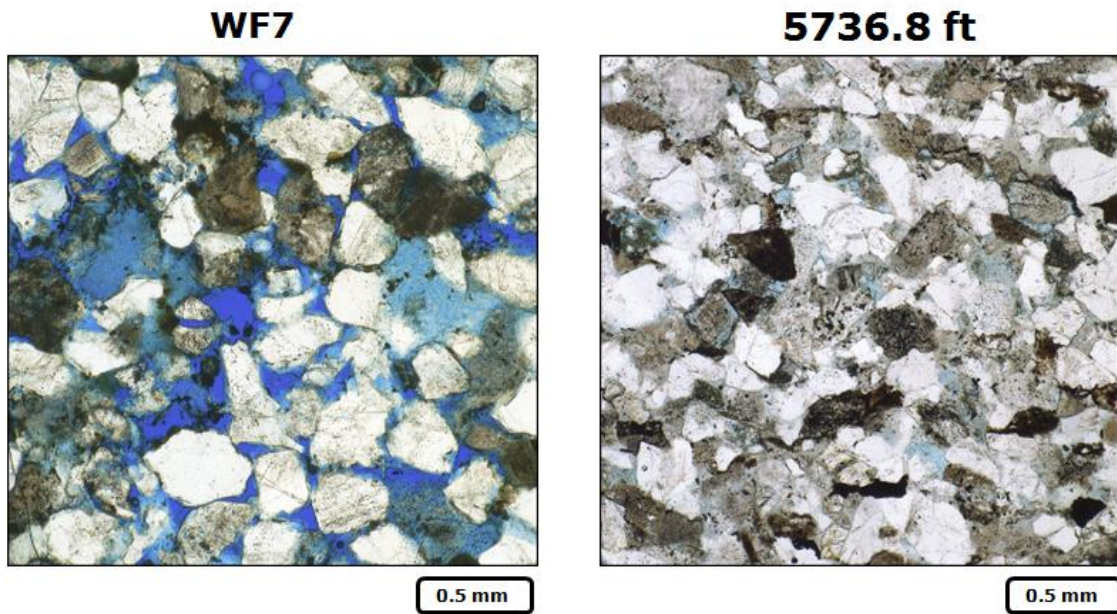


Figure 4.12. Thin section photomicrographs showing the contrasting porosity and quartz cement distribution of outcrop (left image) and subsurface (right image) pairs. Bright blue color represents pore spaces filled with blue-dyed epoxy.

Table 4.4. Point count data and SCI values for the selected sample pairs.

Sample	LD 5733.1	LD 5761.3	WF-7
Type	Subsurface	Subsurface	Outcrop
Framework Grains			
Quartz Grain	66.6	53.0	62.6
Feldspar Grain	8.7	9.5	16.3
Rock Fragments	24.8	37.5	21.1
Cements			
Quartz Cement	7.3	11.0	1.2
Fe-dolomite & Siderite	4.8	4.8	0.0
Calcite cement	0.0	0.0	0.0
Chlorite	0.3	0.0	0.6
Illitic Clays	0.8	2.5	0.0
Kaolinite	trace	0.3	4.0
Primary Pores	0.8	0.0	14.0
Secondary Pores	1.5	0.3	3.6
IGV	16.0	20.0	20.6
Mechanical Properties			
SCI-1	51.8		24.7
SCI-2	52.8		22.9
SCI-3	56.1		17.2
SCI-4	50.1		
SCI-5	37.2		
Average SCI	49.6		21.6
KIC	3.0		0.1
KIC	2.5		0.1
KIC	2.6		0.2
KIC	3.2		0.2
KIC	3.5		
Average KIC	2.9		0.1

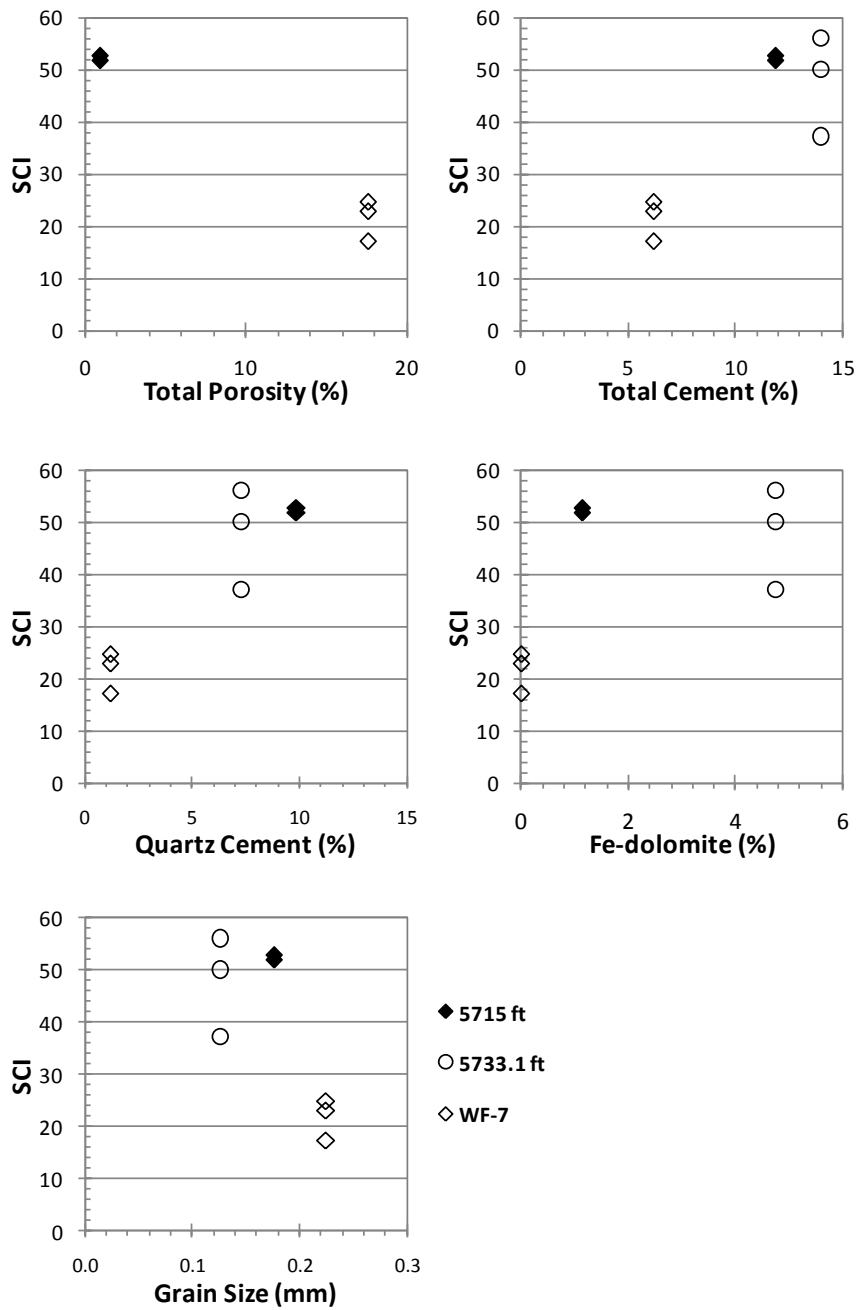


Figure 4.13. Subcritical crack index value versus petrographical parameters for the outcrop and subsurface samples.

4.3.7. Discussion: Is it Possible to Use Rock Mechanical Properties of Outcrop Samples as Analogs of Subsurface Equivalents?

Cementation is the most important process leading to the lithification of sand to form sandstone. Cementation is the occlusion of an intergranular pore volume by the precipitation of authigenic minerals. Quartz cement is typically the most common cement found in the sandstones (McBride, 1989). Brittle deformation, together with grain rearrangement and ductile grain deformation, is a key mechanism of compaction in sandstones. Cementation provides a bond between grains of a sandstone and reduces the compactional effects by preventing grain reorientation, sliding, and rotation. Quartz cementation, by virtue of its impact on sandstone mechanical properties, is expected to affect the compaction progress (Makowitz, 2004).

The depositional characteristics of sandstones such as grain size, sorting and amount of clay matrix remain unchanged during diagenesis. Framework grain composition can change through grain dissolution and grain replacement, but it is not likely to be significant. The diagenetic changes occur mostly as loss of primary pores with compaction and precipitation of cements, mainly quartz. Quartz precipitation in sandstones can be accurately predicted by using diagenetic models where grain composition, surface area and texture, and the extent of thermal exposure are the key determinants of the rate and amount of quartz cementation (Lander and Walderhaug, 1999). The basin modeling results for the outcrop and subsurface samples indicate the differences in their burial and temperature histories (Figure 4.14). For example, during its maximum depth of burial, the Cameo interval of at the base of Williams Fork was thermally exposed to 150 °C at the location of Last Dance well and about 80 °C at the

Rifle Gap outcrop locality. The differences in the highest temperatures reached and time spent in those temperature ranges are reflected in differences of quartz cement between the two localities: more quartz cement is present in the deeper buried subsurface samples than in the outcrop samples (Figure 4.15). In order to use outcrop samples as analogs for rocks in the subsurface, the burial histories should be well understood and amount of quartz cement should be predicted for the subsurface, because the results presented here and by Rijken (2005) show that quartz precipitation can alter the rock mechanical properties.

In addition, outcrop samples of the Williams Fork have kaolinite, Fe-oxide, zeolite, siderite, and calcite cements which appear to be related to outcrop alterations. Overall, this study calls for caution while using outcrop samples as petrographic analogs to subsurface rocks.

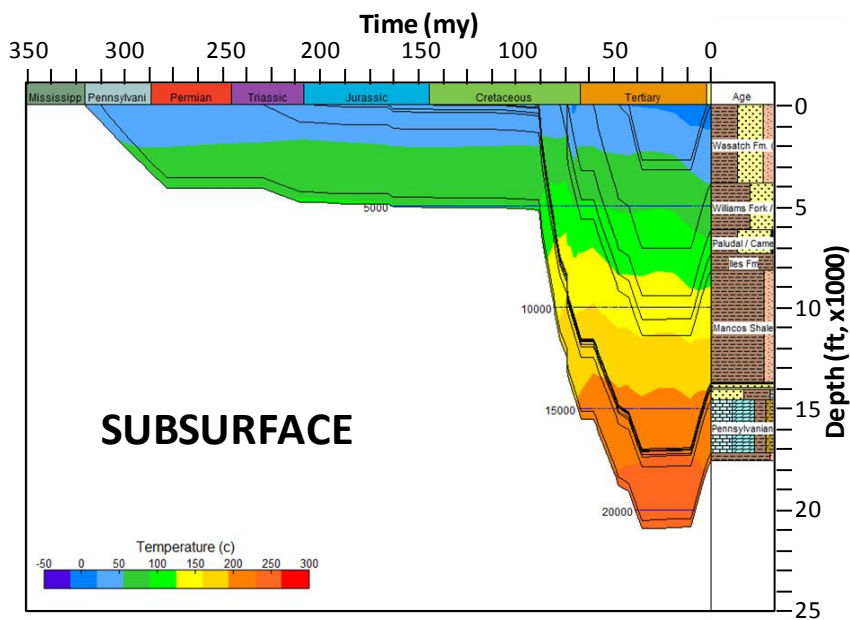
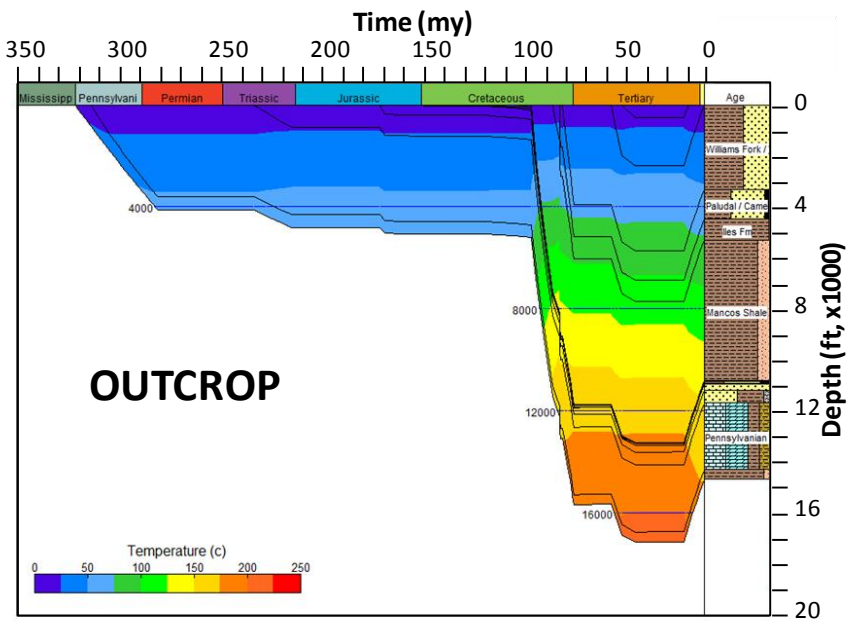


Figure 4.14. 1D Basin Modeling results (Genesis TM) indicate contrasting burial and thermal histories for the outcrop (top) and subsurface (bottom) location.

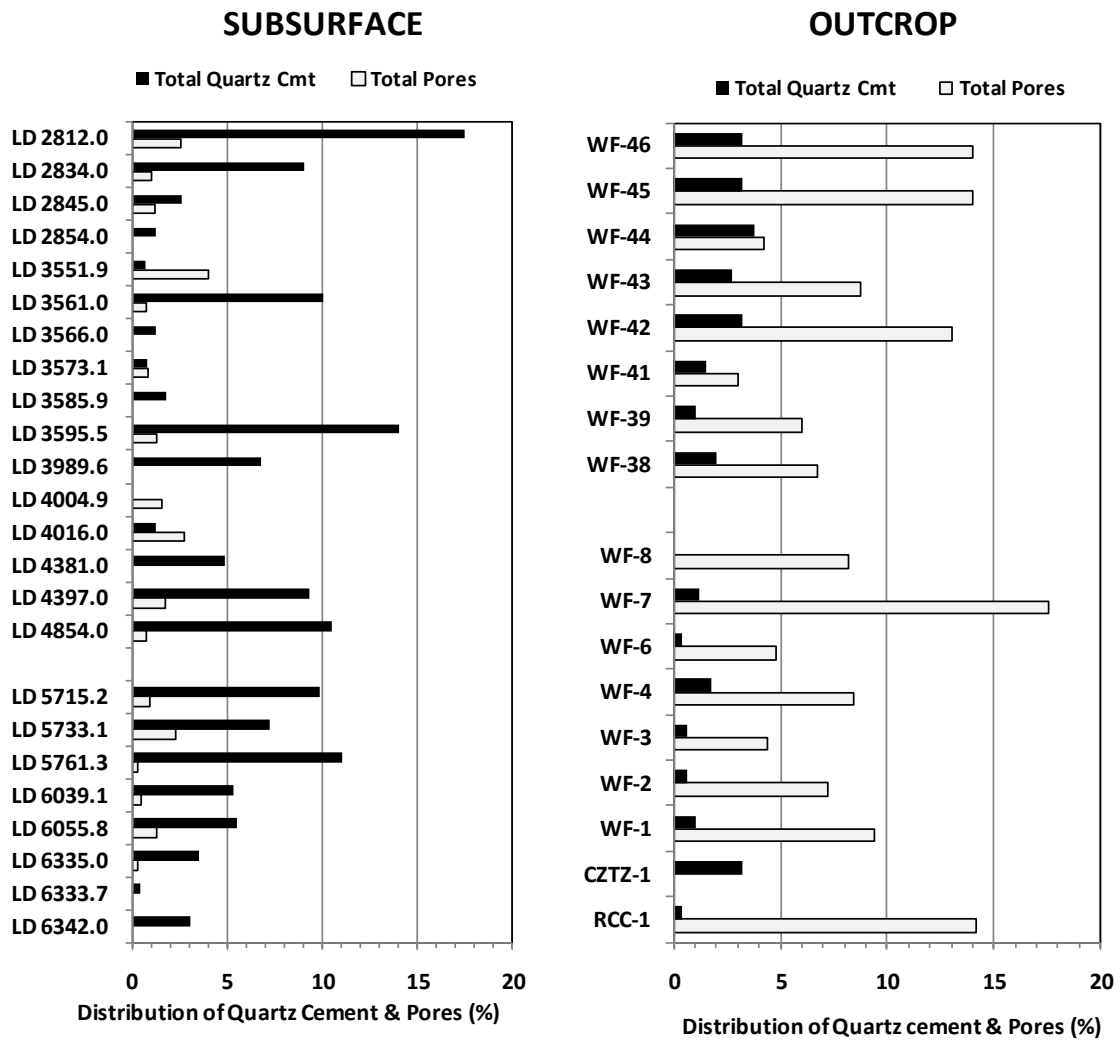


Figure 4.15. Distributions of quartz cement and total porosity at the subsurface (graph on the left) and outcrop (graph on the right). In the subsurface the samples with low quartz cement have grain-coating clays that inhibited quartz precipitation or tight calcite or Fe-dolomite cements filling most of the pores. Controls on quartz precipitation are explained in detail in Chapter 3 (section 3.6).

4.3.8. Conclusions: Outcrop to Core Comparison

The comparison of mechanical properties of subsurface and outcrop Williams Fork samples were done to search for an answer for the question of ‘how do fracture mechanics properties vary in sandstone of a given composition with varying degrees of cementation’. The study shows that rock mechanical properties of weakly-cemented, poorly-consolidated sandstones are quite different from those of well-consolidated, well-cemented equivalents. With this study constraints for subcritical crack index (SCI) values were obtained that can be used in geomechanical fracture distribution models. Using outcrop samples as analogs or guides to the properties of subsurface rocks may be misleading if the burial histories of the two are very different as duration and amount of burial affects quartz precipitation rates and volumes.

Using present-day SCI values measured in the cores for predicting natural fracture distribution may also be problematic because fractures may have developed when the rock was at a different (earlier) diagenetic stage than the rocks sampled. With the help of diagenetic models established using burial history and the present day petrography, amount of quartz cement in the pore system can be predicted for the geologic past. Once sandstone characteristics of rocks in the geologic past at the time of fracture are determined, SCI values can be extrapolated to the sandstone characteristics at the time of fracturing by using the constraining SCI values obtained in this study.

These constraints can also help determining SCI value for very poorly-consolidated sandstones for which preparing samples for the SCI test is greatly difficult. Many geologically young, poorly-consolidated reservoirs produce oil and gas from all around the world. For these samples perhaps fractures do not carry as much importance

in production, however, rock mechanical properties are important for many applications, for example wellbore stability problems (Monus et al., 1992; Wagg et al., 1999; Fredrich et al., 2000; Ispas et al., 2005).

4.4. CASE STUDY: INFLUENCE OF ROCK MECHANICAL PROPERTIES ON FRACTURE DISTRIBUTION IN CORE

The heterogeneity of the Williams Fork sandstones is represented by the twelve lithofacies identified based on cement types, grain populations, and clay matrix content in Chapter 3. These lithofacies are correlated to log responses to create a model that can be used to predict reservoir quality directly from well logs. In this section, using the same well as a case study, I examine whether the lithofacies approach can shed light on aspects of reservoir quality related to natural fracturing. I investigate the control of lithological differences on rock mechanical properties and the degree of fracturing in the study well, located in Sec. 3, T7S, R92W, Mamm Creek field, Piceance Basin (Figure 4.1). Lithological controls over rock mechanical properties are examined within the context of subcritical crack index (SCI), Young's modulus, and Poisson's ratio. The subcritical crack index values are from lab measurements on the core samples. Young's modulus and Poisson's ratio values are derived from acoustic log data.

The increased density of natural fracturing in the deeper Williams Fork intervals of the study well was documented by Cumella and Scheevel (2008) with shear-wave velocity anisotropy, image logs, and whole core data. Overpressure is claimed to play a role in the higher degree of fracturing in the overpressured zones of the Williams Fork below the top gas (Meissner, 1987; Spencer, 1989; Lorenz and Finley, 1991; Law, 2002; Cumella and Scheevel, 2008), but SCI measurements indicate that lithofacies that dominate the deeper, more fractured intervals have lower subcritical crack index values and Poisson's ratios which make them more prone to fracturing. The SCI values vary with petrographical features (mainly amount and type of cement, amount of clay matrix,

and grain size). Young's modulus and Poisson's ratio values also show indications of lithological control, especially by pore-filling cements.

In the last part of this section, a diagenetic modeling approach to determine the rock characteristics at the time of gas generation and fracturing is given for the study well. First, temperature ranges for the fracture opening are obtained from the published microthermometry data (fluid inclusions) on the fracture-filling quartz bridges with crack-seal textures. Once these temperature data are linked to the burial and thermal histories obtained from basin models, approximate timing of fracture opening is determined based on timing of gas generation and independent evidence of fracture history from fluid inclusions in cements deposited during fracture growth. The diagenetic state of the sandstones prior to, during, and after fracturing is determined with *Touchstone*TM by modeling of the evolution of compaction, quartz precipitation, pores, and permeability in the geologic past. These parameters are also calculated for the time of gas generation obtained from the literature. The results indicate that the bulk rock properties of the host sandstones were still diagenetically evolving during gas generation and early fracturing.

4.4.1. Natural Fractures in the Williams Fork Formation

The Williams Fork Formation of the Piceance Basin yields the largest gas production in the Rocky Mountain region (Scheveel and Cumella, 2009). Natural fractures play an important role in the production from these tight gas reservoirs. Presence of extensive fracturing in the Williams Fork is proven with core observations, well tests, leak-off analysis of breakdown treatments, and surface seismic data in various

fields throughout the Piceance Basin. Reservoir-scale tests of individual sandstone intervals document one- to three- order of magnitude higher reservoir permeabilities than the core-measured permeabilities that were restored to reservoir pressures (Lorenz et al., 1989). Pressure dependent leak-off which indicates presence of natural fractures was reported in 61% of the 826 wells tested from Grand Valley, Parachute, Rullison and Mamm Creek fields (Craig et al., 2005). Increased shear-wave velocity anisotropy supported with image log and core data is another indication of presence of fractures (Cumella and Scheveel, 2008).

In the Piceance Basin natural fractures are best documented in the MWX cores of the Rullison field (Lorenz, 2003). Three closely spaced wells (200 ft apart) were drilled as part of a fractured tight gas reservoir research project at the MWX site in early 1980's, and subsequently a slant core was taken between these wells. The wells were extensively cored, logged, stimulated, and flow tested under controlled conditions. The Williams Fork cores were well studied for numerous aspects of fracture characteristics by Barker (1989a), Pitman and Sprunt (1986); Lorenz et al. (1989), Warpinski (1989), Laubach (1997), Lorenz and Finley (1991), Laubach (2003), Gomez et al. (2003), Becker et al. (2009a), Fall et al. (2009), and Hooker et al. (2009). These studies reported that (1) natural opening-mode fractures (extension fractures or joints) and small faults are present and locally abundant; (2) fractures have a wide range of sizes; (3) most contain deposits of quartz and/or calcite and locally clay minerals; (4) quartz and calcite cements are found lining or locally bridging open fractures or sealing fractures; and (5) crack-seal texture that indicates repeated opening of the fractures is observed in the fracture bridging quartz cements (Laubach et al., 2004b).

The natural fracture orientation is west northwest in the Rulison field and it gradually rotates counterclockwise in the Rulison field and oriented approximately west in the Parachute field and to west-southwest in the Grand Valley field (Cumella and Ostby, 2003, Figure 2.1 for field locations). East of the Rullison field, the natural fracture orientation rotates clockwise and approaches N45°W in some areas of the Mamm Creek field (Cumella and Scheevel, 2008). When opening-mode fractures form (natural or those created in hydraulic fracture treatments), they tend to align parallel to the concurrent direction of the most compressive horizontal stress (maximum horizontal stress, or SHmax) (Lawn and Atkinson, 1975; Pollard and Aydin, 1988). The natural fracture strike in the Piceance has been interpreted to be controlled by the horizontal compressive stress orientation in place during the Laramide orogeny (Lorenz and Finley, 1991) but these fractures are also aligned with the current stress field (Zoback and Zoback, 1989). This regional fracturing is an example of load-parallel extension fracturing and basinwide dilatancy at depth, under conditions of high pore pressure and anisotropic, tectonically created, horizontal stress (Lorenz and Finley, 1991).

4.4.2. Causes of Fracturing

Olson et al. (2009) demonstrate that substantial opening mode fracture growth can occur at tiny extensional strains (on the order of 10^{-4}). To grow fracture arrays therefore does not require major tectonic events, or even proximity to or causes like macroscopic structures like folds and faults. Interpretations that rely solely on the alignment of fractures with presumably causative structural features (the arguments of timing from kinematic compatibility) are therefore inherently weak (Hancock, 1985; Engelder, 1985).

Hooker et al. (2009) measured very low extensional strains for representative Piceance Basin fractures arrays (in the Cozzette sandstone of the Iles Formation and within the Williams Fork). The causes of such low strain fracture arrays in Piceance and elsewhere are a matter of great uncertainty. A way to narrow the potential causes of fracturing is to closely constrain the timing and magnitude of loads that could possibly promote fracture, the timing of rock property changes that could also contribute to fracture growth (or cessation), and the timing of fracturing. The timing of fracture is usually challenging to pin down, but evidence from cement deposits can be helpful (Laubach, 1988; Perez and Boles, 2005; Hanks et al., 2006; Makowitz et al., 2006). Here I describe evidence for the timing of processes that promote fracture (gas generation, porosity loss and consequent overpressure development) and rock property changes and compare to fracture distribution and evidence of fracture timing.

Basin-centered gas accumulations are typically characterized by regionally pervasive, abnormally pressured and low permeability gas saturated zones that commonly lack downdip water (Law, 2002). The main trapping mechanism for the gas is believed to be the low permeability of the reservoirs in the vicinity of the basinwide gas kitchen. For the Williams Fork reservoirs, Cameo coals within the coastal plain deposits are the main source of gas. Significant thermal gas generation from these coals started in early Eocene at the time of deepest burial (Johnson and Roberts, 2003). By that time diagenesis resulted in loss of most of the pore space and lowered the permeabilities (Pittman et al., 1989). Due to lower permeabilities and the discontinuous nature of the fluvial sandstone bodies gas could not escape from individual sandstone intervals. Eventually reservoir became overpressured because more gas was being generated and

accumulated than could escape (Meissner, 1987; Spencer, 1989; Law, 2002; Cumella and Scheevel, 2008). The magnitude of overpressuring follows a trend of increasing pressure with increasing stratigraphic depth with the highest values in direct proximity to the coal intervals (Scheevel and Cumella, 2005). A gas-saturated zone is formed by the pressure of the gas phase that overcomes the capillary pressure of the water-wet pores and saturates the reservoir with gas with little movable water. Above this continuously gas-saturated zone is the transition zone that contains both gas and water. Gas-saturated zones within the transition zones exist; however, they are probably related to major fracture and/or fault zones (Cumella and Scheevel, 2008).

The orientations of the fracture populations are predetermined by the orientation of the tectonic stresses at the time of fracturing, but the distribution and intensity of the fracturing are mostly influenced by the history and magnitude of the overpressuring during gas charging (Lorenz et al., 1988; Lorenz and Finley, 1991; Scheevel and Cumella, 2005). Cumella and Scheevel (2008) claim the overall gas distribution and gas pressure in the Williams Fork is probably the direct result of pore-pressure assisted fracturing and subsequent migration through the resulting natural fracture system.

According to their pore-pressure assisted fracturing model, during maturation of the coal-bearing lower Williams Fork pressures were high enough that most rock types got fractured. As pore pressure increases, the lateral normal stress decreases, until the rock experiences tensile effective stress and fractures. Pressure decreases upward away from the areas where gas is being generated; in these lower pressure areas only fracture-prone lithologies fracture which results in stratigraphy to be a more important factor in

the upward and lateral migration of the gas (Scheevel and Cumella, 2005; Cumella and Scheevel, 2008).

Pressure gradients, which can be as high as 0.8 psi/ft in the lower Williams Fork at the structurally deeper part of the basin, decrease upward to hydrostatic gradients (0.43 psi/ft) near the top of the continuously gas-saturated interval (Scheevel and Cumella, 2005). Pressure gradients also decrease with shallower burial depths towards the flank of the basin.

In the study well, the highest pressures exist in the deeper intervals of the Lower Williams Fork near Cameo coal zone (Figure 4.16). Pressure driven from the mud weight data from the study well and pressure log data available from a nearby well both indicate an increase in pressure with depth. The shift in the reservoir pressure is more evident at depths around 5800 feet. The depth of overpressuring was probably shallower in the geologic during the maximum burial while the rocks were in the thermal gas generation zone.

Olson et al. (2009) claims that even subhydrostatic pore pressure could be conducive to opening-mode failure in the tight gas sandstones. They suggest a simplified expression for estimating the magnitude of pore pressure (P_p) relative to vertical stress (S_{vert}) required for opening-mode fracturing as:

$$P_p/S_{vert} \cong \nu / ((1 - \nu) - (1 - 2\nu)\alpha_p) \quad (\text{equation 4.5; Olson et al., 2009})$$

Olson et al. (2009) state when α_p (poroelastic constant) = 1, equation becomes independent of Poisson's ratio (ν) and is always equal to 1. However, when $\alpha_p < 1$, the pore-pressure (P_p) ratio required for fracturing can drop to below hydrostatic (P_p/S_{vert} 0.4)

depending on the value of Poisson's ratio. They suggest that the better the cement and the lower the porosity in a sandstone, the lower its poroelastic constant is expected to be. Consequently, for such rocks, the first-order approximation of the above equation suggests that opening-mode fracturing can occur at pore pressures significantly less than the overburden stress, and given typical elastic values for tight gas sandstones ($\nu < 0.3$ and $0.5 < \alpha_p < 0.7$), even subhydrostatic pore pressure could be conducive to opening-mode failure.

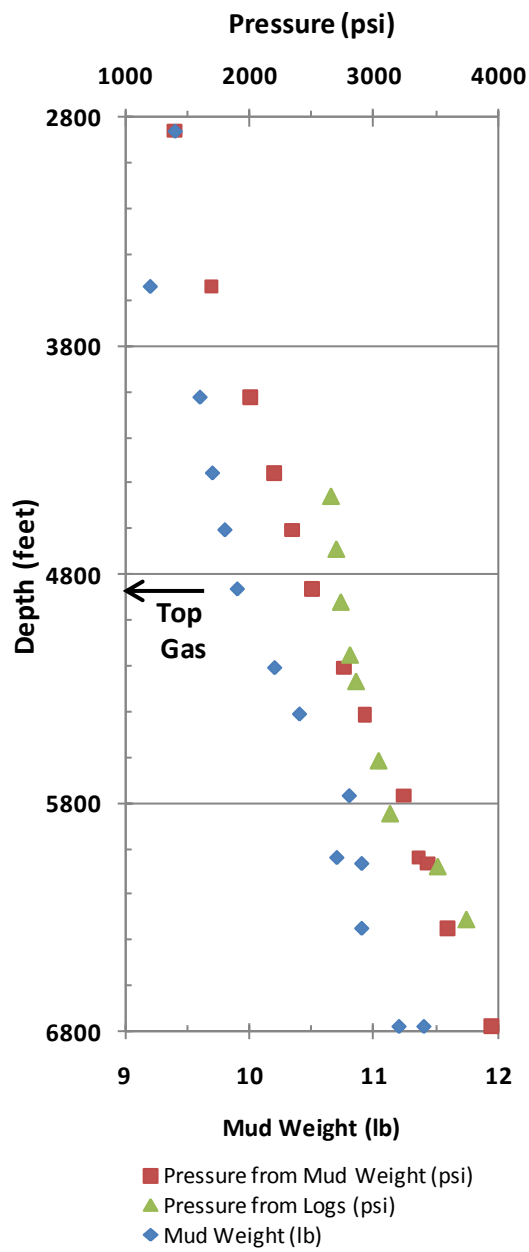


Figure 4.16. Graph showing variation in reservoir pressure with depth. Mud weight data is from the study well and log data is from a nearby well (1 mile distant).

4.4.3. Rock Mechanical Properties of the Williams Fork Lithofacies

In the study well, increased density of natural fracturing in the deeper Williams Fork intervals below top gas was documented based on increased shear-wave velocity anisotropy detected on dipole sonic logs, image logs and core observations (Cumella and Scheevel, 2008; Figure 4.17). There is an agreement in the literature that overpressuring assisted in the fracturing process; however, the presence of sandstones with contrasting diagenetic characteristics in the Williams Fork raises questions about the influence of diagenesis on the rock mechanical characteristics and therefore the fracturing process. For example, differences between the upper and lower Williams Fork in mechanical properties could alter the strength and/or brittleness of sandstone, potentially giving an alternate explanation for the observed differences in degree of fracturing. Differences in the observed degree of fracturing between upper and lower Williams Fork provide an opportunity to examine the effects of lithology on the fracture distribution and rock mechanical properties: subcritical crack index (SCI), Young's modulus (E), and Poisson's ratio (Table 4.5). This information can be used to help interpret fracture observations. For example, the fracture mechanics property subcritical crack index (SCI) governs the tendency for fractures to cluster (Olson, 2004; Olson et al., 2009); if SCI is very high and fractures are strongly clustered, fractures in such zones could be systematically undersampled compared to less clustered fracture patterns, leading to spurious apparent fracture intensity differences for fractures sampled with conventional vertical wellbores, cores and image logs.

Table 4.5. Rock mechanical properties of the Williams Fork Lithofacies. SCI (n): subcritical crack index measured in this study.

Lithofacies	Description	POISSON'S RATIO			YOUNG'S MODULUS (GPa)			SCI (n)
		Min	Max	Average	Min	Max	Average	
A	Chlorite-coated	0.234	0.289	0.263	30.0	33.5	31.0	
B	Illite/Smectite-coated	0.167	0.265	0.230	20.7	31.8	26.1	59.1, 61.8, 62.6, 78.7
C1	Qtz-cemented; medium thick detrital clay coats (Ohio Creek)	0.256	0.270	0.264	27.2	36.0	32.3	
C2	Qtz-cemented; thin detrital clay coats (Ohio Creek)	0.216	0.288	0.258	23.5	39.9	31.6	
D1	Qtz-cemented; mica-rich; sst/siltst	0.214	0.283	0.250	31.0	36.6	34.5	53.9, 78.8, 86.0
D2	Qtz-cemented; thin clay coats, mica rich with CRFs	0.228	0.290	0.256	26.0	42.9	34.4	
E1	Dolostone grain-rich, Qtz- & Fe-dolomite-cemented	0.120	0.282	0.205	29.1	40.9	32.7	37.2, 50.1, 51.8, 52.8, 56.1
E2	Dolostone grain-rich, Qtz- & Fe-calcite cemented	0.200	0.238	0.217	34.3	43.2	38.9	
F	Clay matrix-rich sst	0.201	0.326	0.256	22.0	47.7	35.8	145.2, 168.5
G	Tightly calcite-cemented	0.176	0.293	0.248	23.7	45.4	35.2	89.7, 101.1
H	Fe-dol cemented; Dolostone grain & Qtz-rich	0.159	0.239	0.213	30.9	46.5	39.9	55.5, 58.8, 65.2

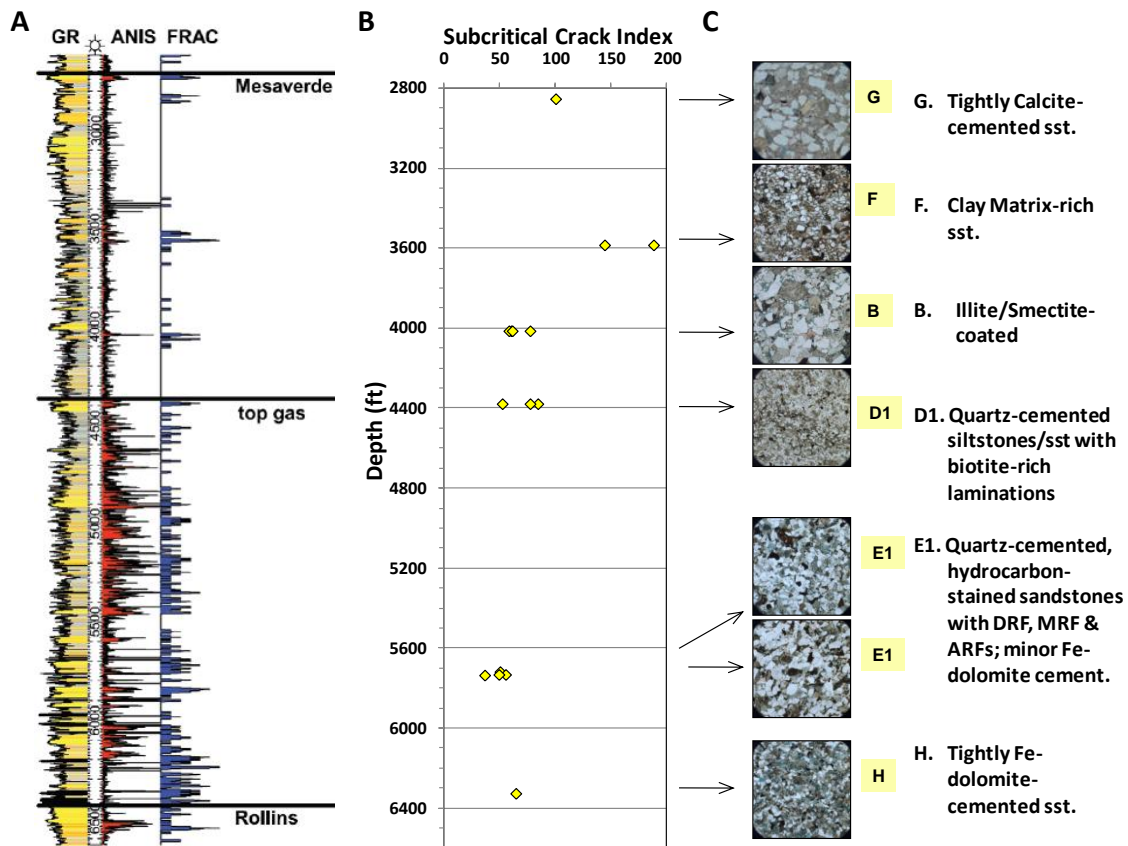


Figure 4.17. (A) Fracture density variation with depth for the study well (Cumella and Scheevel, 2008). Fracture density determined from shear wave anisotropy and image logs is drastically higher below top gas where reservoir pressures are higher. GR: Gamma-ray, ANIS: Shear wave anisotropy from the dipole sonic log and FRAC: Natural fracture density from image log interpretations. Shown in yellow boxes are lithofacies classes. (B) Subcritical crack index values are higher in the sandstones above top gas. (C) Photomicrographs that represent the petrographic characteristics of the lithofacies and associated subcritical crack index values. The images are taken at the same magnification width of the images approximately 1.5 mm.

4.4.3.1. Lithological Controls on Subcritical Crack Index

The subcritical crack index (SCI) values were measured for eight samples from the study well. Overall, the highest SCI values are associated with the calcite-cemented sandstones and clay-matrix rich sandstones. Quartz and Fe-dolomite cemented sandstones have relatively low SCI index values.

The SCI values vary between 59 and 72 for illite/smectite-coated sandstones (B), between 53 and 86 for the quartz-cemented, sandstones and siltstones with mica-rich laminations (D1), between 145 and 168 for the clay matrix-rich sandstones (F), and between 89 and 101 for the tightly-calcite-cemented sandstones (G). These sandstones are observed in the Upper Williams Fork interval above the top gas. On the other hand, the lower Williams Fork interval below the top gas is dominated by DRF (dolostone fragment)-rich, quartz- and Fe-dolomite-cemented sandstones (E1) which has SCI values ranging from 37 to 56 and Fe-dolomite-cemented sandstones with SCI values varying from 55 to 65.

The distribution of SCI values suggests that the lithofacies with greater fracture densities have relatively low SCI values (Figure 4.17). The DRF-rich, quartz- and Fe-dolomite-cemented sandstones (E1) dominate the densely fractured Lower Williams Fork interval from 5700 ft to 6035 ft (Figure 4.16). Although slight variations exist in the abundance of quartz and Fe-dolomite cements within this lithofacies, the framework compositions, pore distributions and cement types are close enough that they were grouped together. These densely fractured sandstones are not only associated with higher reservoir pressures (Figure 4.16) due to their proximity to gas producing coals, but their

SCI values also are lower which makes them more prone to developing dense patterns of relatively closely spaced fractures for a given mechanical layer thickness (Olson, 2004).

4.4.3.2. Discussion: Use of Anisotropy for Fracture Density Distribution

Seismic velocity anisotropy values are used for predicting fractures in the industry. Seismic velocity anisotropy can result from a variety of different causes, including rock fabric, grain-scale microcracks, rock layering, and aligned fractures at all scales, provided that layer thicknesses or fracture lengths and fracture spacing are small relative to the seismic wavelength (Worthington, 2008). Figure 4.18 shows the distributions of anisotropy-estimated fracture density and apparent fracture density (#/ft) from core and image log observations with respect to Williams Fork lithofacies. As seen in Figure 4.18, although shear wave anisotropy and the fracture density from the image logs agree in general, they do not correlate perfectly. This demonstrates that image logs and cores should be used as supporting and validating evidence when using anisotropy data to predict fractures.

When anisotropy and apparent fracture density are examined with respect to the measured SCI values, the highest anisotropy is found to be associated with the lithofacies with lowest SCI values, which is represented by DRF-rich, quartz- and Fe-dolomite-cemented sandstones (E1) that dominates the producing Lower Williams Fork. In addition, apparent fracture density obtained from image logs and cores is higher in the rocks with lower SCI values. The examination of the graph that shows the fracture distribution from image logs (Figure 4.18B) indicates that the sandstones with lowest SCI values (<66) have fracture densities more than 0.3 #/ft.

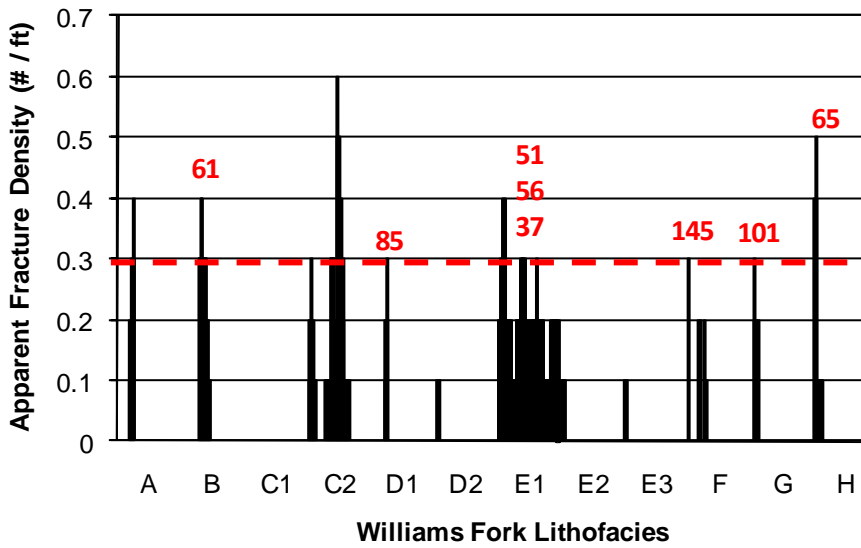
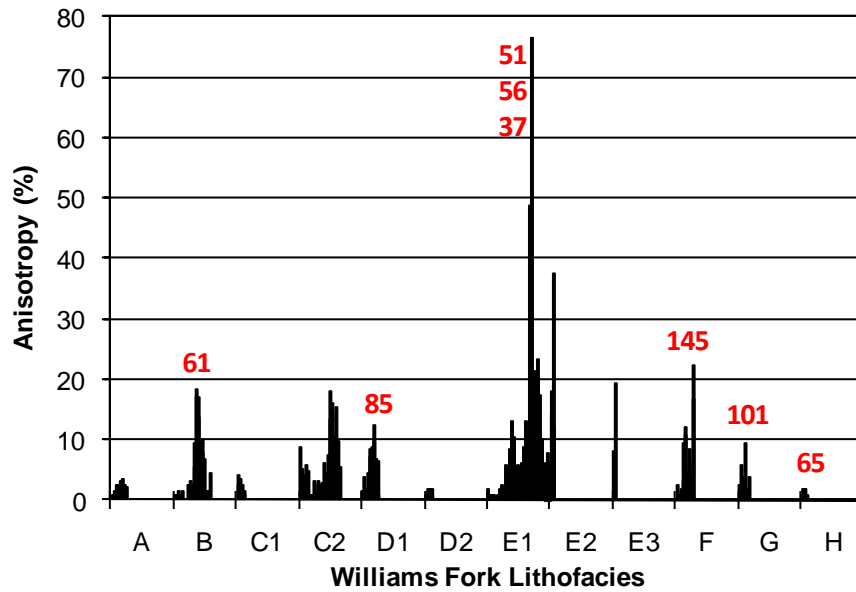


Figure 4.18. Distribution of (A) shear-wave velocity anisotropy, and (B) apparent fracture density from image logs. The values were grouped based on the Williams Fork lithofacies classification. The numbers in blue represent the measured SCI values for the given lithofacies.

4.4.3.3. Lithological Controls on Bulk Mechanical Properties: Young's Modulus and Poisson's Ratio

4.4.3.3.1. Definition of Young's Modulus and Poisson's Ratio

Young's modulus (E , modulus of elasticity) is a measure of stiffness or the ability of a material to withstand changes in length when under lengthwise tension or compression (Lawn and Wilshaw, 1975.; Atkinson, 1987). Young's modulus is equal to the longitudinal stress divided by the strain. Stress and strain may be described as follows in the case of a metal bar under tension (Figure 4.19). If a metal bar of cross-sectional area A is pulled by a force F at each end, the bar stretches from its original length L_0 to a new length L_n (simultaneously the cross section decreases). The stress is the quotient of the tensile force divided by the cross-sectional area, or F/A . The strain or relative deformation is the change in length, $L_n - L_0$, divided by the original length, or $(L_n - L_0)/L_0$ (strain is dimensionless).

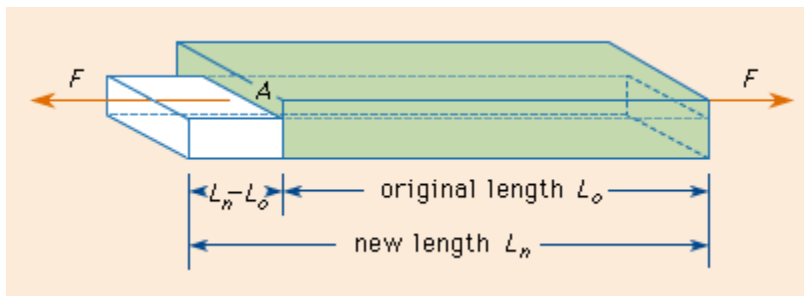


Figure 4.19. Figure showing a metal bar in tension, illustrating the basis of Young's modulus (from Encyclopedia Britannica Inc., 1996).

The units of Young's modulus in the English system are pounds per square inch (psi), and in the metric system Newtons per square meters (N/m^2). The value of Young's modulus for aluminum is about 1.0×10^7 psi, or 7.0×10^{10} N/m^2 . The value for steel is about three times greater, which means that it takes three times as much force to stretch a steel bar the same amount as a similarly shaped aluminum bar.

The Poisson effect describes the tendency of a sample cube of a material such that when it is stretched in one direction, it tends to contract in the other two directions, or when compressed in one direction, it tends to expand in other two directions. Poisson's ratio, ν , is a measure of the Poisson effect. Poisson's ratio (ν) is the ratio of the contraction or transverse strain (perpendicular to the applied load) to the extension or axial strain (in the direction of the applied load) when a sample object is stretched. Most materials have Poisson's ratio values ranging between 0.0 and 0.5. Rubber has a Poisson ratio of nearly 0.5. Cork's Poisson ratio is close to 0 showing very little lateral expansion when compressed. Most steels and rigid polymers when used within their design limits (before yield) exhibit values of about 0.3.

Rocks are subject to Poisson's effect while under stress and undergoing strain. Excessive erosion or sedimentation can either create or remove large vertical stresses on the underlying rock. The rock will tend to expand or contract in the vertical direction as a direct result of the applied stress, and it will also deform in the horizontal direction as a result of Poisson's effect. This change in strain in the horizontal direction can affect or form fractures (for example, joints) and stresses in the rock (Engelder, 1985).

4.4.3.3.2. Dynamic versus Static Rock Mechanic Parameters

The variations in rock mechanical properties (Young's modulus, Poisson's ratio and unconfined compressive strength) control fracture propagation and geometry; and therefore, they are important parameters to be considered in hydraulic fracture design (Zoback, 2007). Rock strength is controlled by mineral composition, density, porosity, fabric, moisture content, state of alteration, shape and size of test specimens, and test conditions such as temperature, and strain rate (Prikryl, 2001). Al-Tahini et al. (2006) studied the effects of cementation on mechanical properties (strength and moduli) of sandstones from the Jauf and Uanzah formations from Saudi Arabia. They demonstrated that the presence of quartz overgrowths (linearly) increases unconfined compressive strength (UCS). They also reported that carbonate cement has less control over the strength compared to quartz cement and that clay cements have the least influence on sandstone strength.

The Young's modulus and Poisson's ratio parameters obtained under laboratory conditions by stress-strain testing are referred as static values and values obtained from acoustic logs (compressional and shear wave velocities from well logs, cross-hole seismic) are referred as dynamic values. Static measurements of rock mechanical properties can be significantly different from dynamic measurements (McCall and Guyer, 1994; Sharma and Tutuncu, 1994; Yale et al., 1995; Al-Tahini et al., 2006). There are studies that relate the non-linearity in the rocks stress-strain behavior to the static / dynamic differences (McCall and Guyer, 1994; Sharma and Tutuncu, 1994). For linear elastic material there is no difference between loading and unloading curves while a non-linear material shows differences (Yale et al., 1995). The dynamic tests sense only the

elastic portion of the rocks response; and therefore, yield higher moduli and different Poisson's ratios than the static tests (Yale et al., 1995). The static measurements are more representative of the reservoirs properties but dynamic measurements have a greater coverage of the reservoirs.

Yale et al. (1995) studied the effects of quartz and chlorite cement on static and dynamic rock mechanical properties. They found that static Poisson's ratios are lower and Young's moduli are higher for the quartz-cemented sandstones compared to the chlorite-cemented sandstones. They also demonstrated that dynamic Young's moduli are nearly twice the static values in the high porosity, low modulus samples but they are only 10% higher in the low porosity, high modulus samples such that weaker chlorite-cemented sandstones have higher static / dynamic differences than fully quartz cemented sandstones which is interpreted to be related to chlorite cement not being as stiff as quartz cement.

4.4.3.3.3. Lithological Controls on Bulk Mechanical Properties: Young's Modulus and Poisson's Ratio

Clear systematic groupings are observed in the bulk rock mechanical properties with respect to Williams Fork lithofacies classification (Figure 4.20). Table 4.5 presents Young's modulus and Poisson's ratio values obtained from acoustic logs (dynamic) for the Williams Fork lithofacies. DRF-rich sandstones (E1) and Fe-dolomite-cemented sandstones (H) have the lowest Poisson's ratio values (mostly < 0.23) (Figure 4.20). In these sandstones, the variation in the quartz and Fe-dolomite cementation probably caused the spread of the Poisson's ratio values. Quartz-cemented sandstones with

medium thick detrital clay coats (Ohio Creek) (C1) have the highest Poisson's ratios (average 0.264). When the depth trends are examined, lithofacies that represent the fracture-prone deepest sandstones (E1 and H) are found to have the lowest Poisson's ratios (Figure 4.20).

Lithological influence on the Young's modulus values are also evident; however, no clear depth trend is observed. The lowest values are associated with the illite/smectite-coated sandstones (B) with an average of 26.1 GPa. Tightly Fe-dolomite-cemented sandstones (H) have the highest Young's modulus values averaging at 39.9 GPa. The clay-matrix rich sandstones (F) (averaging 35.8 GPa) have higher Young's modulus values than the clay-coated sandstones (averaging 26.1 GPa and 31.0 GPa for illite/smectite-coated (B) and chlorite-coated (A) sandstones respectively). The DRF-rich sandstones (E1) that dominate the fractured Lower Williams Fork intervals have Young's modulus values mostly between 26 and 36 GPa (average 32.7 GPa). The variation in the values in this lithofacies was probably controlled by varying amount of quartz and Fe-dolomite cements.

Calcite cement increases the Young's modulus value of the sandstones 2 to 10 GPa. Even when the cementation with calcite is complete, the Young's modulus values are highly variable (Table 4.6). For example, where the Ohio Creek sandstones (C1) are cemented with calcite the Young's modulus value increases from an average value of 33 to 42 GPa and where illite/smectite-coated sandstones are cemented with calcite their Young's moduli go up from the average value of 26 to 32 GPa. This demonstrates the importance of rock properties (framework mineralogy and other cements) present in the system prior to calcite cementation on Young's modulus values.

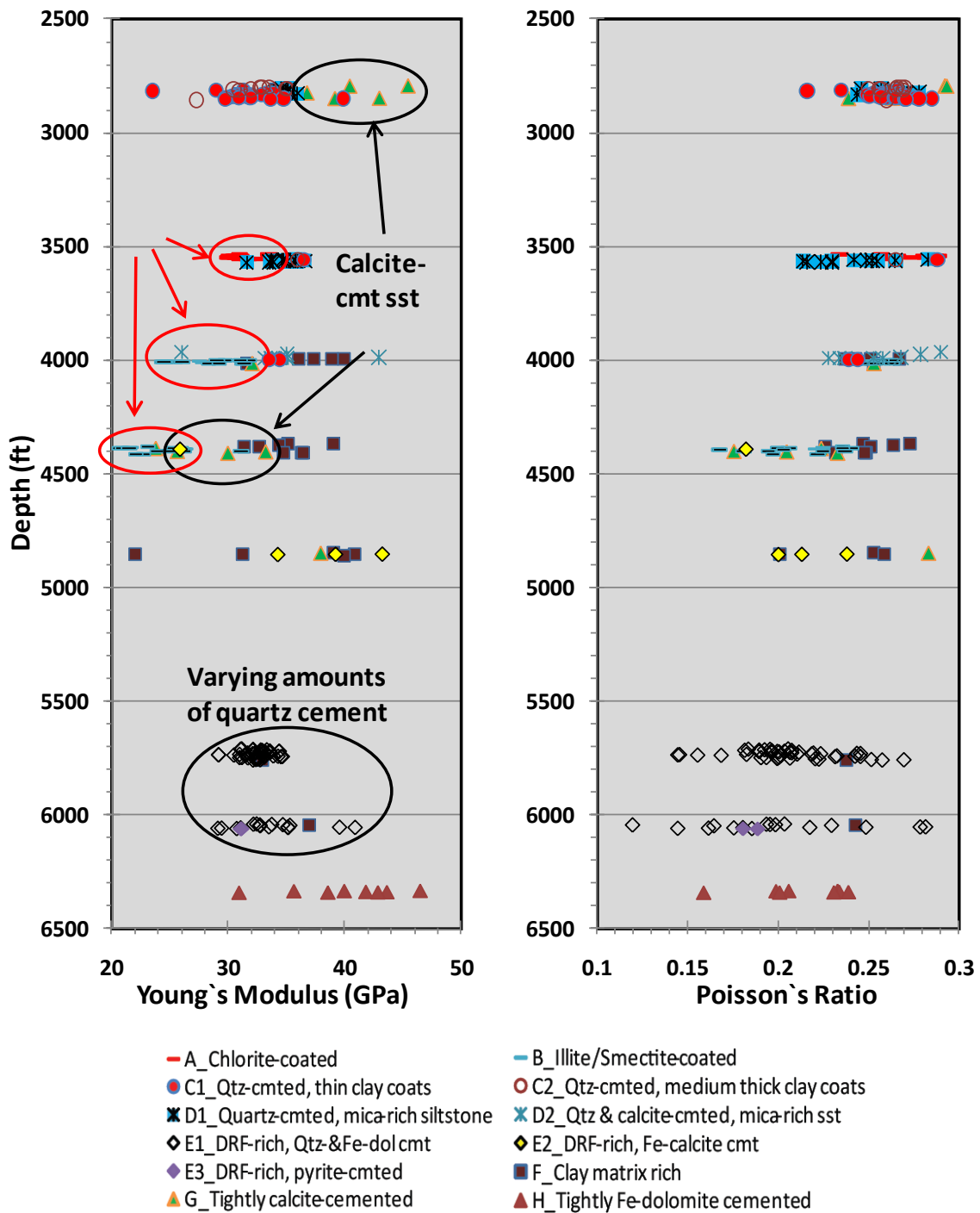


Figure 4.20. Depth distributions of (A) Young's modulus (GPa) and (B) Poisson's ratio calculated from acoustic logs. Young's modulus values are variable throughout the Williams Fork. Lithofacies representing the deeper, more fractured intervals have relatively smaller Poisson's ratio.

Table 4.6. The effects of calcite cement on core measured grain density, dynamic Young's modulus and Poisson's ratio of lithofacies C1, C2 and B. C1: quartz-cemented sandstones with medium thick detrital clay coats (Ohio Creek), C2: quartz-cemented sandstones with thin detrital clay coats (Ohio Creek), B: illite/smectite coated sandstones, and G: tightly calcite-cemented sandstones. The unit of Young's modulus is GPa.

Depth (ft)	Lithofacies	Description	Grain Density (g/cm ³)	Poisson's Ratio	Young's Modulus
2800.2	G	Tightly calcite-cemented, coarser	2.679	0.292	45.4
2801.0	G	Tightly calcite-cemented, coarser	2.679	0.293	40.4
2802.0	C1	Qtz-cemented; medium thick detrital clay coats	2.655	0.268	32.9
2803.0	C1	Qtz-cemented; medium thick detrital clay coats	2.665	0.270	32.7
2804.0	C1	Qtz-cemented; medium thick detrital clay coats	2.663	0.266	33.5
Average	C1		2.661	0.268	33.1
Average	G		2.679	0.293	42.9
2850.0	C2	Qtz-cemented; thin detrital clay coats	2.653	0.264	29.8
2851.0	C2	Qtz-cemented; thin detrital clay coats	2.674	0.265	30.9
2852.0	C2	Qtz-cemented; thin detrital clay coats	2.654	0.285	34.7
2853.0	C2	Qtz-cemented; thin detrital clay coats	2.647	0.278	39.9
2854.1	G	Tightly calcite-cemented	2.659	0.263	43.0
2855.0	G	Tightly calcite-cemented	2.664	0.239	39.2
2856.0	C2	Qtz-cemented; thin detrital clay coats	2.648	0.270	33.7
2857.0	C2	Qtz-cemented; thin detrital clay coats	2.649	0.271	29.8
Average	C2		2.654	0.272	33.1
Average	G		2.662	0.251	41.1
4391.0	B	Illite/Smectite-coated	2.659	0.233	33.6
4391.9	G	Tightly calcite-cemented	2.660	0.226	32.6
4393.0	B	Illite/Smectite-coated	2.652	0.251	31.3
4394.0	B	Illite/Smectite-coated	2.651	0.246	26.8
4394.9	B	Illite/Smectite-coated	2.652	0.236	23.1
4396.0	B	Illite/Smectite-coated	2.649	0.225	21.6
4398.2	B	Illite/Smectite-coated	2.650	0.206	20.9
Average	B		2.652	0.233	26.2
Average	G		2.660	0.226	32.6

4.4.3.4. Discussion: Lithological Controls on Subcritical Crack Index versus Bulk Mechanical Properties

Although the loss of pore space has an influence on the Young's modulus, the main effect appears to be caused by the density of the pore-filling cement (Figure 4.21). It is interesting to see the differences between the effects of quartz cement versus carbonate cement on stiffness. For example, DRF-rich sandstones (E1) have their pore space completely filled with quartz and minor Fe-dolomite cements. While all the available pore space was filled, these sandstones (E1) have lower Young's modulus values than the denser tightly calcite-cemented (G) or tightly Fe-dolomite-cemented (H) sandstones.

In section 4.2 on the microscale textural effects exerted by cement distribution on the subcritical crack index (SCI), I have interpreted the cement growth patterns as the reason for lower SCI values of the quartz- and Fe-dolomite cemented sandstones compared to the tightly calcite-cemented sandstones. Quartz and Fe-dolomite cements precipitating as overgrowths introduce more flaws into the sandstones (overgrowth/overgrowth or overgrowth/grain boundaries) than the very large patches of calcite cement enclosing several grains (poikilotopic distribution). After having examined controls over SCI and bulk mechanical properties, it appears that microscale textural controls are more effective in controlling the SCI, whereas the bulk density of the pore-filling cement has a stronger influence over the Young's modulus. Although, SCI is governed by microtextural controls and the bulk mechanical properties are governed by bulk properties. Crossplots of the average SCI versus Young's modulus and Poisson's ratio demonstrate a positive correlation between the SCI and Poisson's ratio (Figure 4.22).

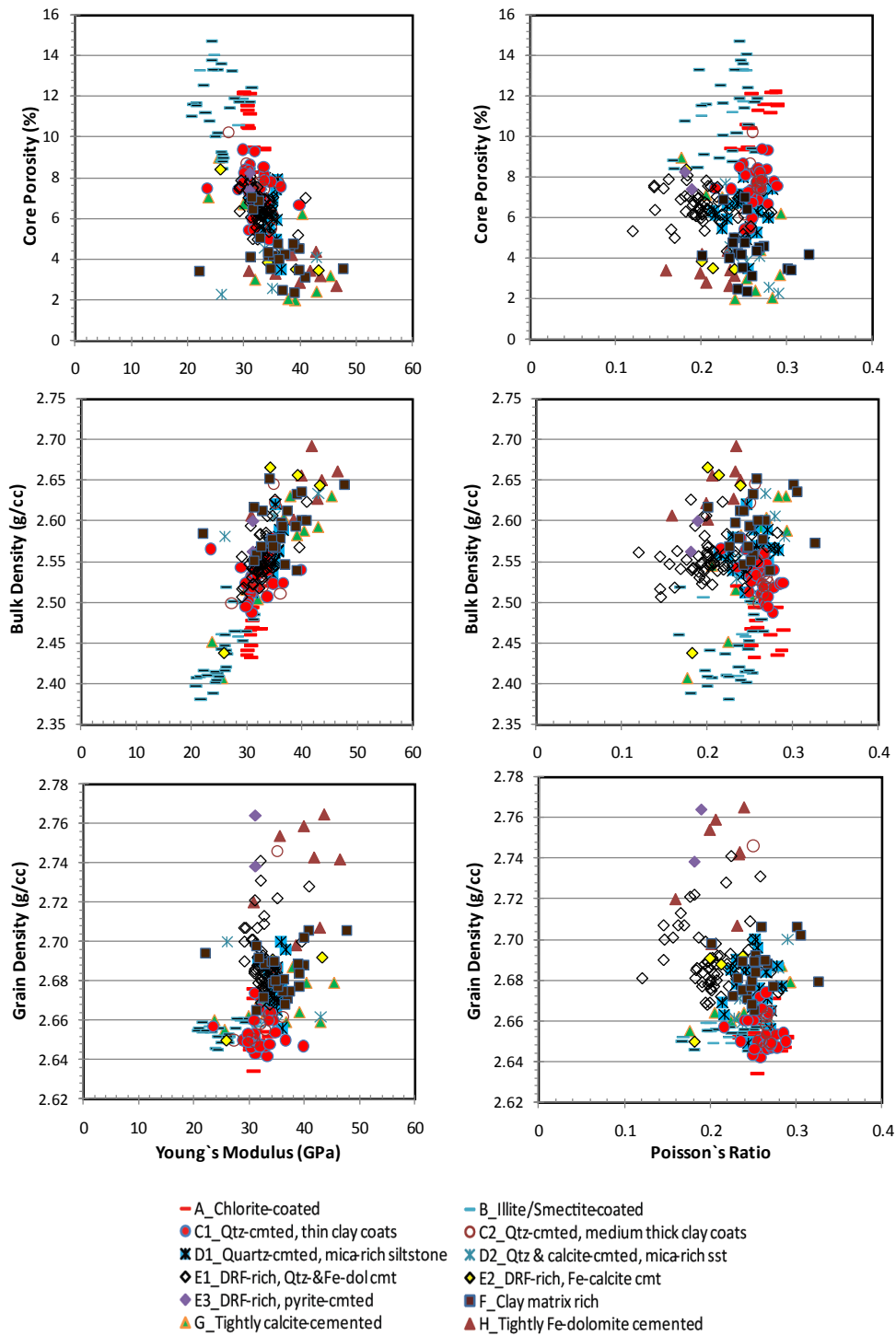


Figure 4.21. Young's modulus and Poisson's ratio plotted against core-measured porosity, log derived bulk density and core-measured grain densities.

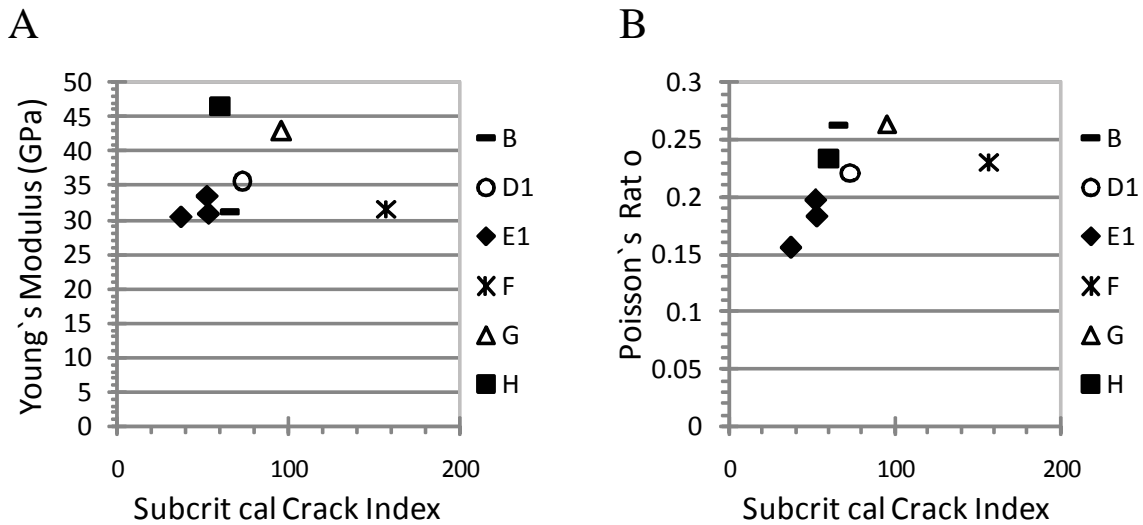


Figure 4.22. SCI versus (A) Young's modulus (GPa) and (B) Poisson's ratio. Distribution is according to the lithofacies classification. B: illite / Smectite-coated; D1: quartz-cemented; mica-rich; sandstone / siltstone; E1: Dolostone grain-rich, quartz- and Fe-dolomite-cemented; F: dolostone grain-rich, quartz- and Fe-dolomite-cemented; G: tightly calcite-cemented; H: Fe-dolomite cemented.

4.4.3.5. Discussion: Predictability of Rock Mechanical Properties and Degree of Fracturing

A cross plot of Young's modulus versus Poisson's ratio displays clear differentiation of the bulk rock mechanical characteristics of some of the lithofacies (Figure 4.23A). Sandstones with the highest degree of fracturing in Figure 4.17 (Lithofacies E1 and H) plot on the regions with relatively low Poisson's ratios and larger Young's modulus values.

Because sandstones representing different lithofacies have systematic variations in the bulk rock mechanical properties, the lithofacies prediction tool introduced in Chapter 3 for the Williams Fork can be used to estimate the rock mechanical properties of the sandstones and to predict the distribution of the fracture-prone lithofacies. As discussed in section 4.4.3.2.2, the values derived from acoustic logs are called dynamic

values and they may be different from the static values measured at laboratory conditions which better represent the rocks. The best estimation of these bulk mechanical properties would be measuring the Young's modulus and Poisson's ratio on representative samples and applying corrections to the dynamic values accordingly.

According to the pore-pressure-assisted fracturing model of Cumella and Scheevel (2008), gas is expelled upward by locally high pressures and fractures the rock. The gas flows to the sandstones with lower pressures and expels the pore water within them so that it migrates the overpressure gas front. This process continues until the pressure is no longer sufficient to fracture the rock or localized shale content is too high to allow gas migration through sand-to-sand migration of an overpressured gas front. Cumella and Scheevel (2008) calculated compression-to-tension thresholds as a function of elastic parameters and pore-pressure gradients. Their plot showing measured rock mechanics data from MWX core samples with compression-to-tension thresholds indicates that pore pressure gradients exceeding 0.8 psi/ft (18.1 kPa/m) may have been sufficient to fracture sandstones and 0.9 psi/ft (20.3 kPa/m) is enough to fracture all rock types (Figure 4.23B).

As can be seen in their figure (4.23B), sandstone and mudstone data points are distributed in distinctly different areas of the cross plot. The lithofacies classification approach introduced in this dissertation helps to further classify the sandstones according to diagenetic characteristics. When the data for the study well is evaluated in a similar way to Cumella and Scheevel (2008) (Figure 23A), it appears that, all conditions being equal, the sandstones least prone to fracturing are clay-coated sandstones (A, B). Fine-grained quartz-cemented sandstones with mica-rich laminations (D1, D2) and clay

matrix-rich sandstones (F) seem to be more prone to fracturing than the clay-coated sandstones. Carbonate cement exerts control such that any given lithofacies that is cemented with carbonate minerals became more prone to fracturing due to the increase in Young's modulus.

Although rock mechanical properties are important inputs for geomechanical models, there are also other input parameters. First, the fractures in the Piceance Basin are partially to completely occupied with quartz, calcite and clay cements; therefore, effects of diagenesis need to be accounted to calculate the effective fracture network permeability (Philip et al., 2005; Olson et al., 2009). Additionally, reservoir geometry (height and width of the sandstone bodies) needs to be considered. Yurewicz et al. (2008) state that as the fractures are nearly vertical and strongly parallel in the Piceance Basin, connectivity depends mainly on fracture density, length, and height. These authors mention that horizontal connectivity in the natural fracture network within fluvial-channel sandstones extends over relatively short distances determined by the channel widths owing to the fact that most natural fractures terminate at sand body margins due to contrasts in mechanical properties among sandstone, siltstone, and shale, and the vertical permeability is limited by sand-body thickness because the fracture spacing increases with sand-body thickness. Yurewicz et al. (2008) suggest that the fracture network connectivity is higher in the proximal-fluvial (Ohio Creek and Upper Williams Fork) and marine sandstones of the Iles Formation than the highly channelized Williams Fork reservoirs because their fractures have much greater bed-parallel lengths because they do not have frequent channel-margin sand-shale contacts to limit the lateral fracture extent.

The conclusion of the two outcrop studies by Lorenz and Finley (1991) and Laubach and Lorenz (1992) is that *observed* mechanical connectivity is low (nearly nonexistent). Greater length distribution does not equate to greater connectivity. This is consistent with the modeling results of Olson (2004) and with relatively low SCI values measured for the Lower Williams Fork intervals, which could account for closely spaced, short fractures, or longer fractures, evenly spaced or clustered, but not necessarily connected. On top of this, the direct evidence from fracture observations (for example, Hooker et al., 2009), the diagenetic sequence, and burial history modeling done in this research, are also consistent with fracture connectivity reduction by the mechanism proposed in Laubach (2003) and applied to fracture patterns by Philip et al. (2005) and Olson et al. (2009) namely, fracture length and connectivity reduction by quartz cement accumulating in the narrow parts of fractures (the emergent threshold effect). Therefore fracture connectivity and length, for static fractures, should be very low; while fractures are growing it can be greater, transiently.

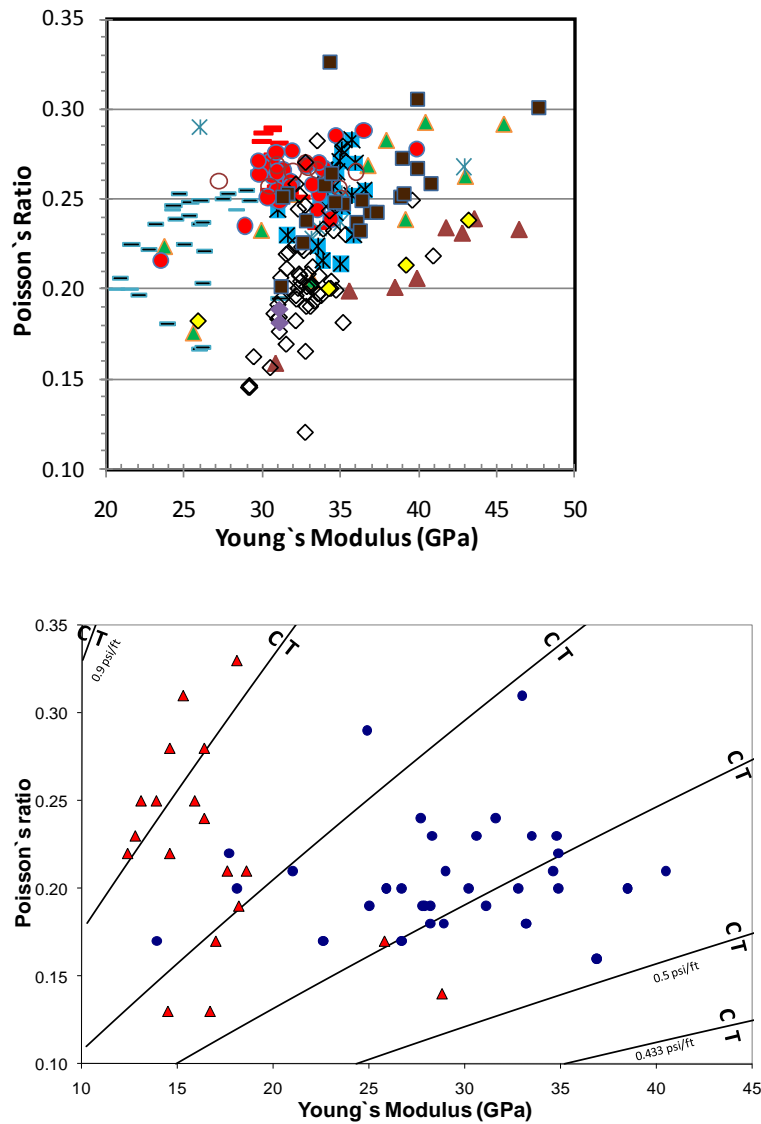


Figure 4.23. Young's modulus versus Poisson's ratio (A) calculated from logs for the study well and (B) measured on core samples from the MWX well (Cumella and Scheevel, 2008). Compression-to-tension thresholds are defined as a function of elastic parameters and pore-pressure gradients. Black lines represent the transition from compressional to tensional (C to T) effective normal stress at the pore-pressure gradient indicated for each curve. The tensional (T) side of the curve is the fracture-prone region. Blue circles are sandstones, and red triangles are mudstones. Fixed parameters for this plot are vertical depth = 7150 ft (2179 m); lithostatic gradient = 1.05 psi/ft (23.75 kPa/m); grain modulus = 44 GPa (6.3×10^6 psi); compressive (tectonic) horizontal strain of +0.018% (yy-axis) and +0.006% (xx-axis).

4.4.4. Diagenetic State and Permeability of Tight Gas Sandstones at the Time of Gas Generation and Fracturing

In this section, the question I try to answer is “Was the sandstone diagenetically involving at the time of fracturing and gas generation”. If the sandstones were still evolving at the time of fracturing the rock mechanical properties were likely changing in concert which would require adjustment of rock mechanical properties to those in effect during fracturing. A diagenetic modeling approach is applied to determine the rock characteristics at the time of fracturing and gas generation for the study well located in Mamm Creek field, Piceance Basin. The basin and diagenetic models are constructed using the procedures explained in Chapter 2. Temperature ranges for fracture opening are obtained from published microthermometry data (fluid inclusions) on the fracture-filling quartz and carbonate cement. Once this temperature data is linked to the burial and thermal histories obtained from basin models, approximate timing of fracture opening is determined. Timing of gas generation is obtained from the literature. The evolution of sandstone’s compaction, quartz precipitation, pores, and permeability in the geologic past is modeled with diagenetic modeling program *Touchstone*TM. The time frame for the fracturing obtained from the literature is imposed on the diagenetic models and the characteristics of the sandstones at the time of fracturing are determined. The results indicate that the sandstones were still diagenetically evolving during fracturing and gas generation.

4.4.4.1. Timing of Gas Generation and Fracturing in the Piceance Basin

The Mesaverde Group was deeply buried, overpressured, and subjected the Late Cretaceous to Early Tertiary Laramide orogeny which produced faults and folds that

surround the basin. Lorenz and Finley (1991) claim that fracturing occurred during a phase of increased Laramide west-compression, and in a pressure-temperature regime compatible with the geologically reconstructed maximum burial depths. They interpret this regional fracturing as an example of load-parallel extension fracturing and basinwide dilatancy at depth, under conditions of high pore pressure and anisotropic, tectonically created, horizontal stress. As explained in section 4.4.2, it has been postulated in the literature that orientation of the fracture systems is determined by Laramide tectonic stress directions (Lorenz and Finley, 1991); on the other hand the distribution and intensity of fracturing have been ascribed to the history of overpressuring during gas charging (Scheevel and Cumella, 2005). Timing of the Laramide orogeny in the Rocky Mountain region generally spanned latest Cretaceous and Paleogene time, roughly 75–50 Ma (Lawton, 2008). According to Scheevel and Cumella (2005), the pore pressure and stress conditions that cause formation of opening-mode fractures existed during gas generation. Although the highest pore pressures were reached during the peak times of gas generation at the time of deepest burial, overpressuring still exists in some areas in the Mesaverde reservoirs within the Piceance Basin. Likewise, although Laramide tectonism accounted for shortening compatible with the east-northeast strike of fractures in the Williams Fork, several different scenarios for Laramide shortening have been proposed (Chapin and Cather, 1981; Greis, 1983; Verbeek and Grout, 1984; Erslev, 2001; Cerca et al., 2004), not all of which are consistent with observed natural fracture strikes. On the other hand, these fracture strikes are compatible with the orientation of current maximum horizontal compression (Zoback and Zoback, 1989). Thus existing constraints

on the timing and origin of fractures are inadequate or at least not fully tested and corroborated.

Gas generation, which likely resulted in overpressuring, started in the Piceance basin at 55 Ma ago and peaked between 47 and 39 Ma, and in the Uinta Basin it started around 42 Ma ago and peaked around 26 to 17 Ma at the structurally deepest regions of both basins (Johnson and Roberts, 2003). Specifically for the MWX site, gas generation began around 51 Ma and peaked at 39 to 20 Ma. This reported peak gas generation time overlaps with the overpressure development from the basin model I reconstructed for the MWX site (Figure 4.24).

Fluid inclusion temperatures obtained from fracture-filling quartz cement from the MWX well by Barker (1989a) indicates temperature ranges 120 to 155 °C at 5,572 ft and 145 to 180 °C at 7844 ft. By linking this temperature data to burial curves, Barker (1989a) interpreted that the fractures were open to precipitation between ~35 to ~9 Ma. He also suggested thermal maturation has not increased since Late Eocene and gas generation must have decreased after thermal stabilization near 35 Ma. The fluid inclusion temperatures referred to in Lorenz and Finley (1991) are also in the range of 120 to 190 °C for the fracture-filling quartz and calcite cement in the samples from MWX core. Their interpretation of fracture opening timing is ~40 to ~36 Ma, during maximum burial with high pore pressure due to organic maturation and during enhanced W-NW tectonic compression. The lower end of the temperature ranges reported for these studies does not actually correspond to the maximum depth of burial. In fact, the Mesaverde sandstone was exposed to these lower-end temperatures (120 – 145 °C) two

times during its burial history, once during the burial and the second time during uplift (Figure 4.24).

It should be noted that the studies mentioned above did not measure fluid inclusion assemblages or relate fluid inclusions to the relative timing of cement deposits. Subsequent studies show that fluid inclusion assemblages in fracture cement deposits are not contemporaneous and many reflect temperatures other than that of maximum burial (Becker et al., 2009a; Fall et al., 2009). These more recent studies combine high resolution SEM-CL (Scanning Electron Microscope/Cathodoluminescence) imaging of quartz bridge cements with microthermometry and Raman microspectrometry to constrain the pressure-temperature-pore-fluid chemical (PTX) evolution during fracture opening and cementation by unraveling relative FIA (Fluid Inclusion Assemblages) timing from crosscutting relations in the crack-seal quartz cement textures in cement deposits (bridges) that precipitated synkinematically in otherwise open fractures with fracture opening in Mesaverde sandstones. These studies indicate that temperature for the fracture-filling quartz cement ranges from $\sim 145^{\circ}\text{C}$ to $\sim 185^{\circ}\text{C}$ in Cozzette Sandstone of the Iles Formation and $\sim 141^{\circ}\text{C}$ to $\sim 177^{\circ}\text{C}$ in the overlying Williams Fork Formation in the cores from MWX / SHCT (nearby slant well) cores, and $\sim 150^{\circ}\text{C}$ to $\sim 172^{\circ}\text{C}$ in the Corcoran Sandstone at the Grand Valley well. Fluid inclusion salinities are reported to be low, ranging from 2 to 3 wt% NaCl equivalent at all examined sites; these values are similar to seawater salinities. These studies also determined that these inclusions were trapped under methane-saturated conditions at trapping pressures ranging from ~ 70 MPa to ~ 100 MPa, suggesting fracture opening occurred under significant pore fluid

overpressures. They constrained the fracture opening and associated hydrocarbon charge between ~42 to ~10 Ma.

When the fluid inclusion temperature and pressure data from Becker et al. (2009a) and Fall et al. (2009) is placed on the basin model reconstructions for the MWX site (described in Chapter 2), the timing of fracture opening is found to range from 42 to 8 Ma (shown as blue-shaded area in Figure 4.25). The timing suggested by Lorenz and Finley (1991), 40 to 36 Ma, is also marked on the figures (yellow shaded area). This timing interpretation coincides with the early development of the overpressures at the base of the Mesaverde. The peak gas generation timing from Johnson and Roberts (2003; 39 to 20 Ma) is in agreement with the overpressure history of the MWX burial reconstructions. The discussion about the diagenetic state of the rock and timing of fracturing and gas generation can be found in section 4.4.4.3.

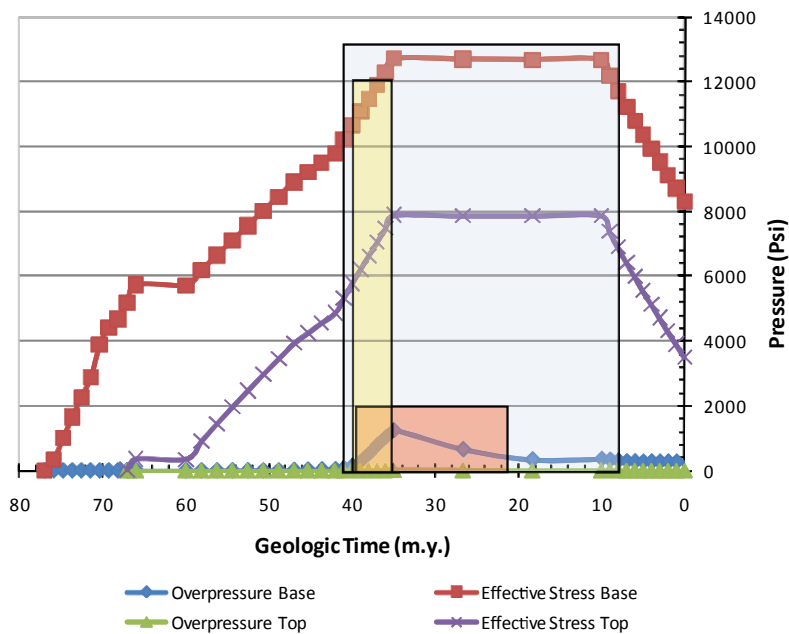
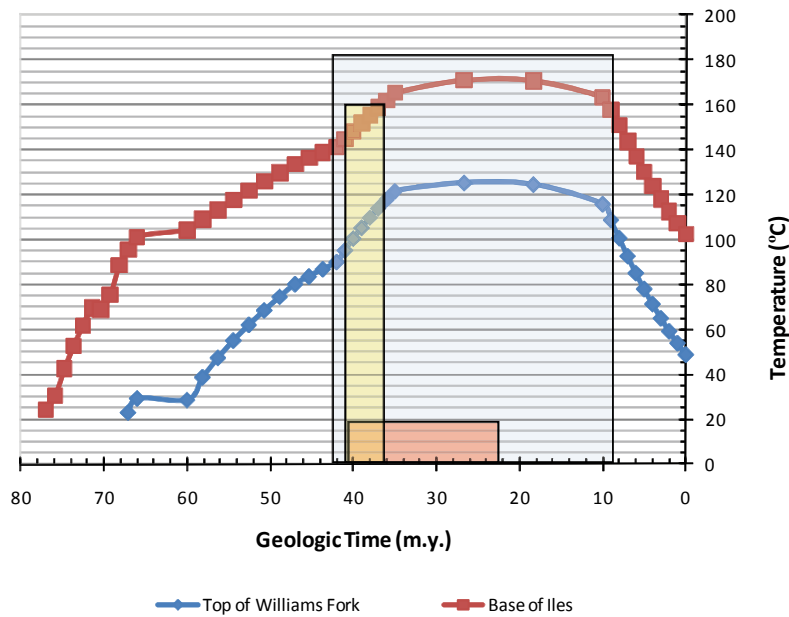


Figure 4.24. Thermal and pressure history curves for the top of Williams Fork and bottom of Iles Formation at MWX well. The fracture opening window is based on the thermal and pressure reconstruction curves. Light blue-shaded area is the fracture opening timing from Becker et al. (2009a) and Fall et al. (2009); yellow-shaded area shows the timing for fracture opening interpreted by Lorenz and Finley (1991), red shaded area is timing of peak gas generation from Johnson and Roberts (2003).

4.4.4.2. Diagenetic Modeling

By following the diagenetic modeling procedures introduced in Chapter 2 (section 2.3.2), I calibrated the IGV (Intergranular volume), quartz cement, core porosity and core permeability parameters (Figure 4.25). In *Touchstone*TM the errors in the compaction model are carried into the quartz model due to the influence of compaction on the available nucleation surfaces. To minimize this compactional effect, *Touchstone*TM can force the calculated IGVs to match the measured IGV. With this approach I optimized a single set of activation energy (Ea) and slope for all samples from the study well and kept the same values for the rest of the modeling (Figure 4.25A & B). After determining quartz precipitation kinetics, I turned off the IGV match option in the program and remodeled the IGV and quartz cement (Figure 4.25C & D). As the final step I modeled the core-measured porosity and permeability to predict the evolution of reservoir quality for the study well (Figure 4.25E and F).

After setting up the calibrations for the IGV, quartz cement, core-measured porosity and core-measured permeability, the evolution of these parameters were modeled for selected samples in geologic time from their burial to present day (Figure 4.26). As discussed in Chapter 3, Williams Fork sandstones are diagenetically heterogeneous. The influence of inherited differences in detrital grain assemblages and depositional setting on the diagenetic pathways indicated by petrographical observations is proven with diagenetic modeling in the Williams Fork sandstones. The modeling results presented in figure 4.26 demonstrate that sandstones that belong to different lithofacies go through significantly different compaction, quartz cementation, and porosity-loss histories. The sandstones plotted in Figure 26 are:

2812 ft.: Lithofacies C1 (Quartz-cemented; medium thick detrital clay coats (Ohio Creek)),

3566 ft.: Lithofacies A (Chlorite-coated),

4016 ft.: Lithofacies B (Illite/smectite-coated),

5733 ft. and 6055 ft.: Lithofacies E1 (Dolostone grain-rich, quartz- and Fe-dolomite-cemented),

6335 ft.: Lithofacies H (Fe-dolomite cemented, dolostone- and quartz grain-rich).

As mentioned previously lithofacies E1 and H are the sandstones that represent the gas-producing Lower Williams Fork.

4.4.4.3. Discussion: Diagenetic Evolution during Gas Generation and Fracturing

Basin-centered gas accumulations are typically characterized by regionally pervasive, abnormally pressured and low-permeability gas saturated zones that commonly lack downdip water (Law, 2002). The main trapping mechanism for the gas is thought to be the low permeability of the reservoirs in the vicinity of the basinwide gas kitchen. For the Williams Fork reservoirs, Cameo coals within the coastal plain deposits are the main source of gas. Significant thermal gas generation from these coals began in early Eocene at the time of deepest burial (Johnson and Roberts, 2003). By that time diagenesis is claimed to have resulted in reduction of most of the pore space and lowered the permeabilities (Pittman et al., 1989). Due to lower permeabilities gas cannot escape from individual sandstone intervals, and eventually the reservoir became overpressured, assisting in the fracturing process (Meissner, 1987; Spencer, 1989; Law, 2002; Cumella and Scheevel, 2008). Although, the permeability is thought to be very low, no studies

have attempted to quantify the porosity and permeability of the tight gas sandstones at the time of gas generation and fracturing. In this section by using the diagenetic modeling approach, I model the evolution of parameters that control the reservoir quality in an attempt to quantify these parameters at the time of gas generation and fracturing.

Evolution of key reservoir quality variables including quartz cementation, intergranular pores, and permeability are shown for selected Williams Fork sandstones. These results were produced by plotting the results of diagenetic models against geologic time (Figure 4.26). The likely time of fracturing adopted from Becker et al. (2009a) and Fall et al. (2009) is shown in the light blue-shaded area. The peak time of gas generation adopted from Johnson and Roberts (2003) is shown as red-shaded area. Diagenetic modeling results indicate that sandstones had higher porosity and permeabilities at the time of early gas generation (51 Ma) as shown in Table 4.7. At about 35 Ma when the rocks reached their maximum depth and thermally stabilized, quartz cement filled up the available pore space and reduction in porosity and permeability stabilized in the sandstones closest to the gas generating Cameo interval (E1, Figure 4.16). Therefore, at the time of peak gas generation the diagenetic state and reservoir quality of the sandstones were close to those observed today (mostly <1 mD permeability).

When the quartz cement and intergranular pore space of the sandstones are constrained, it is observed that the sandstones were still evolving in terms of their cement content and other bulk rock properties during the early phase of fracturing (Figure 4.26). The diagenetic state was not drastically different than the present day characteristics in the Lower Williams Fork interval, but differences in the sandstones of the Upper Williams Fork interval are observed.

In conclusion, although there were not major changes in the diagenetic state (amount of quartz cement) of the analyzed sandstones from the beginning of the fracturing to the end, some of the sandstones were still diagenetically evolving at the time of fracturing, which probably affected their rock mechanical properties. For example, even slight increases of quartz cementation in the rock mass during and after fracturing can be expected to raise Young's modulus about 6 GPa, a value of the difference obtained by comparing similar lithofacies in differing diagenetic states (section 4.4.3.3.3). Such differences could cause fractures to be stiffer than would otherwise be the case, and much harder to close by subsequence burial loading (Olson et al., 2009). Moreover, additional quartz cement of 7.3% found to increase the subcritical crack index about 30 (from 21.7 to 49.6; explained in section 4.4.4.3). Earlier fracturing that occurs when the host sandstone has lower SCI could result in developing dense patterns of relatively closely spaced fractures for a given mechanical layer thickness (Olson, 2004). Therefore, the best approach for prediction of fracture network characteristics is achieved by adjusting rock properties to those in effect during fracturing.

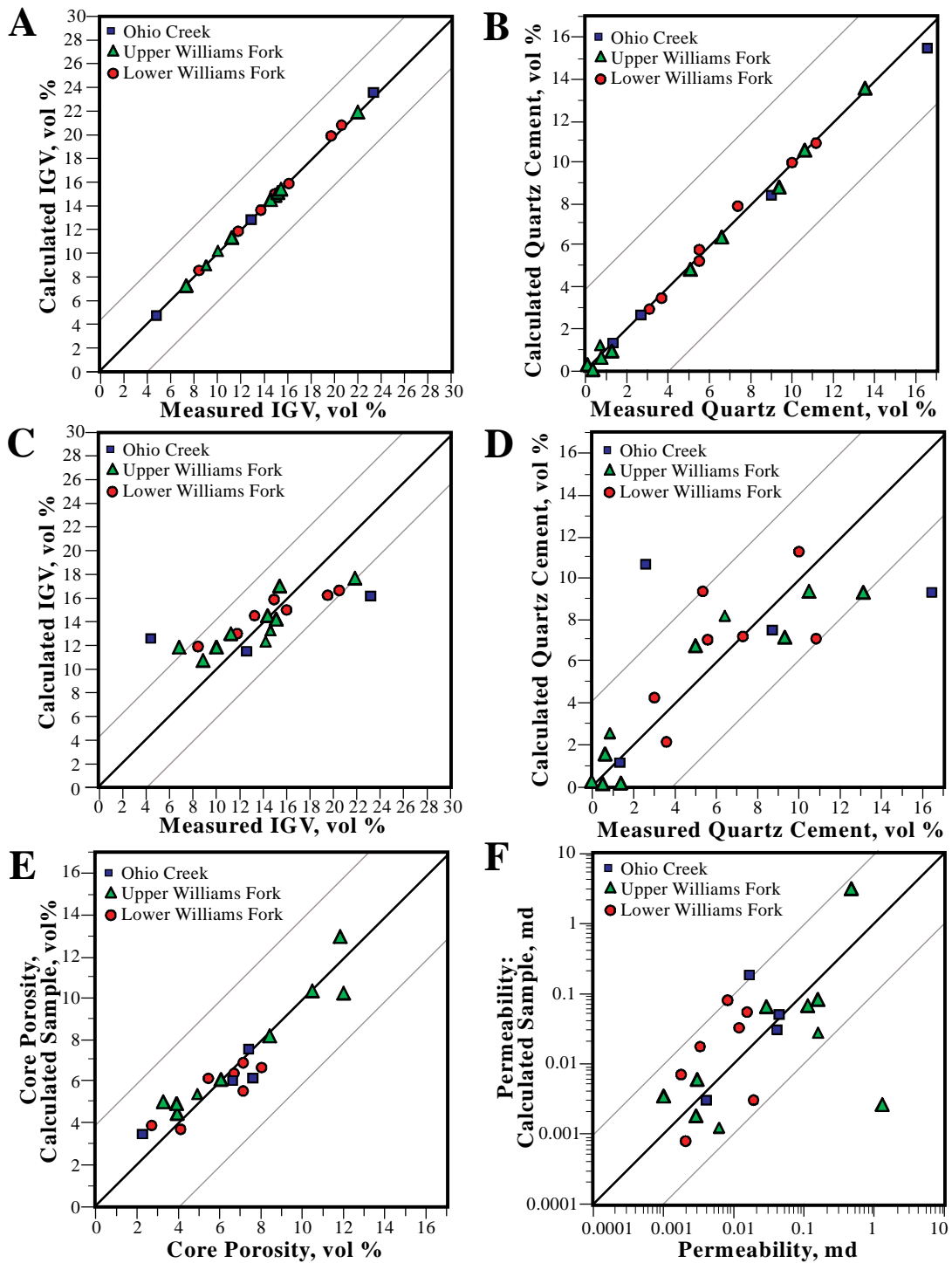
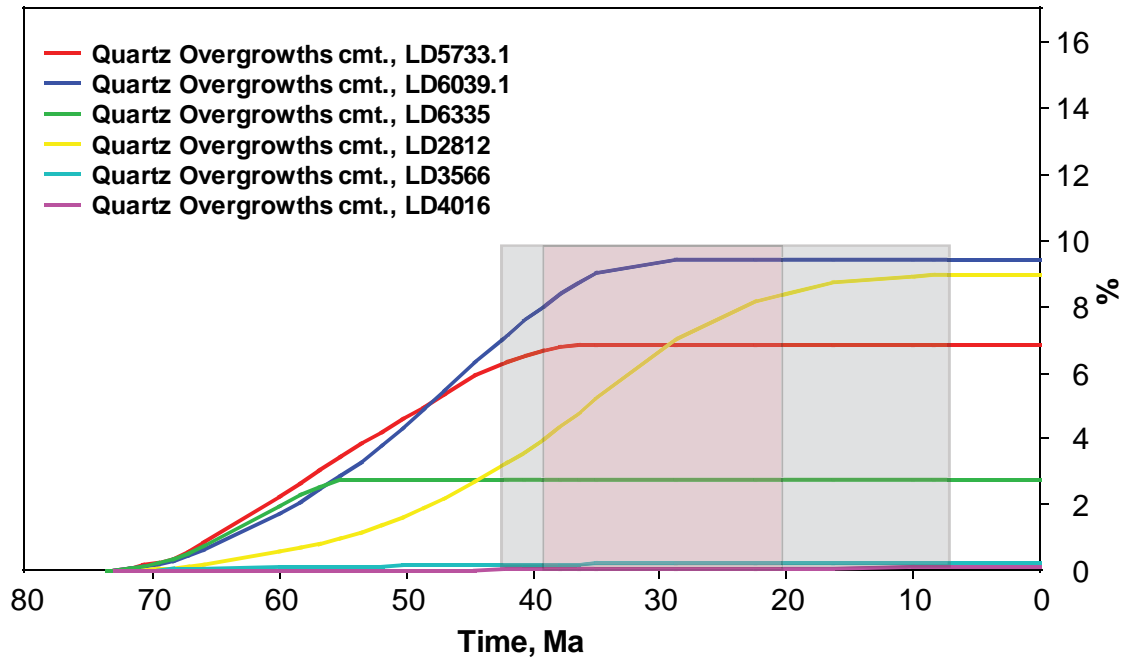
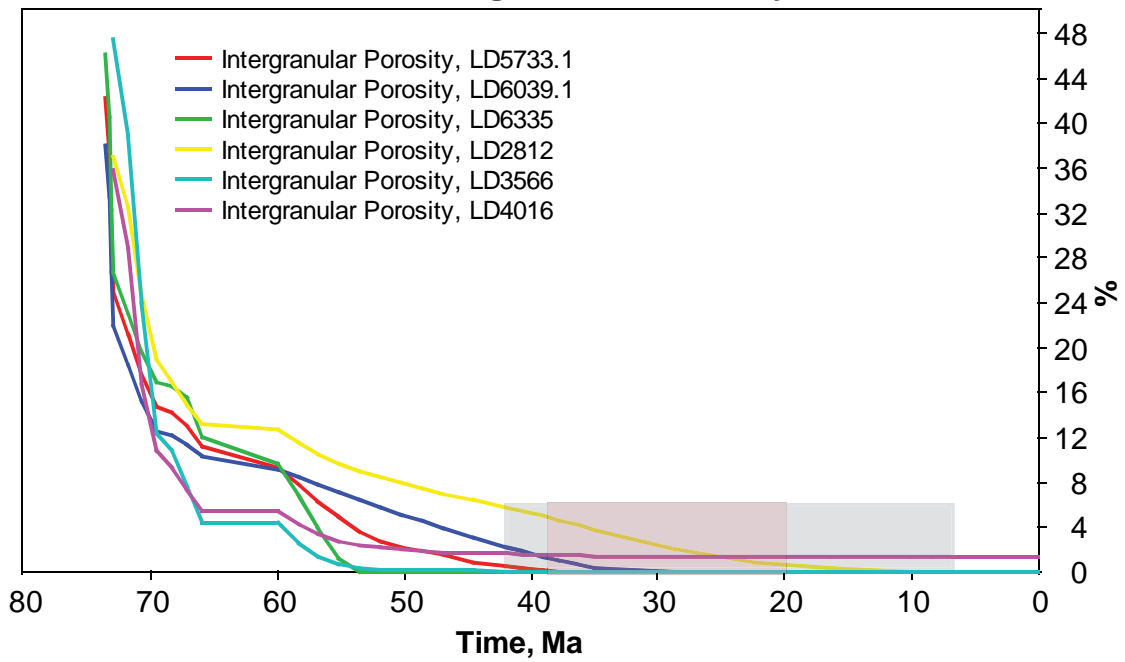


Figure 4.25. IGv, quartz cement, porosity and permeability calibrations for the diagenetic modeling of the Williams Fork Sandstones.

A**Quartz Cement****B****Intergranular Porosity**

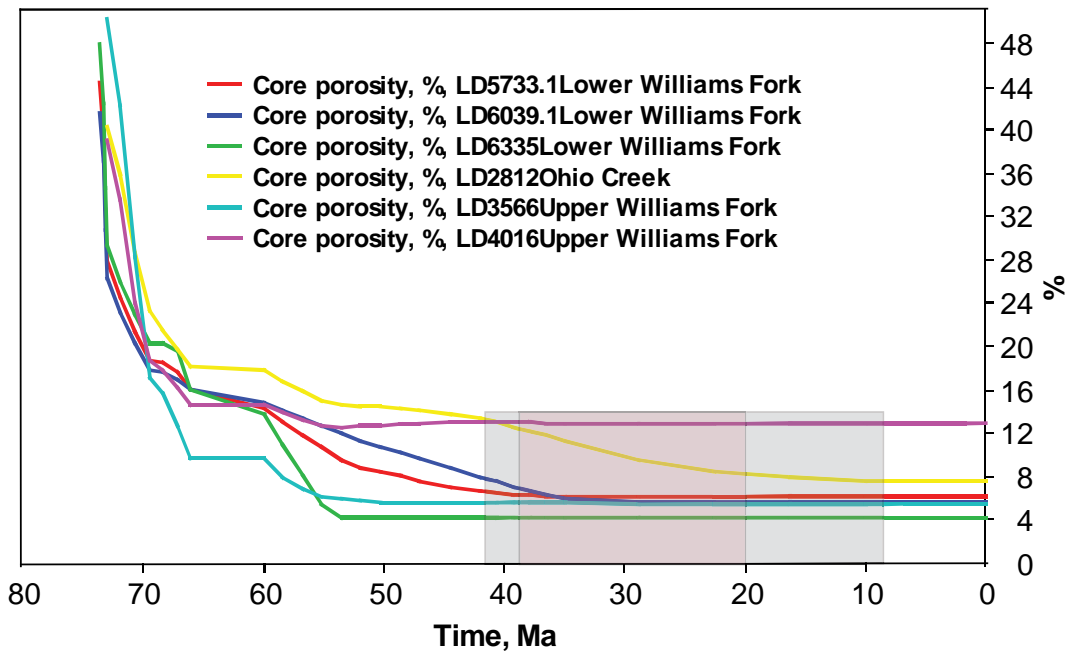
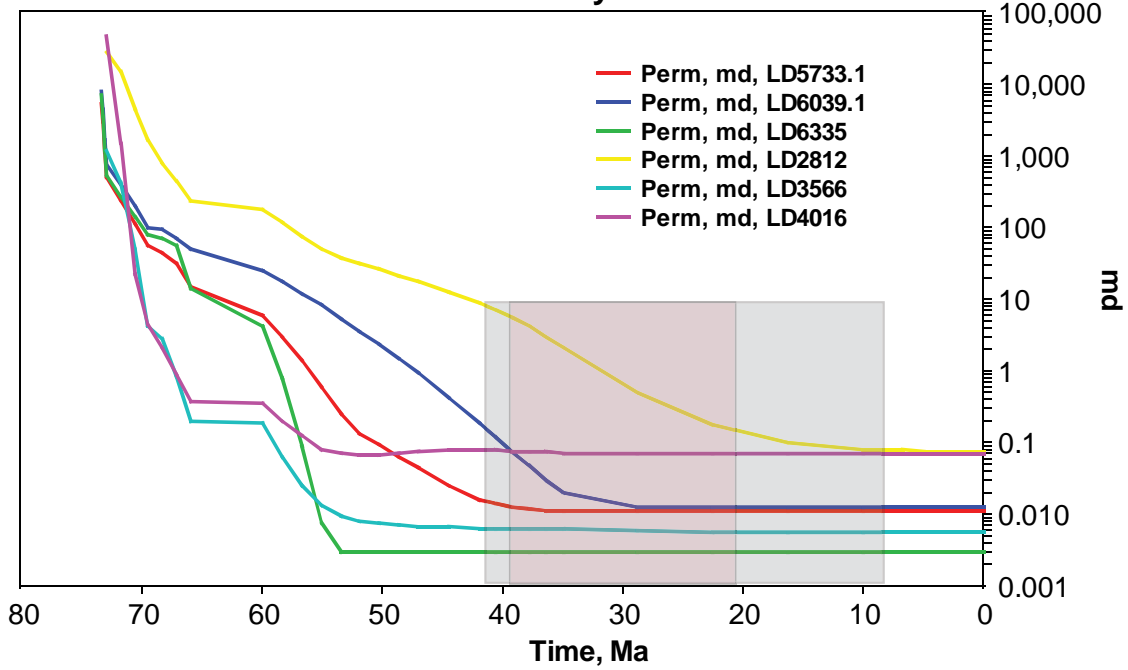
C**Core Porosity With Time****D****Permeability with Time**

Figure 4.26. Evolution of variables that control the reservoir quality over geologic time in selected samples from the Williams Fork: (A) quartz cementation, (B) intergranular pores, (C) core porosity, and (D) permeability. These results were produced by plotting the results of diagenetic models against geologic time. The likely time of fracturing (42 – 8 Ma) is shown with grayish blue-shaded area and peak gas generation (39 -20 Ma) is shown with red-shaded area (Note that gas generation started 51 Ma ago and peaked between 39 and 20 Ma (Johnson and Roberts (2003)).

Table 4.7. Porosity and permeability of selected Williams Fork samples in the geologic past.

Time	Lithofacies C1		Lithofacies A		Lithofacies B	
	2812		3566 ft		4016 ft	
	Perm	Core Porosity	Perm	Core Porosity	Perm	Core Porosity
	md	%	md	%	md	%
Measured	0.0423	7.5	0.0025	5.4	0.0728	12.8
0	0.0767	7.7	0.0054	5.5	0.0961	12.9
1	0.0768	7.7	0.0054	5.5	0.0961	12.9
2	0.0768	7.7	0.0054	5.5	0.0961	12.9
3	0.0768	7.7	0.0054	5.5	0.0962	12.9
5	0.077	7.7	0.0054	5.5	0.0962	12.9
6	0.0772	7.7	0.0054	5.5	0.0962	12.9
7	0.7774	7.8	0.0054	5.5	0.0962	12.9
8	0.07778	7.8	0.0054	5.5	0.0963	12.9
9	0.0783	7.8	0.0054	5.5	0.0963	12.9
10	0.0793	7.8	0.0054	5.5	0.0964	12.9
26.67	0.7147	10.4	0.0054	5.5	0.0984	13
35	7.423	13.8	0.0057	5.5	0.0997	13
37	12.7	14.7	0.0058	5.6	0.1008	13.1
38	15.7	15	0.0059	5.6	0.1016	13.1
39	19	15.3	0.0059	5.6	0.1026	13.1
40	21.9	15.3	0.0059	5.6	0.104	13.1
41	25.1	15.2	0.006	5.6	0.106	13.2
42	29.2	15.1	0.0061	5.6	0.1011	13
44.5	39.8	15.5	0.0064	5.6	0.956	12.9
47	66.6	16.4	0.007	5.7	0.0909	12.7
48.86	1113	17.5	0.0086	5.9	0.0866	12.5
50.71	199	18.8	0.0137	6.3	0.089	12.6
52.57	367	20.4	0.036	7.3	0.1138	13.1
58.14	3736	28.9	3.606	16.8	1.109	16.4
60	10826	34.6	17.5	23	3.316	18.7
67	26216	39.5	55.4	28.9	8.432	20.9
68	27747	39.9	77.2	30.8	11.8	21.9
69	27803	40	88.9	31.6	13.5	22.4
70	27892	40	105	32.7	15.8	22.9
71	28030	40	179	36.1	27.6	25
72	28125	40	239	38.1	43.8	26.4
73	28228	40	323	40.3	124	28.7
73.25	28349	40.1	466	43	466	31.5
73.5	28468	40.1	679	45.9	2016	34.5
75.25	28572	40.1	961	48.7	12069	37.5
77	28313	40.3	1159	50.3	46585	39.2

Table 4.7. (ctd) Porosity and permeability of selected Williams Fork samples in the geologic past.

Time	Lithofacies E1		Lithofacies E1		Lithofacies H	
	5733 ft		6055 ft		6335 ft	
	Perm	Core Porosity	Perm	Core Porosity	Perm	Core Porosity
	md	%	md	%	md	%
Measured	0.0173	7	0.0538	6.8	0.0008	4.1
0	0.011	6.3	0.0254	6.7	0.0031	4.3
1	0.011	6.3	0.0254	6.7	0.0031	4.3
2	0.011	6.3	0.0254	6.7	0.0031	4.3
3	0.011	6.3	0.0254	6.7	0.0031	4.3
4	0.011	6.3	0.0254	6.7	0.0031	4.3
6	0.011	6.3	0.0254	6.7	0.0031	4.3
7	0.011	6.3	0.0254	6.7	0.0031	4.3
8	0.011	6.3	0.0254	6.7	0.0031	4.3
9	0.011	6.3	0.0254	6.7	0.0031	4.3
10	0.011	6.3	0.0254	6.7	0.0031	4.3
18.33	0.011	6.3	0.0254	6.7	0.0031	4.3
26.67	0.011	6.3	0.0254	6.7	0.0031	4.3
35	0.011	6.3	0.0254	6.7	0.0031	4.3
37	0.012	6.4	0.0271	6.8	0.0031	4.3
38	0.0134	6.6	0.0299	7	0.0031	4.3
39	0.0155	6.8	0.0355	7.2	0.0031	4.3
40	0.0182	7.1	0.0469	7.4	0.0031	4.3
41	0.0212	7.4	0.062	7.7	0.0031	4.3
42	0.0257	7.6	0.0811	7.9	0.0031	4.3
44.5	0.0494	8.3	0.1557	8.6	0.0031	4.3
47	0.0936	9	0.2986	9.3	0.0031	4.3
48.86	0.1438	9.6	0.462	9.9	0.0031	4.3
50.71	0.2076	10	0.692	10.4	0.0031	4.3
54.43	1.731	13	2.412	12.1	0.003	4.3
56.29	4.562	14.7	5.282	13.2	0.0095	5.6
58.14	11.8	16.5	11.4	14.4	0.3042	9.6
60	18.6	17.4	24.1	15.7	4.934	13.9
66	27.3	18.2	37.1	16.5	19.5	16.7
67	38.4	19.1	48.4	17.2	42.9	18.6
68	51.8	19.9	61.5	17.9	53.9	19.2
69	64	20.3	70.6	18.2	62.7	19.4
70	78.3	20.9	83.5	18.7	73.9	19.9
71	139	23.6	155	21.2	129	22.4
72	212	25.4	235	22.9	194	24.2
73.25	634	31.2	740	28.7	633	30.5
73.5	1242	35.8	1597	33.4	1452	36.2
75.25	2487	41.1	3540	38.9	3917	43.2
77	3740	44.5	5668	42.6	6997	47.8

4.4.4.4. Conclusions: Influence of Rock Mechanical Properties on Fracture Distribution

In this section, I examined lithological controls over rock mechanical properties by examining the subcritical crack index values measured on core samples and Young's modulus and Poisson's ratio derived from acoustic logs on sandstones representing different lithofacies. I also examined the influence of rock mechanical properties on the degree of fracturing based on the differences in degree of fracturing between the Upper and Lower Williams Fork intervals in the study well.

Overall, lithological controls are evident on the rock mechanical properties. The most obvious relationship is that increased calcite cement increased the SCI and Young's modulus values. The highest fracture density is observed in the Lowest Williams Fork interval that is dominated by DRF-rich sandstones cemented with quartz and Fe-dolomite (E1) and Fe-dolomite cemented sandstones (Lithofacies H). These sandstones are characterized by the lowest SCI values. The lithofacies E1 also has the lowest Poisson's ratio values. Overpressuring probably played the most important role in the degree of fracturing; however, having more fracture-prone sandstones in the intervals below top gas likely facilitated higher degrees of fracturing in the lower Williams Fork.

The evolution of compaction and cementation in the Williams Fork sandstones are modeled in the geologic past from the time of their burial to present day. The modeling results demonstrate that sandstones with different compositions go through significantly different compaction, quartz cementation, and porosity-loss histories. Additionally, the diagenetic modeling study shows that the diagenetic state of sandstones was still evolving and different than the present day characteristics of the sandstones at the start of gas generation and early fracturing. According to the plots of quartz cement

evolution in geologic time, the diagenetic state stabilized around 35 Ma and the sandstones at that time were close to their present day characteristics.

Because rock mechanical properties were estimated to be still evolving in some of the sandstones at the time of fracturing, accurate prediction of fracture network characteristics requires that rock properties be adjusted to the modeled rock-property evolution

Diagenetic modeling is also helpful in constraining the permeability and porosity of the Williams Fork sandstones at the time of gas generation. Diagenetic modeling suggests that the permeability of the sandstones was less than 1 mD for most of the sandstones during gas generation which is in agreement with the theory of basin-centered gas accumulation that requires low permeability sandstones in the vicinity of gas producing intervals for gas accumulation.

CHAPTER 5: CONCLUSION

My research shows that essential information for predicting and understanding fracture patterns in sandstone can be obtained by unraveling cement precipitation (diagenetic) history. Fractures depend on the mechanical properties existing during fracture growth. I show that key mechanical properties such as subcritical crack index, as well as petrophysical behavior and many other properties depend in a systematic way on the thermal exposure (time-temperature history) and the intrinsic grain surface attributes of these deposits. My study tested the hypothesis that the cement precipitation step, governed by thermal exposure and grain surface attributes, governs how sandstone attributes evolve using observations from the Late Cretaceous Williams Fork sandstones from the Piceance Basin, Colorado.

The following are major contributions of this dissertation.

1. Rock mechanical properties such as the subcritical crack index (SCI), Young's modulus, and Poisson's ratio vary with degree of quartz cementation. My results show that chemical evolution governs progressive changes in a rock's mechanical properties. In the case of the SCI this connection is made quantitatively (in Chapter 4), whereas the connections between the other mechanical parameters and cementation are not fully demonstrated, but implied (theoretically).
2. I demonstrate how to identify circumstances in which current properties can or cannot be used to model fractures and show how to obtain mechanical property attributes for past diagenetic states if they are needed. My research provides an example of how the progress of quartz cementation through geological time can be effectively modeled, and

how these mechanical parameters can therefore also be modeled at different times in a rock's burial history. This provides a tool for making predictions of a rock's fracturing behavior at different times in the burial history. I show that modern rock properties at the present state of stress do not always yield information that is useful for understanding fracture patterns in the subsurface.

3. At a microscale, my research demonstrates, using SEM/CL imaging and samples from the SCI experiments, that the diagenetic history of the rock imposes fabric heterogeneities such as cement/grain, cement/pore, cement/cement boundaries that control the growth of fractures. Thus, my dissertation identifies a class of observations and a technical approach that can be used in future research to expand our understanding of fracture mechanics.

4. My study illustrates that lithologic heterogeneity, imposed by the interaction of primary composition, depositional environment, and diagenesis, in the Williams Fork Formation is substantial (12 lithofacies identified) and can be related in a systematic way to reservoir quality (porosity, permeability, and mechanical attributes that govern fracture growth).

5. My results demonstrate a strong correlation between lithofacies of contrasting reservoir quality and log properties, most significantly density and gamma-ray. Thus, these lithofacies and their corresponding reservoir quality can potentially be mapped on a field scale (Ozkan et al., AAPG Bulletin, accepted manuscript in revision).

6. My research shows that rock mechanical properties correlate with these the lithofacies I identified. This result provides an essential ingredient, hitherto lacking (see

for example, Olson et al., 2009; Laubach et al., 2009), for quantitative fracture property prediction.

7. I test the fundamental concept that diagenesis in the subsurface is a progressive process. My data helps to further document (1-6 above) that an integrated assessment of chemical and mechanical processes, using both micro-scale and bulk analytical methods, is a fruitful line of inquiry that can yield predictive tools for understanding reservoir quality in the subsurface.

APPENDIX A: INPUT FOR DIAGENETIC MODELING

MODAL ANALYSES (POINT COUNT AND TEXTURAL DATA)

Abbreviations:

SRF: Sedimentary Rock Fragment, VRF: Volcanic Rock Fragment, MRF: Metamorphic Rock Fragment, PRF: Plutonic Rock Fragment, Petrophys.: petrophysical data, O. Creek: Ohio Creek, UWF: Upper Williams Fork, LWF: Lower Williams Fork, Microxl: microcrystalline, Sid: siderite, Fe-dol: Fe-dolomite, Cmt: cement, Qtz: quartz, Feld: feldspar, Mins: minerals. pf: pore-filling, pl: pore-lining.

Sample Info				Petrophys. Data			Grain Texture			Framework Grains							
Sample	Well	Chronos trat	Burial Depth (ft)	Porosity (%)	Perm. (md)	Grain Density g/cm3	Mean Grain Size (mm)	Sorting	Grain Coating (%)	Qtz	Feld	SRF	VRF	MRF	PRF	Mins	Other Grains
GV2 6910.9	Grand Valley	Cozette	6910.9	5.2	0.003	2.66	0.08	MW	45.0	55.5	6.8	11.8	3.0	1.5	0.3	0.5	0.0
GV2 6938.2	Grand Valley	Cozette	6938.2	7.0	0.002	2.66	0.17	W	50.0	47.3	5.5	10.3	2.8	14.3	0.0	0.3	0.0
GV2 6941.4	Grand Valley	Cozette	6941.4	6.7	0.002	2.68	0.16	W	50.0	44.0	4.5	13.0	3.8	18.3	0.3	0.8	0.0
GV2 6949.5	Grand Valley	Cozette	6949.5	7.3	0.002	2.66	0.21	MW	35.0	41.3	3.0	8.5	3.0	21.5	1.0	0.5	0.0
GV2 6954.1	Grand Valley	Cozette	6954.1	5.9		2.65	0.17	W	4.0	42.3	5.3	4.5	2.8	18.8	0.3	0.0	0.0
GV2 6957	Grand Valley	Cozette	6957.0				0.21	M	75.0	42.0	2.5	24.5	5.3	7.3	3.5	0.0	1.3
GV2 6962	Grand Valley	Cozette	6962.0	5.9		2.73	0.25	MW	75.0	32.3	2.5	16.3	4.8	9.3	1.0	0.0	0.5
GV2 6966	Grand Valley	Cozette	6966.0	5.7	0.002	2.68	0.21	MW	50.0	42.5	2.8	6.5	4.0	33.0	0.5	0.8	0.0
GV2 6972	Grand Valley	Cozette	6972.0	7.0		2.70	0.15	MW	35.0	41.5	3.3	8.3	5.0	21.0	1.0	0.0	0.0
GV2 7122.3	Grand Valley	Cozette	7122.3	4.0		2.72	0.06	MW	40.0	44.3	5.0	28.3	2.3	4.0	0.0	2.0	0.5
GV2 7132.1	Grand Valley	Cozette	7132.1	6.9		2.64	0.09	MW	30.0	46.5	4.0	8.8	5.3	8.3	0.8	0.0	0.5
GV2 7151.1	Grand Valley	Cozette	7151.1	5.2		2.66	0.11	W	70.0	49.0	3.0	5.0	4.8	4.0	0.5	0.3	0.0
GV2 7160.8	Grand Valley	Corcoran	7160.8	11.9	0.001	2.67	0.10	W	70.0	44.8	4.8	8.0	5.3	8.3	0.3	0.0	0.3
GV2 7167.b	Grand Valley	Corcoran	7167.0				0.16	W	40.0	41.0	3.3	17.8	5.8	2.0	3.0	0.0	0.0
GV2 7167.2	Grand Valley	Corcoran	7167.2	9.0		2.67	0.18	M	40.0	44.0	3.5	9.5	5.5	9.5	1.3	0.0	0.3
GV2 7173.2	Grand Valley	Corcoran	7173.2	7.9	0.002	2.66	0.18	W	40.0	40.3	4.3	11.0	2.5	11.8	0.8	0.0	0.0
GV2 7207	Grand Valley	Corcoran	7207.0	7.5		2.68	0.19	MW	40.0	43.8	3.8	3.8	6.8	19.0	0.5	0.5	0.3
GV2 7212.6	Grand Valley	Corcoran	7212.6	8.1	0.002	2.67	0.22	W	40.0	37.8	4.0	7.3	11.3	19.8	2.3	0.3	0.0
GV2 7220.2	Grand Valley	Corcoran	7220.2	7.6		2.67	0.19	MW	30.0	35.5	7.0	7.8	14.0	14.8	0.5	1.0	0.0
GV2 7233	Grand Valley	Corcoran	7233.0	8.6	0.002	2.69	0.11	W	25.0	41.0	7.8	8.0	8.8	7.8	0.8	0.8	0.0
GV2 7247	Grand Valley	Corcoran	7247.0	3.0		2.71	0.10	MW	30.0	40.0	7.8	12.8	6.3	11.3	2.0	0.3	0.0
GV2 7268	Grand Valley	Corcoran	7268.0				0.13	W	30.0	37.5	3.8	17.8	7.0	11.0	4.3	0.5	0.5
LD2812	Last Dance	O. Creek	2812.0	7.5	0.037	2.66	0.30	MW	10.0	33.8	11.5	7.5	10.0	2.0	4.8	0.8	0.0
LD2834	Last Dance	O. Creek	2834.0	7.5	0.039	2.65	0.19	M	30.0	33.3	12.5	11.5	11.0	4.8	9.3	1.0	0.0
LD2845	Last Dance	O. Creek	2845.0	6.7	0.016	2.67	0.14	W	30.0	45.2	13.0	11.0	6.6	7.0	4.8	4.8	0.4
LD2854	Last Dance	O. Creek	2854.0	2.4	0.004	2.66	0.26	MW	30.0	30.5	13.5	7.3	12.5	1.5	5.3	1.3	0.0
LD3551.9	Last Dance	UWF	3551.9	10.4	0.472	2.63	0.22	MW	94.0	32.1	28.0	0.7	11.0	1.6	12.8	0.9	0.0
LD3561	Last Dance	UWF	3561.0	7.6	0.040	2.65	0.21	MW	86.0	33.0	18.5	8.3	17.5	0.0	6.0	1.5	0.0

Sample	Porosity		Cements Quartz		Carbonate						Clay Minerals								
	Inter. Pores	Second. Pores	Quartz cmt	Microxl Quartz	Calcite	Fe Calcite	Fe-Dol	Sid. pf	Sid. pl	Carb Undiff	Illite pf	Illite pl	Illite pb	Smectite	Chlorite pf	Chlorite pl	Kaolinite	Clay Undiff	Other Cmts
GV2 6910.9	0.0	0.0	4.5	0.0	0.0	0.0	0.0	0.0	0.0	0.0	0.0	0.0	0.0	0.0	0.0	0.0	0.0	0.0	0.0
GV2 6938.2	0.3	1.3	9.5	0.0	0.0	0.0	0.3	0.0	0.0	0.0	0.0	0.0	0.0	0.0	0.3	0.0	0.0	0.0	0.0
GV2 6941.4	0.0	1.5	5.8	0.0	0.0	0.0	0.0	0.0	0.0	0.0	0.0	0.0	0.0	0.0	0.8	0.0	0.0	0.0	0.0
GV2 6949.5	1.0	1.0	6.5	0.0	0.0	0.0	0.0	0.0	0.0	0.0	0.0	0.0	0.0	0.0	2.3	0.0	0.0	0.0	0.0
GV2 6954.1	0.3	0.5	12.8	0.0	0.0	0.0	0.0	0.0	0.0	0.0	0.0	0.0	0.0	0.0	0.0	0.0	0.0	0.0	0.0
GV2 6957	0.0	0.8	8.3	0.0	0.0	0.0	0.0	0.0	0.0	0.0	0.0	0.0	0.0	0.0	0.0	0.0	0.0	0.0	0.0
GV2 6962	0.0	0.0	4.5	0.0	0.0	0.0	5.0	0.0	5.3	0.0	0.0	0.0	0.0	0.0	0.0	0.0	0.0	0.0	0.0
GV2 6966	0.0	0.0	6.8	0.0	0.0	0.0	0.0	0.0	0.0	0.0	0.0	0.0	0.0	0.0	0.0	0.0	0.0	0.0	0.0
GV2 6972	0.0	0.0	12.5	0.0	0.0	0.0	0.0	0.0	0.0	0.0	0.0	0.0	0.0	0.0	0.5	0.0	0.0	0.0	0.0
GV2 7122.3	0.0	0.0	3.0	0.0	0.0	0.0	5.5	0.0	0.0	0.0	0.0	0.0	0.0	0.0	0.0	0.0	0.0	0.0	0.0
GV2 7132.1	0.0	0.0	4.3	0.0	0.0	0.0	0.0	0.0	0.0	0.0	0.0	0.0	0.0	0.0	0.0	0.0	0.0	0.0	0.0
GV2 7151.1	0.0	0.3	14.0	0.0	0.0	0.0	0.0	0.0	0.0	0.0	0.0	0.0	0.0	0.0	0.0	0.0	0.0	0.0	0.0
GV2 7160.8	0.0	0.0	12.0	0.0	0.0	0.0	0.0	0.0	0.0	0.0	0.0	0.0	0.0	0.0	0.0	0.0	0.0	0.0	0.0
GV2 7167.b	0.3	1.0	13.0	0.0	0.0	0.0	1.0	0.0	0.0	0.0	0.0	0.0	0.0	0.0	4.0	1.0	0.0	0.0	0.0
GV2 7167.2	0.0	0.0	12.5	0.0	0.0	0.0	0.0	0.0	0.0	0.0	0.0	0.0	0.0	0.0	0.0	0.0	0.0	0.0	0.0
GV2 7173.2	0.0	0.3	12.0	0.0	0.0	0.0	0.0	0.0	0.0	0.0	0.0	0.0	0.0	0.0	0.0	0.0	0.0	0.0	0.0
GV2 7207	0.0	0.3	8.8	0.0	0.0	0.0	0.0	0.0	0.0	0.0	0.0	0.0	0.0	0.0	0.0	0.0	0.0	0.0	0.0
GV2 7212.6	1.0	1.0	7.3	0.0	0.0	0.0	0.0	0.0	0.0	0.0	0.5	0.0	0.0	0.0	0.0	0.0	0.0	0.0	0.0
GV2 7220.2	0.3	0.3	14.0	0.0	0.0	0.0	0.0	0.0	0.0	0.0	0.0	0.0	0.0	0.0	0.3	0.0	0.0	0.0	0.0
GV2 7233	0.0	0.0	12.8	0.0	0.0	0.0	1.3	0.0	0.0	0.0	0.0	0.0	0.0	0.0	0.0	0.0	0.0	0.0	0.0
GV2 7247	0.0	0.0	9.3	0.0	0.0	0.0	2.0	0.0	0.0	0.0	0.0	0.0	0.0	0.0	0.0	0.0	0.0	0.0	0.0
GV2 7268	1.0	0.0	11.5	0.0	0.0	0.0	0.5	0.0	0.0	0.0	0.0	0.0	0.0	0.0	0.0	0.0	0.0	0.0	0.0
LD2812	0.5	2.0	16.5	0.0	1.3	0.0	0.0	0.0	0.0	0.0	0.0	0.0	0.0	0.0	3.0	1.5	0.0	0.0	0.0
LD2834	0.0	1.0	9.0	0.0	0.0	0.0	0.0	0.0	0.0	0.0	0.0	0.0	0.0	0.0	0.8	0.0	0.0	0.0	0.0
LD2845	0.0	1.2	2.6	0.0	0.0	0.0	0.0	0.0	0.0	0.0	0.0	0.0	0.0	0.0	0.0	0.0	0.0	0.0	0.0
LD2854	0.0	0.0	1.3	0.0	20.3	0.0	0.0	0.0	0.0	0.0	0.0	0.0	0.0	0.0	0.0	0.0	0.0	0.0	0.0
LD3551.9	1.8	2.3	0.7	0.0	0.0	0.0	0.0	0.0	0.0	0.0	0.0	0.0	0.0	0.0	0.5	0.0	0.0	0.0	3.2
LD3561	0.0	0.8	9.8	0.0	0.0	0.0	0.0	0.0	0.0	0.0	0.0	0.0	0.0	0.0	1.0	1.3	0.0	0.0	0.0

Sample Info				Petrophys. Data			Grain Texture			Framework Grains							
Sample	Well	Chronos trat	Burial Depth (ft)	Porosity (%)	Perm. (md)	Grain Density g/cm3	Mean Grain Size (mm)	Sorting	Grain Coating (%)	Qtz	Feld	SRF	VRF	MRF	PRF	Mins	Other Grains
LD3566	Last Dance	UWF	3566.0	5.0	1.320	2.70	0.06	M	90.0	41.3	17.8	10.0	6.5	0.5	1.5	6.5	0.0
LD3573.1	Last Dance	UWF	3573.1	6.6	0.147	2.69	0.07	MW	90.0	42.9	23.2	5.4	7.7	1.7	3.9	5.6	0.0
LD 3585.9	Last Dance	UWF	3585.9				0.12	W	15.0	45.8	14.6	7.6	14.6	2.0	0.0	5.2	0.0
LD3595.5	Last Dance	UWF	3595.5	6.1	0.003	2.66	0.10	W	55.0	39.3	15.0	2.3	5.8	4.8	3.8	1.3	0.0
LD3989.6	Last Dance	UWF	3989.6	4.1	0.006	2.66	0.12	MW	45.0	35.0	12.5	5.0	10.8	9.8	1.8	1.5	1.5
LD4004.9	Last Dance	UWF	4004.9	11.9	0.108	2.66	0.17	MW	99.0	47.2	11.4	5.2	11.0	4.8	5.8	0.4	0.0
LD4016	Last Dance	UWF	4016.0	11.7	0.151	2.66	0.38	MW	99.0	45.8	11.8	2.5	10.8	1.8	5.5	0.8	0.0
LD4381	Last Dance	UWF	4381.0	4.1	0.003	2.66	0.07	W	80.0	55.0	13.7	3.7	7.4	4.7	2.7	2.0	0.2
LD4397	Last Dance	UWF	4397.0	8.4	0.030	2.65	0.33	MW	70.0	42.3	12.3	3.8	12.3	4.3	7.0	0.5	0.0
LD4854	Last Dance	UWF	4854.0	3.4	0.001	2.69	0.14	M	40.0	38.5	2.8	11.5	9.5	12.3	4.3	0.5	0.3
LD5715.15	Last Dance	LWF	5733.1	7.1	0.011	2.69	0.18	W	40.0	55.0	6.2	8.7	4.3	4.1	2.5	0.0	0.2
LD5733.1	Last Dance	LWF	5761.3	7.1	0.003	2.71	0.13	MW	30.0	51.8	6.8	9.8	4.3	4.5	0.8	0.3	0.3
LD6039.1	Last Dance	LWF	6039.1	6.7	0.009	2.68	0.20	MW	20.0	48.0	8.3	5.8	9.2	11.9	5.3	0.0	0.0
LD5761.3	Last Dance	LWF	6039.1	5.6	0.002	2.73	0.18	MW	30.0	39.3	7.0	8.8	8.0	7.5	3.5	0.3	0.0
LD6055.8	Last Dance	LWF	6055.8	8.0	0.015	2.70	0.16	MW	20.0	45.0	3.8	12.5	6.8	12.5	3.0	0.0	0.5
LD6335	Last Dance	LWF	6335.0	2.8	0.002	2.76	0.09	MW	20.0	33.3	6.5	22.5	5.3	3.3	0.0	0.5	0.8
LD6342	Last Dance	LWF	6342.9	4.2	0.018	2.72	0.10	MW	20.0	42.0	6.3	21.5	6.0	3.5	0.5	0.0	0.0
MF31 7328	MF31-19G	UWF	7056.2				0.04	M	70.0	31.3	2.0	30.0	7.8	2.3	7.5	0.3	0.0
MF31 7340	MF31-19G	UWF	7068.2				0.04	P	40.0	34.8	1.3	33.5	8.0	2.0	3.8	0.0	0.0
MF31 7362	MF31-19G	UWF	7072.0				0.25	VP	60.0	33.8	3.3	29.5	10.3	2.5	6.8	0.0	0.0
MF31 10294.5	MF31-19G	LWF	8978.3				0.27	MW	45.0	44.3	5.8	15.5	5.5	4.3	2.0	0.5	0.0
MF31 10302.2	MF31-19G	LWF	8986.0				0.27	MW	45.0	45.3	6.3	12.3	8.0	1.8	2.8	0.0	0.3
MF31 11992.25	MF31-19G	Cozette?	#####				0.09	MW	15.0	41.5	7.5	21.8	2.3	5.0	2.3	0.8	3.3
MF31 11992.85	MF31-19G	Cozette?	#####				0.11	W	15.0	43.5	4.5	27.8	3.0	4.0	1.3	0.3	0.0
MF31 12003.4	MF31-19G	Cozette?	#####				0.09	W	15.0	33.3	7.3	28.3	1.5	2.5	0.5	0.0	0.8
MF31 12017.3	MF31-19G	Cozette?	#####				0.09	W	15.0	34.8	2.5	31.5	2.5	2.8	0.5	0.5	0.5
MWX1 5361.5	MWX-1	UWF	5361.5	3.8	0.790		0.17	W	30.0	39.5	6.0	20.5	2.8	6.0	0.8	0.3	0.0
MWX1 5547.6	MWX-1	UWF	5547.6	4.9	0.020		0.29	W	15.0	37.3	7.0	11.8	5.3	16.0	1.8	0.0	0.3
MWX1 5554	MWX-1	UWF	5554.0	5.1	0.020		0.26	W	15.0	44.3	6.8	10.8	5.0	9.5	1.3	0.8	0.0
MWX1 5557	MWX-1	UWF	5557.0	7.0	0.030		0.25	MW	15.0	31.3	5.0	19.5	6.3	12.8	3.3	0.8	0.0
MWX1 5563	MWX-1	UWF	5563.0	6.9	0.040		0.22	W	25.0	45.8	6.0	15.0	3.8	8.8	2.5	0.0	0.0

Sample	Porosity		Cements Quartz		Carbonate						Clay Minerals							
	Inter. Pores	Second. Pores	Quartz cmt	Microxl Quartz	Calcite	Fe Calcite	Fe-Dol	Sid. pf	Sid. pl	Carb Undiff	Illite pf	Illite pl	Illite pb	Smectite	Chlorite pf	Chlorite pl	Kaolinite	Clay Undiff
LD3566	0.0	0.0	1.3	0.0	0.0	0.0	0.0	0.0	0.0	0.0	0.0	0.0	0.0	0.0	1.3	0.0	0.0	0.0
LD3573.1	0.4	0.4	0.8	0.0	0.0	0.0	0.0	0.0	0.0	0.0	0.0	0.0	0.0	0.0	3.7	0.0	0.0	0.0
LD 3585.9	0.0	0.0	1.8	0.0	2.4	0.0	0.0	0.0	0.0	0.0	0.0	0.0	0.0	6.0	0.0	0.0	0.0	0.0
LD3595.5	0.8	0.5	13.3	0.0	1.0	0.0	0.0	0.0	0.0	0.3	0.5	0.0	0.0	1.3	1.5	0.8	0.0	0.0
LD3989.6	0.0	0.0	6.5	0.0	3.5	0.0	0.0	0.0	0.0	0.0	2.3	0.0	0.0	0.0	0.0	0.3	0.0	0.0
LD4004.9	0.6	1.0	0.0	0.0	0.0	0.0	0.0	0.0	0.0	0.0	1.4	0.0	0.0	7.9	0.0	0.0	0.0	0.0
LD4016	1.3	1.5	0.3	0.0	0.0	0.0	0.0	0.0	0.0	0.0	3.0	0.0	0.0	10.0	0.0	0.0	0.0	0.0
LD4381	0.0	0.0	4.9	0.0	0.0	0.0	0.0	0.0	0.0	0.0	0.0	0.0	0.0	0.0	0.0	0.0	0.0	0.0
LD4397	0.5	1.3	9.3	0.0	0.0	0.0	0.0	0.0	0.0	0.0	1.0	0.0	0.0	1.5	0.0	0.0	0.0	0.3
LD4854	0.3	0.5	10.5	0.0	0.0	2.3	0.5	0.0	0.0	0.0	0.5	0.0	0.0	0.0	0.0	0.0	0.0	0.0
LD5715.15	0.2	0.7	9.8	0.0	0.0	0.0	1.1	0.0	0.0	0.0	0.0	0.0	0.0	0.0	0.0	0.0	0.0	0.0
LD5733.1	0.8	1.5	7.3	0.0	0.0	0.0	4.8	0.0	0.0	0.0	0.8	0.0	0.0	0.0	0.3	0.0	0.0	0.0
LD6039.1	0.4	0.0	5.3	0.0	0.0	0.0	0.6	0.0	0.0	0.0	0.0	0.0	0.0	0.0	0.0	0.0	0.0	0.0
LD5761.3	0.0	0.3	11.0	0.0	0.0	0.0	4.8	0.0	0.0	0.0	3.0	0.0	0.0	0.0	0.0	0.3	0.0	0.0
LD6055.8	0.0	1.3	5.5	0.0	0.0	0.0	3.8	0.0	0.0	0.0	0.0	0.0	0.0	0.0	0.0	0.0	0.0	0.0
LD6335	0.0	0.3	3.5	0.0	0.0	0.0	15.0	0.0	0.0	0.0	0.0	0.0	0.5	0.0	0.0	0.0	0.0	0.0
LD6342	0.0	0.0	3.0	0.0	0.0	0.0	10.5	0.0	0.0	0.0	0.0	0.0	0.0	0.0	0.0	0.0	0.0	0.0
MF31 7328	0.0	0.0	2.8	0.3	6.5	0.0	0.0	0.0	0.0	0.0	0.0	0.0	0.0	0.0	0.3	1.0	0.0	0.0
MF31 7340	0.3	1.8	3.8	0.0	2.3	0.8	0.0	0.0	0.0	0.0	0.0	0.0	0.0	0.3	0.8	1.3	0.0	0.0
MF31 7362	0.0	0.5	4.8	0.0	0.0	1.8	0.0	0.0	0.0	0.0	0.5	0.0	0.0	0.0	0.5	1.3	0.0	0.0
MF31 10294.5	0.8	0.3	7.8	0.0	0.0	2.0	0.0	0.0	0.0	3.3	0.8	0.0	0.0	0.0	1.0	0.0	0.0	0.0
MF31 10302.2	0.0	0.3	8.8	0.0	0.0	2.8	0.0	0.0	0.0	0.0	0.0	0.0	0.0	0.8	3.5	0.0	0.0	0.0
MF31 11992.25	0.0	0.0	0.8	0.0	0.0	0.0	3.8	0.0	0.0	0.0	0.0	0.0	0.0	0.0	0.0	3.0	0.0	0.0
MF31 11992.85	0.0	0.0	7.0	0.0	0.0	0.0	4.5	0.0	0.0	0.0	0.0	0.0	0.0	1.3	0.0	0.0	0.0	0.0
MF31 12003.4	0.0	0.0	1.8	0.0	0.0	0.3	10.0	0.0	0.0	2.3	0.0	0.0	0.0	0.0	0.0	0.0	0.0	0.0
MF31 12017.3	0.0	0.0	1.5	0.0	0.0	0.0	13.0	1.5	0.0	0.8	0.0	0.0	0.0	0.0	0.0	0.0	0.0	0.0
MWX1 5361.5	0.0	0.0	8.8	0.0	0.0	4.3	1.0	0.0	0.0	0.0	0.0	0.0	0.0	0.3	0.0	0.0	0.0	0.0
MWX1 5547.6	0.0	0.5	8.0	0.0	0.0	1.3	0.3	0.0	0.0	0.0	0.3	0.0	0.0	0.0	0.0	0.0	0.0	0.0
MWX1 5554	0.0	1.3	9.8	0.0	0.0	1.0	0.0	0.0	0.0	0.0	0.3	0.0	0.3	0.3	0.0	0.0	0.0	0.0
MWX1 5557	0.0	2.5	4.5	0.0	0.0	0.0	0.5	0.0	0.0	0.0	0.3	0.0	0.0	0.0	0.0	0.0	0.0	0.0
MWX1 5563	0.0	0.3	7.5	0.0	0.0	0.0	0.3	0.0	0.0	0.0	0.0	0.0	0.0	0.0	1.3	0.0	0.0	0.0

Sample Info				Petrophys. Data			Grain Texture			Framework Grains							
Sample	Well	Chronos trat	Burial Depth (ft)	Porosity (%)	Perm. (md)	Grain Density g/cm3	Mean Grain Size (mm)	Sorting	Grain Coating (%)	Qtz	Feld	SRF	VRF	MRF	PRF	Mins	Other Grains
MWX1 5710.3	MWX-1	UWF	5710.3	5.3	0.020		0.22	MW	30.0	40.5	7.0	17.3	4.5	12.0	1.0	0.3	0.0
MWX1 5717.2	MWX-1	UWF	5717.2	7.3	0.130		0.25	MW	25.0	41.0	7.3	10.8	11.8	10.5	1.8	0.5	0.3
MWX1 5732	MWX-1	UWF	5732.0	7.4	0.020		0.16	MW	20.0	43.8	7.5	17.0	9.8	6.5	1.5	0.0	0.3
MWX1 5824.2	MWX-1	UWF	5824.2	2.1	0.010		0.13	MW	15.0	31.0	6.5	23.0	7.0	4.8	0.3	0.5	0.0
MWX1 5826.5	MWX-1	UWF	5826.5	1.7	0.010		0.19	MW	25.0	39.3	4.3	19.8	10.3	6.5	0.5	0.0	0.0
MWX1 5829.3	MWX-1	UWF	5829.3	9.3	0.280		0.19	MW	65.0	36.3	5.0	20.5	11.3	7.8	1.5	0.0	0.0
MWX1 5836	MWX-1	UWF	5836.0	6.6	0.080		0.27	MW	75.0	31.0	5.8	15.3	13.3	11.5	1.3	0.0	0.0
MWX1 6513.5	MWX-1	LWF	6513.5	7.5	0.030		0.17	W	20.0	37.0	5.5	20.5	9.8	7.5	1.8	0.0	0.3
MWX1 6532	MWX-1	LWF	6532.0	3.5	0.010		0.10	M	20.0	32.8	5.8	28.5	6.0	5.3	1.0	0.8	0.0
MWX1 6540.5	MWX-1	LWF	6540.5	6.6	0.020		0.21	W	15.0	45.8	3.3	21.3	10.3	4.0	0.3	0.3	0.0
MWX1 6544.7	MWX-1	LWF	6544.7	8.0	0.040		0.13	W	25.0	35.3	10.0	21.8	9.3	6.5	0.8	1.0	0.0
MWX1 6545.8	MWX-1	LWF	6545.8	7.9	0.050		0.19	W	10.0	38.5	6.8	19.0	10.8	6.8	2.0	0.0	0.0
MWX1 6554	MWX-1	LWF	6554.0	2.3			0.17	W	10.0	31.0	3.5	24.3	8.5	7.0	1.8	0.0	0.0
MWX1 7858.5	MWX-1	Cozette	7858.5	5.6	0.010		0.20	M	25.0	45.8	8.3	12.8	8.5	14.0	1.3	0.8	0.0
MWX1 7871	MWX-1	Cozette	7871.0	6.3	0.010		0.13	W	25.0	50.3	5.8	10.3	6.5	9.3	0.0	0.8	0.0
MWX1 7881	MWX-1	Cozette	7881.6	7.5	0.030		0.12	W	50.0	44.3	5.3	13.0	6.8	12.0	0.0	0.8	0.0
MWX1 7892	MWX-1	Cozette	7892.0	7.0	0.030		0.11	W	60.0	49.8	5.5	14.3	1.8	10.0	1.0	1.5	0.0
WF-46	Outcrop	UWF	0.0				0.19	MW	15.0	40.0	8.0	3.3	5.0	10.5	0.8	0.3	0.5
RCC-1	Outcrop	Rollins	0.0				0.20	W	30.0	43.6	7.0	11.2	7.4	10.4	0.0	0.0	0.0
CZTZ-1	Outcrop	Cozette	0.0				0.05	VW	30.0	56.6	4.8	16.2	8.2	5.6	0.0	0.0	0.8
WF-2	Outcrop	LWF	0.0				0.17	W	30.0	51.8	7.8	12.2	11.2	1.4	0.0	0.4	0.0
WF-3	Outcrop	LWF	0.0				0.17	W	30.0	50.8	9.0	7.4	11.0	1.4	0.0	0.0	0.0
WF-4	Outcrop	LWF	0.0				0.14	VW	30.0	47.4	9.0	11.2	8.4	0.4	0.8	0.0	0.0
WF-6	Outcrop	LWF	0.0				0.11	VW	30.0	58.6	6.2	10.8	4.8	2.0	0.0	0.4	0.0
WF-7	Outcrop	LWF	0.0				0.22	W	30.0	45.2	11.8	4.4	8.8	2.0	0.0	0.6	0.0
WF-8	Outcrop	LWF	0.0				0.13	VW	30.0	48.8	7.4	14.2	7.6	1.8	0.2	0.0	0.0
WF-38	Outcrop	UWF	0.0				0.32	M	15.0	43.3	9.5	16.3	8.0	4.5	2.5	2.8	0.0
WF-39	Outcrop	UWF	0.0				0.32	M	15.0	49.0	6.0	24.5	5.8	2.3	2.0	2.5	0.0
WF-41	Outcrop	UWF	0.0				0.26	M	15.0	43.0	9.5	18.0	10.3	5.5	2.8	1.3	0.0
WF-42	Outcrop	UWF	0.0				0.30	MW	15.0	39.0	9.0	14.3	7.3	4.8	1.5	0.0	0.0
WF-43	Outcrop	UWF	0.0				0.34	MW	15.0	49.3	9.8	9.8	5.3	4.3	2.0	0.3	0.0
WF-44	Outcrop	UWF	0.0				0.18	MW	15.0	55.8	9.8	11.0	1.5	3.5	0.8	0.0	0.0
WF-45	Outcrop	UWF	0.0				0.18	MW	15.0	40.0	8.0	3.3	5.0	10.5	0.8	0.3	0.5

Sample	Porosity		Cements Quartz		Carbonate						Clay Minerals								
	Inter. Pores	Second. Pores	Quartz cmt	Microxi Quartz	Calcite	Fe Calcite	Fe-Dol	Sid. pf	Sid. pl	Carb Undiff	Illite pf	Illite pl	Illite pb	Smectite	Chlorite pf	Chlorite pl	Kaolinite	Clay Undiff	Other Cmts
MWX1 5710.3	0.3	0.0	6.3	0.0	0.0	1.8	0.0	0.0	0.0	0.0	0.0	0.0	0.0	0.0	1.0	0.0	0.0	0.0	0.0
MWX1 5717.2	0.0	1.5	5.8	0.0	0.0	0.8	0.0	0.0	0.0	0.0	0.0	0.0	0.0	0.0	0.0	0.0	0.0	0.0	0.0
MWX1 5732	0.0	0.8	3.3	0.0	0.0	0.0	0.3	0.0	0.0	3.3	0.0	0.0	0.0	0.0	0.0	0.0	0.0	0.0	0.0
MWX1 5824.2	0.0	0.0	0.8	0.0	0.0	13.0	0.0	0.0	0.0	0.0	0.0	0.0	0.0	0.0	0.0	0.0	0.0	0.0	0.0
MWX1 5826.5	0.3	0.0	8.3	0.0	0.0	2.8	1.5	0.0	0.0	0.0	0.0	0.0	0.0	0.0	0.0	0.0	0.0	0.0	0.0
MWX1 5829.3	0.3	1.8	8.5	0.0	0.0	1.8	0.3	0.0	0.0	0.0	0.0	0.0	0.0	0.0	0.0	0.0	0.0	0.0	0.0
MWX1 5836	0.0	1.8	5.3	0.0	0.0	4.8	1.0	0.0	0.0	0.0	0.0	0.0	0.0	0.0	0.0	0.5	0.0	0.0	0.0
MWX1 6513.5	0.3	0.0	5.8	0.0	0.0	1.0	4.0	0.0	0.0	0.0	1.0	0.5	0.0	0.0	0.0	0.0	0.0	0.0	0.0
MWX1 6532	0.0	0.0	5.3	0.0	0.0	0.0	10.3	0.0	0.0	0.0	0.0	0.0	0.0	0.0	0.0	0.0	0.0	0.0	0.0
MWX1 6540.5	0.0	0.0	5.5	0.0	0.0	0.0	3.8	0.0	0.0	0.0	0.0	0.0	0.0	0.0	0.0	0.0	0.0	0.0	0.0
MWX1 6544.7	0.0	0.0	4.5	0.0	0.0	0.0	2.3	0.0	0.0	0.0	0.0	0.0	0.0	0.0	0.0	0.0	0.0	0.0	0.0
MWX1 6545.8	0.3	1.3	4.8	0.0	0.0	0.0	1.8	0.0	0.0	0.0	0.0	0.0	0.0	0.0	0.8	0.3	0.0	0.0	0.0
MWX1 6554	0.0	0.0	7.3	0.0	0.0	0.0	7.8	0.0	0.0	0.0	0.0	0.0	0.0	0.0	0.5	0.0	0.0	0.0	0.0
MWX1 7858.5	0.0	0.0	3.3	0.0	0.0	0.0	0.0	0.0	0.0	0.0	0.0	0.0	0.0	0.0	0.0	0.0	0.0	0.0	0.0
MWX1 7871	0.0	0.0	11.8	0.0	0.0	0.0	1.3	0.0	0.0	0.0	0.0	0.0	0.0	0.0	0.3	0.0	0.0	0.0	0.0
MWX1 7881	0.5	0.3	11.5	0.0	0.0	0.0	1.0	0.0	0.0	0.0	0.0	0.0	0.0	0.0	0.3	0.0	0.0	0.0	0.0
MWX1 7892	0.0	0.0	10.3	0.0	0.0	0.0	0.8	0.0	0.0	0.0	0.0	0.0	0.0	0.0	0.0	0.0	0.0	0.0	0.0
WF-46	9.0	5.0	3.3	0.0	0.0	0.0	0.0	0.0	0.0	0.0	0.0	0.0	0.0	0.0	0.0	0.0	4.3	5.0	0.0
RCC-1	7.2	7.0	0.4	0.0	0.0	0.0	0.0	0.0	0.0	0.0	0.0	0.0	0.0	0.0	0.0	0.0	1.0	0.0	0.0
CZTZ-1	0.0	0.0	3.2	0.0	0.0	0.0	3.4	0.0	0.0	0.0	0.0	0.0	0.0	0.0	0.0	0.0	0.0	0.0	0.0
WF-2	5.4	1.8	0.6	0.0	0.4	0.0	0.0	1.4	0.0	0.0	0.8	0.0	0.0	0.0	0.0	0.4	1.8	0.0	0.0
WF-3	2.6	1.8	0.6	0.0	0.0	0.0	0.0	3.0	0.0	0.0	0.0	0.0	0.0	0.0	0.0	0.0	0.4	5.2	0.0
WF-4	4.6	3.8	1.8	0.0	0.0	0.0	0.0	1.2	0.6	0.0	0.0	0.0	0.0	0.0	0.0	0.0	1.6	3.4	0.0
WF-6	3.6	1.2	0.4	0.0	0.0	0.0	0.0	0.0	0.0	0.0	2.6	0.0	0.0	0.0	0.0	0.0	2.6	0.0	0.0
WF-7	14.0	3.6	1.2	0.0	0.0	0.0	0.0	0.0	0.0	0.0	0.0	0.0	0.0	0.0	0.6	4.0	0.0	0.0	0.0
WF-8	4.8	3.4	0.0	0.0	0.6	0.0	0.0	3.2	0.0	0.0	0.0	0.0	0.0	0.0	0.0	0.0	0.0	1.4	0.0
WF-38	2.8	4.0	2.0	0.0	0.0	0.0	0.0	0.0	0.0	0.0	0.0	0.0	0.0	0.0	0.0	0.0	0.0	1.0	0.0
WF-39	2.5	3.5	1.0	0.0	0.0	0.0	0.0	0.0	0.0	0.0	0.0	0.0	0.0	0.0	0.0	0.0	0.0	0.0	0.0
WF-41	1.0	2.0	1.5	0.0	0.0	0.0	0.0	0.0	0.0	0.0	0.0	0.0	0.0	0.0	0.0	0.0	1.5	0.0	0.0
WF-42	7.3	5.8	3.3	0.0	0.0	0.0	0.0	0.0	0.0	0.0	0.0	0.0	0.0	0.0	0.0	0.0	2.0	2.0	0.0
WF-43	4.8	4.0	2.8	0.0	0.0	0.0	0.0	0.0	0.0	0.0	0.0	0.0	0.0	0.0	0.0	0.0	2.0	3.3	0.0
WF-44	2.3	2.0	3.8	0.0	0.0	0.0	0.0	0.0	0.0	0.0	0.0	0.0	0.0	0.0	0.0	0.0	1.3	3.8	0.0
WF-45	9.0	5.0	3.3	0.0	0.0	0.0	0.0	0.0	0.0	0.0	0.0	0.0	0.0	0.0	0.0	0.0	4.3	5.0	0.0

APPENDIX B: INPUT AND OUTPUT DATA FOR BASIN MODELS

B1 Stratigraphy input

B2 Vitrinite reflectance, temperature, and pressure input

B3 Time versus temperature, depth, excess pressure, and effective pressure

B1: Stratigraphy input

MWX Well

Unit, or Event	Top/thickness	Age	Type	Lithology
Uplift and erosion	4700/-4700	0	E	sh100
<i>Hiatus</i>	4700/0	10	H	sh100
Green River Fm.	4700/4100	35	D	ss20/sh60/ml20
Wasatch Fm. (part)	4700/600	42	D	sh40/ss39/si18/co3
Wasatch Fm. (part)	4700	47	N	sh40/ss39/si18/co3
<i>Hiatus</i>	8600/0	60	H	sh100
Mesaverde Group	8600	66	N	sh44/ss52/co4
Mancos Shale	12900	77	N	sh81/si18/ss1
Frontier Fm./Mowry Shale	18400	88	N	ss80/sh20
Dak/Cedar	18450	97	N	sh30/ss55/co15
<i>Hiatus</i>	18500/0	112	H	sh100
Morrison Fm./Sundance Fm.	18500	139	N	ss60/sh30/ml10
<i>Hiatus</i>	18525/0	162	H	sh100
Entrada Ss.	18525	162.5	N	ss100
<i>Hiatus</i>	18675/0	165	H	sh100
Glen Canyon Sandstone	18675	186	N	ss100
<i>Hiatus</i>	18775/0	206	H	sh100
Chinle Fm.	18775	210	N	ss50/sh40/ml10
<i>Hiatus</i>	19275/0	229	H	sh100
Pennsylvanian strata	19275	278	N	ls40/do40/sh20/ssh20
Belden Shale	21875	312	N	sh90/si10
base	22275	320		

LAST DANCE

Unit, or Event	Top/thickness	Age	Type	Lithology
Uplift and erosion	4840/-4840	0	E	sh100
<i>Hiatus</i>	4840/0	10	H	sh100
Green River Fm.	4840/4240	35	D	ss20/sh60/ml20
Wasatch Fm. (part)	4840/600	42	D	sh40/ss39/si18/co3
Wasatch Fm. (part)	4840	47	N	sh40/ss39/si18/co3
<i>Hiatus</i>	8740/0	60	H	sh100
Williams Fork / Fluvial	8740	66	N	sh59/ss40/co1
Paludal / Cameo	11050	73	N	sh40/ss52/co8
Iles Fm	12220	73.5	N	sh56ss43/co1
Mancos Shale	13040	77	N	sh81/si18/ss1
Frontier Fm./Mowry Shale	18540	88	N	ss80/sh20
Dak/Cedar	18590	97	N	sh30/ss55/co15
<i>Hiatus</i>	18640/0	112	H	sh100
Morrison Fm./Sundance Fm.	18640	139	N	ss60/sh30/ml10
<i>Hiatus</i>	18665/0	162	H	sh100
Entrada Ss.	18665	162.5	N	ss100
<i>Hiatus</i>	18815/0	165	H	sh100
Glen Canyon Sandstone	18815	186	N	ss100
<i>Hiatus</i>	18915/0	206	H	sh100
Chinle Fm.	18915	210	N	ss50/sh40/ml10
<i>Hiatus</i>	19415/0	229	H	sh100
Pennsylvanian strata	19415	278	N	ls40/do40/sh20/ssh20
Belden Shale	22015	312	N	sh90/si10
base	22415	320		

MOBIL T2-19G

Unit, or Event	Top/thickness	Age	Type	Lithology
Uplift and erosion	3115/-3115	0	E	sh100
<i>Hiatus</i>	3115/0	10	H	sh100
Uinta Formation (part)	3115/3115	20	D	ss60/sh30/co4/ml6
Uinta Formation (part)	3115	30	N	ss60/sh30/co4/ml6
Green River Fm. (part)	3335	45	N	ss20/sh60/ml20
Wasatch Fm. (part)	5195	49	N	sh40/ss39/si18/co3
Green River Fm. (part)	5565	51	N	ss20/sh60/ml20
Wasatch Fm. (part)	6115	54	N	sh40/ss39/si18/co3
Fort Union Formation	8525	57	N	sh30/ss55/co15
<i>Hiatus</i>	10045/0	60	H	sh100
Williams Fork Fm.	10045	68	N	sh44/ss44/co12
Mesaverde Group	14285	73	N	sh44/ss52/co4
Mancos Shale (part)/Castlegate Ss.	15585	76	N	ss50/sh50
Mancos Sh./Frontier Fm./Mowry Sh.	16335	80	N	ss50/sh50
Dak/Cedar	20285	97.5	N	sh30/ss55/co15
<i>Hiatus</i>	20345/0	112.5	H	sh100
Morrison Fm.	20345	140	N	ss60/sh30/ml10
<i>Hiatus</i>	20765/0	155	H	sh100
Sundance Fm.	20765	159	N	ss60/sh30/ml10
<i>Hiatus</i>	20885/0	162.5	H	sh100
Entrada Ss.	20885	163	N	ss100
<i>Hiatus</i>	21067/0	166	H	sh100
Glen Canyon Sandstone	21067	186	N	ss100
<i>Hiatus</i>	21250/0	207	H	sh100
Chinle Fm.	21250	212	N	ss50/sh40/ml10
<i>Hiatus</i>	21460/0	228	H	sh100
State Bridge Fm.	21460	242.5	N	ss50/sh25/gy25
<i>Hiatus</i>	21960/0	269	H	sh100
Maroon Fm.	21960	279	N	ss80/sh20
Morgan Fm.	23960	305	N	ss80/l20
<i>Hiatus</i>	25960/0	322	H	sh100
Madison Limestone	25960	340	N	sh2,do96,ls2
Base	26360	357		

Shell 1-11-B4 Brotherson

Unit, or Event	Top/thickness	Age	Type	Lithology
Uplift and Erosion	5504/-5504	0	E	sh100
<i>Hiatus</i>	5504/0	10	H	sh100
Uinta Fm.	5504/5504	20	D	ss60/sh30/co4/ml6
Upper part Green River Fm.	5504	37	N	ss20/sh60/ml20
Mahogany oil shale zone"	0	43	N	ss20/sh80
G.R. upper black shale facies	0	45	N	ss20/sh60/ml20
Carbonate marker	0	53	N	ml100
main part Green River Fm.	0	54	N	ss20/sh80
G.R. black shale facies/N.H./Flag.	0	58.3	N	ss50/sh40/l10
Erosion	16428/-100	66	E	sh100
Deposition	16428/100	66.01	D	sh100
Cretaceous rocks undifferentiated	16528	71.5	N	sh10/ss80/co10
Mesaverde Group	0	72	N	sh10/ss80/co10
Mancos Shale	0	82.5	N	ss80/sh20
Erosion	23078/-150	91	E	sh100
Deposition	23078/150	91.01	d	sh100
Dak/Cedar/Mow/Front	23678	96	N	ss80/sh20
<i>Hiatus</i>	24328/0	112.5	H	sh100
Morrison Fm.	0	139.5	N	ss70/sh30
<i>Hiatus</i>	25078/0	154	H	sh100
Stump Fm.	0	155	N	ss70/sh30
<i>Hiatus</i>	25278/0	162	H	sh100
Preuss Sandstone	0	163	N	ss100
Twin Creek Limestone	0	165	N	ls100
<i>Hiatus</i>	26328/0	174	H	sh100
Glen Canyon Sandstone	0	186.5	N	ss100
<i>Hiatus</i>	27528/0	205	H	sh100
Chinle Fm.	0	209	N	ss50/sh40/ml10
<i>Hiatus</i>	27778/0	229	H	sh100
Ankareh Fm.	27778.00	241	N	ss50/sh40/l10
Thaynes Limestone	0	244	N	ls100
Woodside Fm.	0	246	N	ss50/sh40/l10
<i>Hiatus</i>	28628/0	248	H	sh100
Park City/Phosphoria Fms.	0	257	N	ss35/sh35/l50
<i>Hiatus</i>	28928/0	267	H	sh100
Weber Sandstone	0	278	N	ss85/sh15
Base	0	307		

(sh: shale; sst: sandstone; ml: marl; do: dolomite; co: coal; ls: limestone)

B2: Vitrinite reflectance and temperature input

Well	Measured Depth (ft)	Ro (%)	From
Mobil Oil No. T-52-19G	10955	1.56	Johnson & Nuccio (1986)
	11845	1.65	
	11950	1.83	
	12345	1.85	
	17289	3.11	
Arco-Exxon 1-36	6578	1.41	Johnson & Nuccio (1986)
	8380	1.95	
MWX-1	4398	0.82	
	5225	0.96	
	6611	1.4	
	7949	1.94	
MWX-2	7100	1.68	Johnson & Nuccio (1986)
	7153	1.77	
	7202	1.77	
	7226	1.82	
	7241	1.83	
	7380	1.79	
O`Connell F11X-34P *	1475	0.59	Yurewicz et al.(2003)
	2377	0.44	
	2623	0.44	
	2459	0.57	
	4262	0.61	
	4754	0.69	
	6639	0.82	
	5164	1.02	
	5574	1.15	
	6148	1.21	
	7213	1.59	
	7213	1.72	
	7541	1.81	
	7787	1.98	
	8443	2.23	
	9180	2.21	
	9672	2.53	
	10656	2.95	
10246	2.99		
11803	3.13		
11475	3.28		
11230	3.43		
11721	3.43		
11393	3.87		
Rifle Gap /Cameo Coal	0	0.66	Johnson & Nuccio (1986)

Ro: Vitrinite Reflectance

* Neighboring Last

	Depth (ft)	TVD (ft)	Temp (°F)	Temp (°C)	From
Last Dance	35	35	64	18	Cumella, Pers.
	288	288	64	18	Communication
	541	540	69	21	
	726	725	71	22	
	1041	1039	78	26	
	1349	1345	83	28	
	1736	1718	87	31	
	2235	2188	97	36	
	2269	2221	97	36	
	2452	2394	100	38	
	3204	3117	112	44	
	4040	3943	128	53	
	5209	5112	149	65	
	6034	5936	175	79	
6700	6603	200	93		
		TVD (ft)	Temp (°F)	Temp (°C)	
MWX-1		5500	165	74	Johnson & Nuccio (1986)
		7000	200	93	
		8000	233	112	
		TVD (ft)	Uncorrected Temp (°F)	Uncorrected Temp (°C)	
Mobil Oil T-52-19G		10000	190	87.8	Johnson & Nuccio (1986)
		TVD (ft)	Corrected Temp (°F)	Corrected Temp (°C)	
Mobil Oil T-52-19G		10000	240 - 250	115 - 121	Johnson & Nuccio (1986)

Well	Depth (ft)	Pressure (psi)	Mud weight (lb)	From
Last Dance	11	5	9.7	Cumella, Pers. Communication
	806	373	8.9	
	1901	889	9	
	2238	1093	9.4	
	2859	1397	9.4	
	3539	1693	9.2	
	4024	2008	9.6	
	4356	2197	9.7	
	4605	2346	9.8	
	4864	2503	9.9	
	5209	2762	10.2	
	5412	2926	10.4	
	5770	3240	10.8	
	6041	3361	10.7	
	6067	3438	10.9	
	6351	3599	10.9	
	6781	3949	11.2	
6781	4019	11.4		

	Depth (ft)	Pressure (psi)	TVD (ft)	From
Miller 23B *	4534	2657.29	4459	Cumella, Pers. Communication
	4766	2700.12	4691	
	4997	2736.26	4923	
	5229	2809.72	5155	
	5345	2857.96	5270	
	5693	3038.7	5618	
	5924	3130.29	5850	
	6156	3511.58	6082	
	6388	3740.86	6313	

* Neighboring Last Dance

	Depth (ft)	Pressure (psi)	From
MWX-1	5550	3200	Spencer (1987)
	8846	3454	
	6461	4454	
	6538	4545	
	7025	5272	
	7153.8	5318	
	7307	5681	
	7553.8	6000	
	7769.23	6363	
	8000	6370	
	8192	6727	

	Depth (ft)	Pressure (drilling mud, psi)	
MWX-3	2153.8	1020	Spencer (1987)
	2500	1182	
	3000	455	
	3307.7	1727	
	4000	2000	
	4461.5	2046	
	4930.7	2227	
	5346	2363	
	6612	1.4	
	7100	1.68	
	7202	1.77	
	7242	1.83	
	7950	2.09	

B3: Time versus temperature, depth, excess pressure, and effective pressure

MWX Well		Top / Base of Mesaverde						
Time	Temperature		Depth		Excess Pressure		Overburden Pres.	
my	°C		ft		psi		psi	
	Top	Base	Top	Base	Top	Base	Top	Base
78.0	10	24	0	0	0.0	0.0	0	15
77.0	10	33	0	496	0.0	0.0	0	408
75.9	10	45	0	1262	0.0	0.0	0	1063
74.8	10	54	0	1971	0.0	0.1	0	1691
73.7	10	63	0	2641	0.0	0.1	0	2302
72.6	10	71	0	3282	0.0	0.3	0	2902
71.5	10	78	0	3900	0.0	0.4	0	3493
70.4	10	77	0	4499	0.0	0.7	0	4499
69.3	10	83	0	5084	0.0	1.1	0	5032
68.2	10	96	0	5653	0.0	1.6	0	5279
67.1	10	102	0	6211	0.0	2.6	0	5770
66.0	23	108	0	6760	0.0	4.4	22	6317
56.3	42	120	1359	7672	0.0	4.5	1143	7229
54.4	51	124	1961	8118	0.0	6.4	1672	7687
52.6	58	128	2532	8559	0.0	9.0	2186	8142
50.7	65	132	3080	8995	0.1	12.5	2689	8595
48.9	71	136	3608	9426	0.1	19.7	3184	9046
47.0	77	140	4120	9853	0.2	36.2	3671	9495
44.5	83	144	4729	10369	0.4	102.1	4264	10048
42.0	89	148	5326	10886	0.6	199.5	4852	10600
40.8	95	152	5872	11370	1.2	299.2	5382	11103
39.7	101	156	6389	11833	1.7	508.0	5896	11594
38.5	107	161	6878	12280	2.7	885.9	6399	12076
37.3	112	165	7350	12716	4.2	1226.1	6893	12555
36.2	117	168	7809	13146	6.3	1537.5	7382	13030
35.0	121	172	8257	13569	9.3	1793.5	7865	13503
26.7	125	178	8254	13575	6.7	986.1	7850	13487
18.3	124	178	8255	13527	2.1	521.0	7851	13467
10.0	115	171	8253	13525	1.2	810.1	7856	13472
9.0	108	165	7585	12850	0.8	769.0	7326	12944
8.0	99	158	6983	12243	0.6	712.1	6822	12438
6.0	83	144	5915	11172	0.4	676.5	5873	11490
5.0	76	137	5424	10680	0.4	666.9	5417	11034
4.0	68	130	4953	10208	0.4	658.9	4969	10588
3.0	62	124	4502	9755	0.4	651.5	4531	10149
2.0	56	119	4052	9304	0.3	646.8	4099	9718
1.0	51	113	3611	8862	0.3	641.3	3673	9293
0.0	45	108	3178	8428	0.3	635.4	3251	8870

MF31-19G / Mobil T52-19G Wells				Top / Base of Mesaverde				
Time	Temperature		Depth		Excess Pressure		Overburden Pressure	
my	°C		feet		psi		psi	
	Top	Base	Top	Base	Top	Base	Top	Base
76.0	10	11	0	0	0.0	0.0	0	15
74.5	10	19	0	549	0.0	0.0	0	471
73.0	10	34	0	1581	0.0	0.0	0	1354
72.3	10	45	0	2448	0.0	0.1	0	2111
71.6	10	56	0	3257	0.0	0.3	0	2842
70.9	10	65	0	4025	0.0	0.5	0	3556
70.1	10	73	0	4763	0.0	1.0	0	4257
68.7	10	88	0	6173	0.0	2.7	15	5629
68.0	17	95	511	6852	0.0	4.3	427	6304
60.0	17	103	511	6851	0.0	1.5	427	6304
59.0	27	106	1276	7367	0.0	3.6	1068	6837
58.0	37	111	1982	7884	0.1	5.9	1683	7370
57.0	45	115	2648	8398	0.1	7.6	2281	7902
56.3	53	118	3390	8993	0.3	14.6	2968	8525
55.5	60	122	4095	9577	0.6	25.7	3639	9144
54.8	67	126	4772	10153	1.0	59.1	4298	9759
54.0	73	130	5428	10723	1.7	166.6	4948	10372
51.0	82	138	6047	11274	1.6	434.6	5560	10954
49.0	86	142	6385	11583	2.7	862.0	5916	11298
47.7	92	146	6985	12129	4.1	628.6	6534	11893
46.3	98	151	7550	12644	5.9	1014.1	7137	12473
45.0	104	156	8096	13154	7.9	1618.1	7731	13052
37.5	108	163	8167	13223	7.0	1207.1	7817	13137
30.0	110	166	8240	13276	3.7	1189.5	7905	13216
28.3	111	167	8540	13554	5.6	1210.5	8256	13558
26.7	113	168	8868	13860	7.0	1281.0	8621	13913
25.0	115	169	9202	14178	10.0	1455.4	8988	14273
23.3	117	171	9540	14503	16.1	1634.5	9357	14637
21.7	119	173	9879	14832	27.8	1812.5	9725	15001
15.0	122	176	10218	15164	53.7	1897.5	10094	15366
10.0	122	177	10218	15156	51.7	1709.1	10094	15363
8.3	118	174	9658	14592	28.5	962.1	9629	14897
6.7	114	170	9132	14050	16.2	603.2	9180	14440
5.0	108	166	8632	13549	6.8	396.3	8741	14001
3.3	103	162	8152	13069	2.6	223.9	8310	13570
1.7	98	157	7689	12606	0.5	117.5	7887	13147
0.0	93	153	7239	12157	-0.5	48.5	7470	12731

Last Dance Well			Top / Base of Mesaverde					
Time	Temperature		Depth		Excess Pressure		Overburden Pressure	
my	°C		feet		psi		psi	
	Top	Base	Top	Base	Top	Base	Top	Base
77.0	10	24	0	0	0.0	0.0	0	15
75.3	10	33	0	409	0.0	0.0	0	329
73.5	10	48	0	1167	0.0	0.0	0	934
73.3	10	54	0	1659	0.0	0.4	0	1377
73.2	10	59	0	2148	0.0	0.6	0	1818
73.0	10	64	0	2627	0.0	1.0	0	2256
71.8	10	72	0	3100	0.0	0.3	0	2695
70.7	10	78	0	3552	0.0	0.4	0	3245
69.5	10	75	0	3987	0.0	0.6	0	3964
68.3	22	87	0	4411	0.0	0.7	0	4057
67.2	23	93	0	4825	0.0	1.0	30	4368
66.0	28	98	316	5231	0.0	1.6	274	4765
60.0	27	100	316	5231	0.0	0.8	266	4758
58.4	34	103	791	5541	0.0	1.2	655	5075
56.8	41	105	1237	5855	0.0	1.5	1031	5394
55.1	46	108	1662	6169	0.0	1.8	1397	5712
53.5	52	111	2069	6482	0.0	2.3	1756	6030
51.9	57	114	2462	6793	0.0	2.8	2109	6348
50.3	61	117	2843	7102	0.1	3.5	2457	6664
48.6	66	120	3215	7409	0.1	4.4	2800	6979
47.0	70	123	3577	7713	0.1	5.4	3140	7294
44.5	72	125	3790	7893	0.1	5.1	3344	7483
42.0	74	126	4001	8074	0.1	5.5	3547	7673
40.6	78	129	4327	8358	0.3	7.3	3849	7957
39.2	83	132	4639	8633	0.3	8.3	4145	8237
37.8	86	135	4938	8896	0.4	10.8	4435	8512
36.4	90	138	5225	9151	0.5	15.0	4720	8783
35.0	93	140	5505	9400	0.7	23.3	5002	9051
28.8	94	142	5505	9400	0.3	22.5	5002	9051
22.5	94	142	5505	9400	0.2	12.0	5002	9051
16.3	90	139	5505	9399	0.1	6.7	5002	9051
10.0	82	132	5505	9399	0.0	3.2	5002	9051
8.3	76	128	5017	8912	0.0	1.3	4618	8667
6.7	71	123	4573	8469	0.0	0.7	4253	8303
5.0	66	119	4160	8056	0.0	0.2	3901	7951
3.3	62	115	3770	7666	0.0	0.0	3560	7609
1.7	59	111	3398	7295	0.0	-0.2	3228	7278
0.0	46	100	3039	6936	0.0	-0.2	2907	6957

Rifle Gap Outcrop, Outcrop 4 Scenario at the base of Williams Fork

Outcrop 4_Scenario 1				
Time	Temperature	Depth	Excess Pressure	Overburden Pressure
my	°C	feet	psi	psi
0	13	295	0	317
1.25	19	806	0	849
2.5	24	1322	0	1385
3.75	30	1847	0	1924
5	36	2381	0	2467
6.25	41	2927	0	3013
7.5	47	3489	0	3562
8.75	53	4065	0	4117
10	58	4652	0	4684
18.67	58	4652	0	4684
27.33	58	4652	0	4684
36	59	4652	0	4684
39.33	65	5154	0	5169
42.67	71	5688	0	5668
46	77	6245	0	6178
49.33	84	6836	0	6701
52.67	91	7503	0	7258
56	93	8201	0	7828
56.5	88	7493	0	7066
57	82	6755	0	6290
57.5	75	5972	0	5494
58	67	5129	0	4674
58.67	63	4634	0	4189
59.33	59	4125	0	3697
60	55	3619	0	3207
66	53	3619	0	3207
68	46	3000	0	2621
70	39	2354	0	2024
70.67	33	1773	0	1501
71.33	25	1145	0	957
72	16	464	0	390
73	16	464	0	390
73.25	10	0	0	15

Rifle Gap Outcrop, Outcrop 5 Scenario at the base of Williams Fork

Outcrop 5_Scenario 2a				
Time	Temperature	Depth	Excess Pressure	Overburden Pressure
my	°C	feet	psi	psi
0	14.11	0	0	14.7
0.17	21.4	626	0	659
0.33	28.84	1263	0	1309
0.5	36.13	1916	0	1965
0.67	43.06	2590	0	2629
0.83	49.29	3293	0	3299
1	53.92	4021	0	3980
2	54.46	4021	0	3980
4	61	4694	0	3980
6	69	5406	0	4594
8	78	6186	0	5228
10	87	7081	0	5900
22.5	88	7081	0	6621
35	88.5	7081	0	6621
37.33	84.68	6634	0	6621
39.67	80	6163	0	6160
42	75	5661	0	5688
43	72	5203	0	5202
44	68	4735	0	4748
45	64	4255	0	4289
46	60	3763	0	3824
47	57	3279	0	3354
53.5	57.9	3279	0	2888
60	58.47	3279	0	2888
66	58.31	3279	0	2888
67.2	53.19	2709	0	2888
68.4	47.36	2109	0	2351
69.6	40.67	1467	0	1800
70.8	32.73	767	0	637
72	23.6	0	0	14
73	23.73	0	0	14

Rifle Gap Outcrop, Outcrop 6 Scenario at the base of Williams Fork

Outcrop 6_Scenario 2b				
Time	Temperature	Depth	Excess Pressure	Overburden Pressure
my	°C	feet	psi	psi
0	14.11	0	0	14.7
0.13	21.57	628	0	677.7
0.25	29.13	1263	0	1344.5
0.38	36.52	1909	0	2015.8
0.5	43.62	2575	0	2692
0.63	50.36	3258	0	3370
0.75	56.69	3958	0	4057
0.88	62.12	4682	0	4753
1	65.83	5416	0	5466
2	66.69	5416	0	5466
4	74.61	6124	0	6137
6	83.31	6883	0	6829
8	92.96	7718	0	7554
10	101.68	8688	0	8337
22.5	102.41	8688	0	8337
35	100.75	8688	0	8337
36.4	96.58	8131	0	7731
37.8	92.01	7557	0	7118
39.2	86.95	6961	0	6495
40.6	81.27	6330	0	5856
42	75.24	5656	0	5200
43.67	69.56	4885	0	4439
45.33	63.23	4084	0	3664
47	57.11	3279	0	2888
60	58.44	3279	0	2888
66	58.27	3279	0	2888
67.2	53.15	2709	0	2351
68.4	47.33	2109	0	1800
69.6	40.64	1467	0	1231
70.8	32.71	767	0	637
72	23.6	0	0	14.7
73	23.73	0	0	14.7

**APPENDIX C: SUBCRITICAL CRACK INDEX MEASUREMENTS
FOR THE FLATHEAD, FRONTIER AND WILLIAMS FORK
SAMPLES**

Sample	Formation	Type	Locality / Well	SCI (n)	KIC
WF-46	U. Williams Fork	Outcrop	Rifle Gap, CO	44.1	0.8
WF-44	U. Williams Fork	Outcrop	Rifle Gap, CO	30.5	0.2
WF-44	U. Williams Fork	Outcrop	Rifle Gap, CO	38.9	0.9
WF-44	U. Williams Fork	Outcrop	Rifle Gap, CO	36.9	0.8
WF-44	U. Williams Fork	Outcrop	Rifle Gap, CO	20.0	0.4
WF-43	U. Williams Fork	Outcrop	Rifle Gap, CO	46.8	0.2
WF-43	U. Williams Fork	Outcrop	Rifle Gap, CO	62.4	0.2
WF-41	U. Williams Fork	Outcrop	Rifle Gap, CO	52.4	0.1
WF-39	U. Williams Fork	Outcrop	Rifle Gap, CO	47.6	0.8
WF-39	U. Williams Fork	Outcrop	Rifle Gap, CO	48.2	0.9
WF-39	U. Williams Fork	Outcrop	Rifle Gap, CO	48.2	0.9
WF-39	U. Williams Fork	Outcrop	Rifle Gap, CO	43.2	0.7
WF-39	U. Williams Fork	Outcrop	Rifle Gap, CO	56.8	0.7
WF-38	U. Williams Fork	Outcrop	Rifle Gap, CO	14.8	0.4
WF-38	U. Williams Fork	Outcrop	Rifle Gap, CO	24.5	0.5
WF-38	U. Williams Fork	Outcrop	Rifle Gap, CO	21.0	0.4
WF-8	L. Williams Fork	Outcrop	Rifle Gap, CO	68.2	3.5
WF-8	L. Williams Fork	Outcrop	Rifle Gap, CO	126.3	2.3
WF-8	L. Williams Fork	Outcrop	Rifle Gap, CO	71.2	3.4
WF-7	L. Williams Fork	Outcrop	Rifle Gap, CO	10.8	0.1
WF-7	L. Williams Fork	Outcrop	Rifle Gap, CO	24.7	0.1
WF-7	L. Williams Fork	Outcrop	Rifle Gap, CO	22.9	0.1
WF-7	L. Williams Fork	Outcrop	Rifle Gap, CO	17.2	0.2
WF-6	L. Williams Fork	Outcrop	Rifle Gap, CO	18.6	1.1
WF-4	L. Williams Fork	Outcrop	Rifle Gap, CO	42.2	0.7
WF-4	L. Williams Fork	Outcrop	Rifle Gap, CO	17.4	0.9
WF-4	L. Williams Fork	Outcrop	Rifle Gap, CO	35.0	0.9
WF-3	L. Williams Fork	Outcrop	Rifle Gap, CO	44.6	1.1
WF-3	L. Williams Fork	Outcrop	Rifle Gap, CO	64.7	0.5
WF-3	L. Williams Fork	Outcrop	Rifle Gap, CO	71.2	0.8
WF-3	L. Williams Fork	Outcrop	Rifle Gap, CO	69.4	0.3
WF-2	L. Williams Fork	Outcrop	Rifle Gap, CO	30.7	0.2
WF-1	L. Williams Fork	Outcrop	Rifle Gap, CO	66.4	2.9
WF-1	L. Williams Fork	Outcrop	Rifle Gap, CO	27.0	3.1

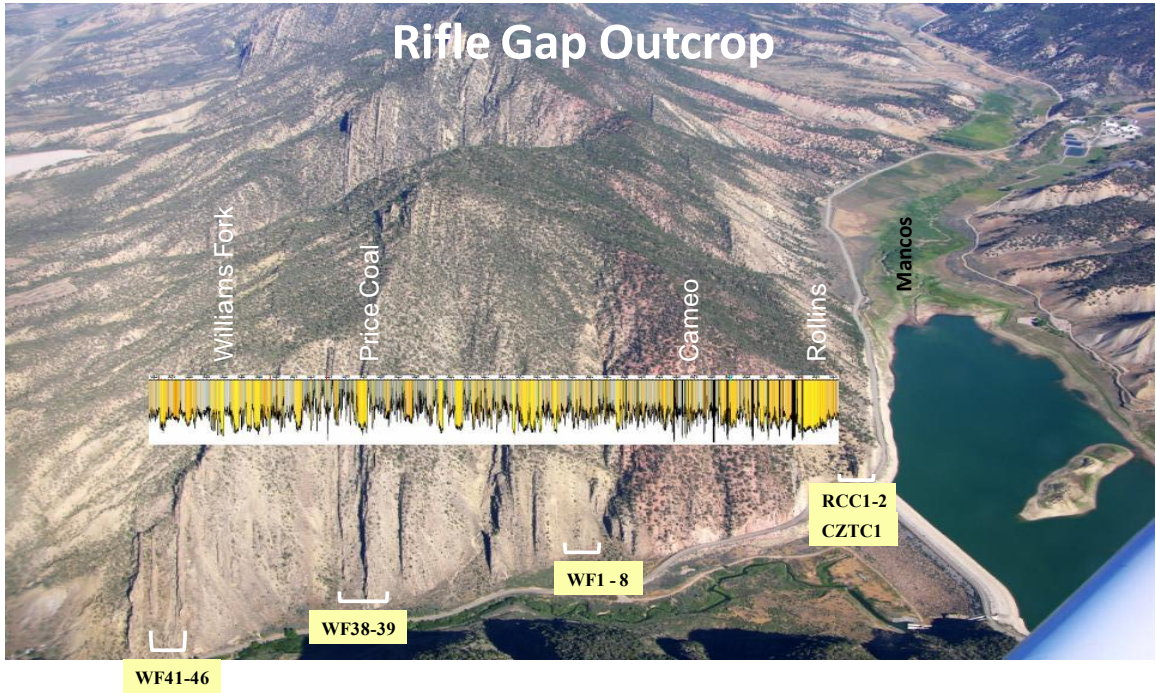
Sample	Formation	Type	Locality / Well	SCI (n)	KIC
RCC-1	Rollins	Outcrop	Rifle Gap, CO	49.7	0.3
RCC-1	Rollins	Outcrop	Rifle Gap, CO	43.6	0.3
RCC-1	Rollins	Outcrop	Rifle Gap, CO	25.2	0.5
RCC-1	Rollins	Outcrop	Rifle Gap, CO	43.1	0.2
RCCC-2	Rollins	Outcrop	Rifle Gap, CO	24.2	0.1
RCCC-2	Rollins	Outcrop	Rifle Gap, CO	35.0	0.1
CZTC-1	Cozette	Outcrop	Rifle Gap, CO	40.6	3.1
CZTC-1	Cozette	Outcrop	Rifle Gap, CO	45.4	2.8
CZTC-1	Cozette	Outcrop	Rifle Gap, CO	46.7	2.4
LD 2854	U. Williams Fork	Core	Last Dance, CO	101.1	2.7
LD 2854	U. Williams Fork	Core	Last Dance, CO	89.7	2.9
LD 3585.9	U. Williams Fork	Core	Last Dance, CO	145.2	3.8
LD 3585.9	U. Williams Fork	Core	Last Dance, CO	168.5	3.6
LD 3585.9	U. Williams Fork	Core	Last Dance, CO	67.8	5.7
LD 4016.9	U. Williams Fork	Core	Last Dance, CO	61.8	1.7
LD 4016.9	U. Williams Fork	Core	Last Dance, CO	59.1	1.3
LD 4016.9	U. Williams Fork	Core	Last Dance, CO	78.7	1.9
LD 4016.9	U. Williams Fork	Core	Last Dance, CO	62.6	1.5
LD 4381	U. Williams Fork	Core	Last Dance, CO	86.0	3.7
LD 4381	U. Williams Fork	Core	Last Dance, CO	53.9	3.5
LD 4381	U. Williams Fork	Core	Last Dance, CO	78.8	3.1
LD 5722.7	L. Williams Fork	Core	Last Dance, CO	51.8	3.0
LD 5722.7	L. Williams Fork	Core	Last Dance, CO	52.8	2.5
LD 5736.8	L. Williams Fork	Core	Last Dance, CO	56.1	2.6
LD 5736.8	L. Williams Fork	Core	Last Dance, CO	50.1	3.2
LD 5740	L. Williams Fork	Core	Last Dance, CO	37.2	3.5
LD 6332.7	L. Williams Fork	Core	Last Dance, CO	65.2	2.8
LD 6332.7	L. Williams Fork	Core	Last Dance, CO	55.5	3.8
LD 6332.7	L. Williams Fork	Core	Last Dance, CO	58.8	5.0
SB 12372	Cozette	Core	Shell Brotherson, UT	56.6	4.9
SB 12372	Cozette	Core	Shell Brotherson, UT	37.3	4.1
SB 12374.5	Cozette	Core	Shell Brotherson, UT	44.3	5.7
SB 12374.5	Cozette	Core	Shell Brotherson, UT	30.0	5.4
MF31 7333.7	Williams Fork	Core	MF31-19G, CO	91.5	3.0
MF31 7333.7	Williams Fork	Core	MF31-19G, CO	65.1	3.3
MF31 7333.7	Williams Fork	Core	MF31-19G, CO	78.7	2.9

Sample Name	Formation	Type	Locality / Well	SCI (n)	KIC
MF31 7362	Williams Fork	Core	MF31-19G, CO	63.9	1.8
MF31 7362	Williams Fork	Core	MF31-19G, CO	51.2	0.4
MF31 10293	Williams Fork	Core	MF31-19G, CO	62.5	2.6
MF31 10293	Williams Fork	Core	MF31-19G, CO	69.9	2.5
MF31 10299	Williams Fork	Core	MF31-19G, CO	53.8	2.5
MF31 10299	Williams Fork	Core	MF31-19G, CO	64.3	2.2
MF31 10302.2	Williams Fork	Core	MF31-19G, CO	62.8	3.3
MF31 10302.2	Williams Fork	Core	MF31-19G, CO	77.4	
MF31 10302.2	Williams Fork	Core	MF31-19G, CO	78.0	3.4
CF-12	Flathead	Outcrop	Canyon Ferry, MT	60.9	6.6
CF-12	Flathead	Outcrop	Canyon Ferry, MT	71.3	7.2
TP-4	Flathead	Outcrop	Canyon Ferry, MT	82.4	3.0
TP-4	Flathead	Outcrop	Canyon Ferry, MT	79.0	3.2
TP-4	Flathead	Outcrop	Canyon Ferry, MT	66.9	3.5
SB-7	Flathead	Outcrop	Canyon Ferry, MT	38.4	4.4
SB-7	Flathead	Outcrop	Canyon Ferry, MT	97.6	3.8
SB-7	Flathead	Outcrop	Canyon Ferry, MT	57.3	3.8
EHPO-16	Flathead	Outcrop	Canyon Ferry, MT	70.5	1.0
JO_F1	Frontier	Outcrop	WY	55.9	1.3
JO_F1	Frontier	Outcrop	WY	73.3	1.1
JO_F2	Frontier	Outcrop	WY	61.4	2.1
JO_F2	Frontier	Outcrop	WY	70.5	2.1
JO_F2	Frontier	Outcrop	WY	46.5	1.9
JO_F3	Frontier	Outcrop	WY	47.6	1.5
JO_F3	Frontier	Outcrop	WY	47.6	1.4
JO_F3	Frontier	Outcrop	WY	60.4	1.1
JO_F4	Frontier	Outcrop	WY	39.8	2.3
JO_F4	Frontier	Outcrop	WY	44.8	2.2
JO_F4	Frontier	Outcrop	WY	46.7	1.9
MWX-1 7892 *	MWX-1/Cozette	Core	MWX-1, CO	66 ± 17	Dry
MWX-1 7892 *	MWX-1/Cozette	Core	MWX-1, CO	64 ± 16	
	Flathead	Outcrop?	WY	77 ± 11	Dry
SHCT 7892 *	SHCT/Cozette	Core	SHCT, CO	66 ± 17	
SHCT 7892 *	SHCT/Cozette	Core	SHCT, CO	64 ± 16	
SHCT 9002 *	SHCT/Cozette	Core	SHCT, CO	58 ± 6	
SHCT 9041 *	SHCT/Cozette	Core	SHCT, CO	54 ± 16	
SHCT 9071 *	SHCT/Cozette	Core	SHCT, CO	50 ± 9	

(* Measurements from Rijken, 2005)

APPENDIX D: SAMPLE COLLECTION LOCATIONS

Location	Location	County	Kelly Bush (ft)
CER Corp, MWX-1	Sec 34 T6S R94W	Garfield Co., CO	5374
Mobil Oil 52-19G	Sec 19 T2S R96W	Rio Blanco Co., CO	6873
Last Dance 43C-3-792	Sec 3 R92W T7S	Garfield Co., CO	6043
Shell 1-11-B4 Brotherson	Sec 11 T2S R4W	Duchesne Co., UT	6198
Rifle Gap	Sec 7 R92W T5S	Garfield Co., CO	Outcrop





Cozette interval with interbedded Mancos Shale, Rifle Gap, Colorado.



Rollins interval with interlayers of Mancos Shale, Rifle Gap, Colorado.



Rollins interval with interlayers of Mancos Shale (close-up), Rifle Gap, Colorado.



Cameo coal zone within lower Williams Fork, Rifle Gap, Colorado.



Cameo coal zone within lower Williams Fork, Rifle Gap, Colorado.



Cameo coal zone interbedded with lower Williams Fork sandstones, Rifle Gap, Colorado.



Resistant isolated fluvial channel sandstones of upper Williams Fork, Rifle Gap, Colorado.



Resistant isolated fluvial channel sandstones of upper Williams Fork, Rifle Gap, Colorado.

**APPENDIX E1: REVIEW OF PREVIOUS WORK ON QUARTZ
CEMENTATION**

Review of Previous Work: Current Understanding of Quartz Diagenesis

Quartz cementation is a temperature-dependant, three-step process that includes dissolution (release of silica to pore fluids), transport (diffusion/advection), and precipitation. Although, quartz cement is one of the most common authigenic phases in sandstones (McBride, 1989), its development mechanisms are not completely resolved. The central debate on quartz cementation has long focused upon sources of silica and its transport (McBride, 1989 and references therein; Worden and Morad, 2000) but recently it has come to be appreciated that the rate-limiting step is precipitation (Walderhaug, 1994, 1996).

Diagenetic models that allow prediction of quartz precipitation and resulting porosity evolution in sandstones have been published by numerous authors (Walderhaug, 1996; Bjorkum et al., 1998; Lander and Walderhaug, 1999; and Oelkers et al., 2000). *Exemplar*TM (developed by Lander and Walderhaug) and *Touchstone*TM (developed by Lander and Bonnell; Lander et al., 2008) are commercially available reservoir quality prediction models that include a model for prediction of quartz cement abundance. These models use precipitation-rate-limiting theory without addressing whether the silica is derived by local diffusion or large-scale advection from remote sources. The models simply assume that silica is supplied to the system at a rate equal or greater than the precipitation rate, which is a reasonable assumption at temperatures more than 80°C and neutral pH conditions. Most subsurface waters are found to be supersaturated with respect to silica (Land, 1997). Successful application of diagenetic models in predicting reservoir quality in rocks of different ages in many sedimentary basins at various temperature and depths demonstrates that precipitation-rate-limiting theory is very likely

correct (Walderhaug et al., 2000; Marchand et al., 2002; Bloch et al., 2002; Makowitz et al., 2006).

On the other hand, Renard et al. (2000) argue that the quartz precipitation process is limited by precipitation rates at shallower depths due to slower reaction kinetics linked to lower temperatures and by silica transport at depths greater than 3 km because reaction kinetics gets faster with increasing temperatures. This appears to be a reasonable assumption; however, at higher temperatures, reaction rates that release silica are also accelerated (e.g., feldspar dissolution, pressure solution, clay transformations) and spatial distributions of quartz cement that would be expected from transport-limited growth (concretions or halo textures) are not generally reported, except at low temperatures such as the case of the Fontainebleau sandstones (Thiry et al., 1988). In their quartz growth experiments, Teinturier and Pironon (2003) observed that quartz growth was only halted by a limited supply of silica at low P-T conditions (<350°C, 400 bar). They also observed that overgrowths are enhanced by decreasing the temperature from a maximum silica oversaturated pore fluid.

Although retarding effects of hydrocarbons were cited as the reason of high porosity zones in the Miller field in the UK North Sea (Marchand, et al., 2000, 2001, 2002), others (Aase & Walderhaug, 2005 and Bonnell et al., 2006) suggested it was the presence of microquartz coatings that slowed down the precipitation of quartz cement in these sandstones. Haszeldine et al. (2003) suggest that quartz precipitation is halted if the pores in sandstone contain less than 20% water, because the residual water no longer provides a connected network to distribute diffusing silica from its source to precipitation site, but such a contention is challenging to test. Walderhaug (1990) has shown presence

of widespread primary oil inclusions in quartz cement which indicates quartz cementation does occur in the presence of hydrocarbons and in fractures copious deposits of quartz locally trap only hydrocarbons (Becker et al., 2009b). Experimental studies done by Bonnell et al. (2006) showed a decline in quartz growth rate with decreasing water saturation at 350°C but no decrease in quartz precipitation rates at 250°C.

Controls on Quartz Crystal Growth Rate: Grain size and Crystallography

It has been long recognized that a quartz overgrowth is a syntaxial rim in optical continuity with the nucleus; that is, the crystal lattices are interconnected (Sorby, 1880). Isolated quartz crystals are typically elongate parallel to the c-axis indicating preferential growth in this orientation. Experimental crystal growth studies demonstrate that quartz precipitation rates are faster when the crystal growth is aligned parallel to the c-axis of the substrate quartz grain compared to the growth along the a-axis (Lander et al., 2008). Other studies agree that in a given quartz crystal most of the growth takes place on the r and Z rhombohedral faces and not on the m prism faces (Iwasaki et al., 1998 and Ihinger and Zink, 2000). Waugh's (1970) study documented that crystals grow, in fact, in optical continuity with the substrate grain and develop most extensively along the c-axis. He observed that cement initiates as small prisms and rhombs that merge and overlap to form larger crystals. Localized defects in the crystal lattice were found to cause an ~10° the misorientation of the overgrowth relative to the substrate. In the famous study of crack-seal texture, Ramsay (1980) reported quartz crystals in optical continuity with the parent grain on the fracture wall except for occasional misfits of up to 3 degrees. He interpreted these as slightly misoriented seed fragments of broken wall. Cabrera and Vermilya (1958) documented that quartz dissolves faster on low-index rhombohedral faces (those

parallel to the c-axis) and slower on high-index pinacoid faces (those representing termination in the c-axis direction). Hurst (1981) has also shown that dissolution and replacive textures are governed by crystallographic properties of the grain.

Experiments done by Lander et al. (2008) demonstrate another textural control on quartz crystal growth rates. Quartz cement growth rates are faster on non-euhedral surfaces; crystal growth slows down about 20 times when the crystal comes to a euhedral termination. Because of this same reason precipitation rates are faster on the larger quartz grain substrates as the smaller grains come to euhedral termination before larger ones. Lander et al. (2008) suggest that this is governed by Steno's law which states that angle between adjacent euhedral faces is always the same irrespective of the crystal's size. So, a non-euhedral surface has to grow further to reach euhedral termination. A linear relation between grain size and quartz overgrowth thickness (e.g., larger grains with thicker overgrowths) was found by Makowitz and Sibley (2001); this shows that quartz crystals in nature follow the pattern observed in the experiments of Lander et al. (2008). Lander et al. (in preparation) show how the drastically different rates of crystal growth on euhedral and fractured surfaces can account for the widespread observation of isolated thick deposits of quartz containing crack-seal texture (bridges) in otherwise open fractures (Laubach, 1988; Laubach et al., 2004b; Laubach and Ward, 2006). Inasmuch as bridge deposits likely reflect quartz accumulation governed by the precipitation step (in conjunction with fracture opening rate), the quartz bridge deposits that are present in the Williams Fork Formation (Laubach, 2003) further support the concept that the precipitation step governs quartz accumulation in my study area.

APPDENDIX E2: DIAGENETIC MODELING: HOW DOES IT WORK?

Diagenetic Modeling

*Touchstone*TM is a process-oriented forward model that contains terms optimized empirically using textural, compositional, and burial history data from natural sandstones. By using *Touchstone*TM, temperature, pressure history, timing and depth of quartz cementation can be simulated. Model inputs include (1) textural and compositional characteristics of each analyzed sample; (2) thermal and effective stress histories derived from basin modeling; and (3) other various model parameters discussed below.

The program assumes, following Walderhaug (1996), that precipitation is the rate-limiting factor (Table E2.1). Compactional porosity loss is assumed to be minor once quartz cementation starts. Therefore, most of the primary porosity loss is assumed to be equal to the amount of silica and any other cements that are precipitated after the initiation of quartz cementation. Total porosity; however, could go up if microporosity is “created” in clays and dissolving grains and by the formation of secondary porosity. There can also be some compaction that continues to occur, particularly if you alter a rigid grain to a non-rigid authigenic material – even after quartz precipitation. These processes could vary depending on the initial composition of the sandstone and other diagenetic processes. Temperature-dependence of quartz cementation is expressed by an Arrhenius equation (Equation E2.1; Walderhaug, 1996). When the sandstone's temperature history is known, precipitation rate per unit surface area can be calculated (Table E2, Equation E2.2, Lander and Walderhaug, 1999). Surface area available for quartz cementation is controlled by parameters such as grain size, sandstone composition (detrital quartz content), degree of clay or other grain coatings, pre-quartz porosity reduction by cementation, and temperature history (Table E2.1, Equation E2.3, Lander et

al., 2008). In order to account for effects of diagenetic alteration on the available nucleation surface area, the timing of non-quartz cement precipitation is defined by paragenetic rules (Table 2.2 and Appendix A). Compaction reduces intergranular porosity, and therefore, may reduce surface area for quartz cement nucleation. To determine the compaction state of the sample Touchstone uses a proprietary compaction algorithm. The IGV_f (stable packing arrangement that represents the minimum likely intergranular volume for a sandstone of given composition and texture) value for each sample provides an optimal match between the present-day calculated and measured IGV values. These values can vary considerably depending on the response of framework grains and pore-fills to compactional effects.

For compaction model parameters, rigidity classes (γ) were defined for pore-filling minerals (as strong pore-fills, weak pore-fills, and matrix). Also defined are parameters that are used for reconstructing the depositional IGV (based on individual grain size and sorting), the rate of compaction with effective stress (β , $1/MPa$) and a rigidity parameter for quartz cement.

For β (MPa^{-1}), the exponential rate of compaction with effective stress, default value of $0.06 MPa^{-1}$ is used as an initial input value. This is the suggested value for quartzose samples by Lander and Walderhaug (1999). However, having a variety of ductile and intermediate grains as framework constituents in the Williams Fork sample set resulted in an increase in the value during simulations; higher values meaning more rapid compaction with effective stress.

The IGV_f term simply refers to the minimum likely intergranular volume expected if the solid portion of the sample was composed of only one type of grain. If the

sandstone was composed of only ductile framework grains due to high degree of grain deformation the IGV_f value would have been much less than if it was composed of only rigid grains (for example quartz).

Table E2.1. Quartz cement volume, precipitation rate, and available surface area estimation equations used by diagenetic modeling programs.

<p>Equation E2.1 Arrhenius equation Temperature dependence of quartz precipitation rates (Walderhaug, 1996).</p>	$K = A_0 e^{-E_a/RT}$ <p>K: Quartz precipitation rate (mole/cm² s) A₀: Pre-exponential or frequency factor E_a: Activation energy (J/mol) R: Gas constant (8.314 J/K mol) T: Temperature (K)</p>
<p>Equation E2.2. Amount of quartz cement precipitation (Lander and Walderhaug, 1999)</p>	$Q = \frac{M}{\rho} \left[\gamma P \frac{6}{D} \right] K (\Delta t)$ <p>Q = Amount of quartz cement precipitation M = Molecular weight of quartz (60.09 g/mol) P = Volume fraction of rock with quartz grains in the model framework of reference ρ = Density of quartz (2.65 g/cm³) γ = Diagenetic surface area reduction coefficient D = Quartz grain diameter K = Rate per unit surface area (obtained from Arrhenius equation) Δt = Time elapsed</p>
<p>Equation E2.3 Available surface area (Lander et al., 2008 and references therein)</p>	$S_q = \left(Q_g \frac{6}{D} \right) \left(\frac{\phi}{\phi_0} \right)^{2/3} (1 - C)$ <p>S_q = Nucleation surface area Q_g = Volume of quartz seed grains (cm³) in the model frame of reference (1 cm³ at deposition), D = Mean diameter of the quartz seed grains (cm), φ₀ = The intergranular porosity at the time of deposition (volume fraction), φ = Current intergranular porosity (volume fraction), C = Grain coat coverage (the fraction of the quartz surface area that is covered by thin coatings of materials that prevent the nucleation of quartz cement)</p>

APPDENDIX E3: VITRINITE REFLECTANCE

Vitrinite Reflectance

Vitrinite is one of the primary components of coals and most sedimentary kerogens that are derived from land plants and humic peats. Vitrinite is therefore common in sedimentary rocks that are rich in organic matter, such as shales and marls with a terrigenous origin, or, at least, some terrigenous content. Vitrinite is derived from thermal alteration (metamorphism) of woody plant material. Vitrinite reflectance is a measure of the proportion of the light reflected from a polished vitrinite grain. It is directly related to the thermal maturity of the vitrinite grain and can be converted to coal rank or used for predicting onset of oil and gas generation from potential source rocks (Dow, 1977).

Time-dependent and time-independent models have been proposed to predict thermal maturity and vitrinite reflectance values based on integrated time-temperature history of the sedimentary basins. Time-dependent models assume that vitrinite metamorphism is a first-order chemical reaction, or that time and temperature are interchangeable factors in changing its reflectance (Karweil, 1955; Lopatin, 1971; Hood and others, 1975; Waples, 1980). Time-independent models suggest that vitrinite equilibrates fairly rapidly, a million years or less, to a given temperature and will not metamorphose further until the temperature is raised meaning that it records the maximum burial temperature to which the vitrinite was subjected (Suggate, 1982; Barker and Pawlewicz, 1986; Barker, 1989b). The maturity models are either Time-Temperature Indexes (TTI) produced by calibrating the maturity with time and temperature in basins (Waples, 1980), or kinetically based models in which reflectance is exponentially related to temperature, but only linearly related to time (Middleton, 1982; Ritter, 1984; Antia,

1986; Armagnac, et al., 1989; Burnham and Sweeney, 1989; Sweeney and Burnham, 1990).

Retardation of vitrinite reflectance and hydrocarbon generation by overpressure is reported by Carr (1999). He claims that overpressure results in the retention of volatiles within the molecular structure which prevents the molecular reorganization necessary to produce higher reflectance values. Law et al. (1989) reported presence of non-linear (often referred as kinky vitrinite profile in the literature) vitrinite reflectance profiles (nonlinear two or more nonparallel segments) in wells drilled into abnormally pressured, low permeability reservoirs in Rocky Mountain basins. They related the kinky profiles to perturbations of the thermal gradient caused by contrasting heat transfer processes associated with the development of abnormally high paleopressures. They claim that heat transfer process varies between gas bearing (conductive and connective transfer), gas and water bearing (convective transfer), and water bearing (conductive transfer) zones which affects the thermal maturity and therefore vitrinite reflectance.

Hydrocarbon generation probably begins over a range of R_o values depending on the specific type of organic matter involved. A summary of three general types of kerogens, their occurrence and potential to generate hydrocarbons are listed in Table 2.1. In the Piceance, Uinta, and Wind River Basins, R_o of 0.73% was used to define the limits of basin-centered gas accumulations (Johnson, 1989; Johnson and others, 1987; Nuccio and others, 1992, 1996). An R_o of 1.10% represents the level of maximum gas generation and expulsion from Type III kerogen (Meissner, 1984).

Table E3.1. Three general types of kerogen, their occurrences and the thermal maturity required to generate hydrocarbons (summarized from Nuccio and Roberts, 2003).

Type of Kerogen	Occurrence	Thermal Maturity Required	
		For Onset of Oil nad Dry Gas Generation	For Onset of Wet Gas / Biogenic Generation
Type I alginite (sapropelic or lipid rich)	Hydrogen rich; occurs primarily in marine and lacustrine rocks; and generates mainly oil during catagenesis.	R ₀ : 0.50% (Dow, 1977). R ₀ : 0.70% (Anders and Gerrild, 1984 and Tissot and Welte, 1984).	Biogenic gas can be generated by organic matter at any level of thermal maturity provided that conditions are suitable for methane-generating microbes.
Type II exinite (phytoplankton, zooplankton, and other microorganisms)	Mainly in marine rocks; but can occur in lacustrine rocks as well; and generates both oil and gas during catagenesis.	R ₀ : 0.45–0.50% for high sulfur kerogen R ₀ : 0.60% for typical Type II kerogen (Waples, 1985).	R ₀ : 0.8 –2.0% for wet gas from mixed lacustrine-marine terrestrial organic matter and thermal breakdown of oil.
Type III vitrinite & huminite (terrestrial plant debris)	Oxygen-rich and hydrogen-poor; occurs mainly in coal, terrestrial shales, and marginal-lacustrine or marginal-marine rocks; and generates mostly dry gas (thermogenic methane) during catagenesis	R ₀ : 0.75% onset of gas generation and 1.1% upper limit of gas generation (Juntgen and Klein, 1975). Upper limit for gas preservation could be as high as 3.5% (Dow, 1977) or 4.0% R ₀ (Waples, 1980).	R ₀ : 1.0–3.0% for dry gas from humic organic matter and thermal breakdown of wet gas.

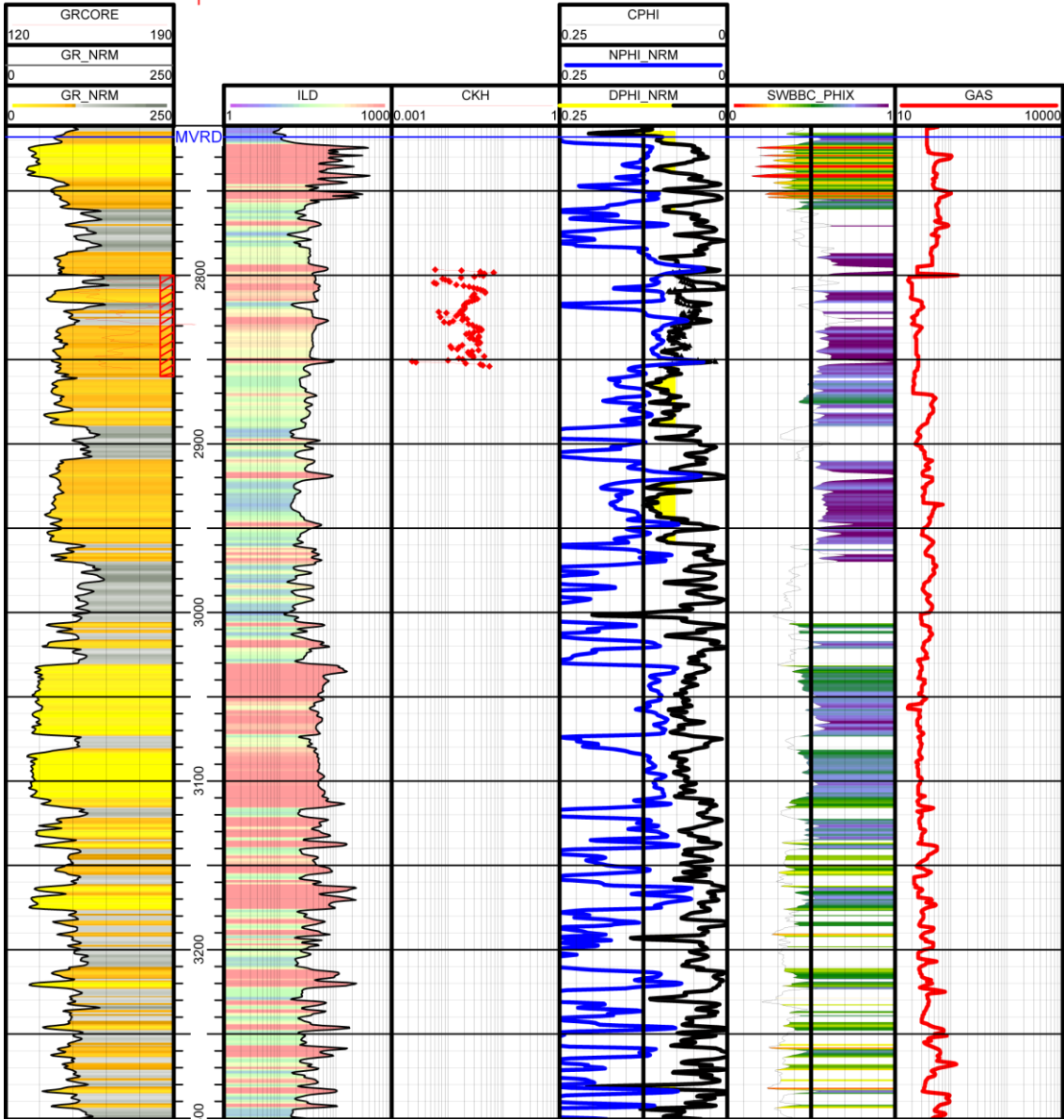
APPENDIX F: TYPE LOG FOR LAST DANCE WELL

GR: Gamma-ray
ILD: Resistivity
CKHI: Permeability
GR: Gamma-ray
CPHI: Core Porosity
NPHI: Neutron Porosity
DPHI: Density Porosity
SWBBC: Water Saturation
Cored Interval: shown with shaded area.

BBC
LAST DANCE
43C-3-792



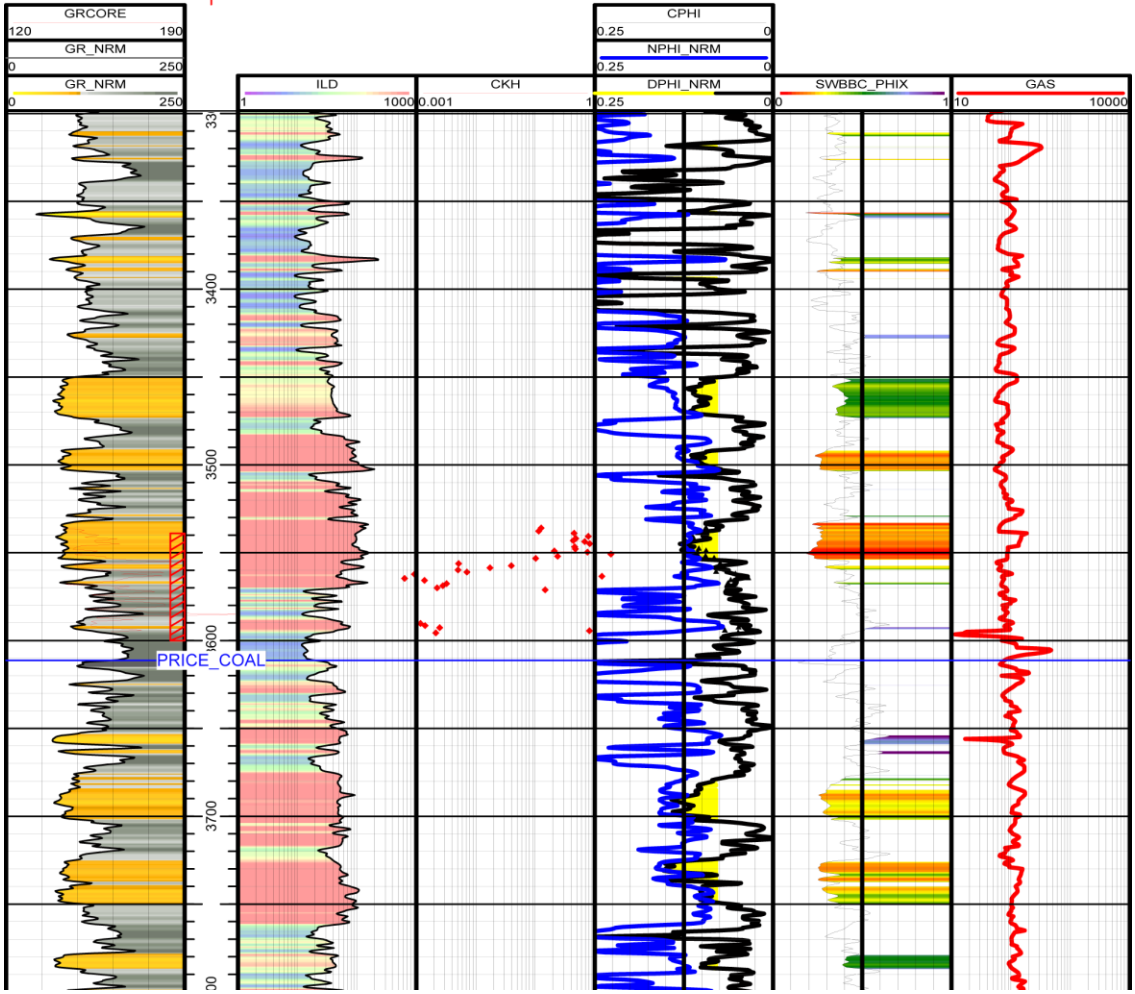
0504511402000
TD : 6,780
T7S R92W S3



BBC
LAST DANCE
43C-3-792



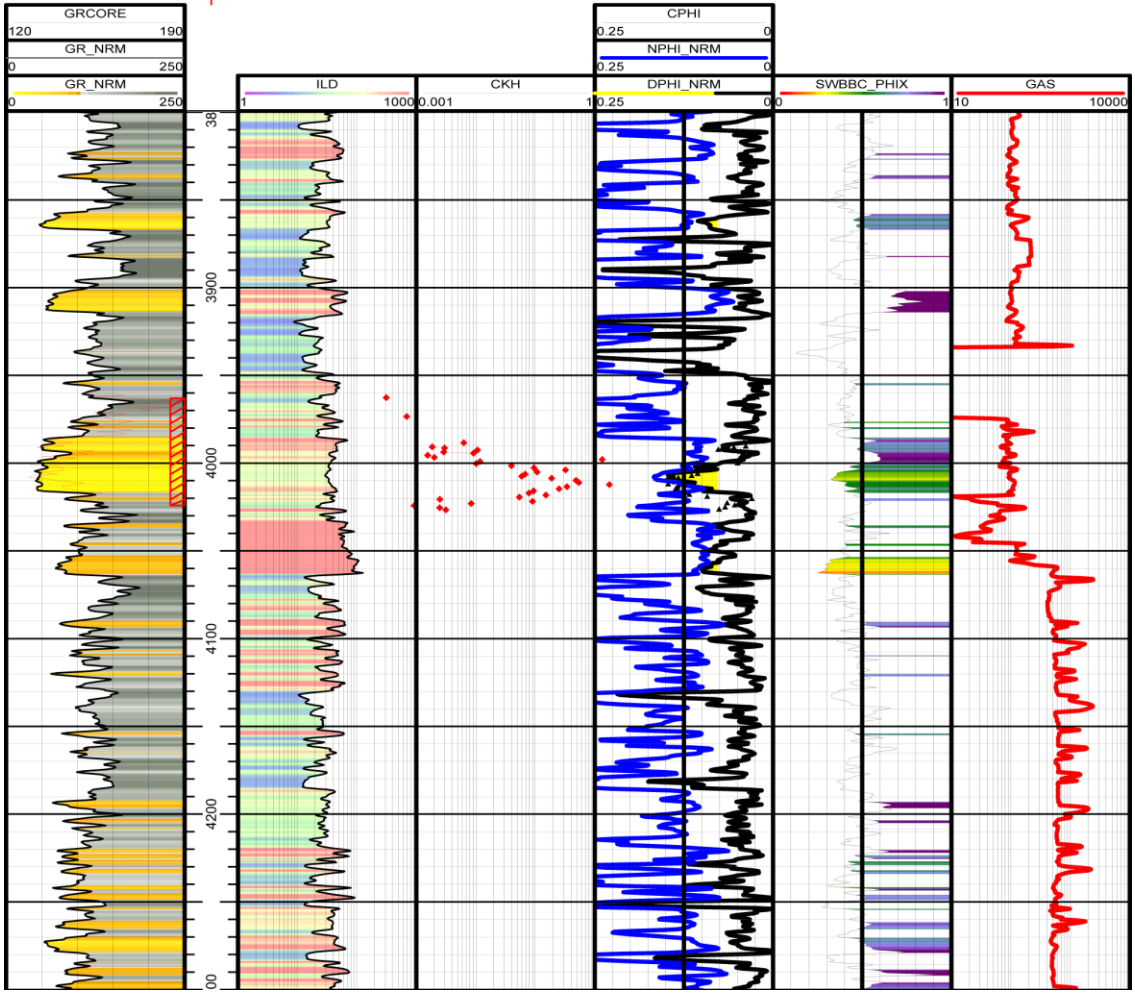
0504511402000
TD : 5.730
T7S R92W S3



BBC
LAST DANCE
43C-3-792



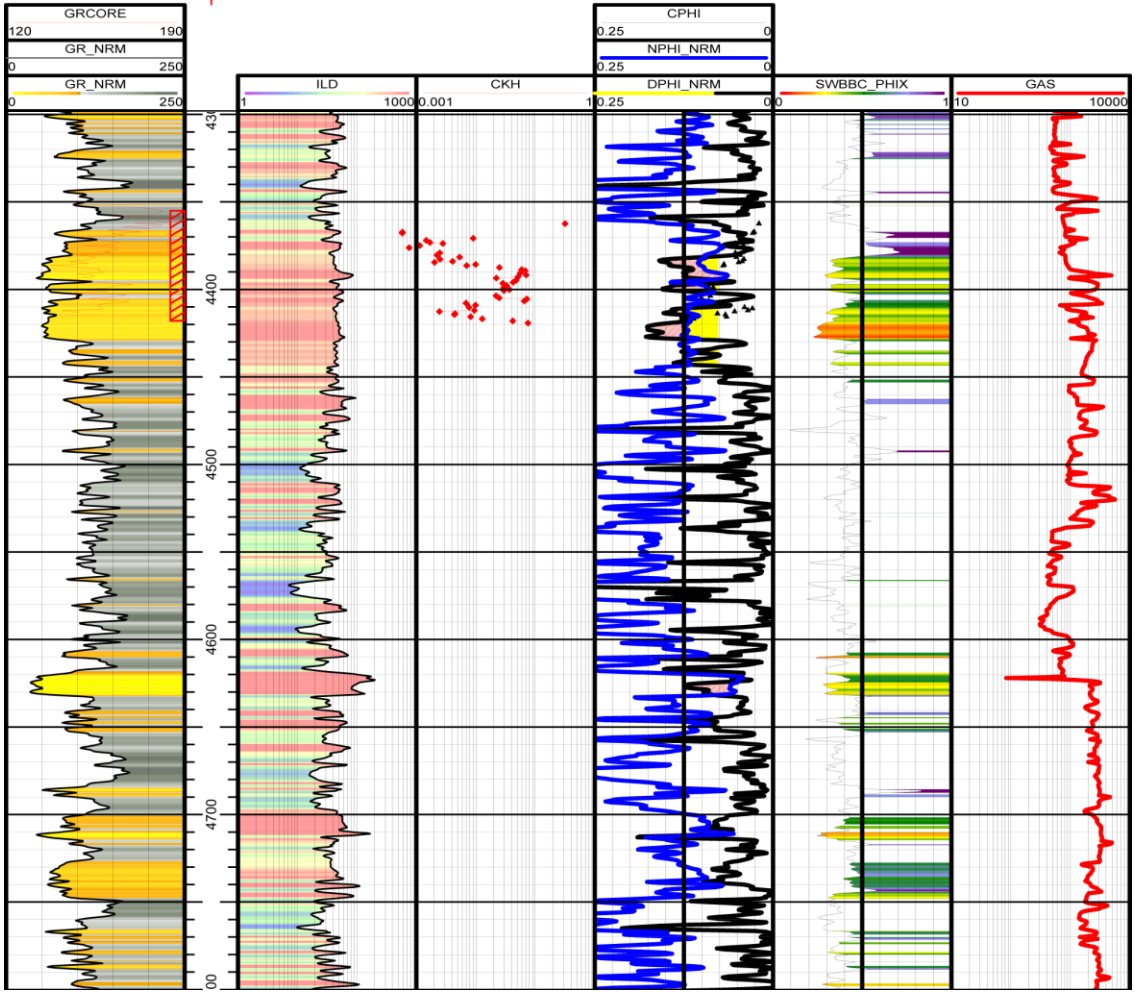
05045114020000
TD : 6.730
T7S R92W S3



BBC
LAST DANCE
43C-3-792



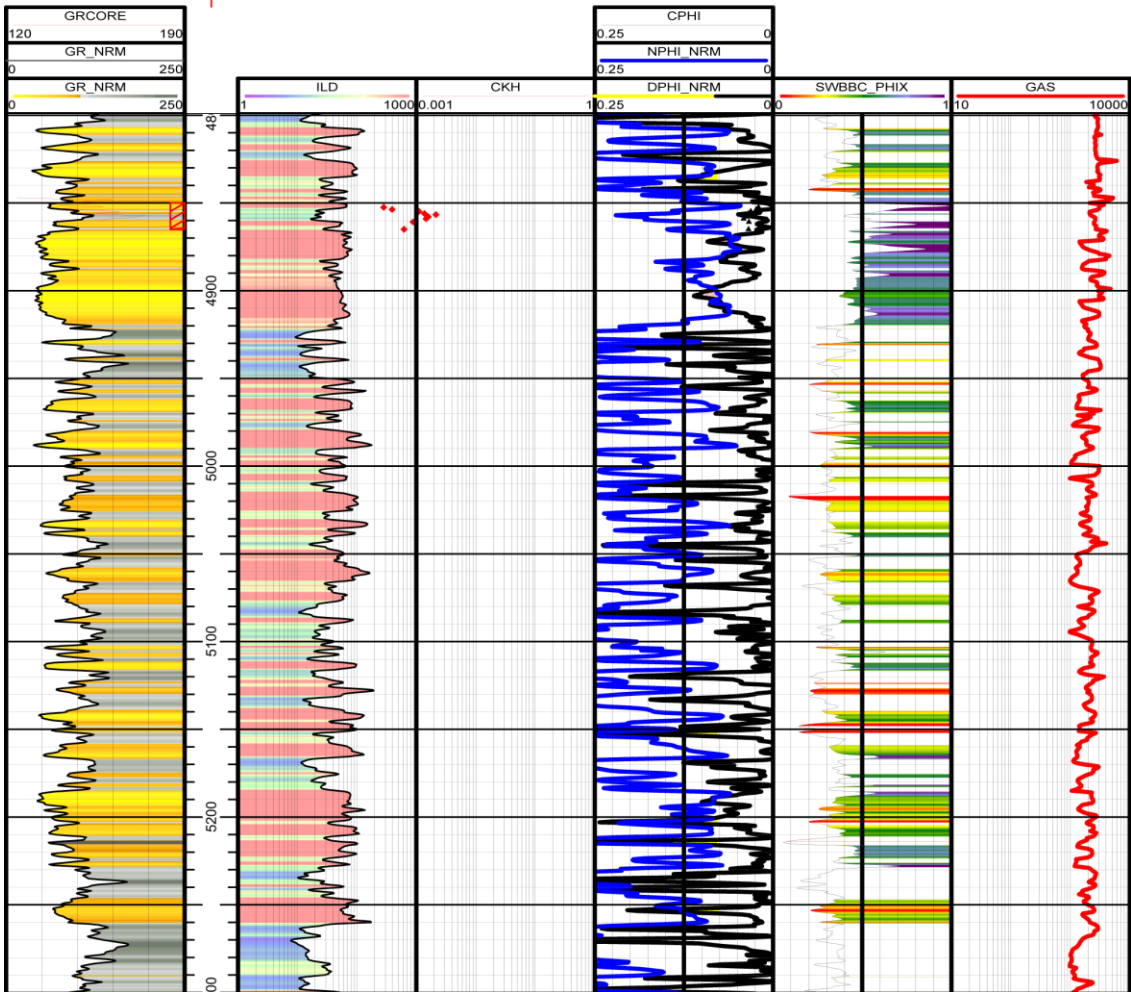
0504511402000
TD : 5.730
T7S R92W S3

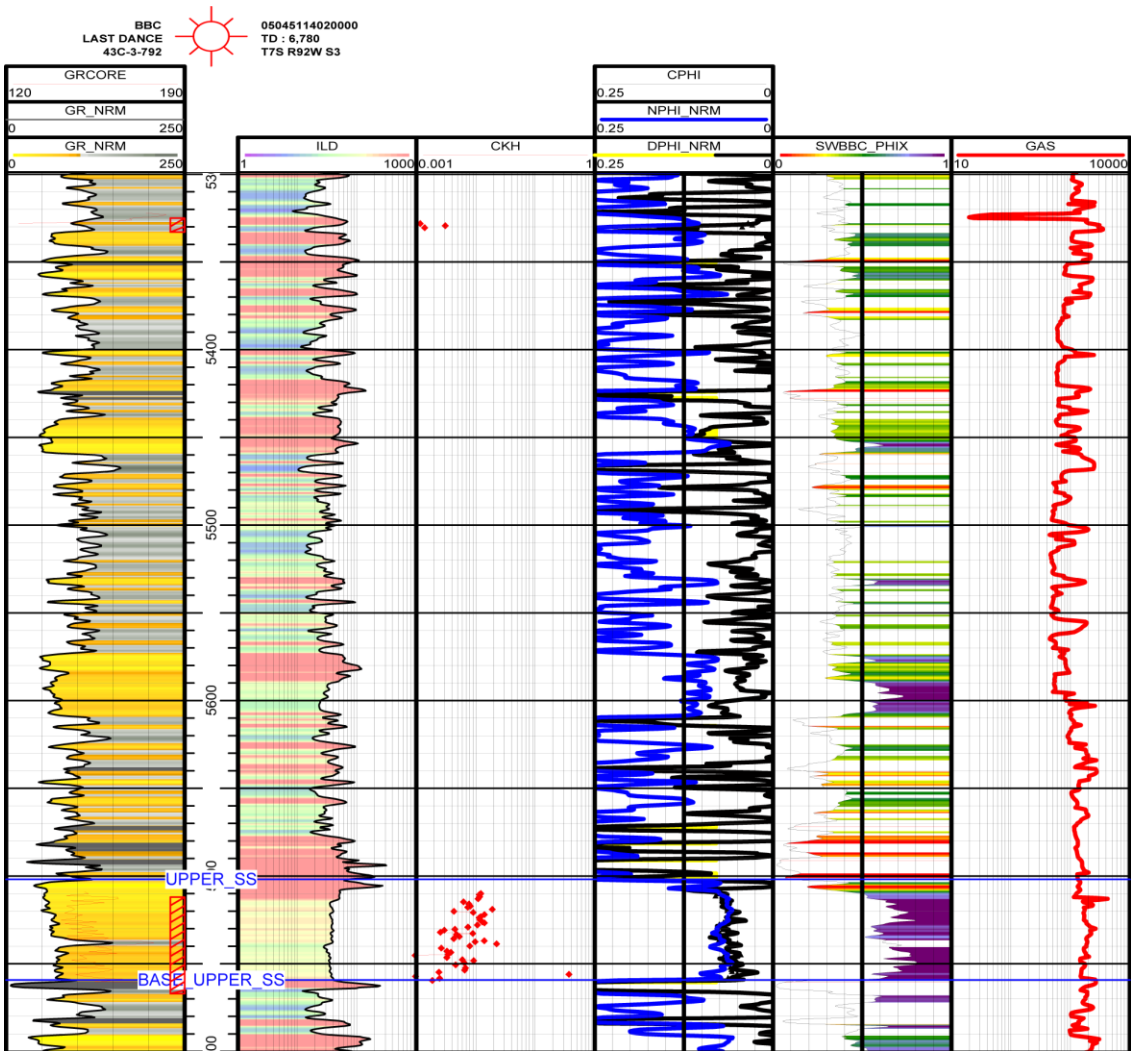


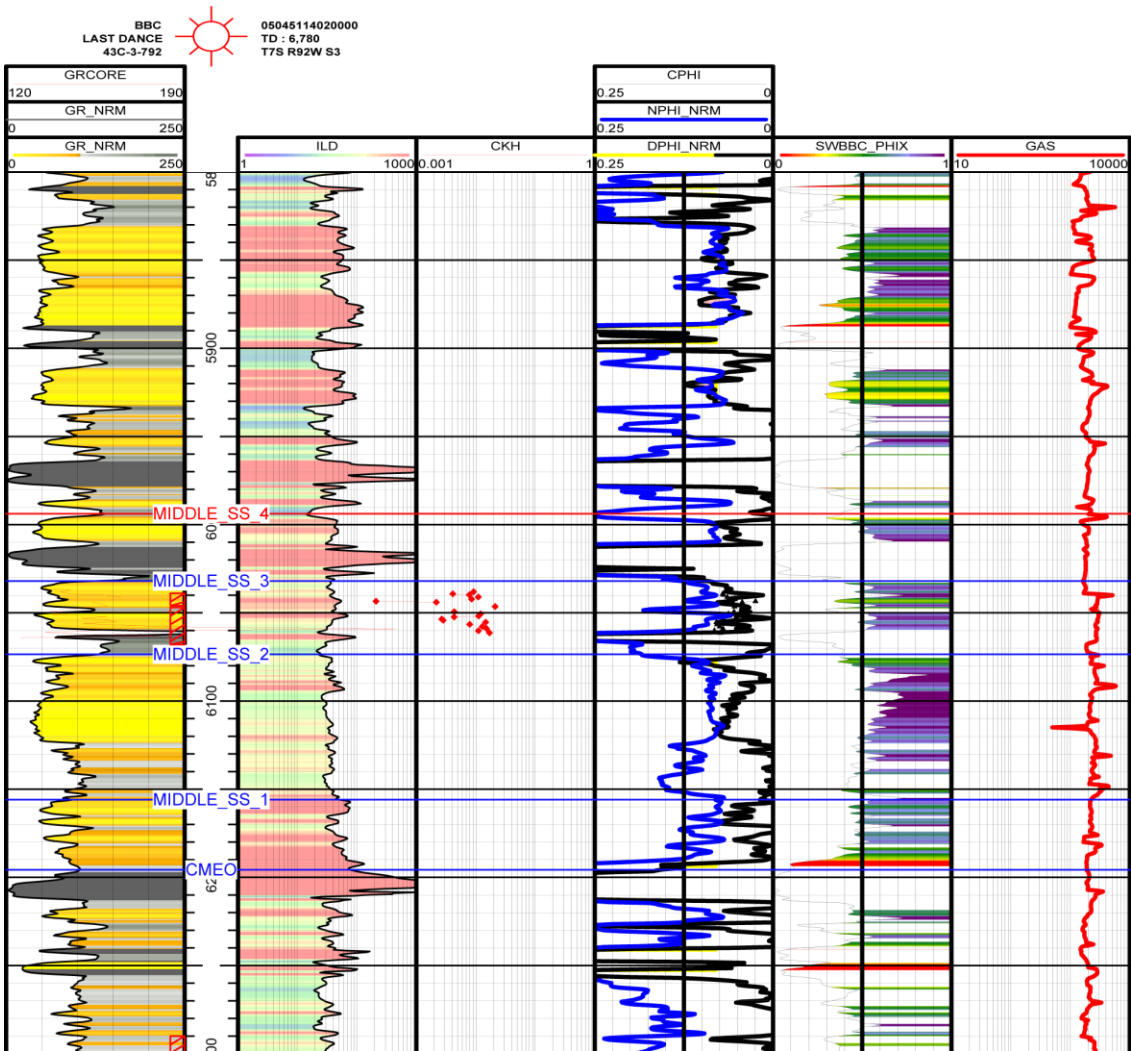
BBC
LAST DANCE
43C-3-792

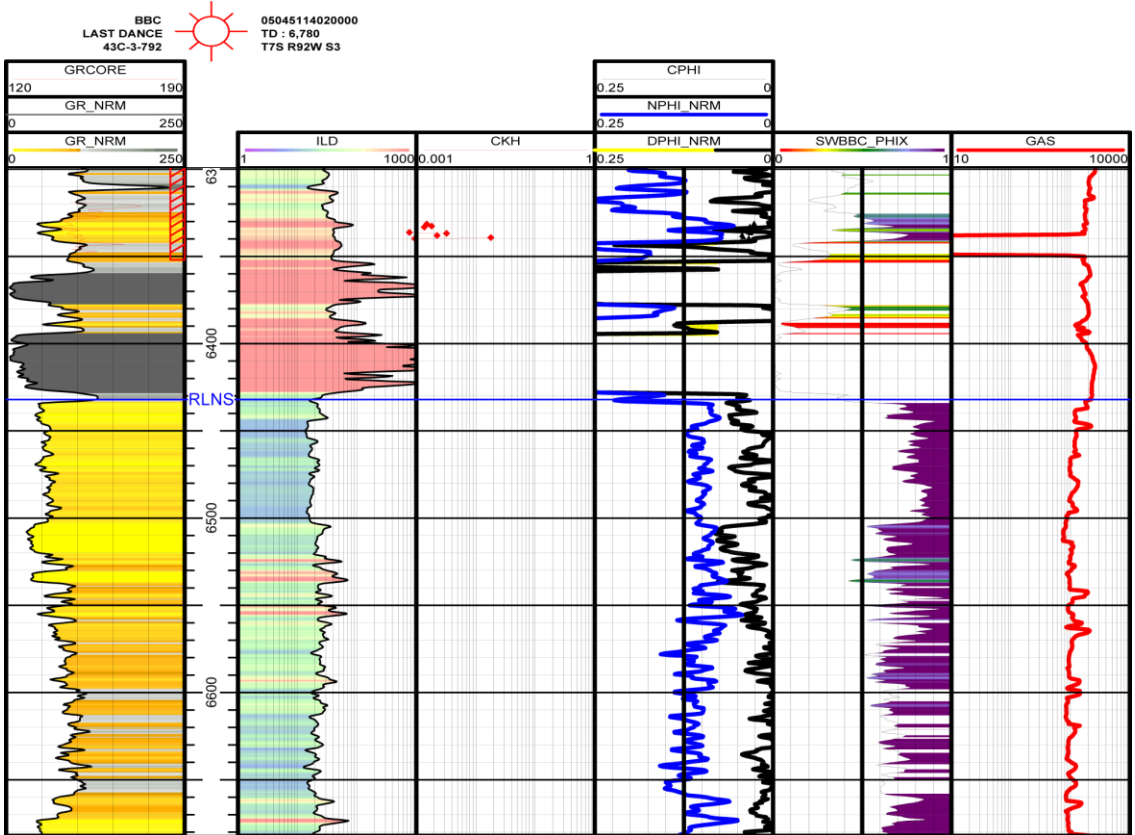


0504511402000
TD : 6,780
T7S R92W S3









REFERENCES

- Aase, N. E., and O. Walderhaug, 2005, The effect of hydrocarbons on quartz cementation: diagenesis in the Upper Jurassic sandstones of the Miller field, North Sea, revisited. *Petroleum Geoscience* 11, 215–223.
- Al-Tahini, A. M., Sondergeld, C. H. and C. S. Rai, 2006, The effect of cementation on the Mechanical Properties of Sandstones, *Society of Petroleum Engineers: SPE Reservoir Evaluation & Engineering*, Paper SPE 89069, p. 308-317.
- Anders, D.E., and P.M. Gerrild, 1984, Hydrocarbon generation in lacustrine rocks of Tertiary age, Uinta Basin, Utah—Organic carbon, pyrolysis yield, and light hydrocarbons, in Woodward, Jane, Meissner, F.F., and Clayton, J.L., eds., *Hydrocarbon source rocks of the greater Rocky Mountain region: Rocky Mountain Association of Geologists*, p. 513–529.
- Antia, D. D. J., 1986, Kinetic method for modeling vitrinite reflectance, *Geology*; July 1986; v. 14; no. 7; p. 606-608; DOI: 10.1130/0091-7613(1986)14
- Armagnac, C., Bucci, J., Kendall, C. G. St. C., and I. Lerche, 1989, Estimating the Thickness of Sediment Removed at an Unconformity Using Vitrinite Reflectance Data, in N. Naeser and T. H. McCulloh (Eds.), *Thermal History of Sedimentary Basins: Springer-Verlag, Berlin*, Ch. 13, p. 217–238.
- Armstrong, R. L., 1968, Sevier orogenic belt in Nevada and Utah: *Geological Society of America, Bulletin*, p. 429–458.
- Atkinson, B. K., 1982, Subcritical crack propagation in rocks: their experimental results and applications, *Journal of Structural Geology*, v. 4, p. 41-56
- Atkinson, B. K., 1984, Subcritical crack growth in geological materials: *Journal of Geophysical Research*, v. 89, no. B6, p. 4077–4114.
- Atkinson, B. K., 1987, Introduction to fracture mechanics and its geophysical applications, in B. K. Atkinson, ed., *Fracture mechanics of rock: London, Academic Press*, p. 1–26.
- Atkinson, B. K., and P. G. Meredith, 1981, Stress corrosion cracking of quartz: a note on the influence of chemical environment: *Tectonophysics*, v. 77, p. T1–T11.
- Atkinson, B. K., and P. G. Meredith, 1989, Experimental fracture mechanics data for rocks and minerals: *Fracture Mechanics of Rock*, B. K. Atkinson (editor), *Academic Press Geology Series, London*, p. 477–526.

- Atkinson, B. K., and V. Avdis, 1980, Technical note, fracture mechanics parameters of some rock-forming minerals determined using an indentation technique: *International Journal of Rock Mechanics, Mining Science & Geomechanics Abstracts*, v. 17, p. 383–386.
- Awwiller, D. N., and L. L. Summa, 1997, Quartz cement volume constraints on burial history analysis: An example from the Eocene of western Venezuela (abs.): *AAPG Annual Meeting Program*, v. 6, p. A6.
- Awwiller, D. N., and L. L. Summa, 1998, Constraining maximum paleotemperature using quartz cement abundances; applications to the hydrocarbon systems of South American fold and thrust belts (abs.): *AAPG Bulletin*, v. 82, no. 10, p. 1888.
- Barker, C. E., 1989a, Fluid inclusion evidence for paleotemperatures within the Mesaverde Group, Multiwell Experiment site, Piceance Basin, Colorado, *in* B. E. Law and C. W. Spencer, eds, *Geology of Tight Gas reservoirs in the Pinedale Anticline area, Wyoming, and the Multiwell experiment site, Colorado*: U.S. Geological Survey Bulletin.
- Barker, C. E., 1989b, Temperature and time in the thermal maturation of sedimentary organic matter, *in* N. D. Naeser and T. H. McCulloh, eds., *Thermal history of sedimentary basins--methods and case histories*: New York, Springer-Verlag, p. 75-98.
- Barker, C. E., 1990, Fluid inclusion evidence for paleotemperatures within the Mesaverde Group, Multiwell Experiment Site, Piceance Basin, Colorado, *in* Law, B.E., and Spencer, C.W., eds., *Geology of Tight Gas Reservoirs in the Pinedale Anticline area, Wyoming, and the Multiwell Experiment Site, Colorado*: U.S. Geological Survey Bulletin 1886, chap. M, p. M1-M11.
- Barker, Ch. E. and M. J. Pawlewicz, 1986, The correlation of vitrinite reflectance with maximum temperature in humic organic matter in *Lecture Notes in Earth Sciences*, Vol. 5 *Paleogeothermics*, edited by G. Buntebarth and L. Stegena © Springer-Verlag Berlin Heidelberg 1986 Volume 5/1986ISBN, 978-3-540-16645-0.
- Becker, S. P., Hooker, J. N., Eichhubl, P., Laubach, S., Lander, R., Bonnell, L., Reed, R. M., and A. Fall, 2009a, History of Fracture Development and Diagenesis in Piceance Basin Tight Gas Reservoirs: Insights from Fluid Inclusion and Fracture Scaling Analyses (abs), *in* AAPG Search and Discovery Article #90090©2009 AAPG Annual Convention and Exhibition, Denver, Colorado, June 7-10, 2009.
- Becker, S. P., Eichhubl, P., Laubach, S. E., Reed, R. M., Lander, R. H., and R. J. Bodnar, 2009b. A 48 m.y. history of fracture opening, Cretaceous Travis Peak Formation, east Texas: *Geological Society of America Bulletin*, v. 121, p. 1709-1724.

- Bjørklykke, K., and P. K. Egeberg, 1993, Quartz cementation in sedimentary basins: AAPG Bulletin, v. 77, p. 1538–1548.
- Bloch, S., Lander, R. H., and L. M. Bonnell, 2002. Anomalously high porosity and permeability in deeply buried sandstone reservoirs: Origin and predictability: AAPG Bulletin, v. 86, p. 301–328.
- Bonnell, L. M., Larese, R. E., and R. H. Lander, 2006, Porosity Preservation by Inhibition of Quartz Cementation: Microquartz Versus Hydrocarbons (Abs.), AAPG Hedberg Conference, Perth Australia.
- Bonnell, L. M., Warren, E. H., and R. H. Lander, 1998, Reservoir quality prediction through simulation of sandstone diagenesis: Cusiana field, eastern Columbia, 1998 International AAPG Conference and Exhibition, Rio de Janeiro, Brazil (abs.): AAPG Bulletin, v. 82, p. 1894.
- Bostick, N. H., and V. L. Freeman, 1984, Tests of vitrinite reflectance and paleotemperature models at the Multiwell Experiment site, Piceance Creek Basin, Colorado, in C. W. Spencer and C. W. Keighin, eds., Geologic studies in support of the U.S. Department of Energy Multiwell Experiment, Garfield County, Colorado: U.S. Geological Survey Open File Report 84-747, p. 110-120.
- Burnham, A. K., and J. J. Sweeney, 1989, A chemical kinetic model of vitrinite reflectance maturation. *Geochim. et Cosmochim. Acta*, 53, p. 2649-2657.
- Cabrera, N. A., and D. A. Vermilyea, 1958, The growth of crystals from solution, in R. H. Doremus, Roberts, B.W., and Turnbull, D., ed., *Growth and Perfection of Crystals*: New York, Wiley, p. 393-410.
- Carr, A. D., 1999, A vitrinite reflectance kinetic model incorporating overpressure retardation, *Marine and Petroleum Geology* 16 (1999) 355-377.
- Cerveny, P. F., and J. R. Steidtmann, 1993, Fission-Track Thermochronology of the Wind River Range, Wyoming - Evidence for Timing and Magnitude of Laramide Exhumation, *Tectonics*, Vol. 12, Issue: 1, p. 77-91.
- Chancellor R. E., and R. C. Johnson, 1988, Geologic and engineering implications of production history from five Mesaverde Wells in Central Piceance Creek Basin, Northwest Colorado, *SPE Formation Evaluation*, Volume 3, Number 2, p. 307 – 314, DOI: 10.2118/15237-PA.
- Chapin, C.E., and S.M. Cather, 1981, Eocene tectonics and sedimentation in the Colorado Plateau-Rocky Mountain area, in Dickinson, W.R. and Payne, W.D., eds., *Relations of Tectonics to Ore Deposits in the Southern Cordillera*: Arizona Geological Society Digest, v. 14, p. 173-198.

- Charles, R. J., 1958, Static Fatigue of Glass, I, *J. Appl. Phys.* 29, p. 1549–1553.
- Cole, R., and S. P. Cumella, 2003, Stratigraphic architecture and reservoir characteristics of the Mesaverde Group, southern Piceance Basin, Colorado, in K. M. Peterson, T. M. Olsen, and D. S. Anderson, eds., *Piceance Basin 2003 guidebook: Rocky Mountain Association of Geologists*, p. 385–442.
- Collins, B. A., 1976, Coal deposits of the Carbondale, Grand Hogback, and Southern Danforth Hills coal fields, eastern Piceance Basin, Colorado: *Quarterly of the Colorado School of Mines*, v. 71, p. 1–138.
- Craig, D. P., Eberhard, M. J., Muthukumarappan, R., Odegard, C. E., and R. Mullen, 2005, Permeability, pore pressure, and leakoff-type distributions in Rocky Mountain basins: *SPE Gas Technology Symposium*, Calgary, April 30–May 2, 2002, *SPE Paper 75717*, 12 p.
- Crossey, I. J., and D. Larsen, 1992, Authigenic mineralogy of sandstones intercalated with organic-rich mudstones: integrating diagenesis and burial history of the Mesaverde Group, Piceance Basin, NW Colorado *in* D.W. Houseknecht and E.D. Pittman, eds., *Origin, Diagenesis and Petrophysics of Clay Minerals in Sandstones*, *SEPM Spec. Publ.* vol. 47, p. 125–144.
- Cumella, S. P., 1981, Sedimentary history and diagenesis of the Pictured Cliffs sandstone, San Juan Basin, New Mexico and Colorado, *Master's Thesis*, University of Texas at Austin, Austin, Texas, 219 p.
- Cumella, S. P., and D. B. Ostby, 2003, Geology of the basin-centered gas accumulation, Piceance Basin, Colorado, *in* K. M. Peterson, T. M. Olson, and D. S. Anderson, eds., *Piceance Basin 2003 guidebook: Rocky Mountain Association of Geologists*, p. 171–193.
- Cumella, S. P., and J. Scheevel, 2008, The influence of stratigraphy and rock mechanics on Mesaverde gas distribution, Piceance Basin, Colorado, in S. P. Cumella, K. W. Shanley, and W. K. Camp, eds., *Understanding, exploring, and developing tight-gas sands 2005 Vail Hedberg Conference: AAPG Hedberg Series*, no. 3, p. 137–155; DOI:10.1306/13131054H33104.
- de Souza, R. S., and E. F. McBride, 2000, Diagenetic modeling and reservoir quality assessment and prediction: An integrated approach (abs.): *AAPG Bulletin*, v. 84, no. 9, p. 1495.
- Decelles, P.G., and K. A. Giles, 1996, Foreland basin systems: *Basin Research*, v. 8, p. 105–123.

- Decker, E. R., 1995, Thermal regimes of the southern Rocky Mountains and Wyoming Basin in Colorado and Wyoming in the United States: *Tectonophysics*, v. 244, p. 85–106.
- Dickinson, W.R., Lawton, T. F., and K. I. Inman, 1986, Sandstone detrital modes, central Utah foreland region: stratigraphic record of Cretaceous–Paleogene tectonic evolution: *Journal of Sedimentary Petrology*, v. 56, p. 276–293.
- Dow, W. G., 1977, Kerogen studies and geological interpretations: *Journal of Geochemical Exploration*, v. 7, p. 79–99.
- Dutton, S. P., and S. E. Laubach, 1993, Comprehensive geologic basin analysis: application of a generic research approach to several tight gas sandstone formations: *In Focus—Tight Gas Sands*, v. 9, no. 1, p. 1–33.
- Dutton, S. P., Clift, S. J., Hamilton, D. S., Hamlin, H. S., Hentz, T. F., Howard, W. E., Akhter, M. S., and S. E. Laubach, 1993, Major low-permeability-sandstone gas reservoirs in the continental United States: The University of Texas at Austin, Bureau of Economic Geology Report of Investigations No. 211, 221 p.
- Eatough, M. O., 1983, Preliminary results of mineralogy and petrology of the fracture zone interval (depth 5690 – 5870 t.), drill core MWX-2, Sandia National Laboratories, Multi-well Experiment Program, Imprint Grand Junction, Colorado: Bendix Field Engineering Corp., 43 p.
- Ehrenberg, S. N., 1995, Measuring sandstone compaction from modal analyses of thin sections: how to do it and what the results mean: *Journal of Sedimentary Research*, v. 65, p. 369-379.
- Encyclopedia Britannica Inc., 1996, Young's Modulus, *Encyclopedia Britannica*, accessed October, 2009, <http://www.britannica.com/EBchecked/topic/654186/Youngs-modulus>.
- Engelder, T., 1985, Loading paths to joint propagation during a tectonic cycle: An example from the Appalachian Plateau, U.S.A., in P. L. Hancock and C. M. Powell, eds., *Journal of Structural Geology*: Amsterdam, Elsevier, v. 7, p. 459-476.
- Fall, A., Eichhubl, P., Becker, S. P., Bodnar, R. J., and S. E. Laubach, 2009, Tracking Fluid Evolution Using Fluid Inclusions In Synkinematic Fracture Cements: Piceance Basin, Colorado, Melt and Fluid Inclusion Analysis in Resource Investigations, *Geological Society of America Abstracts with Programs Oregon 2009*, Vol. 41, No. 7, p. 255.
- Folk, R. L., 1980, *Petrology of Sedimentary Rocks*, Hemphill Publishing Company, Austin, Texas, 182 p.

- Fouch, T. D., Lawton, T. F., Nichols, D. J., Cashion, W. B., and W. A. Cobban, 1983, Patterns and timing of synorogenic sedimentation in Upper Cretaceous rocks of central and northeast Utah. In: Reynolds, M.W., Dolly, E.D., (Eds.), *Mesozoic Paleogeography of West-Central United States*. SEPM Rocky Mountain Section, pp. 305–336.
- Franckzyl, K. J., Pitman, J. K., and D. J. Nichols, 1990, Sedimentology, mineralogy, palynology, and depositional history of Upper Cretaceous and Lower Tertiary rocks along the Utah Book Cliffs east of the Green River: U.S. Geological Survey Bulletin 1787-N, 27 p.
- Fredrich, J. T., Arguello, J. G., Deitrick G. L., and E. P. de Rouffignac, 2000, Geomechanical modeling of reservoir compaction, surface subsidence, and casing damage at the Belridge field, paper SPE 65354, SPEREE (2000).
- Gale, J. F. W., Reed, R. M., and J. Holder, 2007, Natural fractures in the Barnett Shale and their importance for hydraulic fracture treatments: AAPG Bulletin, v. 91, no. 4, p. 603–622.
- Gesing, A. J., and R. C. Bradt, 1983, A microcrack model for the effect of grain size on slow crack growth in polycrystalline Al_2O_3 : *Fracture Mechanics of Ceramics*, v. 5, R.C. Bradt, A. G. Evans, D. P. H. Hasselman, and F. F. Lange (editors), Plenum Press, New York, p. 569–590.
- Gomez, L., Gale, J. F. W., Laubach, S. E., and S. Cumella, 2003, Quantifying fracture intensity: an example from the Piceance Basin, Chapter 6, *in* Peterson, K. M., Olson, T. M., and Anderson, D. S., eds, *Piceance Basin 2003 guidebook: Rocky Mountain Association of Geologists*, p. 96–113.
- Grenet, L., 1899, Mechanical Strength of Glass, *Bulletin Society of Enc.*, Industr. Nat. Paris 4, p. 838-848.
- Griffith, A. A., 1921, The phenomena of rupture and flow in solids, *Philosophical Transactions of the Royal Society of London*, A 221, p. 163–198, <http://www.cmse.ed.ac.uk/AdvMat45/Griffith20.pdf>.
- Hancock, P. L., 1985, Brittle Microtectonics: Principles and Practice, *Journal of Structural Geology* 7, p. 437- 457.
- Hanks, C. L., Parris, T. M., and Wallace W. K., 2006, Fracture paragenesis and microthermometry in Lisburne Group detachment folds: Implications for the thermal and structural evolution of the northeastern Brooks Range, Alaska, *AAPG Bulletin*, Vol.: 90, Issue: 1, p. 1-20

- Hansley, P. L., and R. C., Johnson, 1980, Mineralogy and Diagenesis of Low-Permeability Sandstones of Late Cretaceous age, Piceance Creek Basin, Northwestern Colorado, *The Mountain Geologist*, v. 17, p. 88-129.
- Haszeldine, R. S., A. J. Cavanagh, and G. L. England, 2003, Effects of oil charge on illite dates and stopping quartz cement; calibration of basin models, in J. M. Verweij, H. Doust, C. J. Peach, C. J. Spiers, and R. A. J. Swennen, eds., *Proceedings of Geofluids IV*, Amsterdam-New York, Elsevier, p. 373-376.
- Heller, P. L., Bowdler, S. S., Chambers, H. P., Coogan, J. C., Hagen, E. S., Shuster, M. W., Winslow, N. S., and T. F. Lawton, 1986, Time of initial thrusting in the Sevier orogenic belt, Idaho-Wyoming and Utah: *Geology*, v. 14, p. 388-391.
- Hettinger, R. D., and M. A. Kirschbaum, 2003, Stratigraphy of the Upper Cretaceous Mancos Shale (upper part) and Mesaverde Group in the southern part of the Uinta and Piceance Basins, Utah and Colorado: U. S. Geological Survey Digital Data Series, DDS-0069-B, 21 p.
- Holder, J., Olson, J. E., and Z. Philip, 2001, Experimental determination of subcritical crack growth parameters in sedimentary rock: *Geophysical Research Letters*, v. 28, no. 4, p. 599-602.
- Holditch, S. A., Lee, W. J., and S. R. Gist, 1993, An Improved Technique for Estimating Permeability, Fracture Length, and Fracture Conductivity From Pressure-Buildup Tests in Low-Permeability Gas Wells, *Journal of Petroleum Technology*, Volume 35, Number 5, p. 981-990, DOI:10.2118/9885-PA.
- Hood, A., Gutjahr, C. C., and R. L. Heacock, 1975, Organic metamorphism and the generation of petroleum, *Amer. Assoc. Petrol. Geol. Bull.*, 59, p. 986-96.
- Hooker, J. N., Gale, J. F. W., Gomez, L. A., Laubach, S. E., Marrett, R. A., and R. M. Reed, 2009, Aperture-size scaling variations in a low-strain opening-mode fracture set, Cozzette Sandstone, Colorado: *Journal of Structural Geology*, v. 31, p. 707-718.
- Hurst, A. R., 1981, A scale of dissolution for quartz and its implications for diagenetic processes in sandstones: *Sedimentology*, v. 28(4), p. 451-459.
- Ihinger, P. D., and S. I. Zink, 2000, Determination of relative growth rates of natural quartz crystals, London, Macmillan Journals, p. 865-869.
- Ispas, I., Bray, A. R., and N. G. Higgs, 2005, Prediction and evaluation of sanding and casing deformation in a GOM-shelf well, SPE 87842, JPT, Feb (2005).
- Iwasaki H., F. Iwasaki, V. S. Balitsky, L. V. Balitskaya, and I. B. Makhina, 1998. Growth rates anisotropy of synthetic quartz crystals grown on Z-cut hexagonal seeds and

- computer simulations of growth process, *Journal of crystal growth*, vol. 187, no3-4, p. 481-489.
- Johansen, S. J., 1986, Provenance of the Mesaverde Group of West-Central New Mexico, Ph.D. Dissertation, University of Texas at Austin, 310 p.
- Johnson, R. C., 1989, Geologic history and hydrocarbon potential of Late Cretaceous-age, low-permeability reservoirs, Piceance Basin western Colorado: U. S. Geological Survey Bulletin 1787-E, 51 p.
- Johnson, R. C., and D. D. Rice, 1990, Occurrence and geochemistry of natural gases, Piceance Basin, northwest Colorado: *AAPG Bulletin*, v. 74, p. 805–829.
- Johnson, R. C., and F. May, 1978, Preliminary stratigraphic studies of the upper part of the Mesaverde Group, the Wasatch Formation, and the lower part of the Green River Formation, DeBeque area, Colorado, including environments of deposition and investigations of palynomorph assemblages: U. S. Geological Survey Miscellaneous Field Studies Map MF- 1050, scale 1:1,200, 2 sheets.
- Johnson, R. C., and F. May, 1980, A study of the Cretaceous-Tertiary unconformity in the Piceance Creek Basin, Colorado – The underlying Ohio Creek Formation (Upper Cretaceous) redefined as a member of the Hunter Canyon or Mesaverde Formation, *Contributions to stratigraphy*, U.S. Geological Survey Bulletin, 1482-B, p. B1-B27.
- Johnson, R. C., and R. M. Flores, 2003, History of the Piceance Basin from Latest Cretaceous through Early Eocene and the characterization of Lower Tertiary Sandstone Reservoirs, *Piceance Basin Guidebook*, Chapter 3, Rocky Mountain Association of Geologists, p. 21-61.
- Johnson, R. C., and S. B. Roberts, 2003, The Mesaverde total petroleum system, Uinta-Piceance province, Utah and Colorado, in *Petroleum systems and geologic assessment of oil and gas in the Uinta-Piceance province, Utah and Colorado*: U.S. Geological Survey Digital Data Series DDS-69-B, Chapter 4, 63 p.
- Johnson, R. C., and V. F. Nuccio, 1986, Structural and thermal history of the Piceance Creek Basin, western Colorado, in relation to hydrocarbon occurrence in the Mesaverde Group, in C. W. Spencer and R. F. Mast, eds., *Geology of tight gas reservoirs: AAPG Studies in Geology* 24, p. 165–205.
- Johnson, R. C., and V. F. Nuccio, 1992, Surface vitrinite reflectance study of the Uinta-Piceance Basin area, western Colorado and eastern Utah—Implications for the development of Laramide basins and uplifts: U.S. Geological Survey Bulletin 1787-DD, 38 p.

- Juntgen, H., and J. Klein, 1975, Entstehung von Erdgas aus kohligen Sedimenten: Erdöl und Kohle, Erdgas, Petrochemie, Ergänzungsband, v. 1, p. 52–69.
- Karweil, J., 1955, Die Metamorphose der Kohlen vom Standpunkt der physicalischen Chemie, Zeitschr. Deutsh. Geol. Gesell., vol. 107, p. 132 - 139.
- Kelley, S.A., and D. D. Blackwell, 1990, Thermal history of the Multi-Well Experiment (MWX) site, Piceance Creek Basin, northwestern Colorado, derived from fission-track analysis: Nuclear Tracks and Radiation Measurement, v. 17, p. 331-337.
- Kranz, R. L., 1983, Microcracks in rocks; a review: Tectonophysics, v. 100, Issue 1-3, p. 449-480.
- Land, L. S., 1997, Mass transfer during burial diagenesis in the Gulf of Mexico sedimentary basin; an overview: pp. 29-39, in: Montaneez, I. P.; Gregg, J. M.; Shelton, K. L. (eds.) Basin-wide diagenetic patterns; integrated petrologic, geochemical, and hydrologic considerations: SEPM Special Publication Vol. 57.
- Lander, R. H., S. E. Laubach, and L. M. Bonnell, in preparation, Constraining fracture opening rates in sandstones using quartz cement morphology, Journal of Structural Geology.
- Lander, R. H., and O. Walderhaug, 1999, Porosity prediction through simulation of sandstone compaction and quartz cementation: AAPG Bulletin, v. 83, p. 433–449.
- Lander, R. H., Larese, R. E., and L. M. Bonnell, 2008, Toward more accurate quartz cement models: The importance of euhedral versus noneuhedral growth rates, AAPG Bulletin, v. 92, no. 11 (November 2008), pp. 1537–1563.
- Lander, R. H., V. Felt, L. M. Bonnell, and O. Walderhaug, 1997, Utility of sandstone diagenetic modeling for basin history assessment (abs.): AAPG Annual Meeting Program, v. 6, p. A66.
- Laubach, S. E. and Diaz-Tushman, K., 2009, Laurentian paleostress trajectories and ephemeral fracture permeability, Cambrian Eriboll Formation sandstones west of the Moine thrust zone, northwest Scotland, Journal of the Geological Society (London), v. 166, part 2, p. 349-362.
- Laubach, S. E., 1988, Subsurface fractures and their relationship to stress history in east Texas basin sandstone: Tectonophysics, v. 156, p. 37–49.
- Laubach, S. E., 1989, Fracture analysis of the Travis Peak Formation, western flank of the Sabine Arch, East Texas: The University of Texas at Austin, Bureau of Economic Geology Report of Investigations No. 185, 55 p.

- Laubach, S. E., 1991, Fracture patterns in low-permeability-sandstone gas reservoir rocks in the Rocky Mountain region: Society of Petroleum Engineers, SPE Paper No. 21853, p. 501–510.
- Laubach, S. E., 1997, A method to detect natural fracture strike in sandstones: AAPG Bulletin, v. 81, no. 4, p. 604-623.
- Laubach, S. E., 2003, Practical approaches to identifying sealed and open fractures , AAPG Bulletin, v. 87, No. 4, (April 2003) 561-579.
- Laubach, S. E., and J. F. W. Gale, 2006, Obtaining fracture information for low-permeability (tight) gas sandstones from sidewall cores: Journal of Petroleum Geology, v. 29, No. 2, p. 147-158.
- Laubach, S. E., and K. Diaz-Tushman, 2009, Laurentian paleostress trajectories and ephemeral fracture permeability, Cambrian Eriboll Formation sandstones west of the Moine thrust zone, northwest Scotland . Journal of the Geological Society (London), v. 166, part 2, p. 349-362.
- Laubach, S. E., and M. E. Ward, 2006, Diagenesis in porosity evolution of opening-mode fractures, Middle Triassic to Lower Jurassic La Boca Formation, NE Mexico: Tectonophysics, v. 419, nos. 1-4, p. 75-97.
- Laubach, S. E., Hentz, T. F., Johns, M. K., Baek, H., and S. J. Clift, 1995, Using diagenesis information to augment fracture analysis: The University of Texas at Austin, Bureau of Economic Geology, topical report prepared for Gas Research Institute, under contract no. 5082-211-0708 (GRI-94/0455), 189 p.
- Laubach, S. E., Lander, R. H., Olson, J. E., Eichhubl, P., Bonnell, L. M., and R. Marrett, 2006, Predicting fracture porosity evolution in sandstone: The University of Texas at Austin, Bureau of Economic Geology, final report prepared for the U.S. Department of Energy, under contract no. DE-FG02-03ER15430, 73 p.
- Laubach, S. E., Olson, J. E., and M. R. Gross, 2009, Mechanical and fracture stratigraphy. AAPG Bulletin, v. 93, no. 11, p. 1413-1426.
- Laubach, S. E., Olson, J. E. and Eichhubl, P., in press, Fracture diagenesis and producibility in tight gas sandstones: in Carr, T., and D'Agostino, T., eds., Unconventional Energy Resources - Making the Unconventional Conventional: 29th Annual GCSSEPM Foundation Bob F. Perkins Research Conference, p. 1–14.
- Laubach, S. E., Reed, R. M., Olson, J. E., Lander, R. H., and L. M. Bonnell, 2004a, Coevolution of crack-seal texture and fracture porosity in sedimentary rocks: cathodoluminescence observations of regional fractures: Journal of Structural Geology, v. 26, no. 5, p. 967-982.

- Laubach, S. E., Olson, J. E., and J. F. W. Gale, 2004b, Are open fractures necessarily aligned with maximum horizontal stress?: *Earth and Planetary Science Letters*, v. 570 222, no. 1, p. 191-195.
- Law, B. E., 2002, Basin-Centered Gas Systems, *AAPG Bulletin*; v. 86; no. 11; p. 1891-1919; DOI: 10.1306/61EEDDB4-173E-11D7-8645000102C1865D.
- Law, B. E., Nuccio, V. F., and C. E. Barker, 1989, Kinky Vitrinite Reflectance Well Profiles: Evidence of Paleopore Pressure in Low Permeability, Gas-Bearing Sequences in Rocky Mountain Foreland Basins, *AAPG Bulletin*, vol. 73 August (1989), pp. 999-1010.
- Lawn, B. R., and T. R. Wilshaw, 1975, *Fracture of Brittle Solids*: Cambridge University Press, Cambridge, 204 p.
- Lawton, T. F., 1983, Late Cretaceous fluvial systems and the age of foreland uplifts in central Utah, in Lowell, J.D., and Gries, R., eds., *Rocky Mountain foreland basins and uplifts*: Denver, Rocky Mountain Association of Geologists, p. 181–199.
- Lawton, T. F., 1986, Fluvial systems of the Upper Cretaceous Mesaverde Group and Paleocene North Horn Formation, central Utah; a record of transition from thin-skinned to thick-skinned deformation in the foreland region. In: Peterson, J. A., (Ed.), *Paleotectonics and Sedimentation in the Rocky Mountain Region*, US American Association of Petroleum Geologists Memoir 41, pp. 423–442.
- Lawton, T. F., 2008, Laramide Sedimentary Basins *In Sedimentary Basins of the World*, K. J. Hsü , editor Vol. 5, *The Sedimentary Basins of the United States and Canada*, Andrew D. Miall, The Netherlands: Elsevier, 2008, pp. 429–450, ISBN: 978-0-444-50425-8.
- Lerche, I., 1997, *Geological Risk and Uncertainty in Oil Exploration*, San Diego, California: Academic Press Limited, c. 1997, 658 p. ISBN 0124441742.
- Lopatin, N. V., 1971, Temperature and geologic time as factors in coalification: *Akad., Nauk. SSSR Izv. Serv. Geol.*, no. 3, p. 95–106.
- Lorenz, J. C., 2003, Fracture systems in the Piceance Basin: Overview and comparison with fractures in the San Juan and Green River basins, *in* K. M. Peterson, T. M. Olson, and D. S. Anderson, eds., *Piceance Basin 2003 Guidebook*: Rocky Mountain Association of Geologists, p. 75–94.
- Lorenz, J. C., and S. J. Finley, 1991, Regional Fractures II: Fracturing of Mesaverde Reservoirs in the Piceance Basin, Colorado., *AAPG Bulletin*, v. 75, No. 11, p. 1738-1757.

- Lorenz, J. C., Sattler, A. R., and C. L. Stein, 1989, The effects of depositional environment on petrophysical properties of Mesaverde reservoirs, northwestern Colorado, in *Formation evaluation and reservoir geology*, SPE Publ. No. 64, p. 119-132.
- Lorenz, J. C., Warpinski, N. R., Branagan, P. T., and A. R. Sattler, 1989, Fracture characteristics and reservoir behavior of stress-sensitive fracture systems in flat-lying lenticular formations: *Journal of Petroleum Technology*, v. 41, p. 615–622.
- Lundegard, P. D., 1992, Sandstone Porosity Loss--A "Big Picture" View of the Importance of Compaction, *Journal of Sedimentary Petrology*, v. 62, No. 2, p. 250-260.
- Makowitz A., Lander R. H., and K. L. Milliken, 2006, Diagenetic modeling to assess the relative timing of quartz cementation and brittle grain process during compaction, *AAPG Bulletin*, Vol. 90, Issue: 6, p. 873-885.
- Makowitz, A., 2004, The genetic association between brittle deformation and quartz cementation: examples from burial compaction and cataclasis, Ph.D. Dissertation, University of Texas at Austin, 298 p.
- Makowitz, A., and D. F. Sibley, 2001, Crystal growth mechanisms of quartz overgrowths in a Cambrian quartz arenite: *Journal of Sedimentary Research*. v. 71, p. 809–816.
- Marchand, A. M. E., Haszeldine, R. S., Macaulay, C. I., Swennen, R., and A. E. Fallick, 2000, Quartz cementation inhibited by crestal oil charge: miller deepwater sandstone, UK North Sea. *Clay Miner.* 35, p. 205-214.
- Marchand, A. M. E., Haszeldine, R. S., Smalley, P. C., Macaulay, C. I., and A. E. Fallick, 2001, Evidence for reduced quartz cementation rates in oil-filled sandstones. *Geology* 29, p. 915-918.
- Marchand, A. M. E., Smalley, P. C., Haszeldine, R. S., and A. E. Fallick, 2002, Note on the importance of hydrocarbon fill for reservoir quality prediction in sandstones, *AAPG Bulletin*, v. 86, no. 9 (September 2002), pp. 1561–1571.
- Marin, B. A., Clift, S. J., Hamlin, H. S., and S. E. Laubach, 1993, Natural fractures in Sonora Canyon sandstones, Sonora and Sawyer fields, Sutton County, Texas: *Society of Petroleum Engineers Paper No. 25895*, p. 523–531.
- Marrett, R., 1997, Permeability, porosity, and shear-wave anisotropy from scaling of open fracture populations, in T.E. Hoak, A. Klawitter, and P.K. Blomquist, eds., *Fractured Reservoirs: Characterization and Modeling: Rocky Mountain Association of Geologists Guidebook*, p. 217–226.

- Marrett, R., Laubach, S. E., and J. E. Olson, 2007, Anisotropy and beyond: geologic perspectives on geophysical prospecting for natural fractures. *The Leading Edge*, 26/9, 1106-1111. Reprinted in *Fractured reservoirs: A compendium of influential papers* (2008), AAPG.
- Marvin, R. F., Menhert, H. H., and W. M. Mountjoy, 1966, Age of basalt cap on Grand Mesa: U.S. Geological Survey Professional Paper 550-A, p. 81.
- McBride, E. F., 1989, Quartz cement in sandstones: A review. *Earth Sci. Rev.* 26 (1989), p. 69–112.
- McCall, K. R., and R. A. Guyer, 1994, Equation of state and wave propagation in hysteretic nonlinear elastic material, *Journal of Geophysical Research*, v. 99, p. 23887-23897.
- Meckel, L. D., and M. R. Thomasson, 2008, Pervasive Tight-gas Sandstone Reservoirs: An Overview, in S. P. Cumella, K. W. Shanley, and W. K. Camp, eds., *Understanding, exploring, and developing tight-gas sands - 2005 Vail Hedberg Conference: AAPG Hedberg Series, no. 3, p. 13–27, DOI: 10.1306/13131047H33321.*
- Meissner, F. F., 1984, Cretaceous and Lower Tertiary coals as source for gas accumulations in the Rocky Mountain area, in Woodward, Jane, Meissner, F.F., and Clayton, J.L., eds., *Hydrocarbon source rocks of the greater Rocky Mountain region: Rocky Mountain Association of Geologists*, p. 401–432.
- Meissner, F. F., 1987, Mechanisms and patterns of gas generation/storage/expulsion-migration/accumulation associated with coal measures in the Green River and San Juan Basins, Rocky Mountain Region, U.S.A., in B. Doligez, ed., *Migration of hydrocarbons in sedimentary basins, 2nd Institute Francais du Petrole Exploration Research Conference, Carcais France, June 15–19, 1987: Paris, Editions Technip*, p. 79–112.
- Middleton, M. F., 1982, Tectonic history from vitrinite reflectance: *Royal Astron, Soc. Geophys. Jour.*, v. 68, p. 121-132.
- Milliken, K. L., 1994, The widespread occurrence of healed microfractures in siliciclastic rocks: evidence from scanned cathodoluminescence imaging: in Nelson, P. P. and Laubach, S. E. (eds.), *Rock Mechanics: Models and Measurements, Challenges from Industry*, 1st North American Rock Mechanics Symposium, A. A. Balkema, Rotterdam, p. 825-832.
- Monroe, R. J., and J. H. Sass, 1974, Basic heat-flow data from western United States, in J. H. Sass and R. J. Monroe, eds., *Basic heat-flow data from western United States: U.S. Geological Survey Open File Report 74-9, p. 3.1–3.185.*

- Monus, F. L., Broussard, F. W., Ayoub, J. A., and W. D. Norman, 1992, Fracturing unconsolidated sand formations offshore Gulf of Mexico, SPE 24844 presented at 67th Annual Tech. Conference Exhib. held in Washington DC, p. 817–831.
- Mussler, B., Swain, M. V., and N. Claussen, 1982, Dependence of fracture toughness of alumina on grain size, and test technique: *Journal of The American Ceramic Society*, v. 65, no. 11, p. 566–572.
- Nuccio V. F., and L. N. R. Roberts, 2003, Thermal Maturity and Oil and Gas Generation History of Petroleum Systems in the Uinta-Piceance Province, Utah and Colorado, Chapter 4 of Petroleum Systems and Geologic Assessment of Oil and Gas in the Uinta-Piceance Province, Utah and Colorado By USGS Uinta-Piceance Assessment Team, U.S. Geological Survey Digital Data Series DDS–69–B, SBN=0-607-99359-6.
- Nuccio, V. F., and R. C. Johnson, 1983, Thermal maturity map of the Cameo-Fairfield or equivalent coal zone through the Piceance Creek Basin, Colorado—A preliminary report: U.S. Geological Survey Miscellaneous Field Studies Map MF-1575, scale 1:253,440, 2 sheets.
- Nuccio, V. F., and R. C. Johnson, 1984, Thermal maturation and burial history of the Upper Cretaceous Mesaverde Group, including the Multiwell Experiment (MWX), Piceance Creek basin, Colorado, in C. W. Spencer and C. W. Keighin, eds., *Geologic studies in support of the U.S. Department of Energy Multiwell Experiment, Garfield County, Colorado*: USGS Open-File Report 84-757, p. 102-109.
- Nuccio, V. F., Schmoker, J. W., and Fouch, T. D., 1992, Thermal maturity, porosity, and lithofacies relationships applied to gas generation and production in Cretaceous and Tertiary low-permeability (tight) sandstones, Uinta Basin, Utah, in Fouch, T. D., Nuccio, V. F., and Chidsey, T. C., Jr., eds., *Hydrocarbon and mineral resources of the Uinta Basin, Utah and Colorado*: Utah Geological Association Guidebook 20, p. 77–93.
- Nuccio, V.F., and R.C. Johnson, 1986, Thermal maturity map of the lower part of the Upper Cretaceous Mesaverde Group, Uinta Basin, Utah: U.S. Geological Survey Miscellaneous Field Studies Map MF–1842, 1 sheet.
- Oelkers, E. H., Bjorkum, P. A., Walderhaug, O., Nadeau, P. H., and W. M. Murphy, 2000, Making diagenesis obey thermodynamics and kinetics; the case of quartz cementation in sandstones from offshore mid-Norway, Oxford-New York-Beijing, Pergamon, p. 295-309.
- Olson, J. E, Laubach, S. E., and R. H. Lander, 2009, Natural fracture characterization in tight gas sandstones: Integrating mechanics and diagenesis. *AAPG Bulletin*, v. 93, no. 11, p. 1535-1549.

- Olson, J. E., 1993, Joint pattern development: effects of subcritical crack growth and mechanical crack interaction: *Journal of Geophysical Research*, v. 98-B7, p. 12251–12265.
- Olson, J. E., 1997, Natural fracture pattern characterization using a mechanically-based model constrained by geologic data—moving closer to a predictive tool: 36th U.S. Rock Mechanics Symposium, p. 391.
- Olson, J. E., 2004, Predicting fracture swarms - the influence of subcritical crack growth and the crack-tip process zone on joint spacing in rock, *in* Cosgrove, J.W., and Engelder, T., editors, *The initiation, propagation, and arrest of joints and other fractures*, Geological Society of London Special Publication 231, p. 73-87.
- Olson, J. E., Laubach, S. E., and R. H. Lander., 2009, Natural fracture characterization in tight gas sandstones: Integrating mechanics and diagenesis, *AAPG Bulletin*, V. 93, No. 11 (November 2009), p. 1535-1549, DOI:10.1306/08110909100.
- Olson, J. E., Qiu, Y., Holder, J., and P. Rijken, 2001, Constraining the spatial distribution of fracture networks in naturally fractured reservoirs using fracture mechanics and core measurements: *SPE Annual Technical Conference and Exhibition: New Orleans, LA*, Paper No. SPE 71342.
- Ortega, O. J., Marrett, R. A., and S. E. Laubach, 2006, A scale-independent approach to fracture intensity and average spacing measurement, *AAPG Bulletin*; February 2006; v. 90; no. 2; p. 193-208; DOI: 10.1306/08250505059.
- Ozkan A., Cumella, S. P., Milliken, K. L., and S. E. Laubach, accepted manuscript in revision, *Prediction of Lithofacies and Reservoir Quality Using Well Logs, Williams Fork Formation, Mamm Creek Field, Piceance Basin*, *AAPG Bulletin*.
- Ozkan, A., 2001, *The Diagenesis and Porosity Evolution of the Flathead Sandstone*, MSc. Thesis, University of Texas at Austin, p. 190.
- Park, N., 2006, *Discrete element modeling of rock fracture behavior: fracture toughness and time dependent fracture growth*, University of Texas at Austin, Ph.D. Dissertation, 263 p.
- Paxton, S. T., Szabo, J. O., Ajdukiewicz, J. M., and R. E. Klimentidis, 2002, Construction of an intergranular volume compaction curve for evaluating and predicting compaction and porosity loss in rigid-grain sandstone reservoirs, *AAPG Bulletin* 86, p. 2047–2067.
- Payne, D. F., Tuncay, K., Park, A., Comer, J. B., and P. Ortoleva, 2000, A reaction-transport-mechanical approach to modeling the interrelationships among gas generation, overpressuring, and fracturing : Implications for the upper cretaceous

- natural gas reservoirs of the Piceance Basin, Colorado, Volume 84, Issue 4, p. 545–565.
- Perez R. J., and J. R. Boles, 2005, Interpreting fracture development from diagenetic mineralogy and thermoelastic contraction modeling, *Tectonophysics*, vol. 400, Issue: 1-4, p. 179-207.
- Perez, H. H., Datta-Gupta, A., and S. Mishra, 2003, The Role of Electrofacies, Lithofacies, and Hydraulic Flow Units in Permeability Predictions from Well Logs: A Comparative Analysis Using Classification Trees, paper SPE 84301 presented at the SPE Annual Conference and Exhibition (2003), Denver, CO, October 5-8; *SPE Reservoir Evaluation and Engineering*, 11 p., DOI: 10.2118/84301-MS.
- Philip, Z. G., Jennings, J. W. Jr., Olson, J. E., Laubach, S. E., and J. Holder, 2005, Modeling coupled fracture-matrix fluid flow in geomechanically simulated fracture networks: *SPE Reservoir Evaluation & Engineering*, v. 8, no. 4, p. 300-309.
- Philip, Z., 2003, Incorporating Subcritical Crack Growth Mechanics into Natural Fracture Characterization for Improved Reservoir Simulation, University of Texas at Austin, Ph.D. Dissertation, p. 175.
- Pitman, J. K., and E. S. Sprunt, 1986, Origin and distribution of fractures in lower Tertiary and Upper Cretaceous rocks, Piceance Basin, Colorado, and their relation to the occurrence of hydrocarbons, in Spencer, C.W., and Mast, R.F., editors, *Geology of tight gas reservoirs: American Association of Petroleum Geologists Studies in Geology* 24, p. 221-233.
- Pitman, J. K., Spencer, C. W., and R. M. Pollastro, 1989, Petrography, mineralogy, and reservoir characteristics of the Upper Cretaceous Mesaverde Group in the east-central Piceance Basin, Colorado: *U.S. Geological Survey Bulletin*, 1787-G, 31 p.
- Pittman, E. D., and R. E. Larese, 1991, Compaction of lithic sands; experimental results and applications, *AAPG Bulletin*, v. 75, p.1279-1299.
- Pollard, D. D., and A. Aydin, 1988, Progress in understanding jointing over the past century, *Geol. Soc. Amer. Bull.* vol. 100 (188), pp. 1181–1204.
- Pollastro, R. M., 1984, Mineralogy of selected sandstone/shale pairs and sandstones from the Multiwell Experiment--interpretations from x-ray diffraction and scanning electron microscope analyses, in C. W. Spencer and C. W. Keighin, eds., *Geologic studies in support of the U.S. Department of Energy Multiwell Experiment, Garfield County, Colorado: USGS Open-File Report 84-757*, p. 67-74.

- Porras, J. C., Barbato, R., and L. Khazen, 1999, Reservoir Flow Units: A Comparison Between Three Different Models in the Santa Barbara and Piritual Fields, North Monagas Area, Eastern Venezuela Basin, paper SPE 53671 presented at the Society of Petroleum Engineers Latin American and Caribbean Petroleum Engineering Conference (1999), Caracas, Venezuela, April 21-23, p. 7, DOI: 10.2118/53671-MS.
- Pranter, M. J., Ellison, A. I., Cole, R. D., and P. E. Patterson, 2007, Analysis and modeling of intermediate-scale reservoir heterogeneity based on a fluvial point-bar outcrop analog, Williams Fork Formation, Piceance Basin, Colorado: AAPG Bulletin, v. 91, No. 7, p. 1025-1051, DOI: 10.1306/02010706102.
- Prikryl, R. 2001, Some microstructural aspects of strength variation in Rock Intl. J. Rock Mech. Min Sci. 38 (5): 671-82.
- Ramsay, J. G., 1980, The crack-seal mechanism of rock deformation, London, Macmillan Journals, p. 135-139.
- Reinecke, K. M., Rice, D. D., and R. C. Johnson, 1991, Characteristics and development of fluvial sandstone and coalbed reservoirs of Upper Cretaceous Mesaverde Group, Grand Valley field, Colorado. Guidebook for the Rocky Mountain Association of Geologists Fall Conference and Field Trip September, 17-20, 1991, Rocky Mountain Association of Geologists Denver, Colorado, pp. 209-225.
- Reiter, M., Mansure, A. J., and C. Shearer, 1979, Geothermal characteristics of the Colorado Plateau: Tectonophysics, v. 61, p. 183-195.
- Renard, F., Andréani, M., Boullier, A.-M., and P. Labaume, 2005, Crack-seal patterns: records of uncorrelated stress release variations in crustal rocks, In Gapais, D., Brun, J.-P., & Cobbold, P. R. (eds) Deformation Mechanisms, Rheology and Tectonics: from Minerals to the Lithosphere, Geol. Soc. Lond. Spec. Pub., 243, p. 67-79.
- Renshaw, C. E., 1996, Influence of subcritical fracture growth on the connectivity of fracture networks: Water Resources Research, vol. 32, no. 6., p. 1519-1530.
- Renshaw, C. E., and D. D. Pollard, 1994, Numerical simulation of fracture set formation: A fracture mechanics model consistent with experimental observations, Journal of Geophysical Research-Solid Earth, 99 (B5): p. 9359-9372.
- Rice, R. W., Freiman, S. W., and J. J. Jr. Mecholsky, 1980, The dependence of strength-controlling fracture energy on the flaw-size to grain-size ratio: Journal of The American Ceramic Society, v. 63. no. 3-4, p. 129-136.

- Rijken, P., 2005, Modeling Naturally Fractured Reservoirs: from Experimental Rock Mechanics to Flow Simulation, Ph.D. Dissertation, University of Texas at Austin, p. 239.
- Rijken, P., Holder, J. Olson, J. E., and S. E. Laubach, 2002, Predicting fracture attributes in the Travis Peak Formation using quantitative mechanical modeling and structural diagenesis: Gulf Coast Association of Geological Societies Transactions, v. 52, p. 837–847.
- Ritter, U., 1984, The influence of time and temperature on vitrinite reflectance. *Org. Geochem.*, 6, 473-480.
- Rives, T., Razack, M., Petit, J. P., and K. D. Rawnsley, 1992, Joint spacing: analogue and numerical simulations: *Journal of Structural Geology*, v. 14, no. 8/9, p. 925–937.
- Rushing, J. A., K. E. Newsham, and T. A. Blasingame, 2008, Rock Typing - Keys to Understanding Productivity in Tight Gas Sands, Society of Petroleum Engineers, Texas A&M University, SPE paper 114164 prepared for the 2008 SPE Unconventional Reservoirs Conference, Keystone, Colorado, 10–12 February, 31 p., DOI: 10.2118/114164-MS.
- Sabin, F. F., 1962, Grains of detrital, secondary, and primary dolomite from Cretaceous strata of Western Interior: *Geological Society of America Bulletin*, v. 73, p. 1183-1196.
- Sayers, C. M., Dahi Taleghani, A., and J. Adachi, 2009, The effect of mineralization on the ratio of normal to tangential compliance of fractures, *Geophysical Prospecting*, v 57, no. 3, p. 439-446.
- Scheevel, J., and S. P. Cumella, 2005, Stratigraphic and rock mechanics control of Mesaverde gas distribution, Piceance Basin, Colorado (abs.): Rocky Mountain Association of Geologists Petroleum Technology Transfer Council Fall Symposium, Low Permeability Reservoirs in the Rockies, August 29, 2005, Denver, Colorado.
- Scheevel, J., and S. P. Cumella, 2009, Extracting sub-bandwidth detail from 3D amplitude data: An example from the Mesaverde Group, Piceance Basin, Colorado, U.S.A., *The Leading Edge* 28, 1362 (2009); doi:10.1190/1.3259615.
- Shanley, K. W., Cluff, R. M., and J. W. Robinson, 2004, Factors controlling prolific gas production from low-permeability sandstone reservoirs: Implications for resource assessment, prospect development, and risk analysis, *AAPG Bulletin*; August 2004; v. 88; no. 8; p. 1083-1121; DOI: 10.1306/0325040305.

- Sharma, M. M., and A. N. Tutuncu, 1994, Grain contact adhesion hysteresis: A mechanism for attenuation of seismic waves, *Geophys. Res. Lett.*, 21(21), p. 2323–2326.
- Sorby, H. C., 1880, On the structure and origin of non-calcareous stratified rocks, *Q. J. Geol. Soc. London* 37, p. 49–92.
- Spencer, C. W., 1987, Hydrocarbon generation as a mechanism for overpressuring in Rocky Mountain region: *AAPG Bulletin*, v. 71, p. 368–388.
- Spencer, C. W., 1989, Comparison of overpressuring at the Pinedale anticline area, Wyoming and the Multiwell Experiment site, Colorado, *in* *Geology of tight gas reservoirs, Wyoming and Colorado: U.S. Geological Survey Bulletin*, v. 1886, chapter C, p. C1–C15.
- Spieker, E. M., 1946, Late Mesozoic and early Cenozoic history of central Utah. *US Geological Survey Professional Paper* 205-D.
- Suggate, R. P., 1982, Low-Rank Sequences and Scales of Organic Metamorphism, *Journal of Petroleum Geology*, Volume 4, No. 4, p. 377 – 392.
- Sweeney, J. J., and A. K. Burnham, 1990, Evaluation of a simple model of vitrinite reflectance based on chemical kinetics: *AAPG Bulletin*, v. 74, p. 1559-1570.
- Taylor, T. R., Stancliffe, R., Macaulay, C., and L. Hathon, 2004, High temperature quartz cementation and the timing of hydrocarbon accumulation in the Jurassic Norphlet Sandstone, offshore Gulf of Mexico, U.S.A., *in* J. M. Cubitt, W. A. England, and S. R. Larter, eds., *Understanding petroleum reservoirs; toward an integrated reservoir engineering and geochemical approach: Geological Society (London) Special Publication* 237, p. 257–278.
- Teinturier, S., and J. Pironon, 2003, Synthetic fluid inclusions as recorders of microfracture healing and overgrowth formation rates, p. 1204-1208.
- Thiry, M., Ayraul, M. B., and J. C. Grisoni, 1988, Ground-water silicification and leaching in sands: Example of the Fontainebleau Sand (Oligocene) in the Paris Basin, *GSA Bulletin*; v. 100; no. 8; p. 1283-1290; DOI: 10.1130/0016-7606(1988)100<1283.
- Tinker, S. W., and E. Kim, 2002, It's Gonna be Gas: Let's Make it a Smooth Ride, *Natural Gas Technology: Investing in a Healthy U.S. Energy Future*, Plenary Panel: Balancing the Technology Role, <http://www.netl.doe.gov/publications/proceedings/02/ngt/Tinker.PDF>.
- Tissot, B. P., and D. H. Welte, 1984, *Petroleum formation and occurrence*, 2d ed.: Berlin, Springer, 699 p.

- Tristan-Gonzalez, M., Aguirre-Diaz, G. J., Labarthe-Hernandez, G., Torres-Hernandez, J. R., and H. Bellon, 2009, Post-Laramide and pre-Basin and Range deformation and implications for Paleogene (55–25 Ma) volcanism in Central Mexico: A geological basis for a volcano-tectonic stress model, *Tectonophysics* 471, Special Issue, p. 137–153.
- Verbeek, E. R., and M. A. Grout, 1984, Fracture studies in Cretaceous and Paleocene strata in and around the Piceance Basin, Colorado: preliminary results and their bearing on fracture controlled natural-gas reservoir at the MWX site: U.S. Geological Survey Open-File Report 84-156, 30 p.
- Verbeek, E. R., and M. A., Grout, 1984b, Prediction of subsurface fracture patterns from surface studies of joints - an example from the Piceance Creek Basin, Colorado, USGS, Open-File Report 84-757, p. 75-86.
- Wagg, B., Xie, J., Solanki, S. C., and S. Arndt, 1999, Evaluating casing-deformation mechanisms in primary heavy-oil production, SPE 54116 presented at the SPE Int. Thermal Operations and Heavy Oil Symp., Bakersfield, Calif. USA (1999).
- Walderhaug, O., 1990, A fluid inclusion study of quartz-cemented sandstones from offshore mid-Norway; possible evidence for continued quartz cementation during oil emplacement, p. 203-210.
- Walderhaug, O., 1994, Precipitation rates for quartz cement in sandstones determined by fluid-inclusion microthermometry and temperature-history modeling: *Journal of Sedimentary Research*, v. A64, p. 324–333.
- Walderhaug, O., 1996, Kinetic modeling of quartz cementation and porosity loss in deeply buried sandstone reservoirs, *AAPG Bulletin*, v. 80, p. 731–745.
- Walderhaug, O., 2000, Modeling quartz cementation and porosity loss in Middle Jurassic Brent Group sandstones of the Kvitebjørn field, northern North Sea: *AAPG Bulletin*, v. 84, p. 1325–1339.
- Walderhaug, O., Lander, R. H., Bjørkum, P. A., Oelkers, E. H., Bjørlykke, K. and P. H. Nadeau, 2000, Modeling quartz cementation and porosity in reservoir sandstones—Examples from the Norwegian continental shelf, in R. H. Worden and S. Morad, eds., *Quartz cementation in sandstones: International Association of Sedimentologists Special Publication 29*, p. 39–49.
- Waples, D. W. 1985, *Geochemistry in Petroleum Exploration*: Boston, Mass., International Human Resources Development Corporation, 232 p.
- Waples, D. W., 1980, Time and temperature in petroleum formation— Application of Lopatin’s method to petroleum exploration: *American Association of Petroleum Geologists Bulletin*, v. 64, p. 916–926.

- Waugh, B., 1970. Formation of quartz overgrowths in the Penrith sandstone (lower Permian) of northwest England as revealed by scanning electron microscopy: *Sedimentology*, v. 14(3-4), p. 309-320.
- Wiederhorn, S. M., 1967, Influence of Water Vapor on Crack propagation in Soda-lime glass, *Journal of American Ceramic Society*, Vol. 50, p. 407-414.
- Wiederhorn, S. M., 1974, Fracture Mechanics of Ceramics in R.C. Bradt, D. P. Hasselman and F. F. Lange (eds). *Microstructure, Material and Applications*, Vol. 2, Plenum Press, New York, p. 613–646.
- Williams, D. P., and A. G. Evans, 1973, A simple method for studying slow crack growth, *J. Testing and Evaluation*, 1, p. 264-270.
- Wilson, M. S., Gunneson, B. G., Peterson, K., Honore, R., and M. M. Laughland, 1998, Abnormal Pressures Encountered in a Deep Wildcat Well, Southern Piceance Basin, Colorado, Chapter 12, in B.E. Law, G.F. Ulmishek, and V.I. Slavin, eds., *Abnormal Pressures in Hydrocarbon Environments*, AAPG Memoir 70, p. 195-214
- Worden, R. H., and S. Morad, 2000, Quartz cementation in oil field sandstones: A review of the key controversies, in R. H. Worden and S. Morad, eds., *Quartz cementation in sandstones: International Association of Sedimentologists Special Publication 29*, p. 1–20.
- Worthington, M. H., 2008, Interpreting seismic anisotropy in fractured reservoirs. First break volume 26, p. 57 -63.
- Wu, C. Cm., Freiman, S. W., Rice, R. W., and J. J. Mecholsky, 1978, Microstructural aspects of crack propagation in ceramics: *Journal of Materials Science*, v. 13, p. 2659–2670.
- Yale, D. P., Nieto, J. A., and S. P. Austin, 1995, The effect of cementation on the static and dynamic mechanical properties of the Rotliegendes sandstone., 9.169- 176, Paper Number 95-0169, *In Rock Mechanics* (Jaak J. K. Daemen, Schultz, R. A.) (eds), Balkerna, Rotterdam, ISBN 90 5410 552 6. The 35th U.S. Symposium on Rock Mechanics (USRMS), June 5 - 7, 1995, Reno, NV.
- Yurewicz, D. A., Bohacs, K. M., Kendall, J., Klimentidis, R. E., Kronmueller, K., Meurer, M. E., Ryan, T. C., and J. D. Yeakel, 2008, Controls on gas and water distribution, Mesaverde basin-centered gas play, Piceance Basin, Colorado, in S. P. Cumella, K. W. Shanley, and W. K. Camp, eds., *Understanding, exploring, and developing tight-gas sands 2005 Vail Hedberg Conference: AAPG Hedberg Series*, no. 3, p. 105-136.

- Yurewicz, D. A., K. M. Bohacs, J. D. Yeakel, and K. Kronmueller, 2003, Source rock analysis and hydrocarbon generation, Mesaverde Group and Mancos Shale, northern Piceance Basin, Colorado, in Peterson, K. M., Olson, T. M., and Anderson, D. S., eds., Piceance Basin 2003 Guidebook: Rocky Mountain Association of Geologists, p. 130-153.
- Yurewicz, D., 2005, Controls on gas and water distribution, Mesaverde basin center gas play, Piceance Basin, Colorado (abs.): AAPG Hedberg Conference, Understanding, Exploring, and Developing Tight Gas Sands, April 2005, Vail, Colorado.
- Zhang, E., Hill, R. J., Katz, B. J., and Y. Tang, 2008, Modeling of gas generation from the Cameo coal zone in the Piceance Basin, Colorado, AAPG Bulletin, v. 92, no. 8 (August 2008), pp. 1077–1106.
- Zoback, M. L., 2007, Reservoir Geomechanics, Cambridge University Press, The Edinburgh Building, Cambridge, 449 p.
- Zoback, M. D., Anderson, R. E., and G.A. Thompson , 1981, Cenozoic evolution of the state of stress and style of tectonism of the Basin and Ranges Province of the western United States, Philos. Trans. R. Soc. London, Ser. A300 (1981), pp. 407–434.
- Zoback, M. L., and M. D. Zoback, 1989, Tectonic stress field of the continental United States, in: L.C. Pakiser, W.D. Mooney (Eds.), GSA Memoir, vol. 172, 1989, pp. 523–539.
- Zoback, M. D., and M. L. Zoback, 1991, Tectonic stress field of North America and relative plate motions. - In: Slemmons, D.B., Engdahl, E.R., Zoback, M.D. & Blackwell, D.D. (eds.): Neotectonics of North America, 339-366.
- Zuo J., Xie, H., and H. Zhou, 2009, Experimental determination of coupled thermal-mechanical effects on fracture toughness of sandstone, Journal of Testing and Evaluation Volume 37, Issue 1. Paper ID: JTE101542, DOI: 10.1520/JTE101542.

VITA

Aysen Ozkan was born in Kirikkale, Turkey on July 16, 1974, one of twin daughters to Yuksel and Suleyman Ozkan. She graduated from the Geological Engineering Department at the Middle East Technical University in 1996. She started her MSc. education at the Department of Geological Sciences, University of Texas at Austin in 1998 with a scholarship from Turkish Petroleum. After her graduation she worked for Core Laboratories for four years in Houston, Texas and Calgary, Alberta Offices. She started her Ph.D. degree in Geological Sciences at the University of Texas at Austin in 2005. After her graduation she will be working at Shell, Houston with the Reservoir Quality Group.

Permanent address: 100. Yil Isci Sitesi, Omorfo Mah., 180/8, Ankara, Turkey, 06531

This dissertation was typed by the author.